Part A

Physical
Sciences

PROCEEDINGS
OF THE
INDIAN NATIONAL
SCIENCE ACADEMY
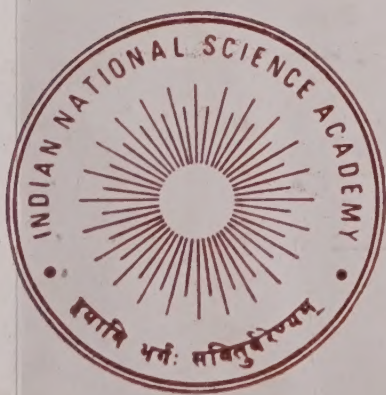
Proceedings of the Indian National Science Academy Part A

(Physical Sciences)

Information to Contributors

Purpose and Scope

PART 'A' of the Proceedings of the Indian National Science Academy is an interdisciplinary Journal in Physical Sciences devoted to publication of papers embodying results of original research in any branch of Physics, Chemistry and Geology. Contributions in Biophysics, Biochemistry, Geochemistry, Hydrology, Meteorology, Radio-Physics, Soil Physics, Soil Chemistry, and Oceanography are also accepted.

Papers presented at the Academy's Symposia, Special Academy Lectures and Original Review articles relating to research and concepts fundamental to Physical Sciences would also be published in the Proceedings.

P. C. MAHALANOBIS MEDAL LECTURE—1984

EVOLUTION OF THE UNIVERSE

G SWARUP

*Radio Astronomy Centre, Tata Institute of Fundamental Research,
P.O. Box 8, Ootacamund 643 001*

1. INTRODUCTION

IT is a great honour to give this Mahalanobis Award Lecture before the distinguished Fellows of the Indian National Science Academy meeting here at Lucknow, one of the most beautiful and romantic cities of India. To a poet, in Lucknow, the entire universe is summed up just in a couplet, and in some eyes here is seen the entire universe ! It is also a fact of the physical nature that the most beautiful scientific theories are condensed just in a few equations and these have allowed us to explore our cosmos in great detail.

There has been a tremendous progress in our understanding of the large scale structure of the Universe in recent years. This has given a wide support to the Big Bang model and has emboldened theoretical astrophysicists to trace the origin and evolution of the universe from a very early age of about 10^{-43} seconds, before which quantum gravitational effects are likely to be predominant, to its current age of about 20 billion light years. However, the ultimate test of all theories rests on observations. In this review, I discuss the evidence which indicates that the observed expansion of the universe originated aeons ago in a primaeval fireball.

To the ancient man, the starry skies beyond the planets seemed totally motionless. Even at the beginning of this century, it was believed that the universe is stationary and static. Also, there was a great controversy whether some of the diffuse nebulae in the sky, firstly catalogued by Messier in the 18th century, were part of our own galaxy or were distant 'island universes' as proposed by William Herschel. This problem could not be resolved till the early part of this century when Slipher measured the displacement of spectral lines in the spectra of prominent nebulae in the sky and discovered that a majority of them were receding away from us with velocities upto about 2000 km s^{-1}. In 1923, soon after the completion of the 100-inch optical telescope at Mt. Wilson, Hubble was able to identify individual stars in the Andromeda Nebula and determined its distance as 800,000 light years (the modern value is 2×10^6 light years). Hence it became clear that our universe consists of a vast number of galaxies lying very much beyond our own Milky Way. Then in 1929, Hubble found a most remarkable result that the farther away the galaxy, the greater is its recession velocity. This result was in conformity with the picture of an expanding universe derived earlier mathematically, by de-Sitter in 1917, Friedmann in 1922 and Lemaitre in 1927, from Einstein's theory of General Relativity and the cosmological principle of isotropy and homogeneity of the

universe. Thus was born the science of modern cosmology, the origin and evolution of the universe.

With the advent of radio astronomy in the fifties, it became possible to probe the universe more deeply because many of the celestial radio sources seemed to be located at much greater distances than the farthest optical galaxies for which redshifts had been measured using the 200-inch optical telescope at Mt. Palomar. Another breakthrough took place in 1965 with the discovery of the microwave radiation background whose spectrum corresponded to a black-body temperature of 2.7 K. This equilibrium temperature fully supported the Big Bang model, according to which the background radiation cooled with the expansion of the universe from about 10^{10}K at t = 1 second to about 3 K at the present epoch.

Simultaneously there has been a great progress in the field of particle physics resulting in Grand Unification Theories (GUTs) for unifying the strong, weak and electromagnetic interactions. To the particle physicists, the very early universe at $t \ll 1$ second is indeed a paradise, full of particles of enormous energies which cannot be produced in the largest of our accelerators. This convergence of cosmology and particle physics has been very fruitful and has been subject of many investigations during the last decade.

In my review, I would first describe the observational and theoretical basis for the expanding universe. I would then concentrate on the important evidence provided by radio astronomy about the evolution of the universe. I would also summarize some of the results obtained by us using the Ooty Radio Telescope located in South India. This would be followed by a description of the very early universe and its subsequent evolution. I finally discuss the epoch of galaxy formation before which there existed only proto-clusters and proto-galaxies from which highly redshifted 21 cm line is expected to be observed at metre wave-lengths. I would briefly describe our plans for discovering such clouds using a proposed Giant Metre-Wavelength Radio Telescope.

In brief, over the next 40 minutes, I plan to give you a grand tour of the universe from its early age of about 10^{-43} seconds to the present age of about 20 billion years. Some of you may find the pace of this tour too fast. But I have given many more details about this fascinating story of the universe in the written version of my talk.

1.1 The Expanding Universe

In order to fathom the universe we must firstly set out to estimate its size and scale. The universe is so vast that it is not an easy thing to measure. However, astronomers have established a variety of ingeneous methods for measuring distances of stars and galaxies. The basic scale depends on the measurement of the parallax of nearby stars (parallax is the apparent shift in the position of a star with respect to the distant background stars when seen from different points of the earth's orbit around the Sun). This method provides distances up to about 30 pc (1 pc = 3.09×10^{18} cm = 3.26 light years). Using this scale, a luminosity-period

relation is established for variable stars which gives distances up to about 4 Mpc. Further, several class of sources have been used by astronomers as 'standard candles' which do not have much spread in their luminosities, e.g. brightest stars in galaxies, eruptive stars such as supernovae, H II regions and brightest galaxies in clusters. Thus, the distance scale has been established by astronomers to very large distances.

The optical spectra of stars and galaxies show a number of emission and absorption lines caused by their excited atoms. The fractional shift in the wavelength of these lines gives the redshift, z, of a galaxy. This Doppler shift is considered to arise due to the motion of a galaxy away from us. In 1929 Hubble made an important discovery that the farther away is a galaxy located from us, faster it is receding. He established a relation

$$v = cz = Hr$$

where v is the recession velocity, c the velocity of light, r the distance and H is now called the Hubble's constant. The value of H has been estimated by measuring v and r for galaxies in the nearby Virgo cluster. Its estimated value lies in the range 50 to 100 km s^{-1} Mpc^{-1} (Tamman and Sandage 1982; de Vaucoulers 1982). In the Big Bang model, the age of the universe now is $\sim 1/H = 20$ billion years for $H = 50$ km s^{-1} Mpc^{-1}.

Assuming that the brighest galaxies in rich clusters of galaxies have the same absolute luminosity, their apparent magnitudes, m, give their relative distances. Hence, a plot of the observable quantities m versus z is a good test of the Hubble's law. In Fig. 1 are shown recent measurements by Sandage (1972). It is seen that
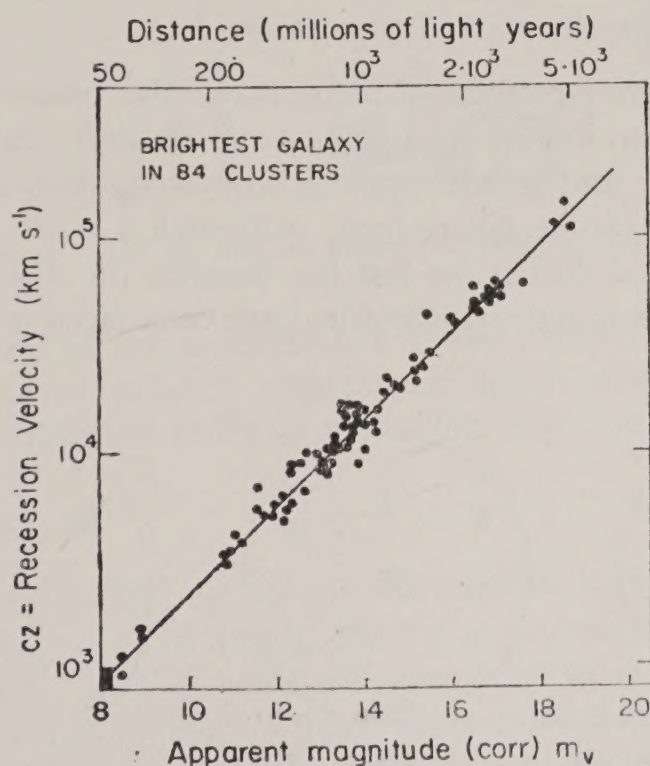

FIG. 1. Hubble's law. Observed data showing that a galaxy's velocity of recession is linearly proportional to the distance from the observer.

Hubble's law is valid for the faintest observed galaxies lying up to a distance of about 5 billion light years (1500 Mpc).

Hence, it has been firmly established that the distant galaxies are moving away from us with velocities proportional to their distances. A dramatic consequence of this result is that the universe is expanding. Following the Coepernicus argument, cosmologists have postulated that our position is not unusual in the universe and, ignoring any local variations, all observers at different position will observe the same gross features in any direction at a given cosmic epoch, i.e. the universe is homogenous and isotropic. Using this principle, it can be shown from Einstein's field equations or even from Newton's laws that the universe cannot remain static and would expand or contract depending upon its matter density. It is interesting to note that the expansion of the universe was predicted theoretically by de-Sitter and by Friedmann well before its discovery by Hubble in 1929.

1.2 Big Bang Model

If the universe is expanding, it may be concluded that its size was very much smaller at an earlier cosmic epoch (Fig. 2). At $t \ll 1$ sec its density was extremely high and it expanded rapidly. The expansion rate is slowed down by gravity. Hence, the deceleration of the universe is dependent on the matter density which determines the curvature of space (Bondi 1960; Sciama 1971; Weinberg 1972; Narlikar 1976; Berry 1976). If the mass density, ρ, is less than a critical value, ρ_c, so that the curvature constant $k = -1$, the universe is 'open' and infinite and its expansion will continue for ever as shown in Fig. 3. In the case of a 'closed' and finite universe with $\rho > \rho_c$ and $k = +1$, the universe will eventually cease expanding and this would be followed by a contraction. For $\rho = \rho_c$ and $k = 0$, the universe will asymptotically expand to infinity.

These models make predictions concerning the observable quantities such as the magnitude—redshift and the angular size—redshift relations, from which the Hubble's constant H_0 and deceleration parameter q_0 (two most important parameters of cosmology) can be determined. Although a great deal of observational effort has been devoted during the last few decades in the 'search of these two numbers', considerable practical difficulties have been faced in finding their accurate
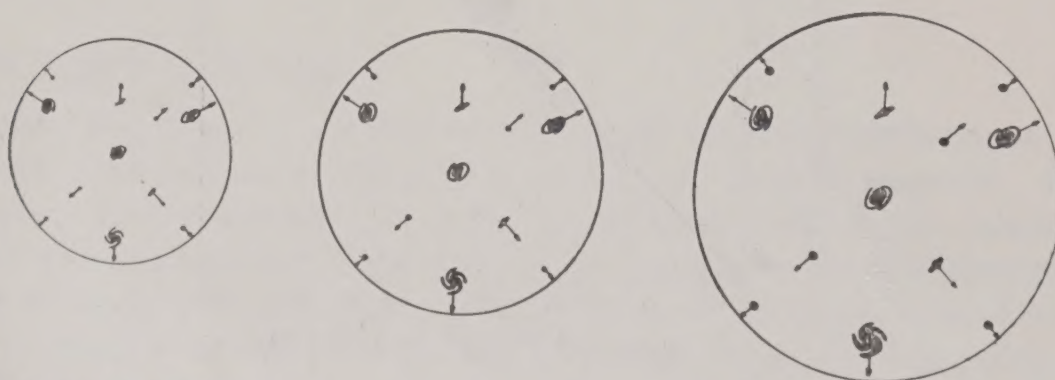
FIG. 2. A sketch showing the expansion of the universe according to the Big Bang model.
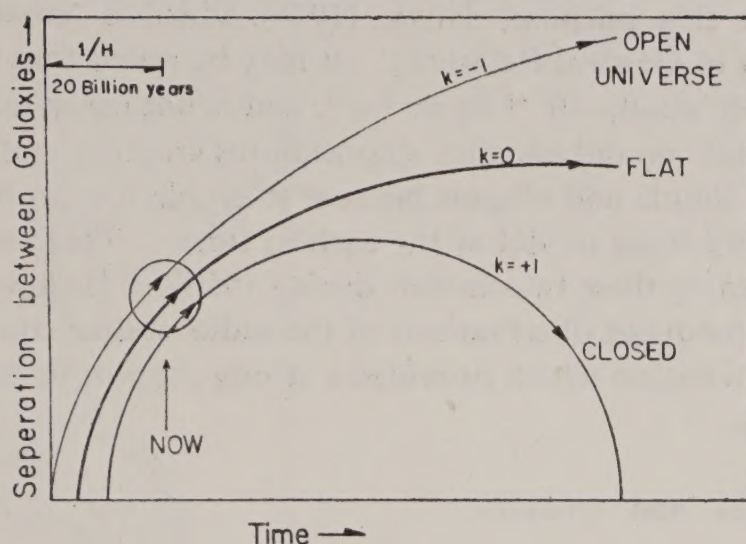
FIG. 3   Expansion of the universe in the Big Bang model depends upon its matter density.
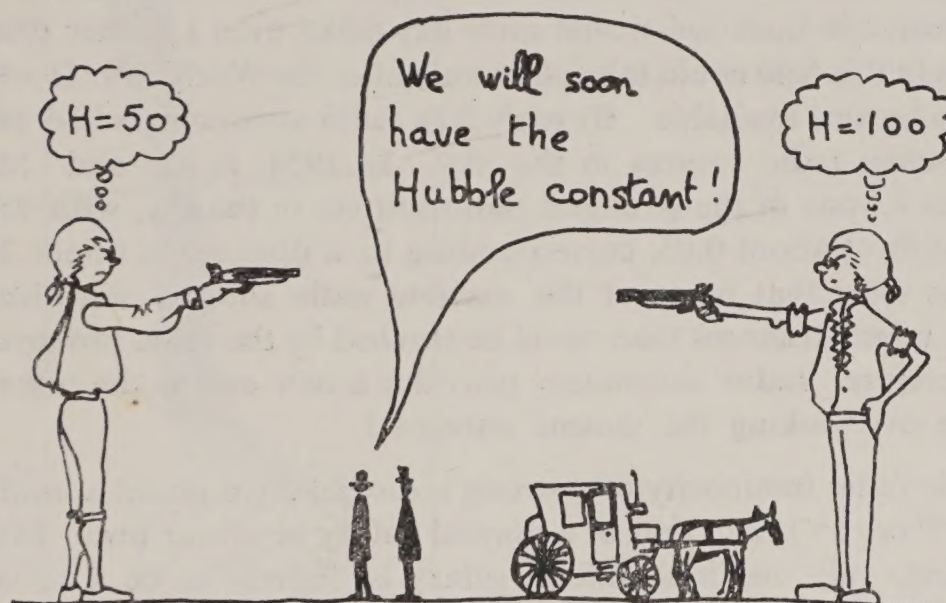
FIG. 4   An old way to derive the Hubble constant !

values mainly because of the uncertainties in the likely luminosity evolution and linear size variations of galaxies with cosmic epoch. Astronomers love intense controversies. Fig. 4 (Paturel 1983) shows an old way of settling these !

1.3   Steady State Model

In the Big Bang model, the matter was created in the beginning.   In 1948 Bondi and Gold proposed the Steady State model, according to which there was no beginning or end.   It is assumed that the universe presents the same average picture to all observers *at all times*.   Hence, the smoothed-out universe is unchanging as well as spatially homogeneous.   In order to keep the mass density, ρ, constant as the universe expands, the Steady State model requires the matter to be created

continuously. For this purpose, Hoyle (1948) added a 'creation term' to the dynamical equation of General Relativity. It may be noted that the required creation rate is extremely small, 10^{-44} kg m^{-3} s^{-1}, and is not measurable in laboratory. Thus, the Steady State model assumes a continuous creation and an infinite age of the universe. It is simple and elegant because it avoids the problem of the initial singularity in the Big Bang model at the earliest time. There was a great deal of lively debate concerning these two models during 1950s. However, the controversy was resolved by subsequent observations of the radio source counts and the microwave background radiation which provided a strong support to the Big Bang model, as discussed below.

1.4 Radio Galaxies and Quasars

Radio astronomy began in 1931 when Karl Jansky discovered that radio noise in the form of a hiss is being emitted from the directions of our Milky way, and not from the industry in New York—he worked at the Bell Laboratories in New Jersey ! (A parallel example could be that of Kanpur and Lucknow and I do hope that a young scientist in Lucknow would some day make even a greater discovery !). A rapid progress in this field could take place only after the World War II when new radio techniques became available. By early 50's radio astronomers had pinpointed many strong discrete radio sources in the sky. In 1954, Baade and Minkowski identified Cygnus A, one of the strongest radio sources in the sky, with an optical galaxy at a redshift of about 0.05, corresponding to a distance of about 300 Mpc. Hence it became clear that many of the discrete radio sources were likely to be located at much larger distances than could be reached by the most powerful optical telescopes. Therefore, radio astronomy provides a new eye to the universe—like Siva's third eye overlooking the violent universe !

The intrinsic radio luminosity of a strong radio galaxy is about a million times larger ($\sim 10^{45-46}$ erg s^{-1}) than that of a normal galaxy or of our own Milky Way. Roughly speaking, only one in a million galaxy is found to be a strong radio source. Typically a radio galaxy is a double radio source with radio lobes located about 100 kpc away on either side of the central optical object (Fig. 5). The presence of radio jets joining the central galaxy to the intense hot spots located at the extremities of the outer radio lobes clearly indicates that the energy is being supplied continuously from the nucleus of the galaxy to the outer radio lobes. The radio emission arises by the synchrotron process in which relativistic electrons spiralling in magnetic fields emit radio waves. To date, radio astronomers have catalogued over 100,000 radio sources in the sky.

Quasars (Quasi-stellar radio sources) were discovered in 1963. They represent certainly the most energetic phenomena in the universe. Most astronomers believe that their observed redshifts imply cosmological distances. Hence, their absolute optical luminosities are found to be more than 100 times larger than that of normal galaxies. Yet their size is incredibly small being less than $\lesssim$ 1–10 pc. Their intensity varies sometimes in less than a day, indicating that their size may be less than $\sim 10^{15}$ cm. In contrast, the size of a normal galaxy is about 30 kpc (10^{23} cm). The
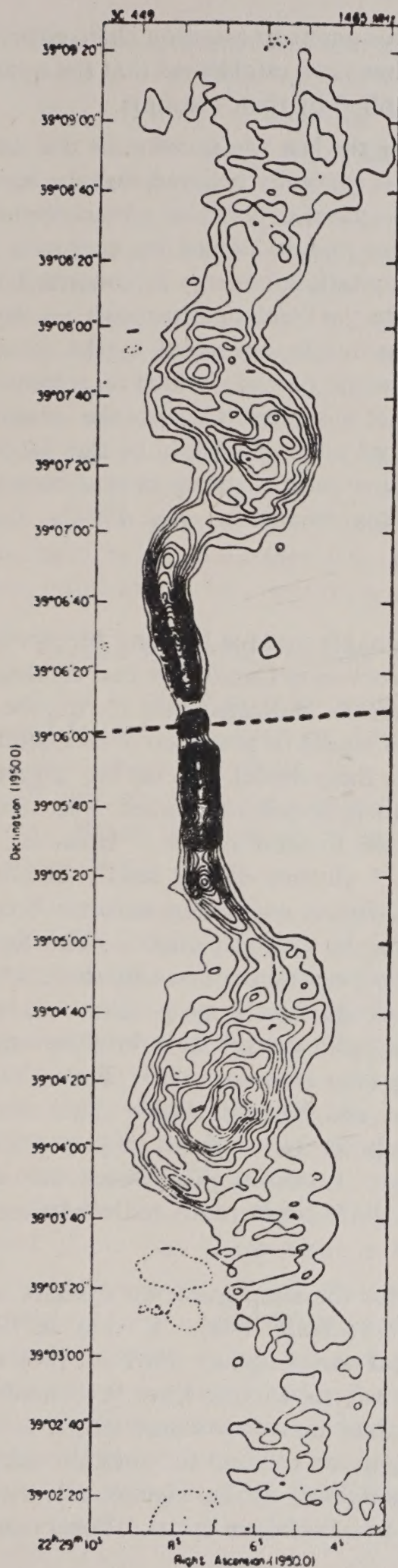
FIG. 5. A map of the radio galaxy 3C 449 showing radio brightness contours. The associated optical galaxy is located near the center where there also exists a compact radio source. A jet of relativistic electrons supplies energy to the outer radio lobes.

extreme properties of quasars have led some astronomers to question their cosmological redshifts. However, a variety of observations have established that the quasars are indeed located at very large distances as implied by their redshifts.

Quasars have been studied extensively during the last two decades in the radio, infrared, optical, X-ray and γ-ray windows. It is generally believed that the central 'engine' or 'prime-mover' of a radio galaxy or a quasar consists of a black hole as massive as hundred million suns ! The black hole may be fuelled by capturing gas or even stars from the surrounding galaxy. Gravitational energy is converted into radiation as the captured material swirls down into the black hole through an accretion disk consisting of hot gas. A funnel and a nozzle supported by the rotation of the surrounding gas give rise to a jet of relativistic particles which is responsible for the double radio source. If the relativistic jet is pointed towards the observer, the intensity of the central component is enhanced a thousand fold by the Doppler effect, giving rise to a flat spectrum radio source with a strong central core (Orr and Browne 1982; Kapahi and Saikia 1982; Vijayanarasimha *et al.* 1984).

1.5 Radio Source and Quasar Counts

Radio source counts have proved to be a valuable tool for probing the structure of the universe. By late-fifties, Ryle and his co-workers at Cambridge had catalogued many hundred discrete radio sources. Their results indicated that the number of weaker radio sources increased more rapidly than would be predicted in an Euclidean model. This provided a strong support to the Big Bang model. To see the argument simply, consider an Euclidean space with an uniform density of sources. The number of sources, $N \propto R^3$, where R is the distance to the farthest source. However, the intensity, or flux density S, decreases as $S \propto R^{-2}$ (inverse-square law). Hence, $N \propto S^{-1.5}$. The exponent would be smaller than 1.5 for an expanding universe because of the decrease of intensity of a receding source by Doppler effect. The Steady State model also predicts a slope of < 1.5. However, numerous radio surveys have indicated that the slope of the log N–log S curve is significantly steeper than 1.5, being about 1.7. The steeper slope indicates that the radio sources were brighter and/or more numerous in the past than they are today (van Hoerner 1973; Peacock and Gull 1981; Swarup *et al.* 1982; Subrahmanya and Kapahi 1982). The number density of radio sources increases approximately as $(1 + z)^\beta$ where β is about 5 (recent models prefer an exponential evolutionary function). Therefore, the radio source counts indicate that there were about 1000 times more radio sources at $z \sim 3$–4 than those at present.

Simlarly, the slope of the number counts for the steep spectrum quasars indicates strong evolutionary effects (Kulkarni 1978; Wall 1983). It may be noted that quasars are seen as blue objects at optical wavelengths. Further, they have strong emission lines. During the last decade several surveys have been made for such objects selected purely optically. It is found that only about 10 per cent of these are radio-loud. The number-optical magnitude relation for optically selected quasars, sometimes called quasi-stellar objects (QSOs) is also significantly steeper than that expected for a uniform distribution in Euclidean space. Total number

of QSOs brighter than absolute magnitude in blue $M_B = -23$ vary from 28 Gpc^{-3} at $z = 0$ to 1600 Gpc^{-3} at $z = 1$ and 10,000 at $z = 3$ (Schmidt 1982).

It is important to note that both the radio source counts and optical surveys indicate that the co-moving space density of radio galaxies and quasars must decrease and converge at redshifts greater than about 3 or 4 (Peacock and Gull 1981; Subrahmanya and Kapahi 1983). For almost a decade the most distant known quasar had a redshift of about 3.4. In 1982 a quasar was found at a redshift of 3.78 (Peterson 1983). Recently a deep survey was made by Osmer (1982) to detect Lyman-α emission from QSOs expected in the redshift range 3.7 to 4.7. By a smooth extrapolation of the evolution function found at lower redshifts, one expected him to see 20 QSOs but none was found. Thus, it seems that quasars appeared in the universe only at redshifts of less than about 4 or 5, i.e. at a cosmic age of more than 15 per cent (3 billion years) of its present age of 20 billion years. I may add here that recently newspapers have published the discovery of a very distant QSO (redshift was not given). The public interest in astronomy (and unfortunately also in astrology) is so great that astonomers come to know of new results well before their publications in scientific journals !

1.6 Angular Size—Flux Density Relation

It is a common experience that the angular size of an object decreases as it is located farther away from us, being inversely proportional to the distance in an Euclidean space. However, as a result of the curvature of space in the universe, a ray of light travels along a curved path rather than a straight line over long distances. Hence, the variation of angular size with distance may be used for choosing a correct world model.

Towards this objective, I proposed in 1963 measurement of angular sizes of a large number of strong and weak radio sources by utilizing the method of lunar occultation for which purpose a special concept for a large steerable radio telescope was developed. Fig. 6 shows the Ooty Radio Telescope which consists of a 530 m long and 30 m wide parabolic cylindrical antenna. Its axis of rotation has been made parallel to that of the earth by placing it on a suitably inclined hill, whose slope in the north-south direction has the same value as Ooty's latitude. Thus, the radio telescope can steer radio sources for about 10 hours/day. The radio telescope was constructed indigenously during 1965–69. The Ooty lunar occulation survey provided the most detailed information on the structure of faint sources till the advent of the Very Large Array in USA in 1980.

As shown in Fig. 7, it is found that the median value of angular sizes decreases statistically from about 100 arcsec for the nearby strong radio galaxies to about 10 arcsec for radio sources of smaller flux densities and then approaches asymptotically a value of about 8 arcsec for the weakest sources (Swarup 1975; Windhorst 1984). Combining these results with the angular size counts for the stronger sources it is found that not only the density of radio sources was higher but also their linear size smaller at earlier cosmic epochs (Kapahi and Subrahmanya 1982). The Ooty group has also investigated many other properties of radio galaxies and quasars,
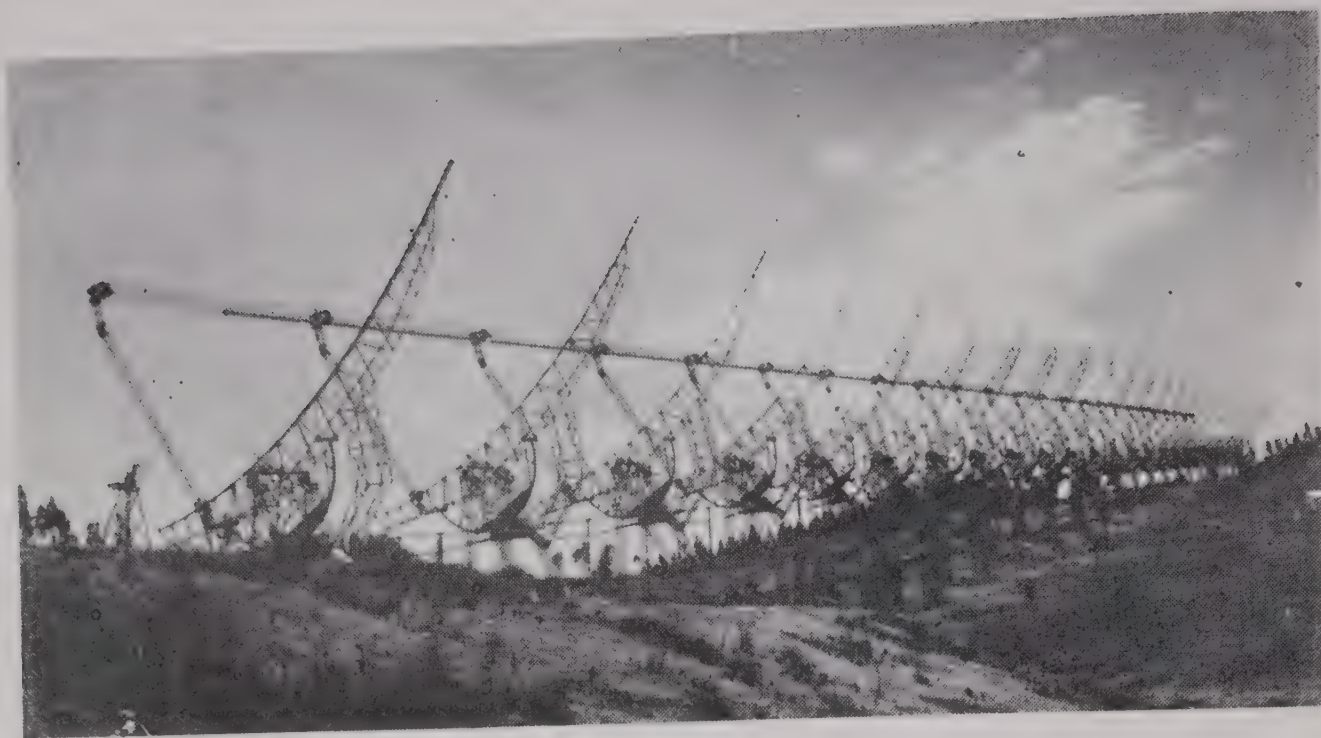
FIG. 6   A photograph of the 530 m long and 30 m wide Ooty Radio Telescope.   It is mechanically steerable from —4^h to 5^{h}30^m and electrically from —40° to + 40°.

FIG. 7   The observed relation between the median values of flux density, S, and angular size, θ. The estimated errors in $θ_m$ are indicated by vertical lines and the ranges in flux density by horizontal lines.

such as their spectral index distribution and statistics of hot spots, jets and cores, for understanding their evolutionary properties.   However, radio galaxies and quasars continue to pose a great number of mysteries and unsolved problems.   A great deal more needs to be done for understanding their physics so that we can use these extra-ordinary objects to study the history of the universe.

1.7 The Cosmic Microwave Background Radiation

Perhaps the most convincing evidence favouring the Big Bang cosmology is the existence of the cosmic microwave background radiation uniformly distributed across the sky and with a temperature of about 2.7 K above absolute zero. This was discovered accidentally by Penzias and Wilson in 1965 when they were making accurate measurements with a horn-type antenna developed for satellite communication. In fact a radiation of about 5 K was predicted in late 1940s by George Gamow and his collaborators as a relict of the Hot Big Bang. Gamow had suggested that nucleo-synthesis of elements took place when the temperature of the universe was about 10^{10} K at about 1 second after the Big Bang. However, it was shown later that no significant amount of elements heavier than helium could be synthesized in the Big Bang because of the absence of stable nuclei with atomic weights of 5 and 8. The heavier elements could be easily produced during the evolution of stars. Hence Gamow's theory went into obscuration and inspite of advances in radio astronomy nobody took a note of his prediction of the relict radiation ! The discovery of the radiation by Penzias and Wilson has been considered as one of the two most golden moments of cosmology, the first being Hubble's work.

As shown in Fig. 8, the spectrum of the microwave background radiation has a Planckian or Rayleigh-Jeans spectrum (Smoot 1983) which peaks like a black body radiation at a wavelength of about 2 mm. However, there are appreciable
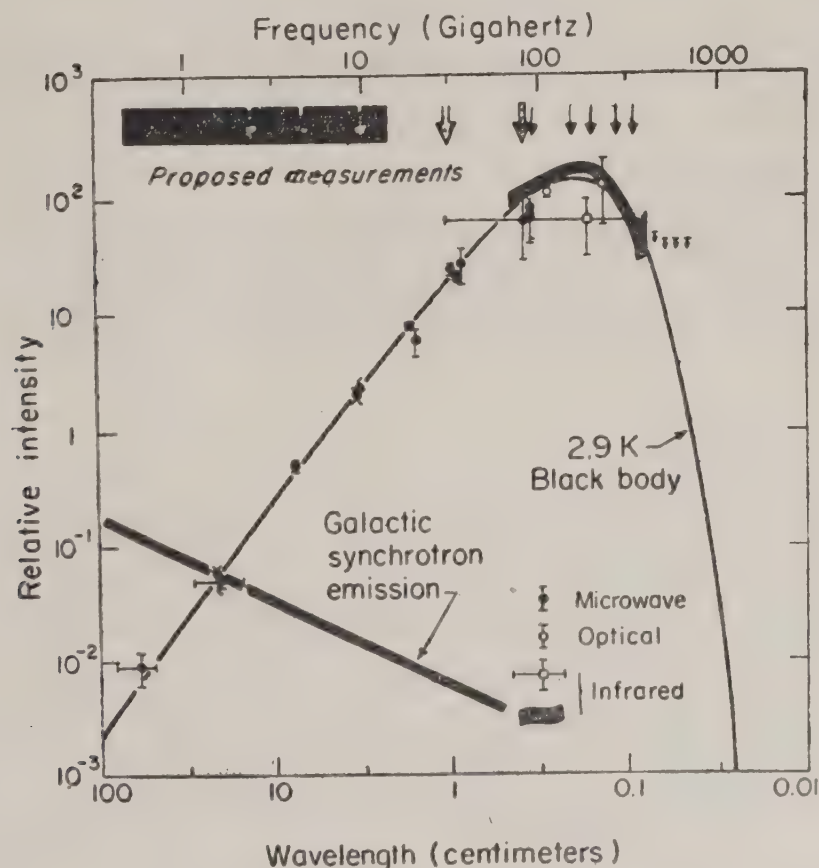
XBL 811-2100

FIG. 8. Current and proposed measurements of Cosmic Microwave Background Radiation Spectrum.

uncertainties in its spectrum at wavelengths shorter than a few mm. Because of the atmospheric absorption at such short wavelengths, measurements have to be carried out at altitudes greater than about 30 km. So far only high flying balloons using total power detectors have been used. Satellite experiments are planned later this decade for measuring its spectrum more accurately and these should provide very valuable information about the universe.

A most important property of the microwave background radiation is its isotropy. The radiation is remarkably uniform across the sky to better than 1 part in 1000 (except for a dipole anistropy due to the motion of the sun and our Galaxy towards the nearby Virgo supercluster). The anistropy is less than 1 part in 10^4 over angular scales of few arc minute and less than 1 part in 3.5×10^4 over $6°$ (Patridge 1982). This remarkable isotropy of the radiation clearly shows that the radiation is not local and is produced at cosmological distances. There seems to be no explanation for such a radiaton in the Steady State theory. It may be noted however that the radiation has been explained by postulating long graphite whiskers in the intergalactic medium distributed over cosmological distances, consistent with a cold Big Bang (Rana 1981). This model also attempts to explain some of the observed departures of the spectrum from the Planckian distribution. However, as discussed elsewhere the overall evidence for the Hot Big Bang is quite overwhelming.

2. Observational Puzzles

A suitable model of the universe should explain its major observational features, as summarized below.

2.1 Expanding Universe

Observations indicate that the universe is expanding. Both optical and radio surveys strongly support that it is homogeneous and isotropic over scales exceeding 100–200 Mpc (in every direction there are galaxies with no bias for one direction or other).

2.2 Abundances of Elements

The universe consists of about 73 per cent hydrogen, 25 per cent helium and only about 2 per cent heavier elements. The abundances of heavier elements can be satisfactorily explained by the nucleo-synthesis in the hot core of stars. However, the lighter elements (D, ^{3}He, ^{4}He and ^{7}Li) are likely to have originated at an earlier cosmic epoch. The primordial abundances of these elements have been estimated by many workers (e.g. Audouze 1982). In particular, the abundance of helium is about 25 per cent by mass of hydrogen in the universe. The abundance of deuterium is only about 0.002 per cent and even this cannot be produced by the stellar nucleo-synthesis.

2.3 Missing Mass

The density of visible matter in the universe has been estimated from the observed mass to light ratio of galaxies and is found to be about 3×10^{-31} gm cm^{-3}.

This is about one-fifteenth of the required density for a closed universe. On the other hand, the matter density is estimated to be very much higher from dynamical considerations, such as from the rotation curves of galaxies or the motion of galaxies in clusters. Therefore, the evidence suggests that over 90 per cent of the mass of the universe is in dark matter (low mass stars? black holes ? neutrinos ?).

2.4. Isotropy of Microwave Background and the Horizon Problem

As discussed above, the 2.7 K microwave radiation is highly isotropic over large angular scales. The corresponding spatial extents are very much larger than the particle horizon at the epoch when matter and radiation decoupled at $z \sim 1000$ (at an age since the Big Bang of about 300,000 years). The particle horizon in an expanding universe represents the limiting distance between two observers beyond which they cannot communicate even by sending a light signal. Therefore, the question arises as to why the 2.7 radiation is the same at distances much beyond the particle horizon.

2.5. Photon-baryon Ratio

The observed value for the ratio is $\sim 10^9 : 1$. This ratio may also be considered a measure of the entropy of the universe. A satisfactory model should explain as to why this value is so high.

2.6. Galaxies, Clusters and Great Voids

The observed large scale distribution of galaxies indicates that a majority of them are clustered over scales of a few Mpc. Further, there are seen super-clusters and cellular or pancake shaped structures, with apparent great voids in the universe where not many galaxies are found (Oort 1983). Also, quasar observations indicate that proto-galaxies may have collapsed to form galaxies only at $z \lesssim 5$–10. These observations obviously pose the important question as to what were the initial density fluctuations in the early universe which gave rise to clusters and galaxies through gravitational instabilities and various dissipative processes. No doubt, a satisfactory theory of galaxy formation is one of the biggest challenges in astrophysics at present.

3. EVOLUTION OF THE UNIVERSE

According to the Big Bang model the universe was extremely dense at an early age, say a 'billion tons in a thimble' ! The universe certainly got off with a spectacular start. As said by the well-known Russian astrophysicist Ya. B. Zeldovich, one really needs courage to imagine the universe compressed in a nutshell and to remain faithful to the physical laws leading to such a seemingly absurd picture. There seems no difficulty, however, in going back to a cosmic time of about 10 milliseconds after the Big Bang when the density of particles in the universe was below the nuclear density and therefore the well-established physical principles can be applied. At this epoch, the temperature $T \sim 10^{11}$ K and the matter literally consisted of a hot soup of protons, neutrons, electrons, positrons, neutrinos, anti-neutrinos and photons. As the universe cooled, there formed hydrogen and helium. These are the building blocks of the present day universe. Over the last decade, astrophysicists have made a remarkable progress in the undersanding of this picture. But, in order to

minimize the number of initial conditions, we must go back to a much earlier epoch. Here, the cosmology provides a valuable testing ground for the Grand Unification theories of the particle physics, concerning the matter at extremely high energies. The era before $t \leqslant 10^{-43}$ second, however, remains very uncertain when the densities $\gtrsim 10^{93}$ gm/cm^{-3} and the scale factor of the universe is less than the Planck-length, $r_p = 10^{-33}$ cm. Before this era, quantum gravity effects are likely to be predominant.

I describe below three major eras of the evolution of the universe : (a) the very very early universe ($t \sim 10^{-43} - 10^{-6}$ sec), (b) the standard Hot Big Bang model and (c) the present large scale structure of the universe and the formation of galaxies. Fig. 9 summarizes the history of the universe according to the Big Bang model.

3.1. The Very Very Early Universe

3.1.1. The Inflationary Period

In the Grand Unified Theories, the strong, weak and electro-magnetic interactions have equal strength at $E \sim 10^{14}$ Gev. There are three important cosmological

HISTORY OF THE UNIVERSE

ERA	COSMIC TIME	EVENT	Z	T
MATTER DOMINATED	20 Billion years	Now : Homo Sapiens	0	2.7K
	5 Billion years	Quasars are born	3	
	2 Billion years	Galaxy formation beings	10	
	300,000 years	Decoupling of matter and radiation	10^3	4000K
RADIATION DOMINATED	1 minute	Nucleo-synthesis of Helium and Deuterium		
	1 second	Leptonic era		10^{10}K
	10^{-6} second	Hadronic era		10^{13}K
EARLY UNIVESE	10^{-35} second	Baryon non conservation		10^{14}Gev
	10^{-45} second	phase transition Planck time		10^{19}Gev
	0	BIG BANG	∞	

Fig. 9　History of the Universe.

consequences of GUTs. The first is the nonconservation of baryon number. In the simplest model, it is estimated that the lifetime of protons is in the range 10^{31} to 10^{33} years. This nonconservation implies that in the beginning, the universe may well have been in the state of a 'vacuum'. The second consequence is the existence of phase transitions when T is of order 10^{14} Gev. The third is the prediction of a high energy density of monopoles, which is however, not observed in the present day universe.

Recently Guth (1981, 1983) made a brilliant suggestion that the universe went through a phase of exponentially rapid expansion when $E \sim 10^{14}$ Gev at $t \sim 10^{-35}$ second. The exponential expansion occurs for a Robertson-Walker metric if the energy density, ϵ, of the no-particle (metastable vacuum) state of the universe remains constant, e.g. when the cosmic repulsion constant in the Einstein's field equation $\lambda > 0$. Hence the pressure is negative : $p = -\lambda = -\epsilon$. According to the first law of thermodynamics, $dE = -pdV$, with $E = \epsilon V$, where V is the volume; for $p = -\epsilon$, we get $d(\epsilon V) = \epsilon dV$ which is consistent with $d\epsilon = 0$ and $\epsilon = $ constant (Zeldovich 1983). A constant energy density with the expansion of the universe implies getting something for nothing, or as Guth put it : the early universe was a free lunch ! It works because negative pressure feeds energy into an expanding system. Alternatively, one can state that the total energy in a closed universe is zero with the positive energy of matter and radiation being exactly compensated by the negative energy of the gravitational interaction between them (Zeldovich 1983).

The inflationary universe model avoids many problems of the standard Big Bang model (Barrow and Silk 1983). There is no significant production of monopoles, as consistant with observations. Before the inflation, the 'horizon' of the universe was larger than the size of the rapidly expanding bubble, which explains why the cosmic microwave background is isotropic over large scales. In the standard model, the two antennas pointed in opposite directions would be pointed over regions which are over 90 horizon lengths and it was not clear as to how they came to have the same microwave background temperature. And finally, the universe is expected to be rather spatially flat in the inflationary model so that the density parameter $\Omega = \rho/\rho_c$ is of the order of unity as observed.

3.1.2. *Baryon Asymmetry of the Universe*

Taking the ratio of the energy density of the 2.7 K microwave background to that for the visible matter in the universe, it is found that the ratio of photons to baryons is about $10^9 : 1$. Further, there are extremely few antiprotons today. How does this fit into GUT scenario ?

Soon after the phase transition at $t \sim 10^{-35}$ seconds, the thermal energies were quite high (10^{14} Gev) so that X and $\overline{X}$ bosons existed according to GUTs. During the cooling X decays to a quark pair or antiquark and positron. Similarly $\overline{X}$ decays to antiquark pair or quark and electron. The masses and decay probabilities of X and $\overline{X}$ are the same but the branching ratios for the decay between the pure quark

or quark-lepton pair may be slightly greater for X than $\overline{X}$. This model explains roughly the observed proton to baryon ratio of $10^9 : 1$.

I may add here that the GUTs also predict proton decay through the intermediate X boson, with the probability of decay decreasing as the mass of X increases. The results of the proton decay experiments being carried out at Kolar Gold fields in India (a pioneering experiment) and now by several other groups in USA, Europe and Japan would be of great fundamental importance for constraining GUT models. Also new results are being obtained using large linear accelerators. These developments are being watched with the greatest interest by both the particle physicists and cosmologists.

3.2. The Standard Hot Big Bang Model

3.2.1. *The Synthesis of Light Elements*

During the earliest phases at $t \lesssim 10^{-6}$ seconds when $T \gtrsim 10^{13}$ K, a wide variety of particles and antiparticles existed with a slightly higher number density for the former. As the universe expanded and the thermal energy kT became less than the threshold of $\sim 10^{13}$ K for the creation of proton-antiproton pair, they annihilated leaving only the primordial excess of 1 baryon in 10^9. At about 1 millisecond, electrons, positrons, neutrionos and antineutrinos were in thermal equibilibrium (Weinberg 1977; Novikov 1983). The time-temperature dependence was $t \propto T_{10}^{-2}$ second, where T_{10} 10^{10} K. By about $t \sim 0.3$ seconds, neutrinos and antineutrinos ceased to interact with matter and decoupled. Subsequently, their number density has remained the same, but their energy density has been decreasing constantly because of the redshift caused by the expansion. If their mass is finite as postulated by many theorists, neutrinos are likely to be responsible for the 'hidden' or 'missing' mass around galaxies and clusters today (Cowsik and Mclelland 1972). At $T \simeq 5 \times 10^9$ K ($kT = 0.5$ Mev $\simeq m_e c^2$), most of the electron-positron pairs annihilated and their energy went exclusively into photons.

At $T > 10^{11}$ K, the protons and neutrons converted into each other constantly in the presence of electrons, positrons, neutrinos and antineutrinos. The neutron to proton ratio decreased with temperature because the creation of proton is energetically more profitable than that of neutron. For $\Omega < 1$, this ratio got frozen to a value of about 0.12—0.14 after the first few seconds of expansion (Wagoner 1973). At $T \lesssim 10^9$ K, nucleo-synthesis started with proton and neutron forming deuterium which combined to give helium. All the neutrons available were converted to ^{4}He nuclei so that the helium abundance became about 0.25. Only very small amounts of ^{4}He, D and ^{7}Li were produced. No heavier elements are produced because no stable nuclei exist with atomic weights 5 and 8. The synthesis of light elements was stopped in about 300 seconds from the Big Bang. The predicted abundances are dependent on the reaction rates of the particles and the expansion rate of the universe, the latter being proportional to $\Omega^{1/2}$. Particularly, the observed value of deuterium to hydrogen ratio of 2×10^{-5} indicates Ω (baryon) $\lesssim 0.03$. This is consistent with the observed matter density in the universe of $\sim 3 \times 10^{-31}$ gm cm^{-3} and $H_0 \simeq 50$ km s^{-1} Mpc^{-1}. Inspite of the low baryon density, the universe may

still be closed ($\Omega \sim 1$), with the missing mass in the form of neutrinos. Therefore, a finite mass of neutrinos is required for a consistent picture. Hence, the problem of laboratory measurements of neutrino mass, which is being pursued by several groups, is of great cosmological interest.

3.2.2. *The First Million Years*

After the temperature dropped below 5×10^9 K, electrons and positrons annihilated and their energy was fully converted into photons. The nucleo-synthesis of the lighter elements was completed by about 300 seconds when the temperature dropped to about 5×10^8K. The equivalent energy density at this epoch was about 1 gm/cm^3. The universe now consisted of photons, neutrinos, anti-neutrinos and the ionized matter made of about 75 per cent protons, 25 per cent helium nuclei and the corresponding number of electrons neutralizing this high temperature plasma. The matter was transparent to neutrinos but was fully opaque to photons due to the scattering by electrons. The energy density of the photons, however, was very much higher than that of the matter. Therefore, this epoch is called the radiation dominated era. With the expansion of the universe, both the matter and photon number densities were proportional to R^{-3} (R is the scale factor) but the photon energy density decreased as R^{-4} because the energy of each photon decreased with increasing redshift as R^{-1}.

By about million years, the temperature fell below 4000 K whence protons and electrons recombined to form neutral hydrogen. Henceforth, the photons were no more scattered by the electrons and the radiation became decoupled to matter. At about the same time, the energy density of matter and radiation also became equal. Subsequently, the radiation cooled as R^{-1}. Since the present temperature of the microwave background is 2.7 K, we can identify the era of recombination to have occurred at a redshift of $z \propto R(t)/R(t_0) = 4000/2.7 \sim 1500$. The density of the matter at this era was about $(1500)^3 \times$ present density of 3×10^{-31}–10^{-21} gm cm^{-3}, which is about 1000 times the average density of matter inside our Galaxy at present. Unless the matter is reionized again at $z \gg 10$, the observed anisotropy of the microwave background at the present era provides direct information about fluctuation density of matter at the epoch of the last scattering surface at $z \approx 1000$.

3.3 The Large Scale Structure of the Universe and the Formation of Galaxies

It is well known that the condensation of geseous matter is governed by a competition between gravitational attraction and pressure (Silk 1980). For a small density enhancement pressure will dominate but for a large one, gravity will. We should also consider the forces exerted by the collisionless neutrinos. Cowsik (1984) has recently derived an important equation for the condensation of matter in the presence of neutrinos, which explains many of the observed features of galaxies, such as their flat rotation curves.

Considerable work has been done over the last decade observationally and theoretically concerning the problem of formation of galaxies and clusters. Galaxies

probably condensed from initial density fluctuations in the universe. Mainly, there are two types of perturbations which have been considered in detail.

In the adiabatic fluctuation model, radiation and matter were perturbed to-gether as pressure oscillations during the radiation dominated era. Fluctuations of short scales containing $< 10^{13}$ M$_\odot$ are attenuated by photon viscosity and diffusion. Only larger scales corresponding to 10^{14-17} M$_\odot$ survived. After the decoupling, the radiation pressure due to photon viscosity drops abruptly and therefore the gravitational instabilities start to grow in amplitude. These lead firstly to the formation of 'pancakes' whose intersections give rise to a cellular struc-ture surrounding voids. Ultimately, galaxies condense by fragmentation at $z \sim 5$–10. Originally this model required density fluctuations with amplitude of more than 1 part in 10^3 at the era of decoupling, if $\Omega \lesssim 0.1$. But, this was ruled out by the observed anisotropy of microwave background of $< 10^{-4}$. However, if massive neutrinos are present in the universe, they could have started condensing into neutrino clouds at a much earlier cosmic epoch, of about 300 yrs, when their velocities became sub-relativistic. It may be noted that neutrinos are not subject to photon pressure. The mass of a neutrino cloud corresponding to the particle horizon of 300 yrs at this epoch is $\sim 10^{15}$M$_\odot$. Ultimately these neutrino clouds would collapse into 'pancakes' and the neutral hydrogen gas would condense therein to form galaxies and clusters at $z \sim 5$ to 10. Thus, the anisotropy of 2.7 K radiation can be quite small. The 'missing mass' would be in the form of neutrinos surrounding galaxies.

In the isothermal fluctuation model only the matter density is perturbed and the photons which are much larger in number are not perturbed. The initial perturbation spectrum is considered to be a power law and remains unchanged dur-ing the radiation dominant era. Inhomogeneities of mass $> 10^5$M$_\odot$. start to con-dense soon after the recombination at $z \sim 1000$. In contrast to the adiabatic model, the galaxies form first and aggregate heirarchically to form clusters later. Although "the adiabatic model is favoured by theoreticians, but in the present state of know-ledge isothermal fluctuations cannot be excluded" (Oort 1983).

According to the standard Big Bang model, galaxies and clusters are likely to have been formed at $z \sim 5$–10, at an epoch when the universe was about 15 per cent of its present age. During this era, most of the gas is likely to be in the form of neutral hydrogen. Hence, the well-known 21–cm (1420 MHz) line radiation caused by neutral hydrogen should be observable from proto-clusters at $z \sim 5$–10. Because of the large redshift, the 21–cm line from the proto-clusters would get redshifted to meter wavelengths, say to ~ 100–300 MHz (some proto-clusters may be present even at 2–3). If the adiabatic model is correct, there will be only a limited number of proto-clusters of relatively large mass, say $\sim 10^{15}$ M$_\odot$, that will be observable, across the sky, in a small redshift range corresponding to the receiver bandwidth of a few percent of a large radio telescope (Sunyaev and Zeldovich 1975; Davies et al. 1978). In contrast, for an isothermal model, there would be a large number of neutral hydrogen clouds, each giving rise to a smaller antenna temperature than in the case of the adiabatic model (Hogan and Rees 1979). Thus, radio astronomy

observations at metre wavelengths using a sufficiently large radio telescope of appropriate design would be extremely valuable in tracing out the thermal history of the gas which led to the formation of galaxies, in fact to test out an important prediction of the Standard Big Bang model that galaxies and clusters were formed at epochs corresponding to $z \sim 3-10$.

For the above purpose and for many other astronomical investigations of fundamental importance, we have proposed the construction of a Giant Metre-Wavelength Radio Telescope (GMRT) to be located in South India. It consists of 34 parabolic cylindrical antennas, each 90 m long and 35 m wide, providing a total area of about 109,000 m². Sixteen of the antennas are placed in a central square array of about 1 km size. Another 18 antennas are distributed along the 3 arms of a Y configuration centered on the square array. It is proposed to construct GMRT during 1985–92 with the first observations taking place by 1990. The metre-wavelength region of the electro-magnetic spectrum has not been well exploited anywhere in the world so far because of the lack of a suitable radio telescope. Particularly, ionosphere has been a great nuisance for high quality observations at these frequencies, but this is no more so because of the recent development of the method of 'closure phase' which eliminates any instrumental or atmospheric phase variations. The relatively low man-made radio interference at these frequencies in India and our experience gained at Ooty are also important factors which have led us to propose the GMRT project. There is no doubt that GMRT would provide very valuable information about the evolution of the universe through studies of radio galaxies, quasars and proto-clusters. It would be an outstanding instrument for studies of pulsars and many other interesting classes of radio sources in our Galaxy.

4. Conclusion

It is now generally believed that the hot Big Bang model offers a consistent theory about the origin of matter and radiation in the universe. Particularly, it has provided a simple explanation for the isotropic 2.7 K background radiation discovered in 1965 and the observed abundance of helium and deuterium. It has also allowed exploration of such basic questions as photon-baryon ratio, preponderence of matter over anti-matter and formation of galaxies. Nevertheless there remain many unanswered questions. There are also counter-views to the Big Bang concept (e.g. see Alfven 1984). New observational data is not easy to get in the field of cosmology. However, because of the rapid advances that are now taking place concerning the ground-based as well as space telescopes, we should soon be able to explore the consequences of the Big Bang model more fully.

References

Alfven H (1984) *J. Astrophys. Astron.,* **5,** 79.
Audouze J (1982) *Astrophysical Cosmology,* Proc. of the Study Weak on Cosmology and Fundamental Physics in 1981, Ed(s) H A Bruck, C V Coyne and M S Longair, Pontificia Academia, Vatican, p. 395.
Berry M (1976) *Principles of Cosmology and Gravitation,* Cambridge University Press, Cambridge.

Barrow J D and Silk J (1983) *Left Hand of Creation,* W Heinmann, London.

Bondi H (1960) *Cosmology,* Cambridge University Press, Cambridge.

Cowsik R (1984) Astrophys. J. Lett. (submitted).

Cowsik R and Mclelland J (1972) *Phys. Rev. Lett.,* **29**, 669.

Davies R D, Pedlar A and Mirabel I F (1978) *Mon. Not. R. astr. Soc.,* **182**, 727.

Guth A H (1981) *Phys. Rev.,* **D23**, 347.

Guth A H (1983) *The Very Early Universe,* Proc. of the Nuffield Workshop, Cambridge in 1982, Ed(s) G W Gibbons, S W Hawking and S T C Siklos, p 1–71, Cambridge University Press, Cambridge.

Hogan C J and Rees M J (1979) *Mon. Not. R. astr. Soc.,* **188** 791.

Hoyle F (1948) *Mon. Not. R. astr. Soc.,* **108**, 372.

Kapahi V K and Subrahmanya C R (1982) *Extragalactic Radio Sources,* IAU Symp. 97 in 1981, Ed(s) D S Heeschen and C M Wade, Reidel, Dordrecht, p. 401.

Kapahi V K and Saikia D J (1982) *J. Astrophys. Astron,* **3**, 465.

Kulkarni V K (1978) *Mon. Not. R. astr. Soc.,* **185**, 123.

Narlikar J (1977) *The Structure of the Universe* Oxford Uiversity Press, Oxford.

Novikov I D (1983) *Evolution of the Universe,* Cambridge University Press, Cambridge.

Osmer P S (1982) *Astrophys. J.,* **253**, 28.

Oort J H (1983) *Ann. Rev. Astron. Astrophys.* **21**, 373.

Orr M J L and Browne I W A (1982) *Mon. Not. R. astr. Soc.,* **200**, 1067.

Patridge R B (1982) *The Origin and Evolution of the Universe,* Proc. NATO Advanced Study Institute in 1981, Ed(s) B J T Jones and J E Jones, Reidel, Dordrecht, p. 121.

Paturel G (1983) *Highlights of Astronomy* Vol. 6, IAU Gen. Assembly in 1982, Ed R M West, Reidel, Dordrecht, p. 301.

Peacock J A and Gull S F (1981) *Mon. Not. R. astr. Soc.,* **196**, 611.

Peterson B A, Savage A, Jauncey D L and Wright A E (1982) *Astrophys. J (Letters),* **260**, L27.

Rana N C (1981) *Mon. Not. R. astr. Soc.,* **197**, 1125.

Sandage A (1972) *Astrophys. J.,* **178**, 1.

Schmidt M and Green R E (1982) *Astrophysical Cosmology,* Proc. of the Study week on Cosmology and Fundamental Physics in 1981, Ed(s) H A Bruck, C V Coyne and M S Longair, Pontificia Academia, Vatican, p. 383.

Sciama D W (1971) *Modern Cosmology,* Cambridge University Press, Cambridge.

Silk J (1980) *The Big Bang,* W H Freeman and Co., San Fransisco.

Smoot G F (1983) *Early Evolution of the Universe and its Present Structure,* IAU Symposium 104 held in 1982, Ed(s) G O Abell and G Chincarini, Reidel, Dordrecht, p. 153.

Subrahmanya C R and Kapahi V K (1983) *Early Evolution of the Universe and its Present Structure,* IAU Symposium 104 held in 1982, Ed(s) G O Abell and G Chincarini, Reidel, Dordrecht, p. 47.

Sunyaev R A and Ya B Zeldovich (1975) *Mon. Not. R. astr. Soc.* **171**, 375.

Swarup G (1975) *Mon. Not. R. astr. Soc.,* **172**, 501.

Swarup G, Subrahmanya C R and Kapahi V K (1982) *Astrophysical Cosmology,* Proc. of the Study Week on Cosmology and Fundamental Physics in 1981 Ed(s), H A Bruck, C V Coyne and M S Longair, Pontificia Acadmia, Vatican, p. 383.

Tamman G A and Sandage A (1983) *Highlights of Astronomy,* Vol. 6, IAU Gen. Assembly 1982, Ed. R M West, Reidel, Dordrecht, p. 301.

de Vaucoulers G (1983) *Highlights of Astronomy,* Vol. 6, IAU Gen. Assembly in 1982, Ed. R M West, Reidel, Dordrecht, p. 315.

van Hoerner S (1973) *Astrophys. J.,* **186**, 741.

Vijayanarasimha U, Ananthakrishnan S and Swarup G (1984). *Mon. Not. R. astr. Soc.* (in press).

Wagoner R V (1973) *Astrophys. J.,* **179**, 343.

Wall J V (1982) *The Origin and Evolution of Galaxies,* Proc. NATO Advance Study Instiute in 1981, Ed(s) B J T Jones and J E Jones, Reidel, Dordrecht, p. 295.

Weinberg S (1972) *Gravitation and Cosmology,* Wiley, New York.

Weinberg S (1977) *The First Three Minutes,* Andre' Deutsch, London.

Windhorst, R (1984) *Ph.D. Thesis,* Leiden.

Zeldovich Ya B (1983) *Highlights of Astronomy,* Vol. 6, IAU Gen. Assembly in 1982, Ed. R M West, Reidel, Dordrecht, p. 29.

MAGNETO–ELECTRET

M L Maji *and* S D Chatterjee* fna

Department of Physics, Jadavpur University, Calcutta 700 032

A comprehensive account of the basic phenomena observed in magneto-electret states has been presented here. Existing theories of magneto-electret states have been elaborately discussed. New explanation for charge separation has been put forward on the basis of existence of temperature gradient in the material sample during preparation of the electret. Charge retention is explained on the assumption of polaron formation and crystallographic orientation which is also dependent on selective ionic trapping at the solid liquid interface or at the surface of formation of the double layer.

Keywords : Magneto-electret; Iso-charge; Idio-charge; Photo induced-depolarisation; Thermally-stimulated Discharge Current; Decay Time Constant; Trap Depth Activation Energy; Small Polaron

INTRODUCTION

THE electrets are usually dielectric bodies possessing long lasting electrization. Heaviside[1] termed a persistently polarized dielectric medium as an electret, which may be considered to be an electrical analogue of the permanent magnet. Now-a-days the electret charges may consist of either surface charges or space charges or effects of polarization or due to their combinations. Electrets are prepared by diverse charging devices. When the persistent electrization of a dielectric is produced gradual cooling in the presence of a constant magnetic field, it is called a Magneto-electret.

Electric polarization of a body by the magnetic field was first postulated by Curie[2], in his famous paper "On symmetry in physical phenomena". After his suggestion, several attempts were made to detect the effect in materials which were supposed to be made up from molecules containing both electric and magnetic dipole moments. If the free rotating molecules of a body could possess an electric dipole moment and also a magnetic dipole moment (like polar paramagnetic substances), then an applied magnetic field should cause a polarization due to the alignment of magnetic dioples against thermal agitation, in the magnetic field. But no one was successful in producing such an effect before 1961. Dzyloshinskii[3] showed theoretically that the polarization by magnetic field could exist in antiferromagnetic materials like Cr_2O_3. The first electric polarization using applied magnetic field on a substance was first observed by Rado and Folen[4]. They placed a Cr_2O_3 single crystal between the poles of an electro-magnet. The metallic films which had been deposited upon either side of the Cr_2O_3 sample were convected to the input

---

*Corresponding address : 91 Ballygunge Palace, Calcutta 700019.

of a vacuum tube electrometer. Switching the electromagnet on, they observed the appearance of some voltage across the sample. The effect was subsequently studied in a number of materials. It was found that the polarization changed linearly with the magnetic field. Those crystals which exhibited this kind of polarization were found to be time asymmetrical magnetic crystals and the effect was called the magneto-electric effect. Here the magnetic polarization is also produced by the influence of electric field on the substance.

The persistent electrification of dielectrics can also be made simple by cooling the melt. If waxes, resins or Sulphur melts are cooled in iron vessels, static electricity is produced on the surface of the dielectric due to contact electrification[5]. The nature of such charge depends on the dielectric materials as also on the surface lining of the materials. It is found that, when carnauba wax is allowed to freeze in contact with Tin foil, it acquires a positive charge of the order of $0.8-1.0$ esu/cm^2. If the melt is frozen in contact with Nickel plate the developed charge is practically one order smaller and is found to be negative[6]. It is also found that electric charge always appears at the interface between the liquid and solid phases in a dielectric[7]. This charge separation depends strongly upon the orientation of the crystalline solid. If Naphthalene single crystals are grown along a direction normal to the cleavage plane, the value of trapped charge is of the order of 32×10^{-9} coul/gm., while for their growth along b–axis the trapped charge is about 2.5×10^{-9} coul/gm. and for growth along a–axis it is about 2.9×10^{-9} coul/gm. During this study Mascarenhas and Freitas[8] explained it to be due to either selective ionic trapping in the solid phase or to be due to the formation of orientation dependent double layer as a result of an equalization of Fermi levels at the solid–liquid interface. During such phase-change if the liquid contains small impurities the charge separation increases. Instead of doubly distilled water, if a solution of amonium hydroxide (5×10^{-5} normal) is allowed to freeze the charge separation is so high that potential difference of about 230 volts is sometimes attained, the water being negative with respect to the ice. For doubly distilled water freezing produces about 60 volts only. The sign and magnitude of the potential differences developed and the quantity of charge separation during freezing are functions of the nature and amount of contaminants in solution with water. The developed voltage changes with the growth of solids. As solidification of a given sample proceeds, the potential difference diminishes and frequently gets reversed in sign[9]. This effect is observed during freezing only. In solid dielectrics temperature-gradient may also produce charge separation. If the solid contains two types of ions having different mobilities the temperature-gradient would cause more rapid diffusion of lighter ions towards cooler parts of the solid. In such a state, a potential difference is usually set up across the solid. The maintenance of a steady temperature gradient across a piece of ice is accompanied by concentration gradients of H$^+$ and OH$^-$ ions which develop an electrical potential in ice crystals, because the much greater mobile H$^+$ ions diffuse more rapidly into the cooler regions of the ice[10].

When a dielectric is cooled gradually from its molten state or even from a solid state at high temperatures, in the presence of a constant magnetic field it may

develop a persistent electrization[11]. Such electrization is dependent on the initial temperature, rate of cooling and the superimposed magnetic field. But the effect is not any linear function of the magnetic field. Its electrization usually persists for more than one month. Such electrized dielectric is termed a "magneto-electret". Benjamin Franklin in 1748 and Faraday[12] studied the long lasting electric charges that imbided in the pores on the surface of glass plates between to electrodes[13]. But systematic studies of persistently polarized dielectric was started by Mototaro Eguchi[14] who produced the electret by freezing the carnauba wax melts in an electric field. Such an electret is called a thermo-electret.

Among the various methods of preparation of electrets the photo-electret is one which is produced by the simultaneous application of light and electric field to the photo-sensitive dielectric[15]. Longlasting electrization obtained by Selenyi[16] depends on the injection of electrons or ions into the insulators. That charging with γ-irradiation is also possible due to compton currents in the dielectrics, was shown by Gross[17]. The characteristics of different types of electrets are more or less different. An attempt is being made here to discuss the properties of the "Magneto-electret" which was first produced in India by C. S. Bhatnagar[11].

INITIAL CHARGE

Preparation

The magneto electrets are prepared by cooling the materials in the presence of a strong magnetic field. The specimen in the form of a disc is sandwiched in a hollow double plated metallic holder and placed between the pole-pieces of an electromagnet. It is heated to a desirable temperature and then a magnetic field of a few K. Oersteds is switched on. The sample is now allowed to cool down gradually at a slow rate (about 1°C/minute or even less) to room temperature. The magneto-electret so formed is taken out of the magnet and the holder. The charges on both the surface are measured by an electrometer using the method of dissectable condenser. To distinguish between the two surfaces, they are designated as 'N' and 'S' surface, where 'N' refers to surface facing the north pole of the electromagnet and 'S' to that which faces the south pole. To ensure that the effect is entirely due to the influence of the magnetic field, blank specimen samples are prepared in which the whole process is repeated without any magnetic field.

Initial charge dependence on the field and substances

The nature of the charge and its magnitude varies from material to material as well as on the physical conditions and parameters under which the magneto-electrets are formed. Just after its preparation the surface charges of carnauba wax magneto-electret on the two faces are found to be of opposite sign. The developed charge increases with magnetic field upto certain range. Then it fluctuates with the field. If starting temperature for the formation of an electret is kept at 85°C, the maximum charge appears for the magnetic field of 10660 Gausses. The value of these surface charges have been found to be 1.8×0.3 esu/cm^2 on the 'S'

surface and — 1.6 × 0.3 esu/cm² on the 'N' surface. These surface charges are much higher than the surface charges developed on the blank samples[11,18]. If the electrets are prepared from the temperature of melting or softening state of the substances and the forming magnetic fields are within the range of 6.16 to 11.89 K. Gauss, the ceresin wax and bees-wax magneto-electrets exhibit negative charge on both the surfaces, while shellac wax, sisal wax and perspex show positive charge on both the surfaces. On the other hand, polythene and paraffin wax magnetoelectrets develop charges of opposite signs on the 'N' and 'S' surfaces[19]. The variation initial surface charge densities of ceresin wax, carnauba wax magneto-electrets with magnetic fields are shown in Figs. 1[19]. The forming temperatures (temperatures from which the cooling starts in the presence of magnetic field) are 85°C, 150°C, 74°C and 140°C respectively. All the curves show that the surface charge densities on the 'N' surface are like mirror images to that of the 'S' surfaces, although both the curves lie in the negative charge region for Fig. 1 (c). It appears
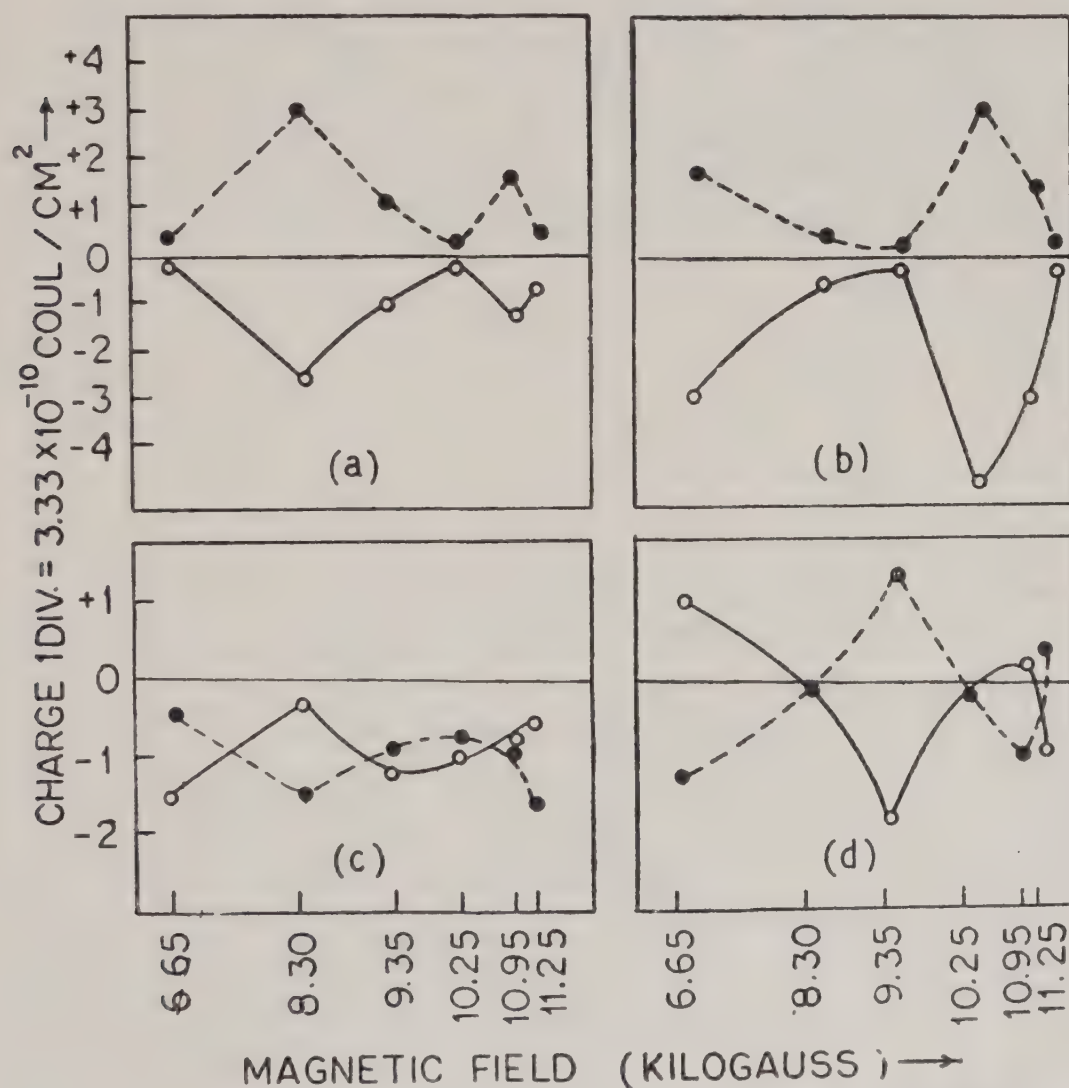

FIG. 1. Variation of initial charge densities of magneto-electrets with magnetic field (O–O–O N— surface, ●–●–● S-surface)

(a) Carnauba wax samples formed at 85°C.   (c) Ceresin Wax samples formed at 74°C.
(b) Polynite samles formed at 150°C.   (d) PVC-samples formed at 140°C.
[Khare & Bhatnagar 1969].

that some sort of polarization is superimposed over the negative charged density for the 3rd & 4th samples. Though the nature of initial charge variation with magnetic field differs from substance to substance. This mirror image type of relationship between the charge densities of 'N' and 'S' surface is common. From this it can be concluded that some kind of polarization is super-imposed over a general charge. The sign of this general charge varies from substances. This leads to the conclusion that magneto-electret consists of two types of charges ; one is a kind of polarization giving positive charge on one surface and negative charge on the opposite one. This kind of charge has been coined by Khare and Bhatnagar as 'idio-charge'. The 'idio-charge' is in fact superimposed over a negative or positive charge of the same sign on the entire sample. This superimposed charge has been termed 'iso-charge'. It appears that 'idio-charge' is strongly dependent on the magnetic field while 'iso-charge' does not appreciably vary with it. At certain field strengths which differs from substance to substance, the 'idio-charge' exhibits a marked rise or fall in its value. This variation does not follow any simple relationship. In some cases as in the case of carnauba wax magneto electret, the direction of polarization may also change for different magnetic fields. When the surface charge density of the 'idio-charge' is less than that of 'iso-charge', the magneto-electret marks the 'iso-charge'. When 'iso-charge' density is less the electret marks the 'idio-charge'. If the charge due to thermo-dielectric effect and that due to friction could be neglected, the amount of 'iso-charge and 'idio-charge' can be determined from the following formulas

$$\sigma_0 = \frac{q_n + q_s}{2} \qquad \qquad \dots (1)$$

and

$$\sigma = \frac{q_n + q_s}{2} \qquad \qquad \dots (2)$$

where q_n and q_s represent the charge densities on the 'N' and 'S' surfaces respectively and σ_0 and σ represent the 'iso-charge' density and idio-charge' density respectively.

One of the origins of the 'idio-charge' is suspected to be due to the freezing of dipoles oriented by the magnetic field[11,20,21]. If it were the only cause of the polarization on 'idio-charge' it would appear on the samples prepared at solid state or in a monopolar dielectric, since no orientation of molecules is observed by the magnetic field for that state. The magneto-electret of nonpolar sulphur prepared at forming temperature of 90°C or 100°C with magnetic field upto 17.8 K. Gauss exhibits positive charge on both the surfaces. But the quantitative magnitude of positive charge is more on the 'N' surface than on the 'S' surface[22,23]. Though no mirror image type relation of initial charge with magnetic field was found or no measurements of the distribution of charge by slicing the electret was made, Sharma and Bhatnagar predicted that the variation of charge densities on the two surfaces were due to the presence of polarization over the greater amount of positive 'iso-charge' throughout the body. Nonpolar Naphthalene magneto electret prepared at forming temperature of 70°C also exhibited similar effect[24-27]. The forming

magnetic field enhances the localization of charge carriers at various trapping centres which may be the cause of the polarization.

The observation of Pillai et al.[23] for the shellac wax magneto-electret differs from that of Khare and Bhatnagar[19]. While Khare and Bhatnagar observed that the surface charge densities of both 'N' and 'S' surface changed with forming magnetic field, Pillai et al.[28] observed that the surface charge densities on the 'N' surfaces remained constant for the field of formation between 4.75 to 12 K. Gauss. This value was higher than the charge observed for blank specimen. However, the charge of 'S' surface varied with the magnetic field.

In polyethelene magneto-electret, 'idio-charge' requires much higher field (14.45 K. Gauss) for its prominence when forming temperature is 90°C[29].

From the thermally stimulated current it is observed that the total charge of carnauba-wax magneto-electret saturates at 14.45 K. Gauss forming field[30].

Temperature Effect on Initial Charge Development

The charge developed on magneto-electret depends strongly upon the temperature from which the cooling starts. This temperture is called the 'Forming temperature'. It is observed that 'idio-charge' increases with the forming temperature while 'iso-charge' decreases with it[31,20]. At lower temperatures of formation, the iso-charge density of some substances is higher than the 'idio-charge' density. At higher temperatures the 'idio-charge' predominates. Thus for perspex magneto-electret 'iso-charge' predominates when the forming temperature is below 120°C i.e. below its softening temperature. But for higher forming temperatures 'idio-charge' predominates (Fig. 2)[33]. The surface charge densities of magneto-electrets may fluctuate with the increase of forming temperatures. Fig. 3 shows the charge variation for carnauba wax[18]. With the variation of formation temperature ; 'Idio-charges' may also change their sign. In most of the cases when carnauba wax magneto-electret is prepared at higher temperatures, positive charge develops on the 'N' surface and negative charge on the 'S' surface. But for lower forming temperatures negative charge appears on the 'N'—surface and positive charge on the 'S' surface. In the remaining cases charges of some sign (either negative or positive) appear on both the surfaces. The maximum amount of surface charge of Naphthalene magneto-electret prepared at forming temperatures between 30° to 70°C is observed at 60°C. The total charge of carnauba wax magneto-electret increases temperature of the forming field with the increase kept below 14.45 K. Gauss at which field the total charge saturates[20]. Though Bhatnagar[18] observed that surface charge of carnauba wax develops only during the application of magnetic field at room temperature ; Pillai et al.[28] observed that no surface charge develops when magnetic field is applied to the shellac wax kept at room temperature.

Usually one kind of iso-charge (either positive or negative) develops for all the forming temperatures and for all magnetic fields when the substance and the contact metal remain the same. But for polythelene magneto-electret prepared at 130°C forming temperature, both the 'N' and 'S' surface acquire positive charges for all the forming fields except for 14.45 K. Gauss. For 90°C forming temperature, both
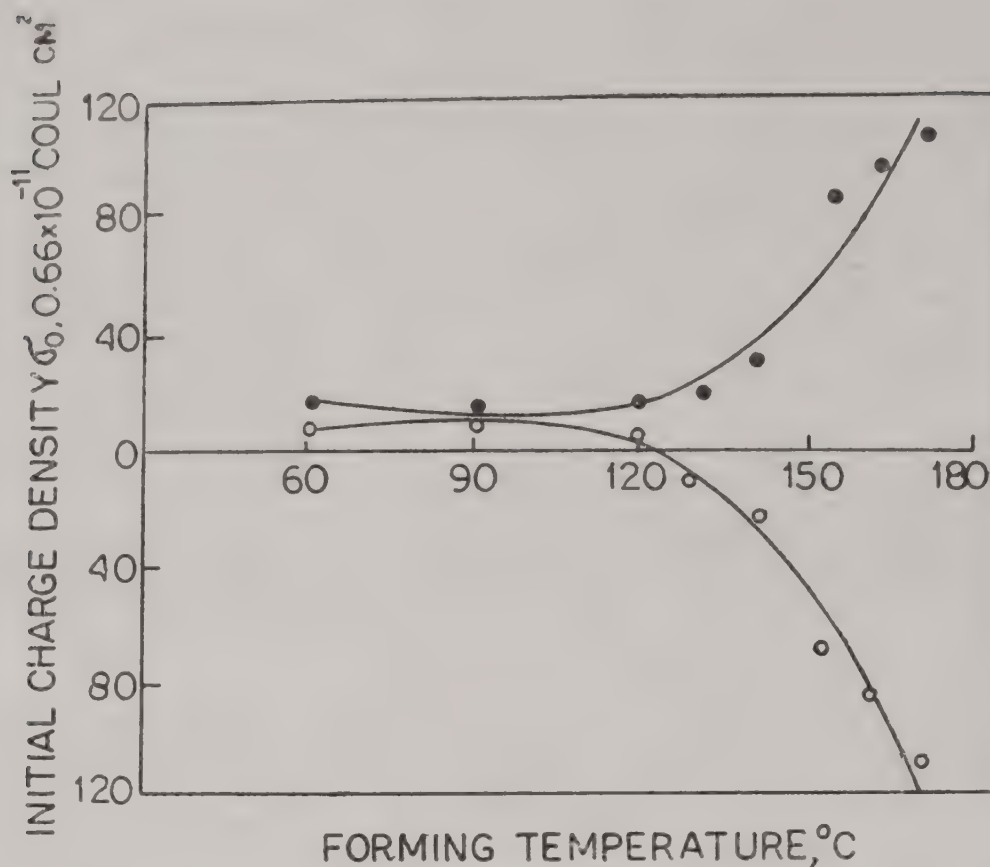
Fig. 2. Variation of initial charge density with forming temperature for perspex magneto-electret prepared at 8.4 K. Gauss. (●–●–● N–surface ◯–◯–◯ S–surface).

the surfaces exhibit negative charge for lower forming field. Jain and Bhatnagar[29] assumed it to be due to the formation of three types of charges, (i) iso-charge, (ii) idio-charge and (iii) a short duration polarization charge acting in the direction opposite to that of idio-charge. The sign of iso-charge also changes for higher forming temperatures of polypropylene magneto-electret. When the electret is prepared at below 130°C forming temperature positive iso-charge develops on both the surfaces. But for forming, temperature 130°C and higher values, negative iso-charge appears on both the surfaces for polarizing time above 2 hours. It is suspected to be due to oxidation of the surfaces[34].

The magneto-electret is usually prepared with uniform temperature of the substances. If perspex magneto-electret is prepared with temperature gradient along the direction perpendicular to that of the applied magnetic field the maximum idio-charge is developed along the direction of the temperature gradient when the forming temperature is 160°C. The minimum charge is developed along the direction of applied field. Charge fluctuation is also observed on all the faces with forming magnetic field and with forming temperature. At forming temperatures below softening state iso-charge predominates[35,36].

Effect of Duration of Polarization

The surface charge density of the magneto-electret does not depend upon the duration of applied magnetic field[31]. But slower rate of cooling produces higher
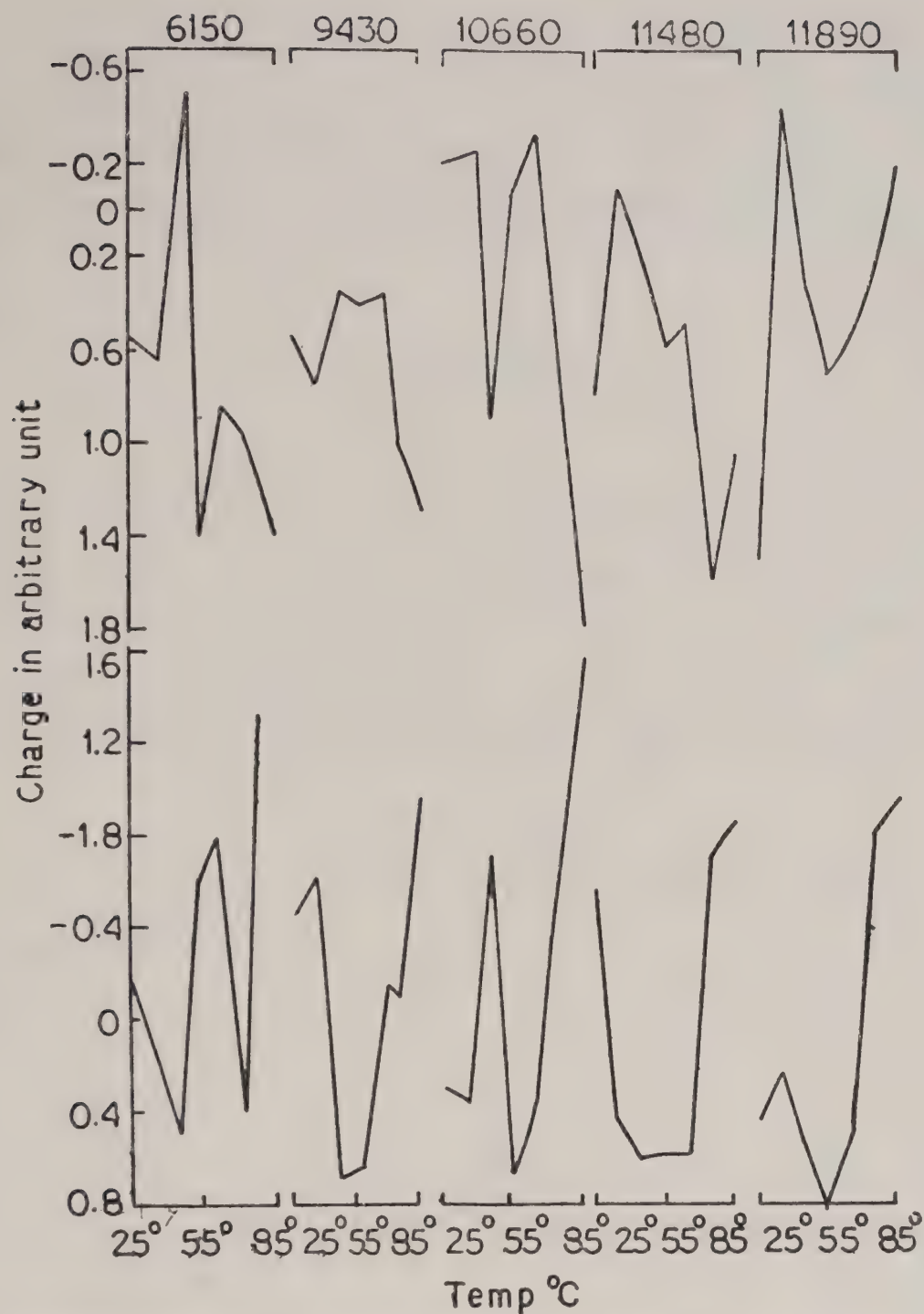
FIG. 3. Temperture variation of initial charge on the south (A) and north (B) surfaces for different strengths of the magnetic field of carnauba wax magneto-electret.[18]

charge density[11]. For Sulphur the initial surface charge increases regularly with magnetic field upto ~ 10.3 K. Gauss for the polarising time of 2 to 3 hours and forming temperatures between 90°C and 100°C. It is irregular for 4 hours polarizing time duration[22,23]. Pillai et al.[28] observed that surface charge of shellac wax magneto-electret increases with the increase of polarizing time. But they suspected it to be due to slower rate of cooling. In the case of polypropylene magneto-electret positive charge develops on both the surfaces when it is prepared below 130°C forming temperature and $2\frac{1}{2}$ hours polarizing time. But both the surface acquires negative charge for higher forming temperature and longer polarizing time. This may be due to oxide formation at the surface[34].

Effect of Lining Materials

The initial surface charge density depends upon the lining material. For PVC & Polyethelene Tubular magneto-electret, brass container is superior to the mild steel[37]. If the magneto-electret is formed with shorted or unshorted lining of tin metal, the surface charge becomes higher for unshorted condition. But the nature of variation of initial surface charge density with magnetic field remains the same for both the cases.

DECAY OF CHARGE

Normal Depolarization

Both 'iso-charge' and 'idio-charge' decay with time[31]. The rate of decay is usually higher at the begining and then gradually attains more or less a constant value as shown in Fig. 4 for carnauba wax and Fig. 5 for perspex. But in some cases an initial rise of surface charge is observed. After attaining a maximum the charge begins to decrease, at first at a higher rate, then gradually attains a constant value (Fig. 6). Carnauba wax magneto-electret surface charge decays regularly upto 26 days after which the charge remains more or less steady[18]. The surface
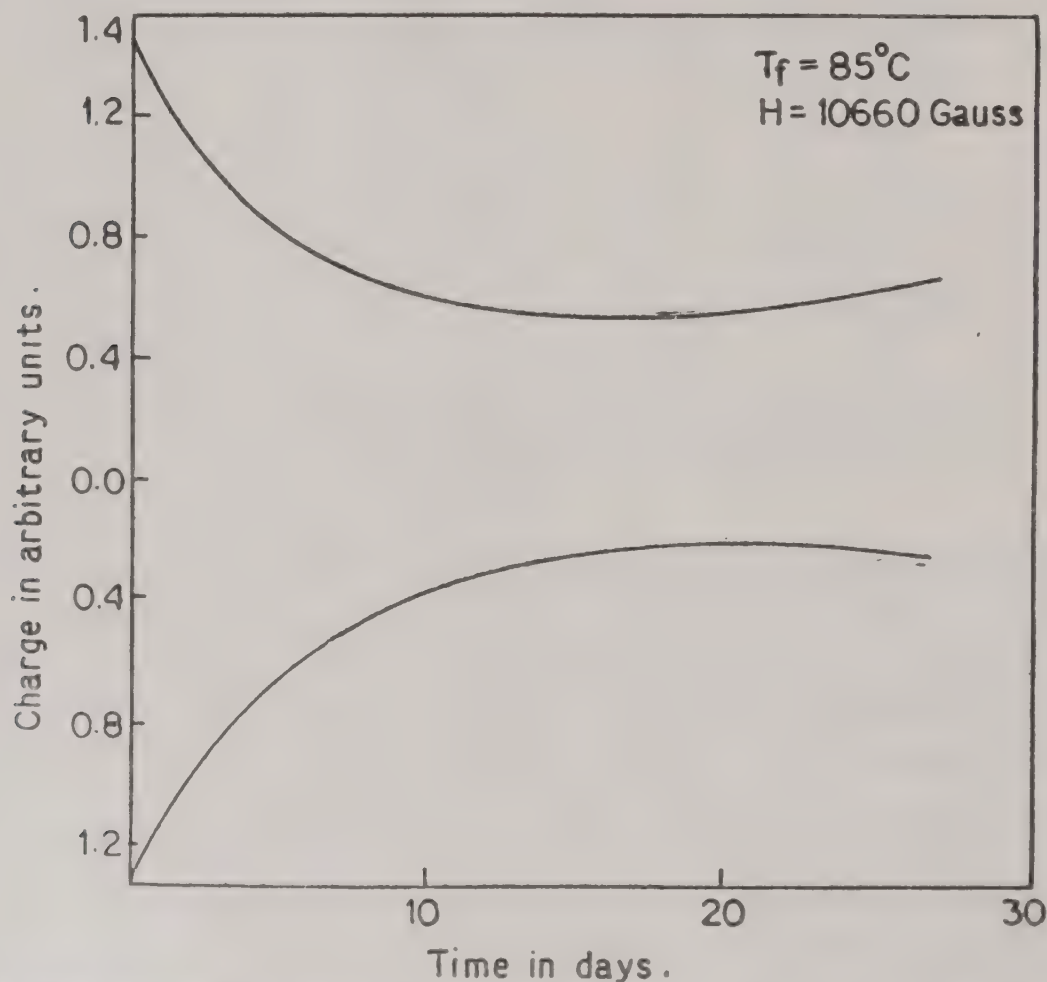

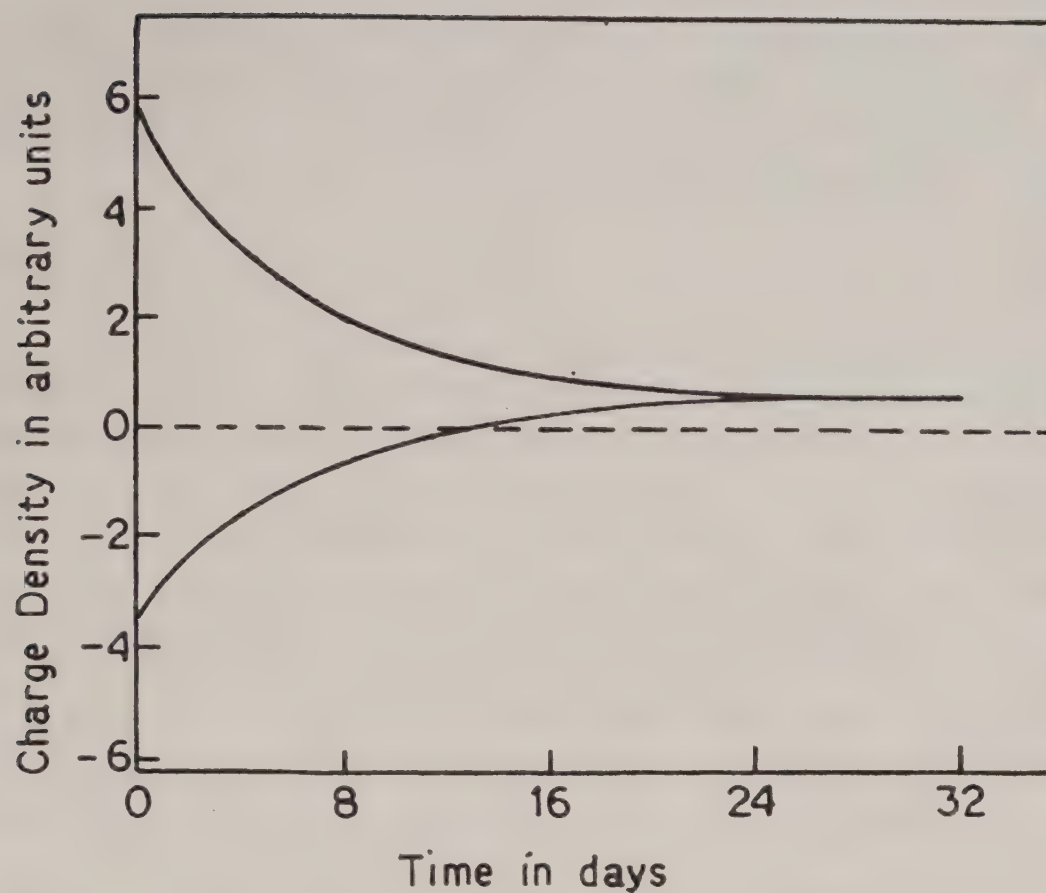FIG. 4. Charge decay curve of magneto-electrets of prime yellow carnauba wax prepared at 85°C.[18]

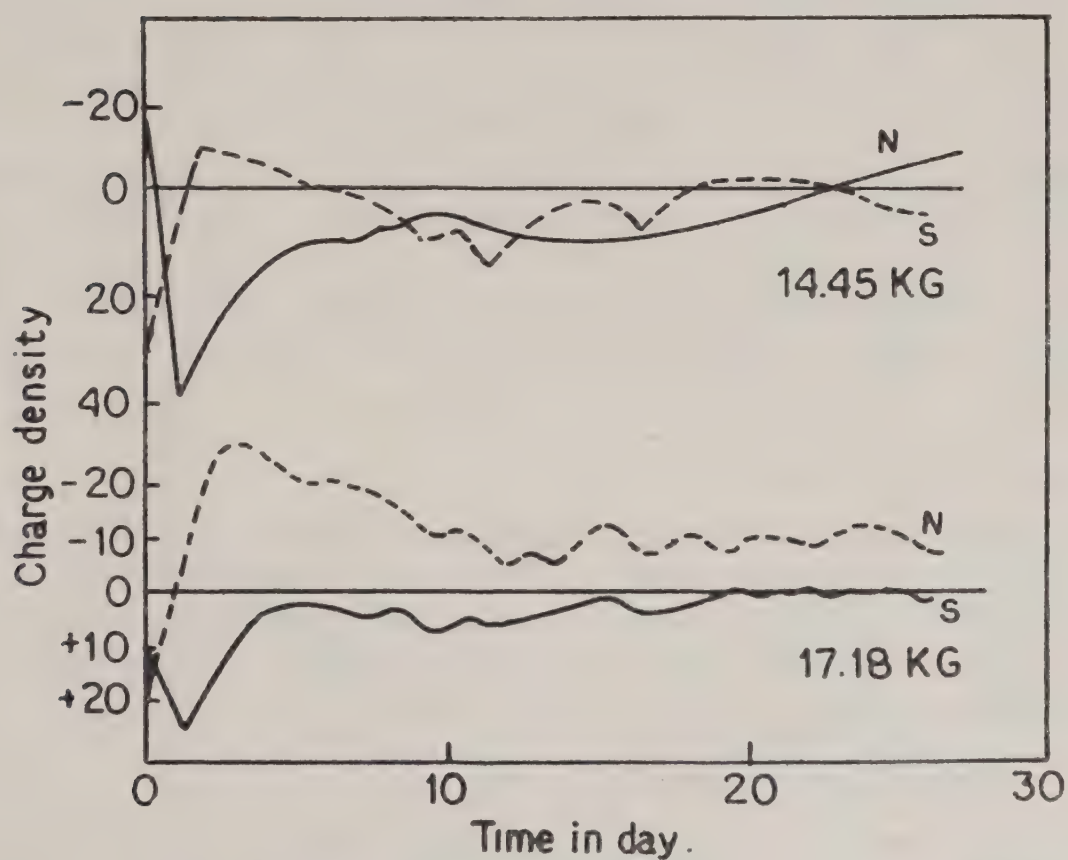FIG. 5. Charge decay in perspex magneto-electret prepared at 170°C[38]

FIG. 6. Charge decay in polyethylene magneto-electret prepared at 130°C[20]

charge of perspex magneto-electret decays exponentially with time as shown in Fig. 5[38]. If the perspex magneto-electret is prepared by applying magnetic field in the direction perpendicular to the temperature gradient produced along two face of a cube then the developed surface charges on the different faces also decay exponentially. The decay constant is defined as

$$\tau = - t/\log \frac{\sigma_t}{\sigma_0} \qquad \qquad \cdots (3)$$

where σ_0 and σ_t represent the initial surface charge and its value after a time t. The variation of the decay constant with varying magnetic field and temperature are regular on the surfaces facing the magnetic pole pieces and also on the faces where heat is applied to produce a temperature gradient. This variation is irregular on the surfaces facing the pole pieces for forming temperature of 140°C[35,36].

At times more than one time constant are required to explain the decay. The positive charges of both the surfaces of Napthelene magneto-electret prepared at forming temperature of 70°C with magnetic field varying from 0.6 to 15.09 K. Gauss decay exponentially in darkness. But instead of a single time constant at least two time constants are required to explain the dark decay. Considering this decay to be due to thermal activation the activation energy can be calculated and its values are obtained as 0.9 ev and 0.8 ev approximately[24-27]. The decay of surface charge of cylindrical magneto-electret prepared from silicon-rubber appears as an exponential curve[21].

For polyethelene magneto-electret positive charge develops on both the surfaces of the sample prepared at forming temperature of 130°C with forming fields between 1.57 to 17.28 K. Gauss except at 14.45 K. Gauss. Within a few days the decay produces appearance of idio-charge with negative charge on the surface facing the north pole and positive charge on the south pole facing surfaces. Finally the idio-charge remains unchanged. This is explained on the assumption of the existence of three types of charges (i) iso-charge, (ii) idio-charge and (iii) short life polarization, which appears along the direction which happens to be opposite to that of idio-charge. The initial charge is the cumulative result of these charges. However the short life polarization decays quickly allowing the 'idio-charge' and 'iso-charge' to remain[29].

Photo-Induced Depolarization

The surface charge decay of a magneto-electret consisting of photo-sensitive material enhances on exposure to light. The amount of surface charge of sulphur magneto-electret that decays in seven days in dark, requires only 30 minutes when it is illuminated by mercury vapour lamp. This optically induced depolarization obeys the exponential law

$$\sigma_t = \sigma_0 \exp\left(-t/\tau_1 + \sigma_0\right) \exp\left(-t/\tau_2\right) \qquad \qquad \cdots (4)$$

representing a two staged decay with two time contents τ_1 and τ_2. At the first stage the decay follows an exponential law with a time constant τ_1. But after some

time the decay follows another exponential law of greater time constant (Fig. 7, 8, 9)[22,23]. If monochromatic light is used to depolarize the surface charge of Sulphur magneto-electret the depolarization shows its dependence on the wave length of the radiation. It is observed that the depolarizations of the samples with wave lengths 365 and 436 mμ follow the exponential eqation given above. The depolarization is greater for shorter wavelength eg. 365 mμ. If the depolarization be induced by the radiation of 542 mμ wave length the decay rate is greater than the above. But after some time the decay rate is slower than the depolarization rates by 365 and 436 mμ wave length. However, the depolarization with 577 mμ is not quite appreciable[32].
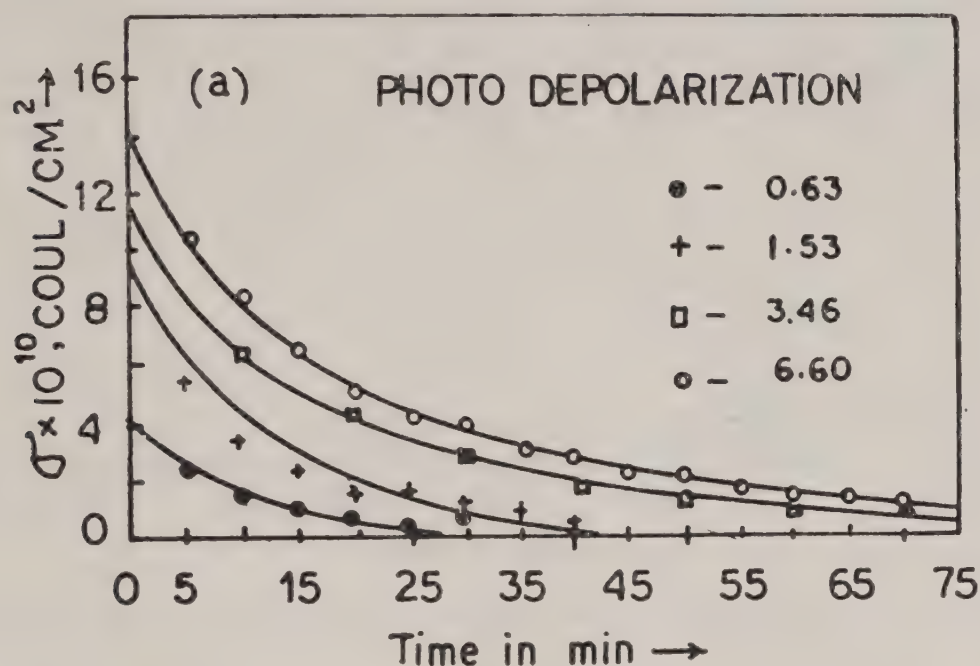
FIG. 7. Photo-depolarization of Sulphur magneto-electret prepared at temperature 100°C[22]
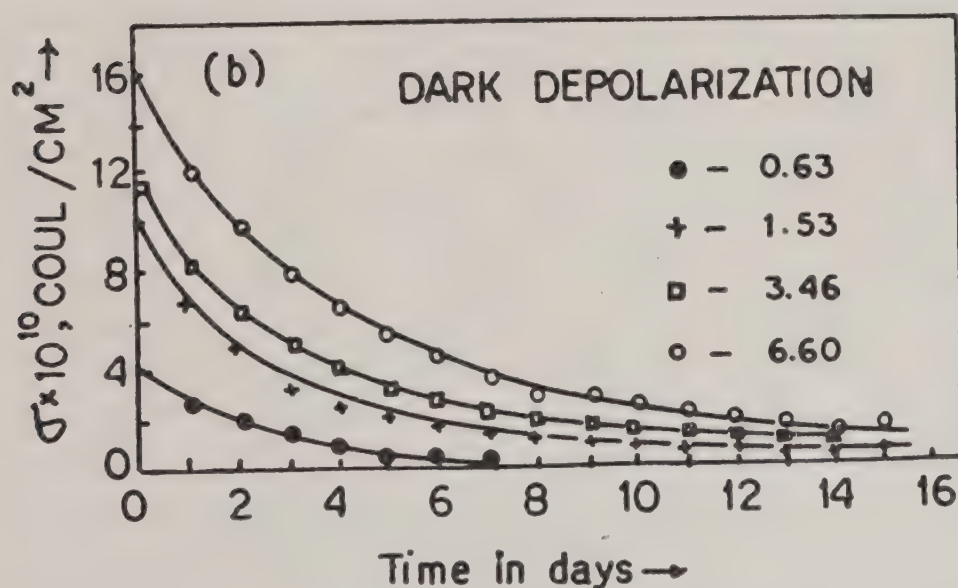
FIG. 8. Dark depolarization of Sulphur magneto-electret prepared at tempetature 100°C[22]
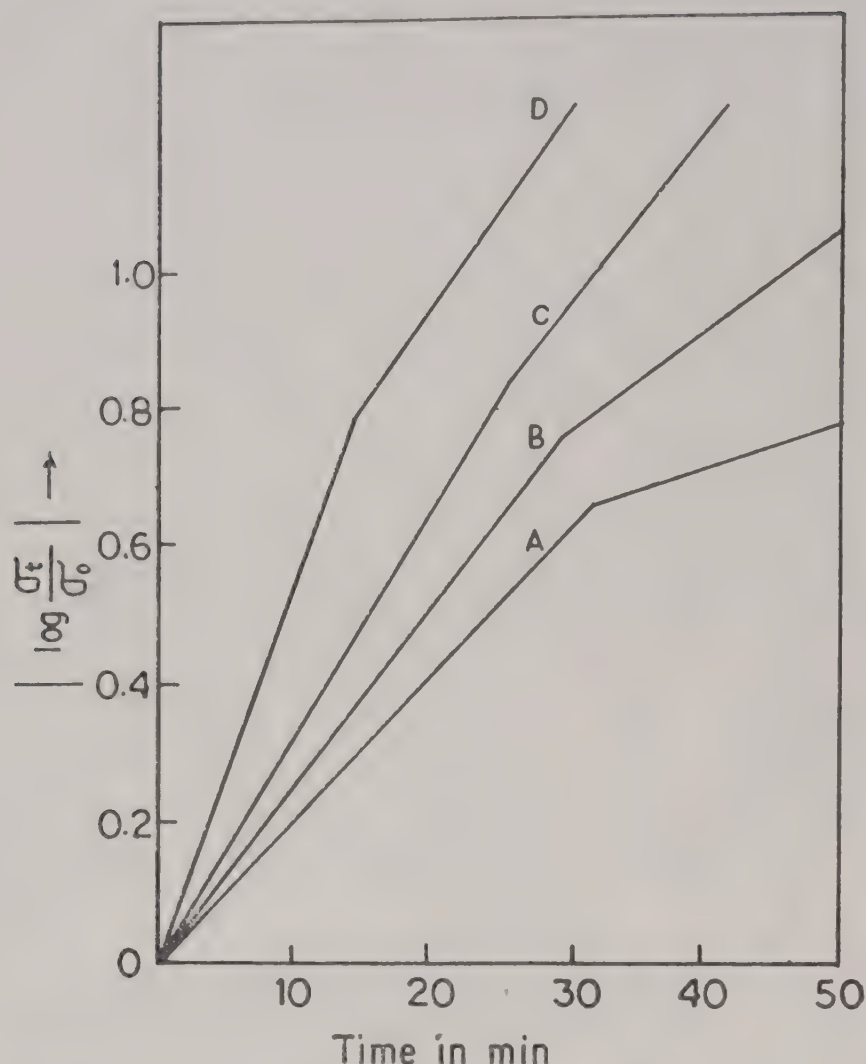
FIG. 9. Photo-depolarization of sulphur magneto-electret prepared at 100°C with white light.[22]

Photo-depolarization of Naphthalene magneto-electret also shows exponential decay of surface charge. For low intensity photo-depolarization the charge decays exponentially in two stages. At the first stage greater amount of surface charge decays exponentially with a lower time constant. Afterwards some amount of charge decays exponentially with a greater time constant. However, a small amount of charge remains unchanged. If the forming magnetic field be higher than ∼ 7.5 K. Gauss the depolarization by light of lower intensity shows that the decay time-constant decreases with the decrease of forming magnetic field. But with incident light of greater intensity, the depolarization decay time-constant within the same range of magnetic field, increases with the decrease of forming magnetic field. But such regularity is observed only if the forming magnetic field is kept low. Samples prepared in the magnetic fields higher than ∼ 9.4 K. Gauss shows the increase of decay rate with the increase of intensity of light. But for ∼ 9.4 and ∼ 7.5 K. Gauss it decreases with the intensity. For higher intensity of depolarizing light the two time constants become the same in most of the cases. Photo-depolarization with monochromatic radiation follows an exponential law. In low range of polarizing field the charge carriers are localized in some identical manner in the traps corresponding to trap depths 2.16 ev and 3.4 ev. respectively. In the

high field range these values are 2.84 ev and 3.06 ev. With a polarizing field of ~ 7.5 K. Gauss a sort of optical quenching effect is observed with white radiation. In general, an increase in magnetic field enhances the localization of charge carriers.

Thermally Stimulated Discharge Current

The thermally stimulated discharge current is an important tool for electret studies. It allows determination of the activation energy and dipolar relaxation time from the mesurment of the depolarization current obtained upon heating the electret. When a magneto-electret is heated slowly at a uniform rate few peaks of current are sometimes obtained with rising temperatures[30,39]. The thermally stimulated discharge current of carnauba wax magneto-electret produces there peaks at temperatures 67±0.5°C, 71.5±0.5°C and 75.5±0.5°C respectively (Fig. 10). If

FIG. 10. Depolarization current versus temperature of carnauba wax magneto-electret prepared at 70°C with 14.45 K. Gauss magnetic field.
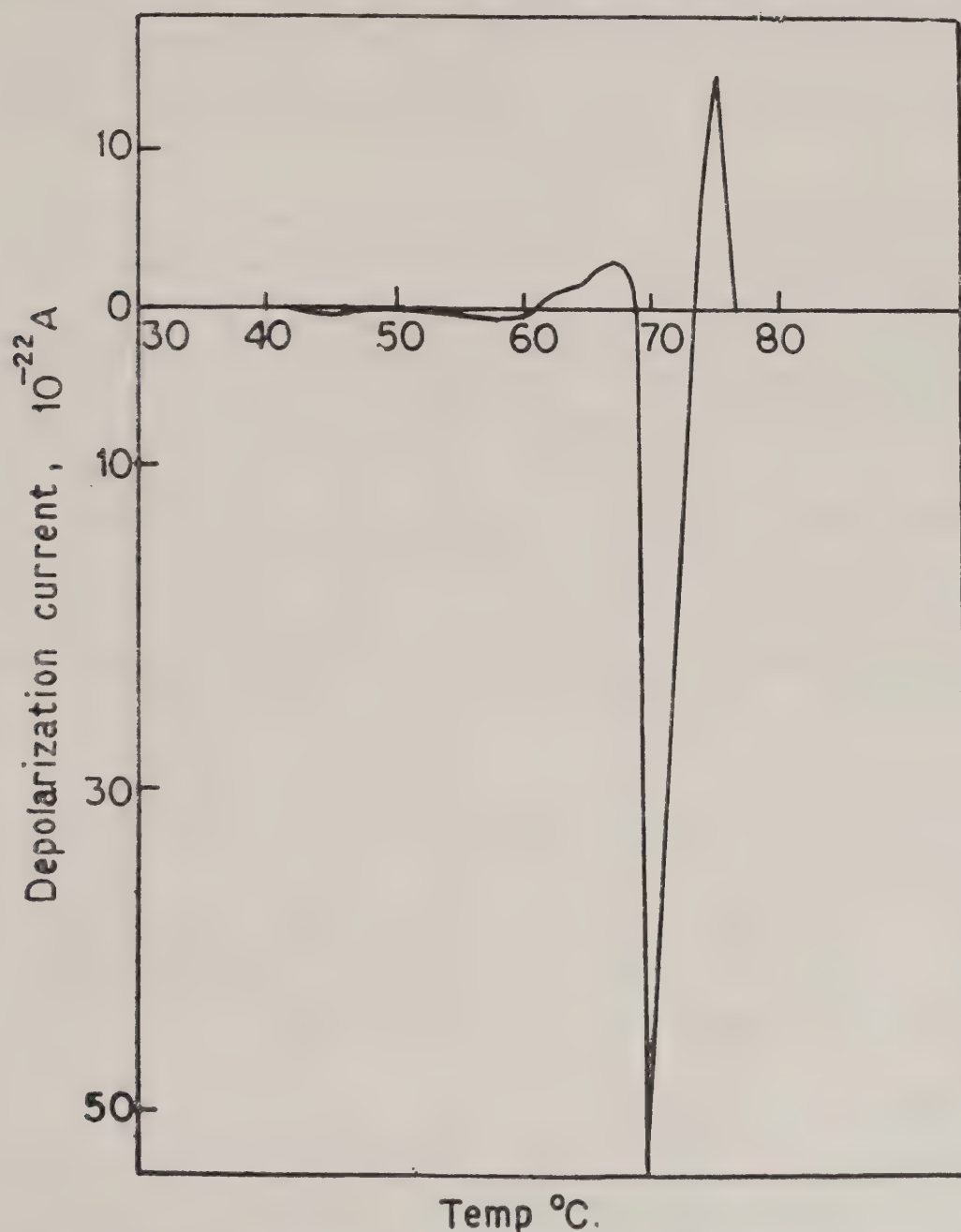
the terminals connecting the lining metals of the two faces of the electret with the electrometer be interchanged the first peak remains unchanged but the second and third peaks indicate reverse direction of currents. Usually the current corresponding to the second and third peaks depend upon the condition of formation. If the electret be kept short circuited for 10 minutes after its preparation and then the thermally stimulated discharge current be measured the first and second peaks become reduced in size. After 8 days of short circuiting, the first and second peaks completely disappear. From this it can be inferred that the first peak may be due to shallow trapped 'iso-charge' while the second and third peaks may be due to 'idio-charges[30]. TSDC curves for tubular magneto-electrets of perspex prepared in a magnetic field $\sim$ 5.04 K. Gauss and at various forming temperatures viz 80°, 100°, 120° and 140°C respectively shows that three current maxima are discernible which occur at temperatures 54°±3°, 134°±3° and 148°±3° respectively. These are termed as β, α and ρ peaks respectively. It can be seen that the position of three peaks do not change for tubular magneto-electrets of perspex prepared at different temperatures (both below and above softening temperature (120°C)). On the other hand the height of the maxima, i.e. I_{max} increases with forming temperature of the sample[40].

In Fig. 10 are shown the TSDC spectra for tubular perspex magneto-electret prepared at forming temperature of 100°C and with different magnetic fields viz 3.11, 4.45, 5.04 and 5.96 K. Gauss respectively. The position of the peak is unaffected by the forming magnetic field, although the magnitude of I_{max} is found to increase with increase in forming magnetic field. The TSDC curves flatten out near the temperature region where the α peak is expected but at higher temperature the current goes on increasing and the ρ peak is totally absent. For samples prepared at higher magnetic fields both the α and ρ peaks are present and I_{max} is larger for samples prepared at higher magnetic fields. TSDC using different heating rates show that low heating rates are more useful.

According to Perlman[41] the discharge current $J(T)$ at an absolute temperature T is given by

$$J(T) = A \exp\left[-\frac{E\alpha}{K_\beta T} - (\beta\tau_0)^{-1} \int_{T_0}^{T} \exp\left(-\frac{E\alpha}{K_\beta T} dT\right)\right] \quad \ldots (5)$$

where $E\alpha$ is the activation energy, A is a constant, β is the heating rate, K_B is Boltzmann's constant and τ_0 is the pre-exponential factor of relaxation time. It can be shown[50] that low temperature tail of eqn. (5) is given by

$$Ln\ J(T) = C - \frac{E\alpha}{K_b T} \quad \ldots (6)$$

where C is a constant. Thus the activation energy $E\alpha$ can be determined from a plot of Ln $J(T)$ VS $1/T$. (This is the initial rise method of Garlick and Gibson).

If one differentiates eqn. 5 to obtain the temperature T_m at which maximum current occurs, one has

$$\tau_0 = \frac{K_\beta T^2{}_m}{\beta E\alpha \, \exp \, (E\alpha/K_\beta T_m)} \qquad \ldots (7)$$

Thus by knowing activation energy $E\alpha$, the pre-exponential factor of relaxation time (τ_0) can be determined from eqn. (3). Table I shows the calculated values of $(E\alpha)$ and τ_0 and determined values of I_{max} for the samples prepared at magnetic field of 5.04 K. Gauss and at various forming temperatures.

TABLE I

Forming temperature $(T_F)°C$	Activation energy. ev	Pre-exponential factor of relaxation time $(\tau_0{}^0)$ Sec.	I_{max} A.
80	0.68	6.55×10^{-15}	1.0×10^{-10}
100	0.425	1.04×10^{-17}	2.0×10^{-10}
120	1.18	2.81×10^{-14}	2.6×10^{-10}
140	1.89	3.39×10^{-30}	4.5×10^{-10}

Though multiple peaks are observed in carnauba wax and perspex magneto electrets, a single peak is observed in Naphthalene magneto-electrets at a temperature of $40.0 \pm 0.5°C$. The calculated trap depths have been found to vary from 1.024 to 1.206 ev[12].

The thermally stimulated discharge current of Sulphur magneto-electret shows two peaks. The first peak is detcted as to be for iso-charge and the second one is identified as to be for idio-charge. The calculated energy of the trap levels of the charge carriers producing the charge separation are 5.11 ev and 0.77 ev. The high value of the activation energy corresponding to first peak is assumed to be due to the trapping of the ions creating iso-charge. The second peak is supposed to be due to trapping of electrons producing idio-charge[40].

The thermally stimulated discharge current of silicon rubber magneto-electret shows two peaks. The first peak corresponding to activation energy 0.81 ev is explained to be due to idio-charge caused by dipolar orientitation while the second is for iso-charge caused by ionic trapping[40].

Theory and the Associated Effects

The expected reasons for charge development in the magneto-electret are the following : (i) orientation of dipoles, (ii) separation of charge carrier like ions and electrons and (iii) charge transfer from the metallic linings. Most of the substances used as the magneto-electret forming materials are diamagnetic in nature. The molecules possess different magnetic susceptibilities along different directions. Due

to this anisotropy, when the molecule is placed in an uniform magnetic field it tries to align itself along the direction of its maximum suspectibility parallel to the field. In liquid state the molecules are more or less free for such rotation. Most of the molecules being anisotropic in nature, magnetic field helps to align the molecules. If the molecules possess electric dipole moment one may expect polarization due to this alignment[11,21]. But the thermal agitation hinders such orientation. The volume of a molecule is of the order of 10^{-23} c.c. Anisotropy of volume suspectibility is of the order of 10^{-7} c.g.s. unit. The magnetic field used is some K. Gauss. Then corresponding energy change due to the alignment of the molecules from minimum susceptibility direction to its maximum value parallel to the field is of the order of 10^{-21} ergs, where as the thermal energy near the melting point of the electret forming materials are $KT \sim 10^{-14}$ ergs. The potential energy change being rather small as compared to hindering energy, the alignment would not be appreciable to direct. If the molten substances be allowed to cool gradually in the presence of the magnetic field the molecular grouping in the melt is accentuated as it solidifies leading to crystalline structures or semicrystalline structures like cybotactic states which can be stronglly oriented by the magnetic field. When the volume of those crystallites become of the order of 10^{-13} cc the potential energy change is expected to be of the order of KT. Thermal agitation would be weaker than the rotating force causing stronger orientation. On solidification these sligned crystallites would be constrained to remain unchanged and the solid should show anisotropic property like crystallites even in the adsence of the magnetic field. Such orientation was observed by several workers during study of various properties.

To study the orientation condition of molecules in the magneto-electret, the electrets are formed from the molten substances with the help of a few K. Gauss magnetic field. Suitable capillary specimens are constructed from the slab of a magneto-electret and placed before the X-ray beam such that the direction of magnetic field applied during the formation of electret and that of incoming X-rays are mutually perpendicular to each other. The intensities of the flat plate transmission patterns for (110) K_β, (110) K_α and (200) K_α rings are measured along the circumference at regular angular intervals. Fig. 11 represents the variation of intensity along the circumference of the (110) K_β, (110) K_α and (200) K_α rings. The non-uniformity of intensity at different angles immediately suggests a preferred orientation of the crystallites of magneto-electret[43,44]. Similar photograph of unpolarised control specimen shows only uniform intensity along the rings, since the molecules are now randomly oriented in the specimen and reveal no anisotropy.

An elegant way of detecting the molecular orientation in the magneto-electret is to study the magnetic anisotropy of the sample. According to Raman and Krishnan[45] the dimagnetic anistropy of a unit-cell in a crystal depends upon the relative orientation of the molecules within the cell and the anisotropy of the molecules. However, the diamagnetic moments induced in neighbouring cel's are so feeble that their mutual influence is negligible. As most of the molecules are anisotropic in nature the preferred orientation of molecules in the substance will exhibit magnetic anisotropy of the bulk. The experimental results show that on
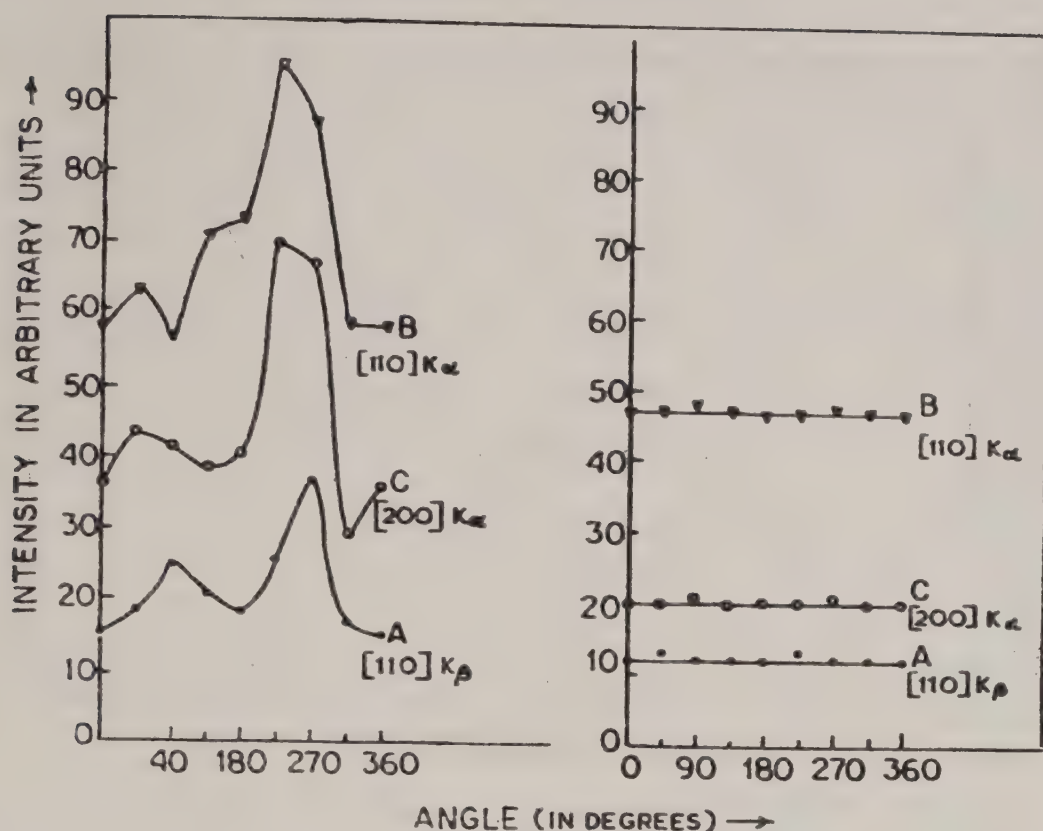
FIG. 11.   Intensity along the ring of a carnauba wax magneto-electret prepared with 10,000 gauss from its molten state and along the control specimen[43].

preparation of magneto-electret from its molten state or softening state the diamagnetic anisotropy develops of the order of the value as that of a crystal[46,51]. This indicates the oriented states of molecules in the magneto-electret. The analysis of the results show that during solidification when small crystals or semi-crystalline groups are formed of 10^{10} to 10^{11} molecules it will experience sufficient force to align itself, against thermal agitation, by the magnetic field of the order of a few ~ K. Gauss[51]. The nature of the variation of alignment with the preparing magnetic field may be obtained from the curves given in Figs. 12 & 13[46,47]. Such fluctation is also observed in the initial charges of magneto-electret. It is observed that in all cases of magneto-electrets prepared from molten states of different substance the maximum susceptibility lies along the direction of the preparing magnetic field. No anisotropy is developed if the initial forming temperature is far below the melting point.

Due to different polarizibility along the different directions as well as of a crystal, the crystalline orientation would also develop optical anisotropy of the magneto-electret if it is prepared from the molten state of the substance. Such anisotropic refractive index due to crystalline orientation is also observed for higher forming temperatures[48]. Both in the study of magnetic anisotropy and optical anisotropy, the anisotropy once developed, remains unchanged for a good length of time. This indicates that once solidified the molecular alignment remains unchanged for a long period. As the diamagnetic moments induced in neighbouring cells are two feeble to influence sufficiently its neighbouring molecules the magnetic field would have only the orientation effect and non deformation of crystalls and are
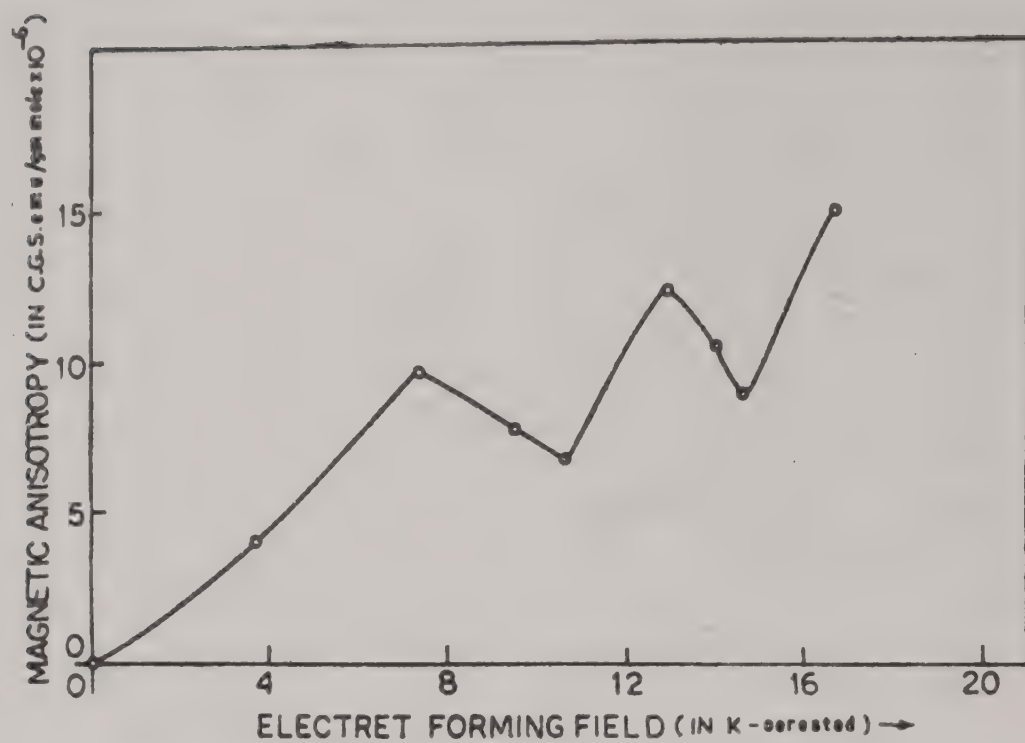
FIG. 12.   Dependence of magnetic anisotrophy of a magneto-electret of Carnauba wax on electret forming magnetic field.[46]

FIG. 13.   Magnetic field variation of magnetic anisotropy of Polysterene magneto-electret prepared at 122°C.[59]

expected. It is unexpected to have any resultant diople moment of the crystals containing 10^{10} to 10^{11} molecules in normal growth without any electric field. Even if these crystals might have any resultant diople moment no polarization would be observed after their distribution of orientation in the presence of magnetic field during phase change. This can be shown in the following way.
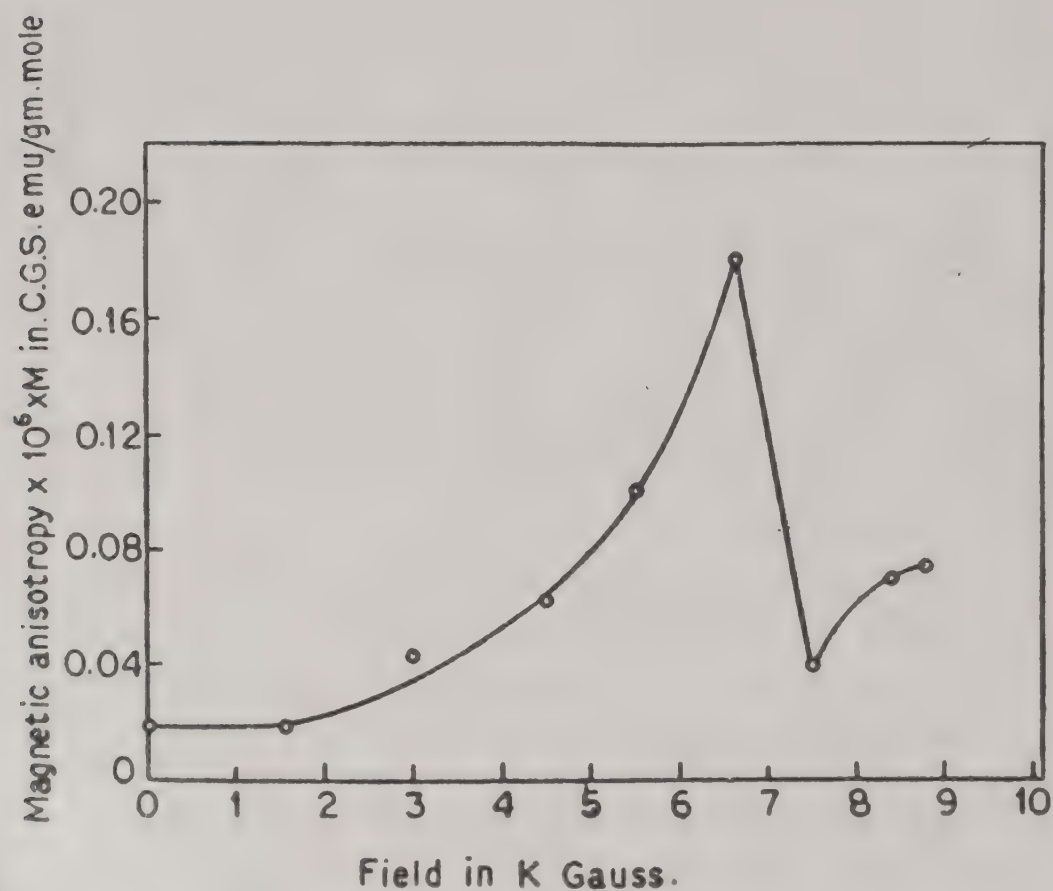
To understand the reason for the absence of polarization due to only orientation by the magnetic field, it is useful to consider such a small crystals participating in the orientation. Let the three principal volume susceptibilities of the microcrystals be K_1, K_2 and K_3 ($K_1 < K_2 < K_3$). The resultant dipole moment of the microcrystal, if any, lies, say, along any direction perpendicular to the maximum susceptibility direction. In the presence of magnetic field these crystals would try to keep the direction of maximum susceptibility along the field. Then the dipole moment of the crystal would have equal probability to lie along any direction on the plane perpendicular to the magnetic field. The resultant dipole polarization should be zero. Next let us consider the dipole moment P to lie along K_3 direction. The magnetic field H is applied along the Z-direction of a space-fixed co-ordinate system X, Y, Z. In the presence of magnetic field during phase change these crystallites would try to keep the maximum susceptibility direction along the field, against thermal agitation, if it is still free to rotate. Different microcrystals would aquire different orientation with greater probability to keep K_3 along the magnetic field direction. Let one of the microcrystals be considered to be aligned such that P (K_3) makes an angle (θ, ϕ) with the Z-direction. Then K_1 and K_2 would lie on the plane perpendicular to the K_3 direction. This would also distribute K_1 and K_2 on that plane due to their different values. Let K_1 makeh an angle β with the line of interaction between the two planes containing (K_1, K_2) and $(X–Y)$. Then, following the component of K_1, K_2 and K_3 of the microcrystal concerned along the field is

$$(K_1 \cos^2 \beta + K_2 \sin^2 \beta) \sin^2 \theta + K_3 \cos^2 \theta \qquad \text{...(8)}$$

The energy of the microcrystal will be

$$U = -\tfrac{1}{2}VH^2(K_1 \cos^2 \beta + K_2 \sin^2 \beta) \sin^2 \theta + K_3 \cos^2 \theta \qquad \text{...(9)}$$

where V is the volume of the microcrystal.

The component of the diople moment P along the field is P Cos θ. Now the probability of finding a molecule between the angle θ and $\theta + d\theta$, ϕ and $\phi + d\phi$, β and $\beta + d\beta$ is

$$dW = \frac{\exp\left(-\dfrac{U}{K_\beta T}\right) \sin\theta\, d\theta\, d\phi\, d\beta}{\displaystyle\int_0^\pi \int_0^{2\pi} \int_0^{2\pi} \exp\left(-\dfrac{U}{K_\beta T}\right) \sin\theta\, d\theta\, d\phi\, d\beta} \qquad \text{...(10)}$$

where K_β is the Boltzmann's constant and T is the temperature of the body. So the mean electric polarization in the direction of the applied field is

$$P_i = N \int_0^\pi \int_0^{2\pi} \int_0^{2\pi} P \cos \theta \, dW = 0 \qquad \qquad \dots (11)$$

Where N is the number of molecules/c.c. This shows that the dipole moment along the magnetic field is zero. This is quite natural. As the susceptibility is not a vector quantity and the alignment is controlled by the susceptibility components, the probability of laying the dipole **P** along any direction in the magnetic field is equal to its probability along the opposite direction[58]. The polarization perpendicular to the magnetic field would also be zero. Because the component of the dipole along the direction perpendicular to the magnetic field would lie with equal probability along only direction on that plane. The same reason indicates that for **P** lies along any direction the resultant polarization after distribution of the micro-crystals by the magnetic field would be zero if there is no other electric field. If instead of the micro-crystals it would be molecules the some results would be obtained. The next probable reason is the trapping of charge carrier separated by any means. When the temperature of the dielectrics is increased free charge carriers are produced due to the excitation of the impurity atoms or dissociation of molecules. When the magnetic field is applied to the dielectric the charge carrier will experience a force of amount $F = e \, [V_a B]$ due to the interaction of the magnetic field and current due to the thermal motion of the charge carriers. This force may separate charge carriers. It the temperature of the body be uniform through out its volume then average thermal velocity along any direction is zero. Therefore no charge separation is possible. If, on the other hand a temperature gradient is established charge separation is quite possible. Such type of magneto-electret study had done by Deshpande and Bhatnagar[35,36]. A similar effect is the Nornst-Ettingsheusen effect in semiconductor[52,53]. Latham and Mason[10] showed the charge separation of dielectric ice to be due to diffusion of thermally dissocited ions. In the magnetoelectret studies the substances used are very poor condoctors of heat. During cooling appearance of temperature gradient is quite possible. Applied heat may produce charge carriers by dissociation of molecules or due to excitation of impurity atoms they may release some electrons. Due to the temperature gradient these charge carriers would have concentration gradiant along the temperature gradient. It will cause the diffusion of the ions or electrons. But the diffusion coefficient being different for different charge carriers greater amount of ions of higher diffusivity will reach the colder part. This charge separation will produce an electric field. When a steady temperature gradient is maintained across the sample a steady state will be reached eventually in which no net flow of current occurs but a steady potential difference will be established. The diffusive flux of ions maintained by the temperature gradient will then be balanced by a 'reverse' current maintained by the potential gradient. During this diffusion some charge carriers will be trapped into the trap centres present within the samples. When a magnetic field is applied the charge carriers will remain for a longer time in the vicinity of a particular atomic site. If this time interval be long enough for the displacement of the surrounding atoms to take place, a potential–well may be created which would lead to trapping of the charge carriers. This induced lattice deformation is called the

small polaron. The polaron has a lower energy than a free electron and cannot move without changing the position of the neighbouring atoms. The reduction in energy of the small polaron relative to that of an electron in the undistorted latice is called the binding energy of the small polaron. The basic postulate of the formation of small polaron was developed by Holstein[54]. Thus magnetic field would cause the higher probability of formation of small polaron. The binding energy will also depend on the magnetic field. So the charge of magneto-electret and its decay time constant will depend upon the forming magnetic field. For this trapping of the available mobile charge carrier from the colder part of the sample will be lesser than the total charge carrier present in the colder part. As a result more diffused charge will accumulate on the colder part to develop higher potential gradient which will cause the drift of the mobile carriers. A steady state will again be reached for no net flow of current. In many cases like Sulphur, Napthalene etc the negative charge carriers are electrons and its mobility is much higher than the positive ions. As a result the negative ions will accumulate on the colder part and a part of these negative charge will be trapped. This separation and trapping of negative charge will strongly depend upon the applied magnetic field and scattering machanism. But the positive ions being much less mobile they will not move appreciably and their trapping will also less prominent. If C be the concentration of the negative charge at the colder part BC will be the concentration of trapped charge carriers and $(1-B)\,C$ be the available mobile carriers at that part. Here B is the trapping probability of the negative ions. The current of the negative ions per unit cross section is

$$i_- = D_-\,e\,\frac{dc_-}{dx} + \tfrac{1}{2}D_-\,e\,\frac{C_-}{T}\,\frac{dT}{dx} - (1-B)\,e\,C_-\,U_-\,\frac{dv}{dx} \qquad \text{...(12)}$$

and the current of positive ions per unit cross section is

$$i_+ = D_+\,e\,\frac{dc_+}{dx} - \tfrac{1}{2}D_+\,e\,\frac{C_+}{T}\,\frac{dT}{dx} - e\,C_+\,U_+\,\frac{dv}{dx} \qquad \text{...(13)}$$

where D_+ and D_- are the diffusion co-efficients for $+ve$ and $-ve$ ions, U_+, U_- the ionic mobilities of the colder ions. $-\dfrac{dc}{dx}$ the concentration gradient of ions in the direction of the temperature gradient, $-\dfrac{dT}{dx}$ and $\dfrac{dv}{dx}$ are the temperature gradient and potential gradient set up by the space charge. The eqn. (5) and (6) are nonlinear integro-differential equations for the distribution of space charge. For simplicity we have assumed that, in the steady state, with no net current flowing, the internal field set up by the space charge may, to a first approximation, be regarded as uniform with the separated charges appearing on opposite ends of the specimen. Under this conditions

$$C_+ \simeq C_-,\ \frac{dc_+}{dx} \simeq \frac{dc_-}{dx} \text{ and } i_+ + i_- = 0 \qquad \text{... (14)}$$

Then

$$\frac{dv}{dx} = \frac{4\pi\sigma}{\epsilon} = \frac{(D_- - D_+)\left[\frac{dc}{dx} + \frac{C}{T}\frac{dT}{dx}\right]}{C\,[U_+ + (1-B)\,U_-]} \qquad \ldots (15)$$

where σ is the surface density of charge at the end of the specimen and $\in$ is the static permitivity of the dielectric.

Again

$$D_+ = \frac{U_+ K_\beta T}{e}, \qquad\qquad D_- = \frac{U_- K_\beta T}{e}$$

$$\frac{dc}{dx} = \frac{dc}{dT} \cdot \frac{dT}{dx}$$

We have

$$\sigma = \frac{\epsilon}{4\pi} \cdot \frac{K_\beta T}{e} \left(\frac{U_- - U_+}{(1-B)\,U_- + U_+}\right) \left(\frac{1}{C}\frac{dc}{dT} + \frac{1}{2T}\right)\frac{dT}{dx} \qquad \ldots (16)$$

The concentration of charge carries developed by the thermal dissociation or excitation may be obtained from the relation

$$C_+\,C_- \simeq C^2 = \alpha \exp\left(-\phi/K_\beta T\right)$$

where ϕ is the activation energy

$$\therefore \quad \frac{1}{C}\frac{dc}{dT} = \frac{\phi}{2K_\beta T^2}$$

So

$$\sigma = \frac{\epsilon K_\beta}{8\pi e} \left(\frac{(U_-/U_+) - 1}{[(1-B)\,U_-/U_+] + 1}\right) \left(\frac{\phi}{K_\beta T} + 1\right)\frac{dT}{dx} \qquad \ldots (17)$$

If the negative charge carriers be electrons then $U_- \gg U_+$

Therefore,

$$\sigma = \frac{\epsilon K_\beta}{8\pi e}\frac{1}{1-B}\left(\frac{\phi}{k_\beta T} + 1\right)\frac{dT}{dx} \qquad \ldots(18)$$

The bound electret charge is

$$\sigma' = \frac{\epsilon K_\beta}{8\pi e}\frac{B}{1-B}\left[\left(\frac{\phi}{K_\beta T} + 1\right)\right]\frac{dT}{dx} \qquad \ldots(19)$$

As the magnetic field is applied the mobility and trapping of charge carries will change. Thus B will be higher for the application of magnetic field. Therefore more charges would be separated. As one side of the sample acquires higher negative charge while the other side positive charge, the sample would acquire 'idio-charge'. The amount of this 'idio-charge' would depend upon the scattering mechanism, diffusion and trapping.

It is observed that the specific conductance of a dielectric increases with temperature. Fig. 14 shows the change of specific conductance with temperature and Fig. 15 shows the change of dielectric constant with temperature of carnauba wax (unpublished). These are probably due to higher charge mobility and production of larger amounts of charge carriers. So at higher temperatures charge separation and the formation of electret charge will have higher probability. When the magneto-electret is prepared from the molten substance charges would appear on the solid liquid interface[7,9]. During solidification newly formed small crystals or crystalline groups will be oriented by the magnetic field[8]. Due to this orientation the charge separation on solidification would enhance as is observed for Napthalene[56]. These separated trapped charge would show magnetic field dependence since the orientation depends upon the field.

Another possibility for charge separation is that the field may not be strictly uniform. It will deviate from being uniform near the boundaries of the disc where magnetic lines of force might be distorted due to difference in permeability of the wax and the brass container. This would cause a field gradient which would force the ions to move causing separation[18].

If once the ions are separated due to either temperature gradient or field gradient a high electric field would appear near the ions. This may cause polarization due to dipolar orientation if it is prepared from molten state.

Total sum of the charge on 'N' and 'S' faces would be zero if it would be due to dipolar orientation or due to the separation of ions or electrons formed from the
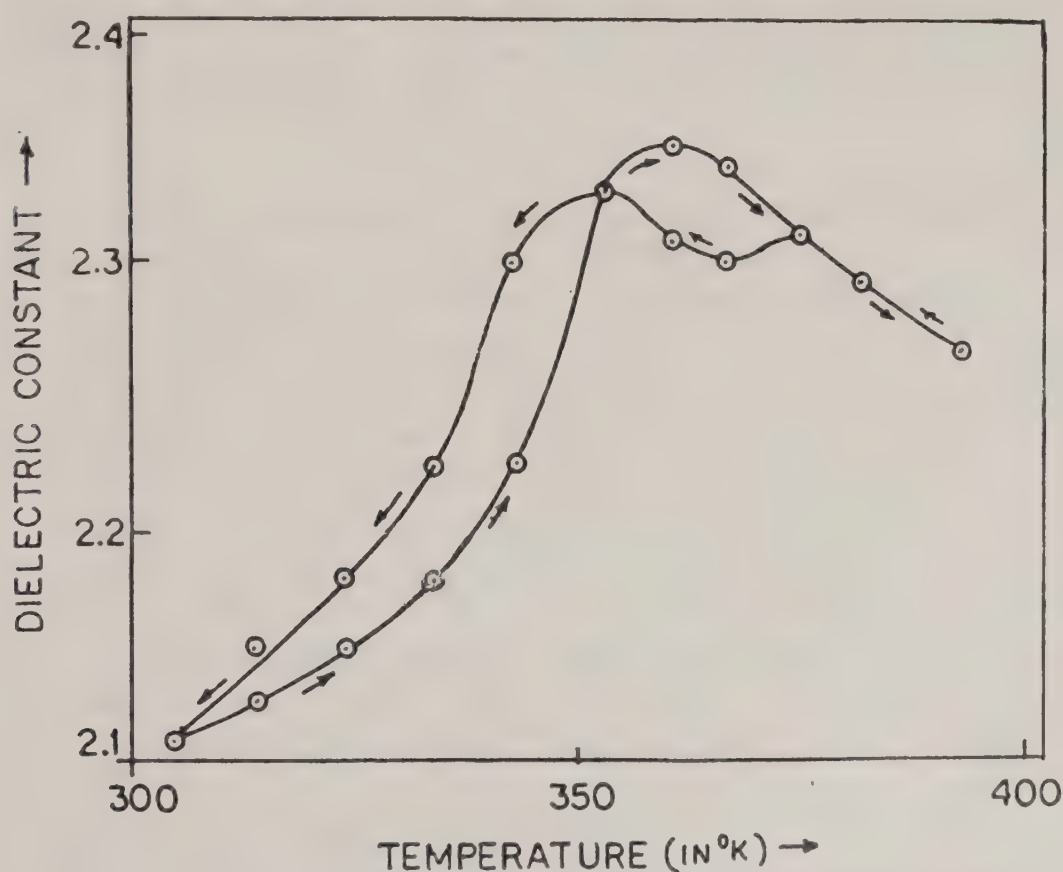
FIG. 14. Temperature variation of dielectric constant of carnauba wax.
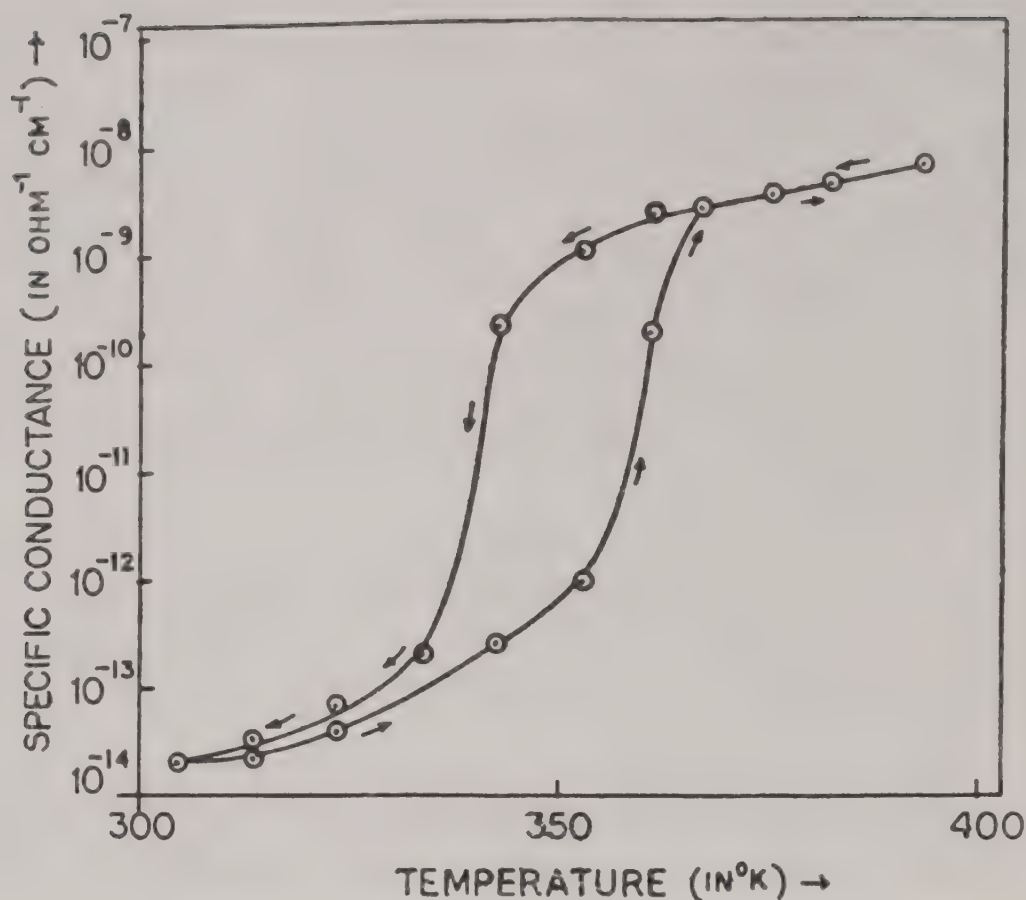
FIG. 15.   Variation of conductivity with temperature of carnauba wax.

molecules within the material. But a net total charge is observed and it is called 'Iso-charge'. No net charge of one sign can be produced from a neutral material. So one type charge must come from or go to the lining material. These influx of charges from the lining material would depend open the material and the metal lining[6].

The magneto-electret charge decays with passage of time. This may be explained from the detrapping of the charge carriers. After the removal of the magnetic field utilised for preparation, the trapped charges would be induced to be free gradually due to the thermal agitation. The charge released would be proportional to the product of the no. of trapped charge and $\exp(-\phi/k_B T)$ where ϕ is the activation energy of the trapped charges. These free charge carriers will move due to internal electric field to neutralize the charge. Thus the charge will decrease exponentially. But during their motion charge carriers may be retrapped. This will cause some deviation from purely exponential decay. Such exponential type of decay has been observed in several cases[18,38,24-27]. In some cases however, more than two types of charge carriers may form. Then their diffusion and trapping at different levels will produce charges which would decay with different rates. This may cause non exponential decay like that shown in Fig. 6.

The study of magnetic anisotropy and refractive index of magneto-electret indicates that the oriented molecules in the solid state do not reorient with time[46,48].
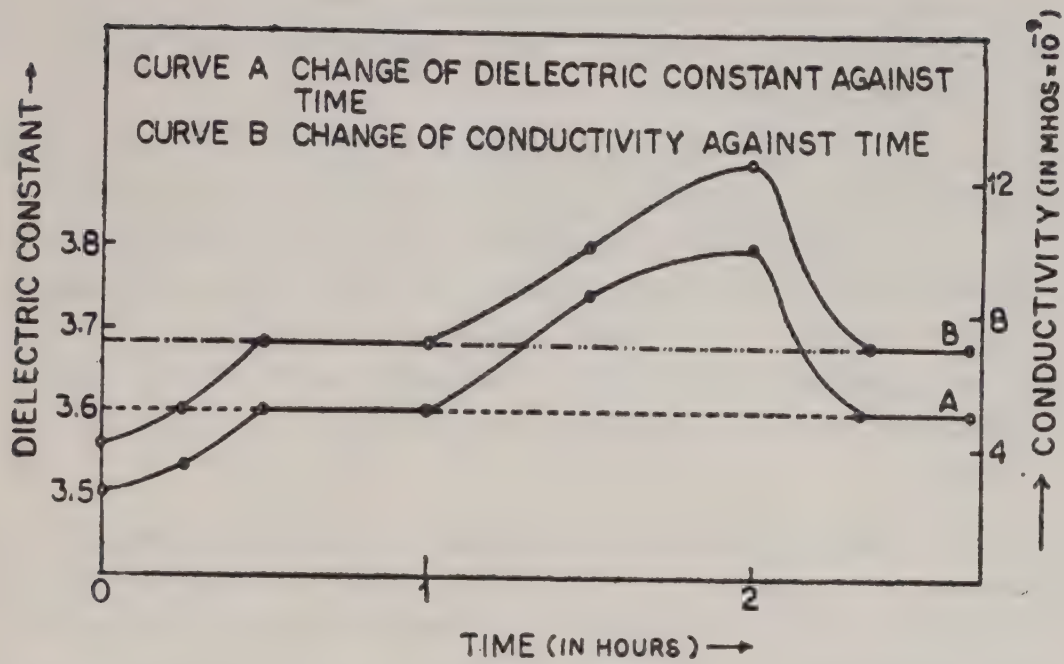
FIG. 16. A–Change in dielectric constant and

B–Change in conductivity against time of Nitrobenzene magneto-electret

(a)

(b)
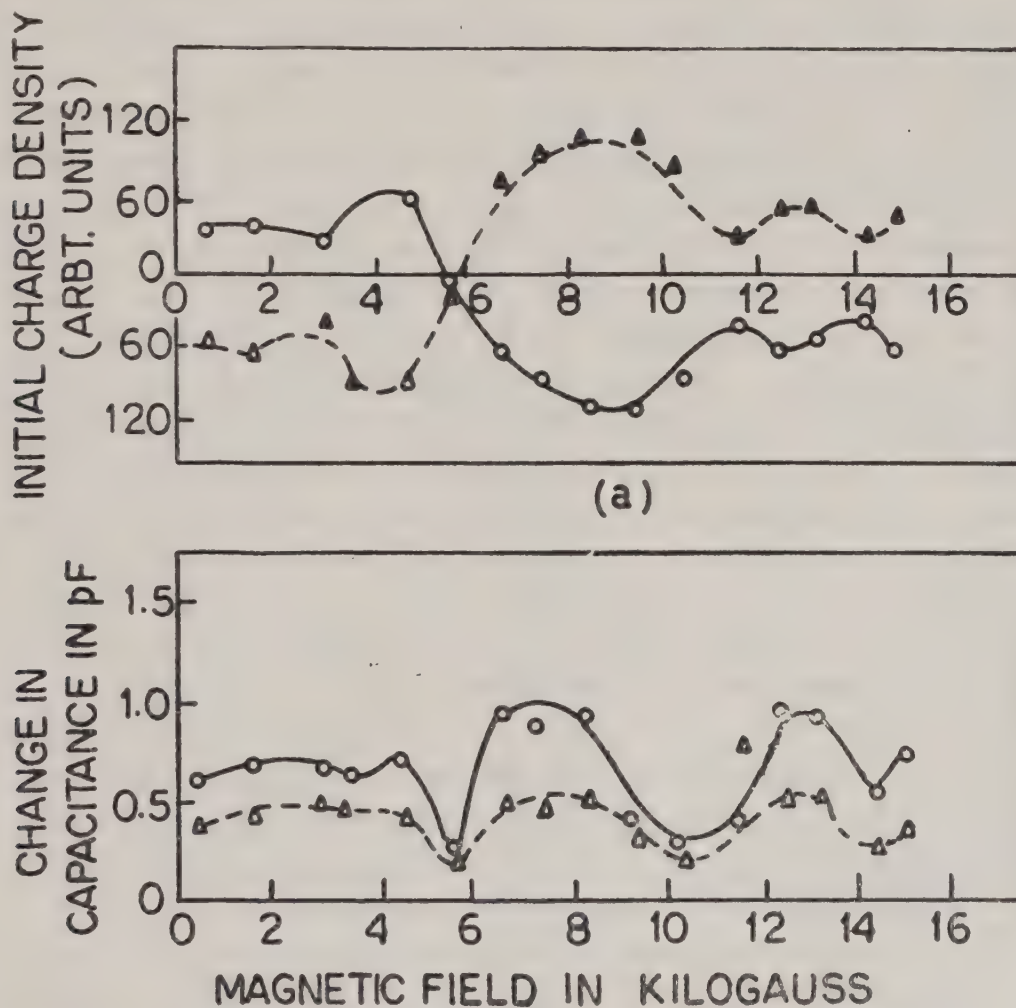
FIG. 17. (a) Variation of initial charge with magnetic field for perspex formed at 170°C[32] (O–O–O N–surface △–△—△ S–surface).

(b) Variation in change in capacitance (O–O–O C_i–C_p △–▲–▲ C_f–C_p).

So the charge due to dipole orientation would be expected not to decay with time. The residual polarization of carnauba wax magneto-electret may therefore be assigned entirely to its polarization[18].

During the study of photo-depolarization of sulphur it is observed that the decay time constants increases gradually when the forming magnetic field is within 6.6 K. Gauss. This decay of time dependence on magnetic field may be due to the formation of small polaron of different binding energies. After withdrawal of the magnetic field the trapped charge carries will be detrapped by the thermal energy, with different time constants for different trapping levels. For a single forming magnetic field two decay time constants of magneto-electret is due to trapping at two different levels.

Detrapping of charge carriers is expected to produce some change in the dielectric constant and conductivity of the substance for the time before recombination of the charge carriers or retrapping. Charge migration from or to the lining material would also change the dielectric constant of the sample. It is observed that when magneto-electret is prepared at forming temperatures above softening temperature or above melting point the dielectric constant decreases just after the withdrawal of the magnetic field. With the passage of time the dielectric constant increases to a value higher than that of untreated sample and then finally decreases to its normal (untreated) value[53,18]. But if the forming temperature is below the softening state of the substance and if only isocharge is formed on magneto-electret formation dielectric constant increases from its initial value when positive isocharge is formed and decreases when negative isocharge is form [38,55,56]. The decrease in dielectric constant is due to the orientation of molecular groups. When the molecular group orients at softening state by the magnetic field due to its magnetic anisotropy it will be accompanied by a change in anisotropy of dielectric constant[57]. This causes a decrease in dielectric constant along the direction of forming magnetic field. The trapped charge carriers when released from the traps become mobile and it would cause some rise in dielectric constant before its recombination. Free charge carriers formed by other means like electron emission by the field of aligned dipole, as suggested by Chatterjee and Raychoudhuri[58] may also be the cause of the increase in dielectric constant. After recombination of the charge carriers the substance regains its original value. The higher initial increase in capacitance for lower forming temperature is due to formation of iso-charge[38]. For the same reason the conductivity of the magneto-electret will change. It is observed that the conductivity of nitrobenzene magneto-electret changes in the same manner as the dielectric constant changes[53]. The variation of dielctric constant closely follows the charge variation of the magneto-electret[38]. Fig. 17(a) shows the charge variation of perspex magneto-electret and Fig. 17(b) shows the variation in the change of capacitance of a parallel plate condensor having magneto-electret as dielectric. The solid curve shows the variation immediately after formation. The dotted curve is 30 days after formation. The upper curve, the charge variation, follows the variation of dielectric constant. The dielectric constant does not dpend on the direction of polarization.
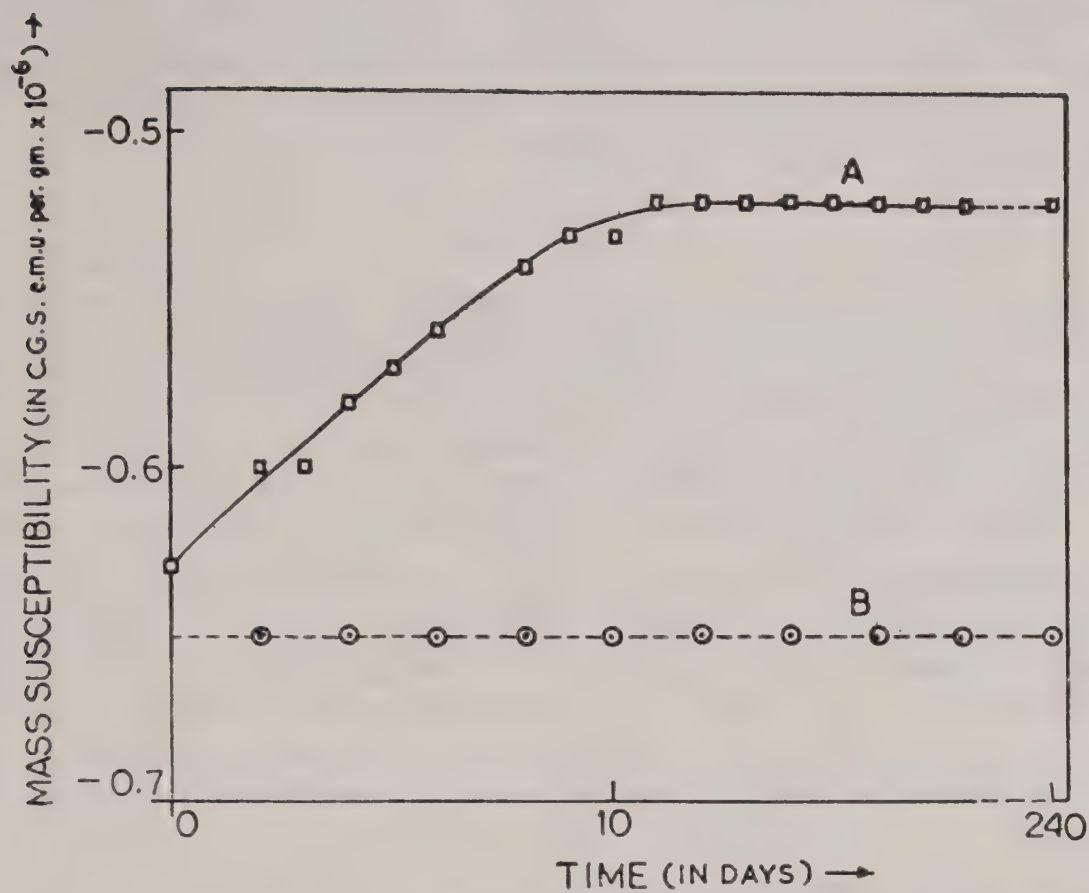
FIG. 18. Time variation of magnetic susceptibility of carnauba wax magneto-electret[46].
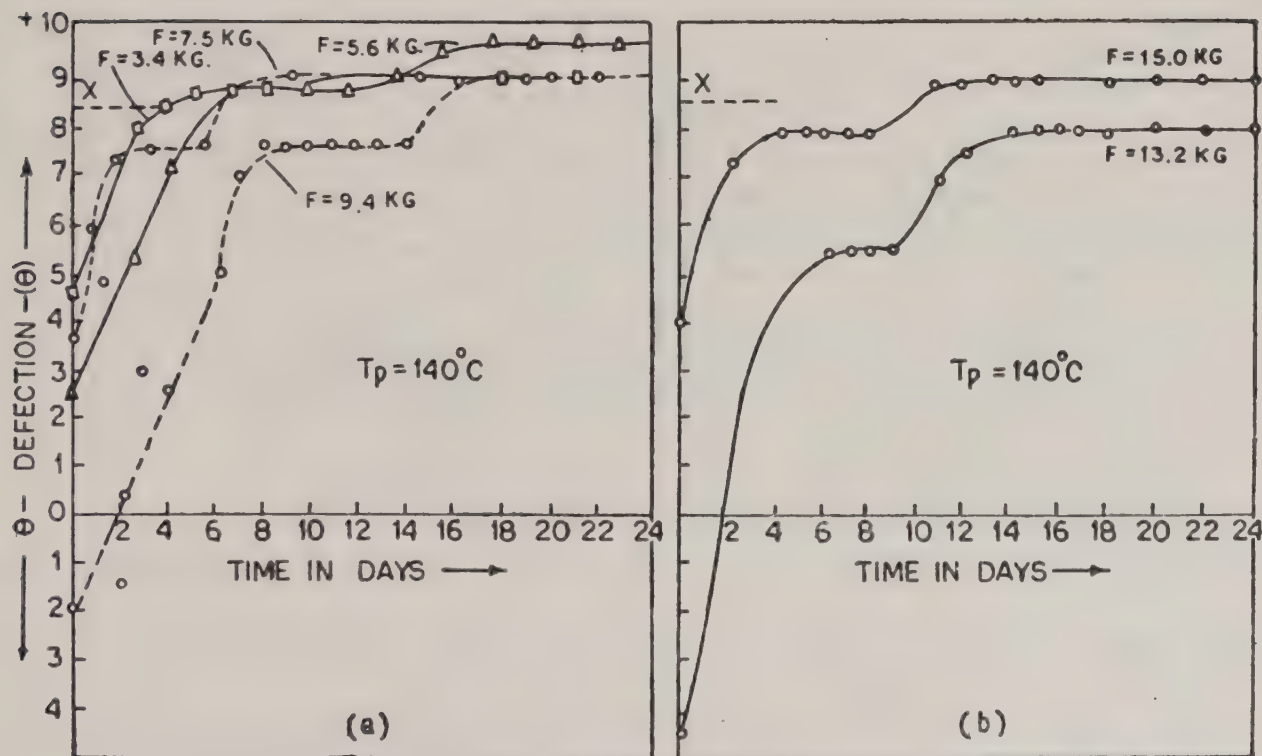
VARIATION OF SUSCEPTIBILITY WITH TIME FOR ELECTRETS PREPARED AT 140°C

FIG. 19. Variation of magnetic susceptibility with time for perspex magneto-electrets prepared at 140°C.[2]

Another change of property of the substance associated with the formation of magneto-electret is the change in magnetic susceptibility of the substance. In carnauba wax and perspex magneto-electret the diamagnetic susceptibility decreases but for Naphthalene magneto-electret it increases[59,60]. Fig. 18 & 19, shows the variation of magnetic susceptibility with time.

CONCLUSION

In this review article an attempt has been made to incorporate a comprehensive account of the basic phenomena observed in Magneto-electrets. Existing theories of the magneto-electret have also been discussed. It has been stated that uniform magnetic field and temperature cannot produce any charge separation in the diagmagnetic material. Attempt has also been made to explain the appearance of surface charge from the consideration of the presence of temperature gradients and formation of small polarons. The temperature gradient diffuses the charge carriers which are produced on account of impurity excitation of thermal dissociation. Small polarons are formed due to the persistence for longer periods of charge carriers in the neighbourhood of the atoms by the influence of magnetic field. These small polarons would acquire binding energies that would depend on the forming magnetic field. Thus magnitude of charge and its retention would depend on the strength of the magnetic field. When magneto-etectrets are formed from its molten or softening state, the charge separation do strongly be dependent on the crystalline orientation by the magnetic field.

REFERENCES

1   O Heaviside, *Electrical Papers.* New Yorks, Vol. 1   (1892) p 488.
2   P Curie,   *J. Physique*, 3 Series III. (1894)   393.
3   I E Dzyloshinskii,   *Soviet Phys. J. E. T. P.* **10**   (1960) 628.
4   G T Rado, and V J Folen,   *Phys. Rev. Letter* **7**   (1961) 310.
5   S Gray,   *Philos. Trans. R. Soc.* A **37** (1932)   285.
6   P A Thiessen, A Winkel and K Herrman,   *Physik Z.* **37**   (1936) 511.
7   J Costa Riebeiro,   *Anals. da Academia Brasilira de Ciencias* **22**   (1980) 3.
8   S Mascarenhas and L G Freitas,   *J. Appl. Phys.* **31**   (1960) 1684.
9   E J Workman, and S E Raymold,   *Phys. Rev.* **78** (1950)   254.
10   J Latham, and B J Masson,   *Proc. Ray. Soc.* A (GB) **260** (1961) 523.
11   C S Bhatnagar,   *Indian J. pure. Appl. Phys.* **2**   (1964) 331.
12   M Faraday, *Experimental Research in Electricity.* Vol. 1 Taylor and Francis, London   (1839)
          1234–1250, 1269.
13   A D Moor,   *Electro statics and its application*, John Wiley & Son. Inc. (1973).
14   M Eguchi,   *Proc. Phys. Math. Soc. Japan.* **1**   (1919) p 326.
      ———   *Japan J. Phys.* **1** (1922)   10; *Philos. Mag.* **49** (1925)   p 178.
15   G Nadzhakov,   *Compt. Rend.* **204** (1937)   1865.
16   P Selenyi,   *Z. Tech. Phys.* **9** (1928)   45.
17   B Gross, *Z. Phys.* **155**   (1959) 479.
18   C S Bhatnagar,   *Indian J. pure. Appl. Phys.* **4**   (1966) 355.

19 M L Khara, and C S Bhatnagar, *Indian J. pure. Appl. Phys.* **3** (1965) 356.

20 ——— *Indian J. pure. Appl. Phys.* **7** (1969) 160–162 & 497–499.

21 R K Shrivastava, and C S Bhatnagar, *Indian J. pure. Appl. Phys.* **19** (1981) 19.

22 L N Sharma, and C S Bhatnagar, *Indian J. pure. Appl. Phys.* **8** (1970) 500.

23 ——— *Indian J. pure. Appl. Phys.* **13** (1975) 229.

24 B M Agrawal, and C S Bhatnagar, *Indian J. pure Appl. Phys.* **11** (1973) 413.

25 ——— *Indian J. pure. Appl. Phys.* **12** (1974) 95.

26 ——— *Indian J. pure Appl. Phys.* **12** (1974) 404.

27 ——— *Indian J. pure Appl. Phys.* **13** (1975) 370.

28 P K C Pillai, K Jain, and V K Jain, *J. Electro-Chem. Soc.* **118** (1971) 1675.

29 V K Jain, and C S Bhatnagar, *Indian J. pure Appl. Phys.* **9** (1971) 339.

30 A P Rajinder, M L Khare and C S Bhatnagar, *Indian J. pure. Appl. Phys.* **13** (1975) 802.

31 M L Khare and C S Bhatnagar, *Indian J. pure. Appl. Phys.* **8** (1970) 700.

32 L M Sharma and C S Bhatnagar, *Indian J. pure. Appl. Phys.* **9** (1971) 240.

33 M S Qureshi, and C S Bhatnagar, *Indian J. pure. Appl. Phys.* **13** (1975) 797; **9** (1971) 361.

34 S Asghar Hussain, M L Khare, and C S Bhatnagar, *Indian J. pure Appl. Pnys.* **19** (1981) 1062.

35 A N Deshpande, and C S Bhatnagar, *Indian J. pure. Appl. Phys.* **11** (1973) 410.

36 ——— *Indian J. pure. Appl. Phys.* **12** (1974) 254.

37 S P Saxena, M L Khare, and C S Bhatnagar, *Indian J. pure Appl. Phys.* **14** (1976) 955.

38 M S Qureshi and C S Bhatnagar, *Indian J. pure. Appl. Phys.* **10** (1972) 220.

39 R K Shrivastava, M S Qureshi, and C S Bhatnagar, *Japan J. Appl. Phys.* **17** (1978) 1537.

40 V T Shrivastava, M S Qureshi, and C S Bhatnagar, *Indian J. pure. Appl. Phys.* **17** (1979) 4.

41 M M Perlman, and R A Creswell, *J. Appl. Phys.* **41** (1970) 2365.

42 A K Bhatnagar, M S Qureshi, and C S Bhatnagar, *Indian J. pure. Appl. Phys.* **21** (1983) 534.

43 H De, and S D Chatterjee, *Science & Culture* **35** (1969) 585.

44 N R Pan, *Indian J. pure. Appl. Phys.* **13** (1975) 806; **14** (1976) 800.

45 K S Krishnan, and C V Raman, *Proc. R. Soc.* A **155** (1927) 549.

46 S D Chatterjee, K D Roychoudhuri, and K Banerjee, *Acta. Physica Polonica* A **51** (1977) 643.

47 M L Maji, M Saha, and S D Chatterjee, *Proc. Indian natn. Sci. Acad.* **49** (1983) 347.

48 J K Qumara, M L Khare, and C S Bhatnagar, *Indian J. pure. Appl. Phys.* **14** (1976) 147.

49 M L Maji, and S D Chatterjee, *Indian J. pure. Appl. Phys.* **20** (1982) 44.

50 G F J Garlick, and A F Gibson, *Proc. Phys. Soc.* **60** (1948) 574.

51 M L Maji, M Saha and S D Chatterjee, *Indian J. pure. Appl. Phys.* **18** (1980) 611.

52 P S Kirrev, *Semiconductor Physics.* Mir Publishers, Moscow (1979) 324–328.

53 S D Chatterjee, and K D Roychoudhari, *Phys. State. Sol.* (a) **2** (1970) K 121.

54 T Holstein, *Ann. Phys.* (NY) **8** (1959) 325.

55 A K Bhatnagar, J K Quamara, and C S Bhatnagar, *Indian J. pure. Appl. Phys.* **20** (1982) 215.

56 A K Bhatnagar, M L Khare, and C S Bhatnagar, *Indian J. pure. Appl. Phys.* **21** (1983) 365.

57 M L Maji, *Indian J. Phys.* **55**A (1981) 259.

58 M L Maji and S D Chatterjee, *Indian J. pure. Appl. Phys.* **20** (1982) 986.

59 S D Chatterjee and K D Roychoudhuri, *Phys. Stat. Sol.* (a) **2** (1970) K 121.

60 M Bondopadhyay and M L Khare, *Indian J. pure. Appl. Phys.* **13** (1975).

HALL EFFECT IN AN ARC PLASMA

S N Sen *and* B Ghosh

Department of Physics, North Bengal University, Darjeeling, India

The Hall voltage in a mercury arc plasma carrying a current of 3 amperes with a background air pressure of .2 torr has been measured for a range of magnetic field varying from 64 gauss to 526 gauss. Taking into consideration the variation of arc current and radial electron density in a transverse magnetic field as deduced by Sen and Das[1] from the theoretical formulation of Beckman[2], the expression for Hall voltage in an arc plasma has been deduced. The value of electron density and drift velocity have thus been calculated which are in agreement with literature values. The utility of the method as a plasma diagonostic tool has been discussed.

Keywords : Hall Effect; Arc Plasma; Magnetic Field; and Electron Density

INTRODUCTION

THE Hall effect is a standard diagnostic method for determining the charged particle density and mobility in semi-conductors and it has also been utilized for measurement of plasma parameters in a glow discharge. The effect of a transverse magnetic field on the positive column of a glow discharge has been studied among others by Beckman[2] and the variation of current in a variable transverse magnetic field has been studied by Sen and Gupta[3]. With regard to the effect of a transverse magnetic field on an arc discharge, Allen[4] observed in the case of a heavy current pulsed arc discharge in hydrogen that the voltage current characteristic showed a slight negative gradient over the range of 25 to 80 amperes with no magnetic field, but became increasingly negative with increase of magnetic field. Forrest and Franklin[5] have described a theoretical model for a low pressure arc discharge in a magnetic field in which predictions have been made for radial electron number density profile and radial light emission profile. Anderson[6] investigated the Hall effect in the positive column in the glow discharge in some rare gases and obtained the drift velocities of electrons for a range of (E/P) values. In his calculation he utilised the expressions for the radial electron density distribution provided by Beckman[2] and reported results for drift velocities in agreement with literature values. Axial electron density variation in a magnetically confined arc has been investigated by Mashic and Kwen[7], who showed that the variation is more pronounced in the high pressure region ($p \sim 10$ torr) and is weakly dependent upon magnetic field. The voltage current characteristics and the power relation have been investigated in a mercury arc carrying current from 1.3 amp. to 2 amp. in presence of a transverse magnetic field upto 3000G by Sen and Das[1]. The Hall effect in a toroidal discharge plasma has been investigated by Zhilinsky *et al.*[8] and Goldferb[9] has

presented some diagnostic techniques for the arc plasma. In contrast to semi-conductors or metals it is to be noted that when an arc or a glow plasma is placed in an external magnetic field the radial electron density distribution and discharge current are significantly altered and this effect has to be taken into consideration in calculating the Hall coefficient in a plasma. In the present investigation results are reported on the measurement of Hall effect and calculation of axial density and drift velocity of electrons in a mercury arc plasma.

THEORETICAL TREATMENT

The Hall voltage E_y per unit length when the conductor carrying a current i is placed in a transverse magnetic field H is given by

$$E_y = \frac{iH}{ne} \qquad \ldots(1)$$

where i is the current per unit area and n the electron density. It has, however, been shown that in the case of an arc current gradually decreases in a transverse magnetic field. Sen and Das[1] have shown following an analysis by Beckman[2] that the electron density decreases and the electron temperature increases in an arc plasma in a transverse magnetic field. The electron density n_H in presence of a magnetic field H has been shown to be given by

$$n_H = n_0 \exp(-aH) \qquad \ldots(2)$$

where a is defined below. Taking these two effects into consideration, Sen and Das[1] deduced the expression for the arc current i_H in a transverse magnetic field as

$$\frac{i_H}{i} = \frac{\exp(-aH)}{\left[1 + r \log\left\{\frac{1}{(1 + C_1 H^2/P^2)^{1/2}}\right\}\right]^{1/2}} \qquad \ldots(3)$$

In this $a = \dfrac{eEC_1^{1/3}\mu}{2KT_eP}$ where E is the axial electric field, μ the electron mobility, K the Boltzman constant, T_e the electron temperature, P the pressure and $C_1 = \left(\dfrac{e}{m}\dfrac{L}{v_r}\right)^2$ where L is the mean free path of the electron in the gas at a pressure of 1 torr, v_r is the random velocity of the electron and $r = \dfrac{2Te}{T_e + 2eV_{i/k}}$ where V_i is the ionization potential of the gas.

As both current and radial election density change when the arc is placed in a magnetic field we get then from equation (1), (2) and (3)

$$E_y = \frac{iH}{n_0 e\left[1 + r \log\left\{\frac{1}{(1 + C_1 H^2/P^2)^{1/2}}\right\}\right]^{1/2}} \qquad \ldots(4)$$

Hence by measuring the Hall voltage for a range of values of the magnetic field the electron density in an arc plasma can be obtained. Further as i the current density

$n_0 e v_d$ where v_d is the drift velocity of the electron it is possible to calculate the drift velocity as well.

EXPERIMENTAL SET UP

The Hall voltage measurement has been carried out in a mercury arc plasma which has been produced within a cylindrical glass tube of radius 1.32 cm. and a distance between the two mercury pool electrodes of 26.4 cms. The arc is run on d.c. voltage (220 volts) with regulating rheostats in series : arc current has been varied from 2 amp. to 3 amps. The background air pressure within the arc is maintained ata .2 torr. Two horizontal metallic plates (2.5 cm. × 1 cm.) at a distance of .8 cm. are introduced within the arc tube for measuring the Hall voltage. The magnetic field which is at right angles to both to the direction of the flow of current and measuring electrodes has been provided by an electromagnet. The power to run the electromagnet has been supplied by a stabilised power supply. The magnetic field which has been varied from zero to 550 gauss has been measured by an accurately calibrated gauss meter. The gauss meter operates on the principle of the Hall effect. The Hall probe is made of a highly pure indium arsenide crystal and is encapsulated in a nonmagnetic sheath of approximately 50 mm. × 5 mm. × 2 mm. and is connected to a three feet cable. A transparent cap is provided for the protection of the probe. The accuracy of the reading is ± 2.5 per cent upto 10 kilogauss. The Hall voltage developed in the arc plasma has been measured by a V.T.V.M. (Simpson Model No. 321–1). The valve tube voltmeter is a Versatile instrument designed for accurate measurement of voltage (both a.c. and d.c.). The d.c. voltages upto 1500 volts can be measured in seven stages, input impedance is 35 megaohms in all the ranges and the accuracy of reading is ± 3 per cent.

RESULTS AND DISCUSSION

Experimental results are reported here for a mercury arc plasma carrying a current of 3 amp. and the transverse megnetic field varying from 64 G to 526 G. The results are entered in Table I.

Values of n, the electron density in the third column of Table I have been calculated from the relation $E_v = \dfrac{iH}{ne}$ (eq. 1) which assumes that the current and radial distribution of charged particles are the same as in the absence of magnetic field. The results consequently show that the electron density in absence of magnetic field shows a decrease with the increase of the magnetic field which however should be constant for all values of magnetic field as the magnetic field used for producing the Hall effect has been used here as a probe only. To take into effect the radial distribution of charged particles in presence of the transverse magnetic field and also the change of current we have used equation (4) for the Hall voltage, and have taken T_e, the electron temperature to be 25000 K after Karelina[10] and confirmed by Sadhya[11] in this laboratory by a spectroscopic method, the value of r has been calculated to be 0.1887 as in the previous paper by Sen and Das[1]. C_1 is the square

TABLE I

Magnetic field in Gauss	Hall voltage volts/cm.	Value of n from the relation by $E_y = \dfrac{iH}{ne}$	$\left[1 + r \log \dfrac{1}{(1 - C_1)\,(H^2/P^2)^{1/2}}\right]^{1\cdot2}$	Value of n_0 from eqn. (4)
64	.34	3.599×10^{12}	.9910	3.631×10^{12}
112	.71	3.533×10^{12}	.9763	3.620×10^{12}
166	1.15	3.501×10^{12}	.9576	3.656×10^{12}
216	1.76	3.483×10^{12}	.9515	3.662×10^{12}
256	2.17	3.423×10^{12}	.9374	3.652×10^{12}
306	2.62	3.356×10^{12}	.9123	3.678×10^{12}
356	3.07	3.253×10^{12}	.8993	3.617×10^{12}
406	5.57	3.180×10^{12}	.8772	3.624×10^{12}
456	3.92	3.165×10^{12}	.8756	3.606×10^{12}
476	4.40	3.108×10^{12}	.8712	3.569×10^{12}
526	4.62	3.068×10^{12}	.8610	3.563×10^{12}

of the mobility of the electron in mercury vapour at a pressure of 1 torr and has been taken as 2×10^{-6} by Mc Daniee[12]. Using these values of r and C_1 the numerical values of the term in equation (4) have been calculated for values of magnetic field varying from 64 gauss to 526 gauss, and the results are entered in the fouth column of Table I. Now utilizing equation (4) the value of n_0 the axial electron density in absence of the magnetic field has been calculated and the results are entered in the fifth column of Table I. The Hall effect is used here as a diagnostic tool and the axial electron density in absence of magnetic field should be independent of magnetic field used for measuring the Hall effect. The results show that the axial electron density in absence of magnetic field is almost a constant for values of magnetic field varying from 64 gauss to 526 gauss and for higher values of magnetic field there is a fall in the value of n_0. This result is also consistent with the earlier observation by Sen and Das[1] that equation (3) as deduced from the expressions of Beckman[2] is valid for values of magnetic field upto 1000 gauss and as in the present investigation the maximum magnetic field is 526 gauss equation (3) will hold in this region of magnetic field as well. The average value of electron density is 3.638×10^{12}. From this value of n_0, the drift velocity of electrons can be calculated.

$$i = n_0 e v_d$$

$$\frac{3}{3.14 \times (1.32)^2} = 3.638 \times 10^{12} \times 1.6 \times 10^{-19}\, v_d$$

So that $v_d = .94 \times 10^6$ cm/sec. which is in agreement with the result reported by Brown[13].

It is thus concluded that the Hall effect can be utilised as a useful diagnostic technique for measurement of electron density and drift velocity of electrons in an

arc plasma. The radial particle density distribution and the change of arc current due to magnetic field have to be taken into account in calculating the parameters of the plasma. Work is in progress with other arc sources and results will be reported.

ACKNOWLEDGEMENT

REFERENCES

1. S N Sen and R P Das, *Inter. Jour. Electron.* **34** (1973) 527.
2. L Beckman, *Proc. Phys. Soc.* **61** (1948) 515.
3. S N Sen and R N Gupta, *Proc. Phys. Soc. J. Phys. D. Appl. Phys.* **4** (1971) 510.
4. N L Allen, *Proc. Phys. Soc. B.* **64** (1951) 276.
5. J R Forrest and R N Franklin, *Brit. Jour. Appl. Phys.* **17** (1966) 1961.
6. J M Anderson, *Phys. Fluids.* **7** (1964) 1517.
7. M E Mashick and L I Kwen, *Jour. Appl. Phys.* (U.S.A) **48** (1977) 3713.
8. A P Zhilinsky, B V Kuteev, A S Smirnov and R S Tahvatulin, *Beetr. Plasma Phys.* **19** (1979) 131.
9. V M Goldferb, *High Temp.* **11** (1973) 150.
10. N A Karelina, *J. Phys.* **6** (1942) 218.
11. S K Sadhya, *"Investigation on the Properties of Magnetised Plasma*, Ph.D. Thesis, North Bengal University (1981).
12. E W Mc Daniel, *Collision Phenomena in Ionised Gases*, John Wiley and Sons, Inc. U.S.A. (1964).

STOCHASTIC ANALYSIS OF FLOODS

N P Singh

Unit of the Project Coordinator (R & M), H.A.U., Hisar-125 004

The applications of extreme values theory to the flood frequency analysis were discussed. An analysis of excessive water discharges (floods) was carried out by using a stochastic model given by Todorovic and his coworkers. For the illustration purpose the data of water discharges for a partial duration series from 1948 to 1977 of river Narmada at two stations, i.e., Mortakka and Gardeshwar were used. A fairly good agreement between theoretical and observed results is seen.

Keywords : Stochastic; Exceedance; Fourier Series; and Floods

1. Introduction

The analysis and prediction of excessive water discharges (floods) have been subject to numerous invesigations by many authors. The common approach to these problems consists of either applying Gumbel's distribution or selecting a flood frequency distribution function based on the criterion of 'best curve fit' to the observed largest water discharge values at a lapes of time. The criterion of 'best curve fit' seems somewhat adhoc on physical grounds and more cumbersome. Also the application of Gumbel's extreme value distribution is based on the following two assumptions.

(i) the sequence of daily water discharge values of whole year form a sequence of independent and identically distributed random variable.

(ii) These random variables are assumed to have an distribution with an exponential tail.

For the limitations of physical basis of these assumptions the Gumbel[1] state ment is quoted as :

"It must be admitted that the good fit cannot be foreseen from the theory which is based on three assumptions."

(i) the distribution daily discharges is of exponential type.

(ii) $n = 365$ is sufficiently large.

(iii) the daily observations are independent.

Assumption (i) cannot be checked since the analytic form of the distribution of daily water discharge values is unknown. $n = 365$ is not sufficiently large number for the covergence of a distribution function to the Gumbel extreme value distribution. The third assumption definitely does not hold as the daily observations are in general not independent.

On the basis of this criticism by Gumble one can say that mathematical assumptions underlying the classical extreme value theory may not always be applicable to a water discharge series. If the time interval of interest is less than a year which is often the case in most countries under the influence of monsoon, then the use of an asymptotic distribution function can hardly be justified in the light of above criticism of the application of asymptotic theory. This criticism points out the need to develop a theory that is physically more meaningful for flood frequency analysis than the classical extreme value theory.

The first attempt to develop such a theory from the properties of stream flow (rather than to explain the properties of stream flow from such a theory) is that of Todorovic and his coworkers[2,3,4]. Their formulaism is based on the partial duration series of water discharges. The sequence of water discharges in such a series within fixed time interval is represented by random variables. It is worth mentioning that Zelehasic[5] has shown that functional form of the distribution function of the largest exceedances derived by this approach, is similar to Gumbel's extreme value distribution.

In this paper author reviewed the results of Todorovic and his coworkers in section 2. In section 3 these results were applied to the water discharges series of river Narmada at two points (stations), i.e. Mortakka and Gardeshwar. The data refer to the period 1948 to 1977 for a partial duration series (starting from 1st July to October 28) for every year. If the water discharge exceeds a certain level in a fixed time interval, it is termed as an exceedance in this analysis. The expected numbers of these exceedances in a fixed time interval for both the stations were expressed by a Fourier expansion. The distribution function of magnitude of exceedances is assumed to be exponential. To demonstrate the goodness of fit achieved the theoretical and observed results were also presented graphically.

2. DISTRIBUTION FUNCTION OF EXCEEDANCES

This section deals with the problem of flood analysis based on the recent developments in the theory of exterme values given by Todorovic[6]. In his approach Todorovic utilizes a stochastic model to describe and predict the behaviour of floods. He starts with a stochastic process $X(t)$ defined as the highest magnitude of rondom variable (maximum water discharge) in an interval of time (o, t). Since the number of flood peak discharges in (o, t) exceeding a certain level x_0 and the magnitude of these peaks are random variables, the foregoing stochastic model seems to confirm well to the flood phenomenon.

Let $Q_{i,j}$ be the flood peak values that exceeds a suitable choosen base level x_0 and $Z_i = Q_i - x_0$. We call Z_i as the magnitude of the i-th exceedance.

If the sequence of these peak discharge values is multiple peaked i.e. if the daily discharges exceed the fixed base discharge x_0, for more than one day continuously without being less than x_0, then the practical aspects suggest that the entire peak discharges should not be considered but only the maximum peak discharge is taken as an exceedance.

The distribution function of supremum and infimum of $Z_{i,s}$ are given by

$$F_{t_s}(x) = EP \mid \operatorname*{Sup}_{\tau(k)<t} Z_k \leqslant x/\eta(t) \mid \qquad \text{...(2.1)}$$

$$F_{t_i}(x) = EP \mid \operatorname*{Inf}_{\tau(k)<t} Z_k \leqslant x/\eta(t) \mid \qquad \text{...(2.2)}$$

Where $\eta(t)$ is the number of exceedances over x_0 in the time interval $(0, t)$. It is a non-decreasing function of time and assumes values $0, 1, 2, —, —, —$. And $\tau(k)$ is the time of the k-th exceedance. Todorovic and Zelenhasic[5] assumed that these exceedances are governed by a poisson process which has a time dependent intensity function. Expectation of (2.1) and (2.2) is given by

$$F_{t_s}(x) = P [\operatorname*{Sup}_{0<k<n} Z_k \leqslant x \cap E_n^t] \qquad \text{...(2.3)}$$

and

$$F_{t_i}(x) = 1 - P [\operatorname*{Inf}_{0<k<n} Z_k \leqslant x \cap E_n^t] \qquad \text{...(2.4)}$$

Under the assumptions that (i) the sequence of $Z_{k,s}$ is a sequence of independent random variables with common distribution function $F(x)$ and (ii) the number of exceedances $\eta(t)$ are independent of their magnitude Z_k, the distribution functions (2.3) and (2.4) can be written as

$$F_{t_s}(x) = \sum_{n=0}^{\infty} [F(x)]^n P[E_n^t] \qquad \text{...(2 5)}$$

$$F_{t_i}(x) = 1 - \sum_{n=1}^{\infty} [1 - F(x)^n P[E_n^t] \qquad \text{...(2.6)}$$

Where $P[E_n^t]$ is the probability that n event will occur in $(0, t)$. Substituting the probability of a poisson process for $P[E_n^t]$ one can get.

$$F_{t_s}(x) = \exp[- \wedge (t)] [1 - F(x)] \qquad \text{...(2.7)}$$

$$F_{t_i}(x) = 1 + \exp[\wedge(t)] - \exp[\wedge(t) F(x)] \qquad \text{...(2.8)}$$

If the magnitudes of exceedances are exponentially distributed with distribution function.

$$F(x) = 1 - e^{-\alpha x}; \alpha > 0, x \geqslant 0 \qquad \text{...(2.9)}$$

Then the distribution function of Sup Z_k is given by

$$\tau(k) \leqslant t$$

$$F_{t_s}(x) = \exp[\wedge(t) e^{-\alpha x}]; \alpha > 0, x \geqslant 0 \qquad \text{...(2.10)}$$

It may be noted that the functional form of the above distribution function is similar to Gumbel's extreme value distribution function. However, Gumbel's distribution is an asymptotic expression of the distribution of the maximum in an independent identically distributed sequence of exponential random variables, whereas the expression (2.10) represents an exact (non-asymptotic) expression governed by possion process of independent identically distributed exponential random variables. The distribution function (2.10) will be used for illustration in the next section.

3. Illustration

In this section the application of the distribution function (2.10) on the river Narmda at Mortakka and Gardeshwar is considered. It may be recalled that data are taken only for a partial duration series starting from July 1st to October 28 for every year at both the stations. The data available refer to the period 1948 to 1977. The expression (2.10) indicates that the estimation and prediction of floods is possible through it, if one has the estimate of $\wedge(t)$, the average number of exceedance in $(0, t)$. The function $\wedge(t)$ for Martakka and Gardeshwar is denoted by $U(t)$ and $V(t)$ respectively and determined in the following manner.

The partial duration series of water discharges values is divided into eight equal intervals of fifteen days period for every year. The base level x_0 is taken as 150,000 c.f.s. (cubic feet per second) for both the stations and only isolated water discharges greater than x_0 were taken into consideration. Zelenhasic[5] has expressed the function $\wedge(t)$ as a finite Fourier series based on the analysis of data. Using the same method, the expression for $U(t)$ and $V(t)$, the expected number of exceedance at Mortakka and Gardeshwar are given as follows :

$$
\begin{aligned}
U(t) = {} & - 5.2142856 + 14.0396824\ t \\
& + 6.5357143\ t^2 - 0.6944444\ t^3 \\
& - 0.0181875 \cos 45\ t - 0.0106729 \sin 45\ t \\
& + 0.0238095 \cos 90\ t + 0.0738095 \sin 90\ t \\
& + 0.0554091 \cos 135\ t + 0.0583746 \sin 135\ t \\
& + 0.0111111\ (-1)^t \qquad\qquad\qquad\qquad\qquad\qquad ...(3.1)
\end{aligned}
$$

$$
\begin{aligned}
V(t) = {} & - 1.500000 + 5.7871573\ t + 7.525940\ t^2 \\
& - 0.7373737\ t^3 - 0.0157369 \cos 45\ t \\
& - 0.0110213 \sin 45\ t + 0.0113997 \cos 90\ t \\
& + 0.0838383 \sin 90\ t + 0.0647711 \cos 135\ t \\
& + 0.0288776 \sin 135\ t + 0.0086580\ (-1)\ t \qquad\qquad ...(3.2)
\end{aligned}
$$

To demonstrate the appropriateness of the above model observed and expected values of $U(t)$ & $V(t)$ are shown in Fig. 1 and Fig. 2. This has come to be an excellent fit.
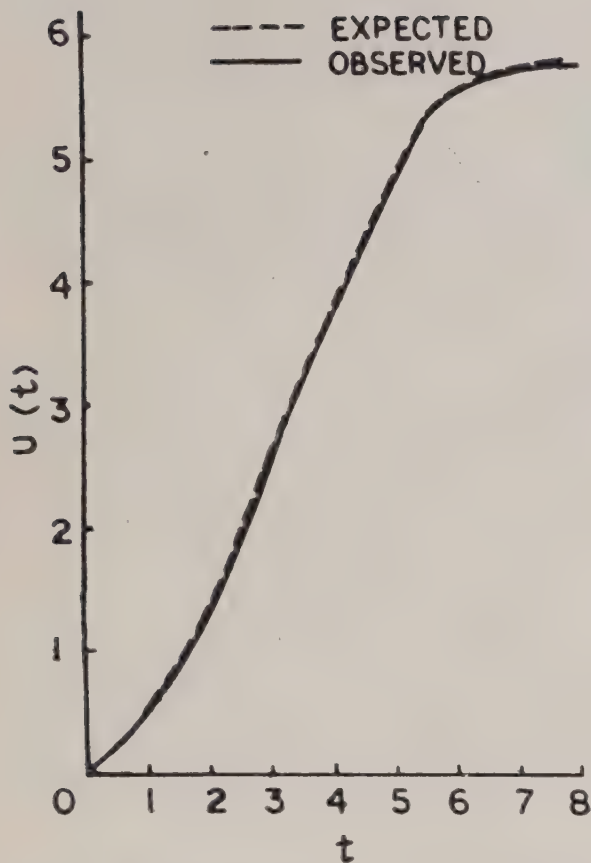
FIG. 1. Observed $U(t)$ and fitting function. Unit interval on t axis stands for 15 days period.
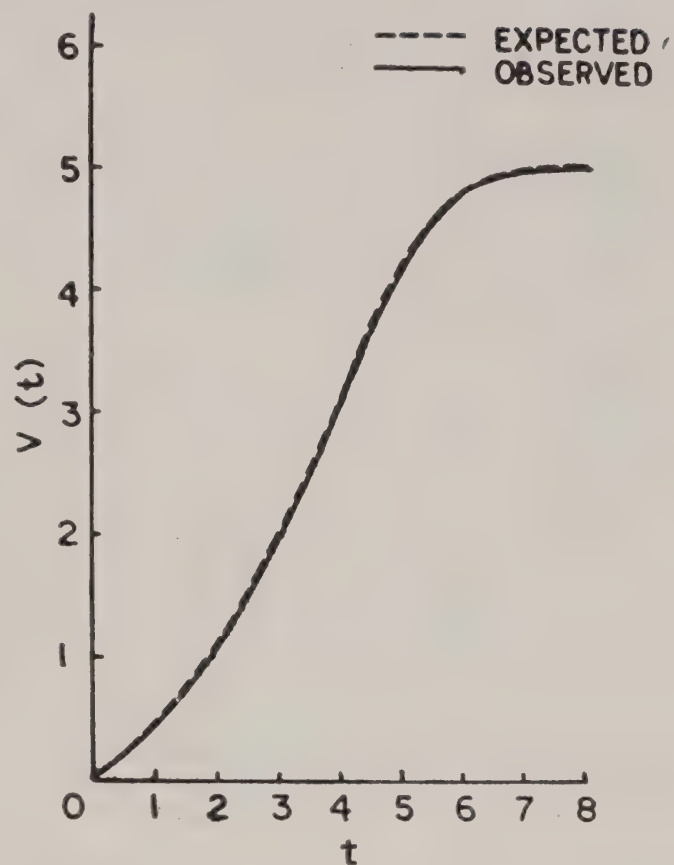
FIG. 2. Observed $V(t)$ and fitting function. Unit interval on t axis stands for 15 days period.

The next step is to evaluate the distribution function (2.10) in terms of its fitness to the given data for the magnitude of exceedances. The magnitude of the exceedances have a common distribution function (2.9) with an unknown parameter (α). For both the stations the value of this parameter of the distribution function (2.9) is estimated by the well known method i.e. maximum likelihood method and presented in the following table.

TABLE I

Station		$E(Z_k)$	$\alpha = [E(Z_k)]^{-1}$
Mertakka	(α_1)	241837.93	4.1487246×10^{-6}
Gardeshwar	(α_2)	343391.88	2.9121247×10^{-6}

The distribution function (2.9) can be calculated now for the different values of x. The observed and corresponding theoretical distribution functions of the flood peak exceedances are presented in Fig. 3 and Fig. 4.

The distribution functions of the largest flood exceedances for both the stations can now be written as

$$F_{t_\bullet}(x) = \exp(-5.7333333 \exp(-4.1487246 \times 10^{-6} x)) \qquad ...(3.3)$$
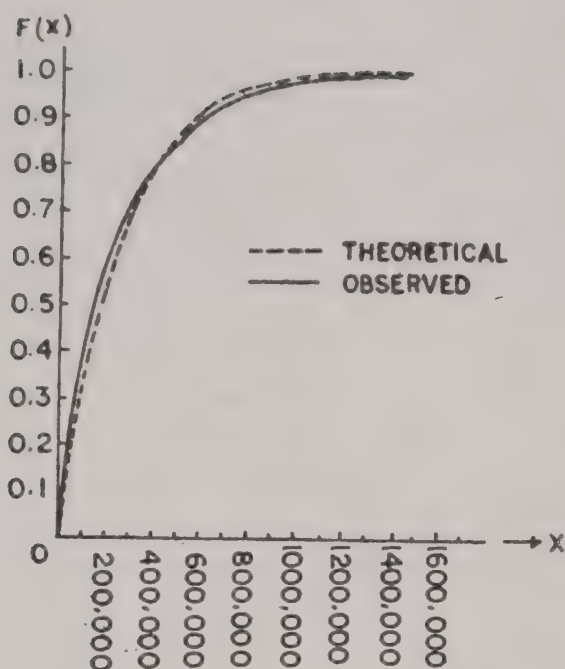
FIG. 3. Observed and theoretical distri-
bution functions of exceedanes
for the Narmada River at
Mortakka for 120 days period.
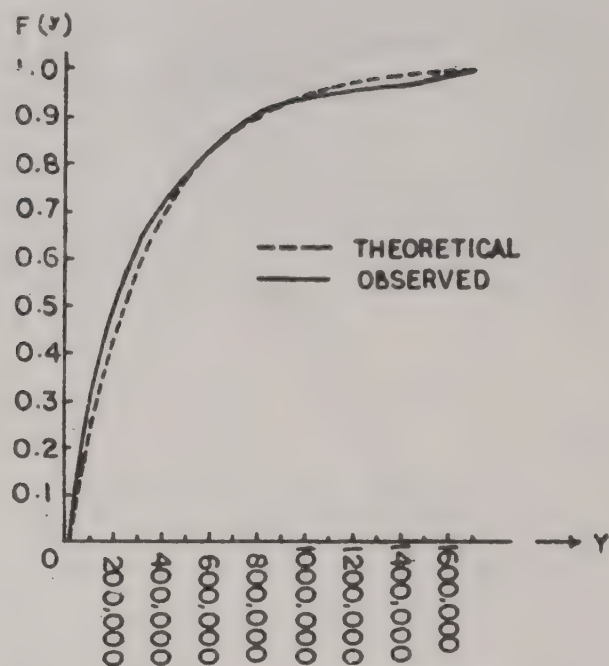
FIG. 4. Observed and theoretical distribution
functions of exceedanes for the
Narmada River at Gardeshwar for
120 days period.
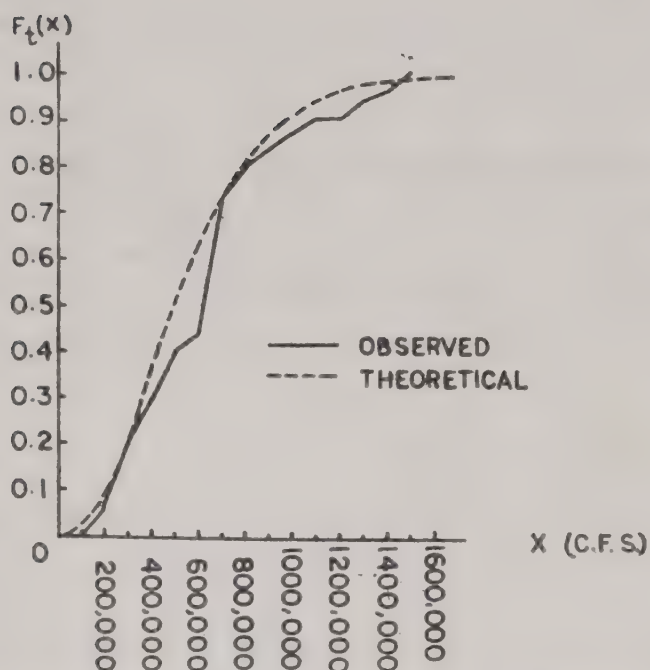
FIG. 5. Observed and theoretical distribution
function of the maximum flood peak
exceedances for the Narmada river at
Mortakka.

FIG. 6. Observed and theoretical distribution
function of the maximum flood peak
exceedances for the Narmada river at
Gardeshwar.

at Mortakka, and

$$F_{t_s}(y) = \exp\left(-5.5.0333333 \exp\left(-2.9121247 \times 10^{-6} y\right)\right) \qquad \ldots(3.4)$$

at Gardeshwar, where the time of interest was from July 1st to October 28.
Fig. 5 and Fig. 6 compare graphically the distribution functions (3.3) and (3.4) and

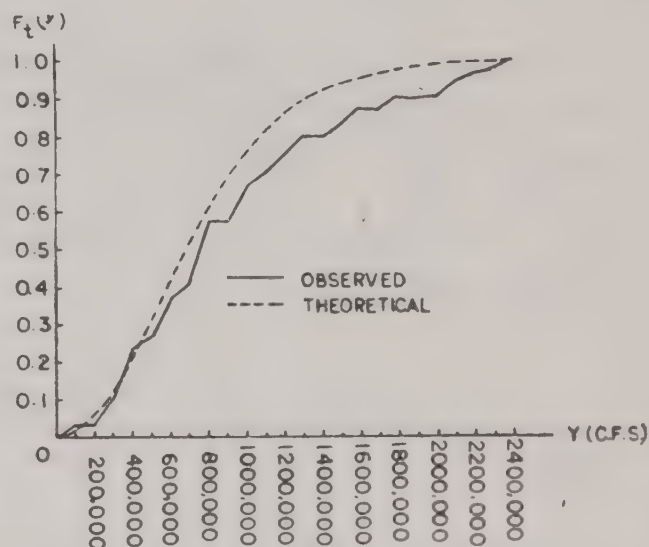corresponding observed distributions. A fairly good agreement between theoretical and observed results is seen.

4. Conclusion

Fairly good agreement between theoretical and observed results confirms the application of the distribution function (2.10) to describe and predict the behaviour of floods.

Acknowledgement

References

1. E J Gumbel, *Statistics of exteremes*, Columbia University Press, N. Y. (1958).
2. P Todorovic and E Zelenhasic, *Wat. Resour. Res.* **6** (1970) 1641.
3. P Todorovic and J Rousselle, *Wat. Resour. Res.* **7** (5) (1971) 1144.
4. P Todorovic and D A Woolhiser, *Wat. Resour. Res.* **8** (1972) 1433.
5. E Zelenhasic, Theoretical probability distribution for flood peaks. *Hydrol. Rap.* 42, Colo. Stat. University, Fort-Collins (1970).
6. P Todorovic, *Ann. Math. Statist.* **41** (1970) 1959.

COMPUTER BASED STUDY OF TRANSIENT CREEP PROBLEMS

Tapan Chattopadhyay

Mechanical Engineering Department, Jadavpur University, Calcutta-700 032

A method is presented here to demonostrate the Finite element analysis of the transient creep study of two dimensional stress concentrated parts subjected to load in their own plane. In this investigation two hardening creep laws : the time hardening law and strain hardening law have been used.

Introduction

The creep represents the slow deformation of solid when it is subjected to load for a long period. Creep is usually associated with high temperatures, but whether the temperature required is high or not really depends upon application. Experience has shown that, for the design of equipment subjected to sustained loading at elevated temperatures, little reliance can be placed on the usual short time tensile properties of metals at those temperatures. Under the application of a constant load it has been found that materials, both metallic and non-metallic, show a gradual flow or creep even for stresses below the proportional limit at elevated temperatures. Similar effects are present in low melting metals such as lead at room temperature.

In metals, creep is a plastic deformation caused by slip occurring along crystallographic directions in the individual crystals, together with some flow of the grain-boundary material. After complete release of load, a small fraction of this plastic deformation is recovered with time. Most of the flow is non-recoverable for metals.

There are many theoretical and experimental investigations on the creep problems[1-17]. The problems of thick walled cylinders and rotating disks were investigated both theoretically and experimentally. The two dimensional creep problems of infinite plate with discontinuity and torsion of prismatic bar have also been investigated.

In this study the Finite element method is used to analyse the two dimensional transient creep problems The sequential steps and the general algorithm is presented in details for two hardening creep laws : the time hardening law and the strain hardening law. The difference between the computed results from two hardening laws is discussed in detail.

Analytical Procedure

During elastic deformation, the stress-strain relations are linear and the strains are uniquely determined by the stress state without regard to how the stress state is

attained.   However   in the plastic range, the relations are generally nonlinear.   The strains are not uniquely determined by the stress state but depend on the history of how the stress state was reached.

Under creep conditions the relationship between stress and strain rate is generally nonlinear.   The stresses must be considered as a combined effect, rather than separately, which greately complicates a creep-stress analysis.

In calculation of elastic deformation the history of loading is not important and the strain at a given time may be related to the stress at that time.   However, in nonelastic deformation the history of loading is important and it seems preferable to relate stress to increments of strain.   It is convenient, therefore in developing a creep analysis to work with the strain increments in unit time or in other words, the strain rates.

The constitutive equations for time-dependent creep are somewhat similar to those of plasticity in that they require a flow rule, a prescribed uniaxial creep relationship for strain rate vs. time at constant stress levels, and a hardening rule.   The flow rule is similar to the Prandt-Reuss flow rule for plasticity, i.e., the creep strain rate is proportional to the deviatoric stress

$$\dot{\epsilon}_{cij} = \tfrac{3}{2} \left[\bar{\dot{\epsilon}}_c / \bar{\sigma} \right] \sigma'_{ij} \qquad \qquad \qquad ...(1)$$

where $\dot{\epsilon}_{cij}$ and σ'_{ij} are the components of creep strain rate and deviatoric stress tensors, respectively $\bar{\dot{\epsilon}}_c$ is the effective creep strain rate and $\bar{\sigma}$ is the effective stress.

The components of the creep, strain rate can be expressed from Eqn. 1 as

$$\dot{\epsilon}_{cx} = \tfrac{3}{2} \left(\bar{\dot{\epsilon}}_c / \bar{\sigma} \right) \left(\sigma_x - \sigma_m \right) = \left(\bar{\dot{\epsilon}}_c / \bar{\sigma} \right) \left\{ \sigma_x - \tfrac{1}{2} \left(\sigma_y + \sigma_z \right) \right\}$$

$$\dot{\epsilon}_{cy} = \tfrac{3}{2} \left(\bar{\dot{\epsilon}}_c / \bar{\sigma} \right) \left(\sigma_y - \sigma_m \right) = \left(\bar{\dot{\epsilon}}_c / \bar{\sigma} \right) \left\{ \sigma_y - \tfrac{1}{2} \left(\sigma_x + \sigma_z \right) \right\}$$

$$\dot{\epsilon}_{cz} = \tfrac{3}{2} \left(\bar{\dot{\epsilon}}_c / \bar{\sigma} \right) \left(\sigma_z - \sigma_m \right) = \left(\bar{\dot{\epsilon}}_c / \bar{\sigma} \right) \left\{ \sigma_z - \tfrac{1}{2} \left(\sigma_x + \sigma_y \right) \right\}$$

$$\dot{\gamma}_{cxy} = \tfrac{3}{2} \left(\bar{\dot{\epsilon}}_c / \bar{\sigma} \right) \tau_{xy}$$

$$\dot{\gamma}_{cyz} = \tfrac{3}{2} \left(\bar{\dot{\epsilon}}_c / \bar{\sigma} \right) \tau_{yz}$$

$$\dot{\gamma}_{czx} = \tfrac{3}{2} \left(\bar{\dot{\epsilon}}_c / \bar{\sigma} \right) \tau_{zx} \qquad \qquad \qquad ...(2)$$

Where, σ_m represents mean stress.

Several experiments have shown that these equations give satisfactory representation of constant stress, steadystate multiaxial creep tests.

The treatment of creep to determine the creep-law is based on the data obtained from constant-stress tests in uniaxial tension.   Usually this is prescribed in equation form to fit the data.   If need be, different equations can be used at different stress levels.   Among the many hardening rules that can be considered, the two most generally compared are time-hardening and strain-hardening.   These hardening rules dictate the path from one stress state to another.   Now to illustrate the problems it is assumed that the constant-stress creep strain may be expressed as

$$\bar{\epsilon}_0 = A_1 \bar{\sigma}^m t^n \qquad \qquad \qquad ...(3)$$

where, A_1, m and n are material constants.   Taking n th, root of each side of Eqn. 3, the new form will be

$$\bar{\epsilon}_0^{1/n} = A_1^{1/n} \bar{\sigma}^{m/n} t \qquad \qquad ...(4)$$

Differentiating Eqn. 3 and 4 we get the creep rates as

$$\dot{\bar{\epsilon}}_c = n A_1 \bar{\sigma}^m t^{(n-1)} \qquad \qquad ...(5)$$

$$\dot{\bar{\epsilon}}_c = n A_1^{1/n} \bar{\sigma}^{m/n} \bar{\epsilon}^{(1-1/n)} \qquad \qquad ...(6)$$

Eqns. 5 and 6 are of the general form

$$\dot{\bar{\epsilon}}_c = f(\sigma, t) \text{ and } \dot{\bar{\epsilon}}_c = g(\sigma, \bar{\epsilon})$$

respectively when the temperature is taken as constant.   These expressions have been given the names "Time-hardening and strain hardening" respectively.   The names are chosen because the equation represent the known tendencies of material to be influenced by time at temperature and by prior strain.   The strain hardening rule assumes that at constant stress and temperature the creep strain depends on the existing total creep strain, while the time-hardening rule assumes that at constant stress and temperature, the creep strain rate depends on the existing time (from the beginning of the creep process).

Substituting Eqns. (5) and (6) to Eqn. (2), the creep strain rate components can be expressed for both hardening laws.

For time-hardening law

$$
\begin{Bmatrix} \dot{\epsilon}_{cx} \\ \dot{\epsilon}_{cy} \\ \dot{\epsilon}_{cz} \\ \dot{\gamma}_{cxy} \\ \dot{\gamma}_{cyz} \\ \dot{\gamma}_{czx} \end{Bmatrix} = n A_1 \bar{\sigma}^{(m-1)} t^{(n-1)}
\begin{bmatrix}
1 & -\frac{1}{2} & -\frac{1}{2} & 0 & 0 & 0 \\
-\frac{1}{2} & 1 & -\frac{1}{2} & 0 & 0 & 0 \\
-\frac{1}{2} & -\frac{1}{2} & 1 & 0 & 0 & 0 \\
0 & 0 & 0 & \frac{3}{2} & 0 & 0 \\
0 & 0 & 0 & 0 & \frac{3}{2} & 0 \\
0 & 0 & 0 & 0 & 0 & \frac{3}{2}
\end{bmatrix}
\begin{Bmatrix} \sigma_x \\ \sigma_y \\ \sigma_z \\ \tau_{xy} \\ \tau_{yz} \\ \tau_{zz} \end{Bmatrix} \quad ...(7)
$$

For strain-hardening law

$$
\begin{Bmatrix} \dot{\epsilon}_{cx} \\ \dot{\epsilon}_{cy} \\ \dot{\epsilon}_{cz} \\ \dot{\gamma}_{cxy} \\ \dot{\gamma}_{cyz} \\ \dot{\gamma}_{czz} \end{Bmatrix} = n A_1^{1/n} \bar{\sigma}^{((m/n)-1)} \bar{\epsilon}^{(1-(1/n))}
\begin{bmatrix}
1 & -\frac{1}{2} & -\frac{1}{2} & 0 & 0 & 0 \\
-\frac{1}{2} & 1 & -\frac{1}{2} & 0 & 0 & 0 \\
-\frac{1}{2} & -\frac{1}{2} & 1 & 0 & 0 & 0 \\
0 & 0 & 0 & \frac{3}{2} & 0 & 0 \\
0 & 0 & 0 & 0 & \frac{3}{2} & 0 \\
0 & 0 & 0 & 0 & 0 & \frac{3}{2}
\end{bmatrix}
\begin{Bmatrix} \sigma_x \\ \sigma_y \\ \sigma_z \\ \tau_{xy} \\ \tau_{yz} \\ \tau_{zz} \end{Bmatrix} \quad ...(8)
$$

where,

$$\bar{\sigma} = \frac{1}{\sqrt{2}}\Big[(\sigma_x - \sigma_y)^2 + (\sigma_y - \sigma_z)^2 + (\sigma_z - \sigma_x)^2$$

$$+ 6\,(\tau_{xy}^2 + \tau_{yz}^2 + \tau_{zx}^2)\Big]^{1/2}$$

$$\bar{\epsilon} = \frac{\sqrt{2}}{3}\Big[(\epsilon_x - \epsilon_y)^2 + (\epsilon_y - \epsilon_z)^2 + (\epsilon_z - \epsilon_x)^2$$

$$+ \frac{3}{2}\,(\gamma_{xy}^2 + \gamma_{yz}^2 + \gamma_{zx}^2)\Big]^{1/2} \qquad \ldots(9)$$

PLANE STRESS PROBLEM

The above equations can be extended for the plane stress state under the assumptions that the solid is isotropic, it obeys Von Mises flow rule and the creep strains are incompressible. The creep strain rates then can be obtained from Eqns. 7 and 8 for both hardening laws.

Time hardening law :

$$\begin{Bmatrix} \dot{\epsilon}_{cx} \\ \dot{\epsilon}_{cy} \\ \dot{\gamma}_{cxy} \end{Bmatrix} = nA_1\bar{\sigma}^{(m-1)}t^{(n-1)} \begin{bmatrix} 1 & -\frac{1}{2} & 0 \\ -\frac{1}{2} & 1 & 0 \\ 0 & 0 & \frac{3}{2} \end{bmatrix} \begin{Bmatrix} \sigma_x \\ \sigma_y \\ \tau_{xy} \end{Bmatrix} \qquad \ldots(10)$$

Strain hardening law :

$$\begin{Bmatrix} \dot{\epsilon}_{cx} \\ \dot{\epsilon}_{cy} \\ \dot{\gamma}_{cxy} \end{Bmatrix} = nA_1^{1/n}\bar{\sigma}^{((m/n)-1)}\bar{\epsilon}^{(1-(1/n))} \begin{bmatrix} 1 & -\frac{1}{2} & 0 \\ -\frac{1}{2} & 1 & \frac{1}{2} \\ 0 & 0 & \frac{3}{2} \end{bmatrix} \begin{Bmatrix} \sigma_x \\ \sigma_y \\ \tau_{xy} \end{Bmatrix} \qquad \ldots(11)$$

From Eqn. 9

$$\bar{\sigma} = [\sigma_x^2 + \sigma_y^2 - \sigma_x\sigma_y + 3\,\tau_{xy}^2]^{1/2} \qquad \ldots(12)$$

$$\bar{\epsilon} = \Big[\frac{4}{9}\,(\epsilon_{cx}^2 + \epsilon_{cy}^2 - \epsilon_{cx}\epsilon_{cy}) + \frac{1}{3}\,\gamma_{cxy}^2\Big]^{1/2}$$

$$= \int_0^t \Big[\frac{4}{9}\,(\dot{\epsilon}_{cx}^2 + \dot{\epsilon}_{cy}^2 - \dot{\epsilon}_{cx}\dot{\epsilon}_{cy}) + \frac{1}{3}\dot{\gamma}_{cxy}^2\Big]^{1/2} dt \qquad \ldots(13)$$

The relation between the nodal forces $\{F_i\}$ and the nodal displacements $\{\delta_i\}$ of the element is

$$\{F_i\} = [k]\{\delta_i\} - [B]^T[D]\{\epsilon_{ci}\}\,tA$$
$$= [B]^T[D][B]\,tA\,\{\delta_i\} - [B]^T[D]\{\epsilon_{ci}\}\,tA \qquad\qquad \text{...(14)}$$

where,

$[B]$ = strain-displacement matrix of the element used in elastic analysis

$[B]^T$ = Transpose of B-matrix

$[K]$ = stiffness matrix of the element

$[D]$ = Elasticity matrix

$\{\delta_i\}$ = Nodal displacements at any time after loading

$$\{\delta_i\} = \sum_{j=1}^{i} d\delta_j$$

$\{\epsilon_{ci}\}$ = creep strains at any time after loading

$$\{\epsilon_{ci}\} = \sum_{j=1}^{i} d\epsilon_{cj}$$

t = thickness of the specimen

A = Area of the element

COMPUTATIONAL STEPS

In this investigation a plate having diamond shaped discountinuity has been used. Fig. 1 shows the shape of the specimen. The preparation of the element data is a
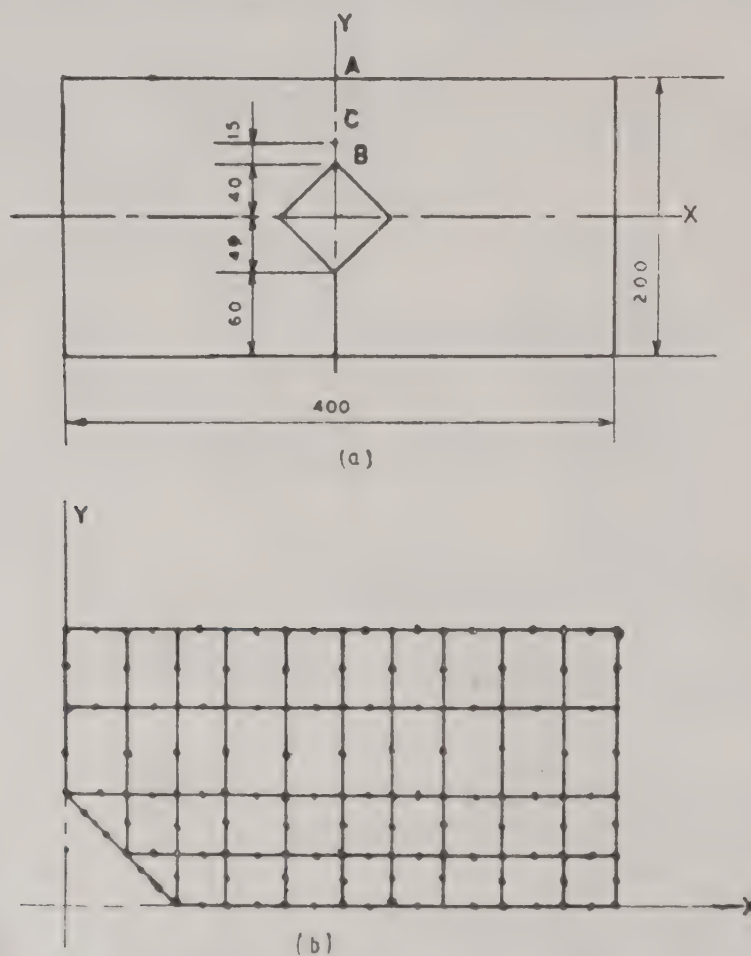

FIG. 1

time consuming task. A program has been developed to generate automatically the triangular element data. The sequential steps of this investigation are given below.

1. Determine the elastic stress, strain and displacements without considering $\{\epsilon_{ci}\}$ in the first cycle.

2. Assume that the stresses obtained in step 1 remain constant over a very small initial increment of time δt_0 and calculate the increment of creep strains $\{\delta \epsilon_{c1}\} = \{\epsilon_{c1}\}$ that occur in the increment time $\Delta t_1 = \delta t_0$ by using time hardening law.

3. Then by substituting the increment of creep, strains into Eqns. 14 calculate the stresses, strains etc. at time $t = \Delta t_1$. for time hardening law.

4. Choose a suitable increment of time Δt and determine the stresses at the end of the time interval Δt by using both time hardening and strain hardening law.

5. Continue the above steps until the desired time has reached.

NUMERICAL EXAMPLE AND DISCUSSIONS

Figure 1 (a) shows the shape of the plate and its dimension used in this study. The following material properties are considered for the analysis :

Poisson's ratio, μ	$= 0.3$
Young's modulus, E	$= 7870$ kg/mm²
$A_\perp$	$= 4.36 \times 10^8$
m	$= 3, 4, 5$
n	$= 0.2$

In this study triangular elements have been generated by using a mesh generation program. This program generates the element date for the Finite-element programs. Here a group of eight-node quadrilateral regions have been used to define the body under consideration. Fig. 1(b) shows the quadrilateral regions for the finite element idealiation. The program is capable of modeling two-dimensional domains that are composed of rectangles and triangles having second-order curved boundaries.

Figure 2 to fig. 6 illustrates the results of this study fig. 2 shows the variation of σ_x in section AB with time for both time and strain hardening laws. This figure clearly tells that the stress σ_x decreases abruptly at B i.e. at the discontinuity and its vicinity with the increase of time. But the values of σ_x increases a little with time in the range 9mm from B and onward. Figure 3 shows the variation of creep strain ϵ_{cx} in Section AB with time for both strain and time hardening laws. Figure 4 is plotted to show the distribution of ϵ_x in section AB with time. Both ϵ_x and ϵ_{cx} at point B increases monotonously with time.

It is clear from figure 2 and 4 that the difference in the stresses from two hardening laws is quite considerable amount at point-B but the difference in the strains is small. Figure 5 plots the variation of σ_x in section AB at time 10^{-4} hr. for the different values
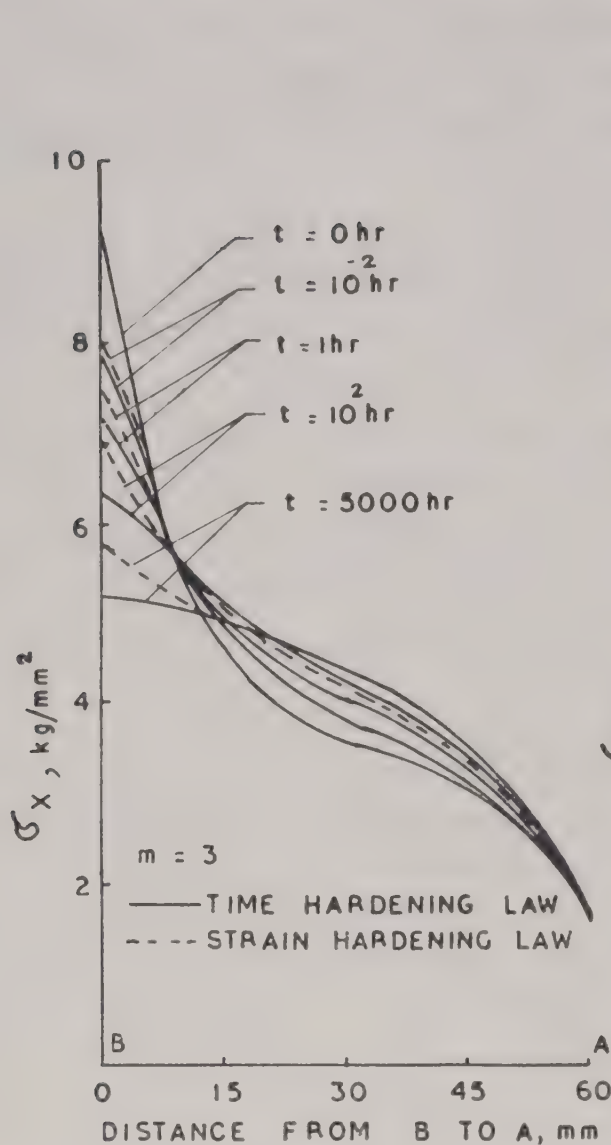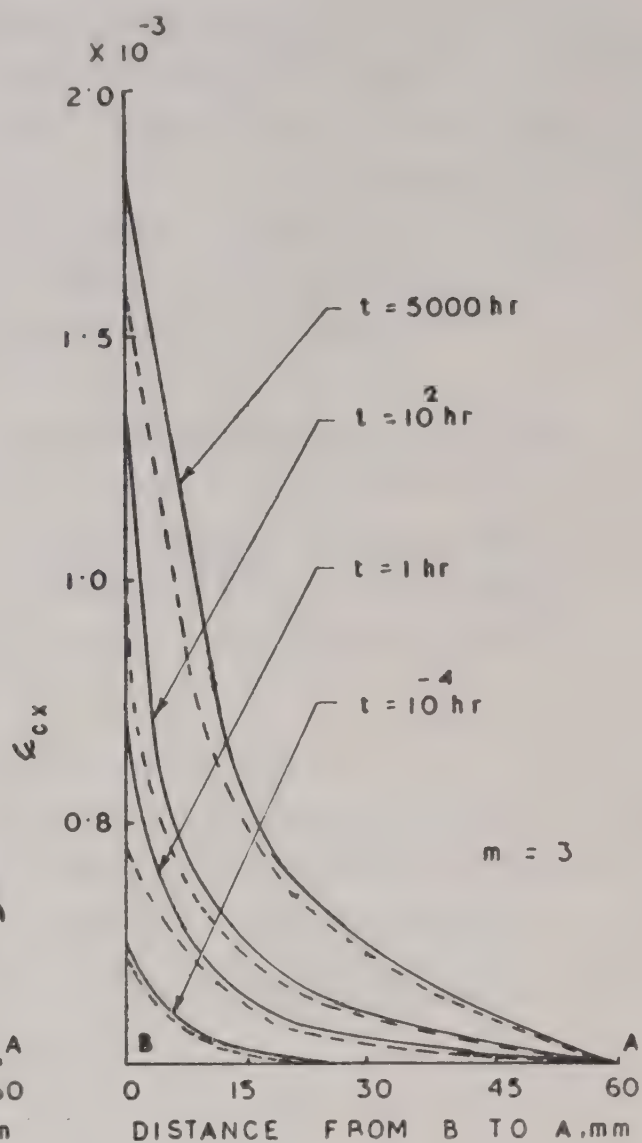
FIG. 2

FIG. 3

of the costant "m".   It shows that the values of σ_x at point B is decreasing with the values of m and the maximum stress which exist at B in a moment of loading is somewhat displaced from the point B with the lapse of time.   Figure 6 shows the varia- tion of σ_x with time at points A, B and C along the section AB.

From the study of this numerical result it is found that most of the variation of stresses occurs near the notch edge at the initial time.   The difference between the results based on time and strain hardening law is very little.

CONCLUSION

The present investigation gives an idea of computational strategies for transient creep problems.   The variation of stress and strain due to creep in plane stress-concentrated part has been studied by using the Finite-element method.

The Finite-element method is well established now and has proved its uniqueness in various fields of Engineering. In this method accuracy of the solution will depend on the selection of the grid and solution algorithm.   An acceptable grid is one that can approximate the actual field quantities within acceptable accuracy.   Due to
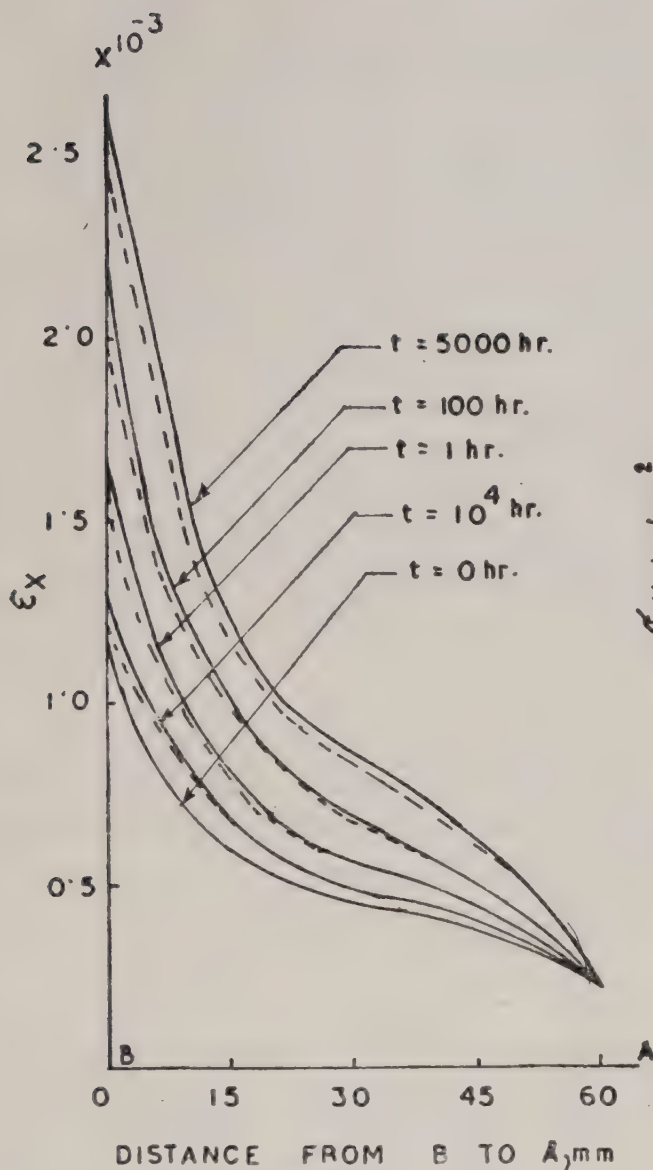
FIG. 4
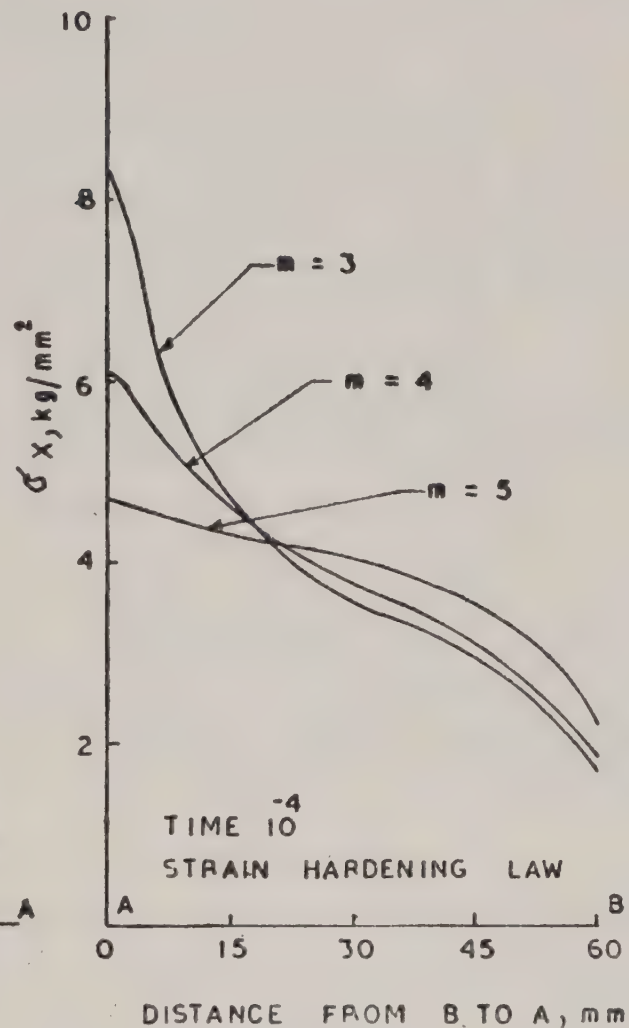
FIG. 5

inadequate experience the only way to be sure that the grid yields the required accuracy is by successive grid refinement. An effective grid is one that can be generated easily, can be readily changed during an analysis and results in a minimum amount of computing time (which usually depends on the number of degrees of freedom and density of the stiffness matrix). In general, efficiency of a finite-element grid is increased as the displacement distribution within the finite-elements used are more representative of the actual displacements that exist. This has led to the development of specialized and 'higher order' finite element. But the use of such higher order elements will increase the cost of solution.

Another factor that governs the convergence, accuracy and economy of the problems involving plasticity and creep (examples of material nonlinearity) is the solution algorithm. In the incremental solution algorithm of the nonlinear problems, the size of the increment is an obvious quantity that is commonly used as a basis of comparison between competing successive linearization schemes. But it has been proved that if the step size is "small enough" the method should always provide accurate solutions. The question arises, however, that what constitutes "small enough", and can the step size be increased without affecting accuracy ? Much

FIG. 6

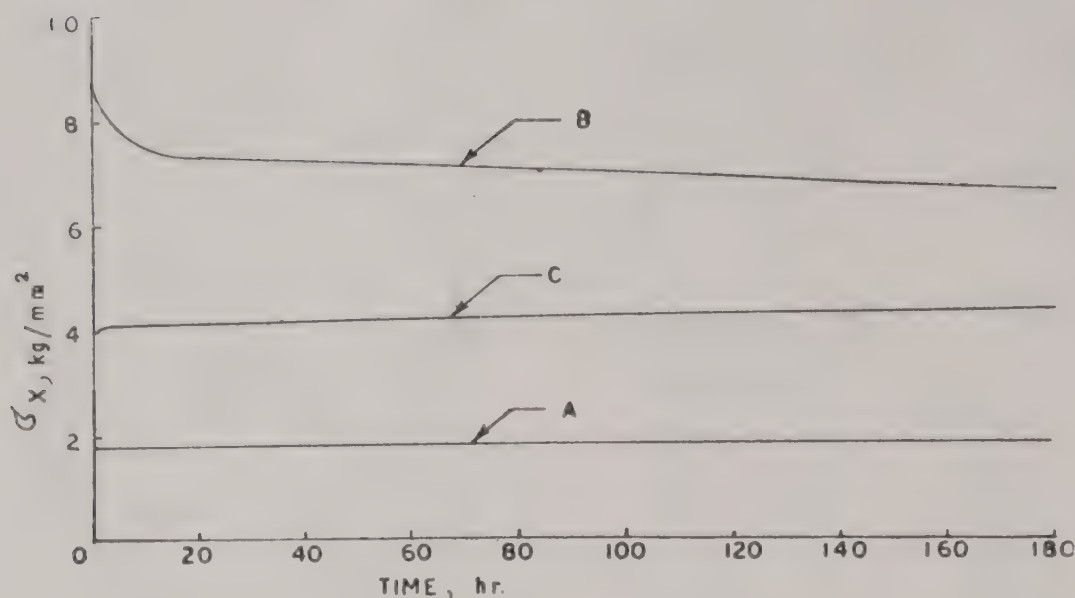attention has been given to the time-step increment strategy as this governs efficiency and accuracy of the solution technique. The time-step is always kept within certain bounds. If the time step is too large accuracy suffers and instability may occur, and if the time step is too small the expense of solving a problem is very high. For stability and accuracy the time-step is evaluated based on total strain

$$\Delta t = \Gamma \overline{\epsilon}_{total} / \overline{\dot{\epsilon}}_c$$

where, ϵ_{total} is the maximum effective total strain, $\overline{\dot{\epsilon}}_c$ is the effective creep strain rate and Γ is the time-step constant. In general, values of the constant Γ is in the range 0.1 to 0.15. But much lower values in the range 0.01 to 0.05 are suggested near collapse. The accuracy in creep strain is linearly proportional to the admissible time-step constant Γ.

Based on the experimental data an "equation-of-state" approach for time-dependent creep is generally used in finite element programs. The constitutive equations here are somewhat similar to those of plasticity. While other more complicated models may be more accurate, it has been determined in several cases that the strain-hardening rule adequately describes the hardening behaviour. But the strain hardening rule is acceptable as long as load reversal does not occur.

Finally it must be concluded that in order to perform a meaningful analysis of the complex nonlinear problems, by Finite element method, one must understand and justify the employed finite-element grids, solution algorithms, modelling techniques and constitutive relations.

REFERENCES

1. E N Andrade, da C., *Proc. Roy. Soc. (London)* A **84** (1) (1910).
2. E N Andrade, da C., *Proc. Roy. Soc. (London)* A **90** (1914) 329.
3. R Hill, "The mathematical theory of Plasticity", Oxford Univ. Press, London (1950).
4. W Bhattacharya, W K A Congreve and F C Thompson, *J. Inst. Metals*, **81** (1952) 83.

5. O H Wyatt, *Proc. Phys. Soc.* (London) B **66** (1953) 459.
6. A. Mendelson, M H Hischberg and S S Manson, *J. Basic Eng., Trans. Am. Soc. Mech. Engg.,* **81** (ser. D) (1959), p. 585.
7. N C Dahl, *J. Basic Eng.* **81** 1959, *J. Basic Eng.* **81** (1959) 595.
8. A E Johnson, *Met. Review* **5** (1960) 447.
9. I Finnie and W R Heller, *Creep of Fngineering materials*, Mc Graw-Hill (1959).
10. F A Leckie and J B Martin, *J. Appl. Mech., Am. Soc. Mech. Eng.* (1967) 411.
11. G A Greenbaum and M F Rubinstein, *Nucl. Eng. Des.* **7** (1968) 379.
12. R K Penny and D R Hayhurst, *Int. J. Mech. Sci.* **11** (1969) 23.
13. R E Nickell "Thermal stress and creep", in Structural Mechanics Computer Programs (Ed. W Pilkey, K Saczalski and H Schaeffer), University Press of virginia, Charlottesville, (1974).
14. N A Cyr and R D Teter, *Comp. Struct.* **3** 849.
15. O C Zienkiewiez and J C Copmean, *Int. J. Num. Meth. Engng.* **8** (1974) 821.
16. M B Kanchi, D R J Owen and O C Zienkiewicz, *An implicit scheme for Finite-element solution problems of visco-plasticity and creep*, C/R/252/75, University College of Swansea, (1975).
17. O C Zienkiewicz, *The Finite-element method in Engineering Science*, McGraw-Hill, (1977).

VIBRATIONAL SPECTRA AND NORMAL COORDINATE TREATMENT OF MOLYBDENUM TRIOXIDE

K G Ravikumar, S. Rajaraman *and* S Mohan

Division of Applied Sciences, Madras Institute of Technology, Anna University, Chromepet, Madras

This paper presents the near infrared spectrum and Fourier far infrared spectrum of molybdenum trioxide from 625–4000 cm^{-1} and 100–650 cm^{-1} respectively. The vibrational analysis is made on the basis of C_{3v} symmetry and general quadratic valence force constants are determined. The fundamental frequencies of MoO_3 are : $A_1 = 850, 350$ cm^{-1}; $E = 1000, 373$ cm^{-1}. Further using the values of the present potential constants, other molecular constants are also evaluated. The thermodynamic properties are presented over the temperature range 298.16 K to 1000 K.

INTRODUCTION

Molybdenum oxide has several important industrial applications at relatively high temperatures as catalysts and thus the structural and spectroscopic data are of great value. Structure of known trioxides, which have hitherto been investigated[1,2] fall into two categories, those having D_{3h} symmetry such as SO_3 and others having C_{3v} symmetry such as WO_3. In the course of our investigation on the study of molecular constants of pyramidal type molecules our attention has turned to molybdenum trioxide.

Nagarajan[3] carried out the normal coordinate analysis of MoO_3 using the estimated frequencies for a D_{3h} symmetry. The vibrational frequencies of this molecule has been given by Hewett *et al.*[1] on the basis of C_{3v} symmetry. According to Hewett *et al.*[4], the symmetric stretch (Mo-O) frequency is higher than the asymmetric stretch frequency. But later studies revealed that the asymmetric frequency is much more intense than the symmetric frequency for slightly non-planar molecules[5-7]. On this basis we assigned higher value for the asymmetric frequency in the present study. Further[1] proposed the bending frequencies viz., $v_2(A_1)$ and $v_4(E)$ from the combination band.

The present study was initiated to obtain the complete vibrational frequencies of MoO_3 and to determine whether a C_{3v} configuration may be adopted to explain vibration of MoO_3 in agreement with normal coordinate analysis.

EXPERIMENTAL

Molybdenum trioxide was obtained from Fluka A.G., Chemische Fabrick, Schweiz. The infrared spectra of MoO_3 have been recorded on Perkin Elmer IR–257 double

beam grating spectrophotometer in the region 625 to 4000 cm^{-1}. The Fourier transform IR spectra has also been recorded on polytec FIR–30 in the region 100–650 cm^{-1}, and the observed frequencies are listed in Table I. The frequencies for all sharp bands are expected to be accurate to $\pm$ 1 cm^{-1}.

RESULTS AND DISCUSSION

Four fundamental absorption bands have been observed at 1000, 850, 375 and 350 cm^{-1}. The band at 1000 cm^{-1} is very much stronger than that at 850 cm^{-1}. The observed frequencies along with their assignments are given in Table I.

The vibrational representation of a XY_3 planar (D_{3h}) molecule is represented as $\Gamma = A_1 + A_2' + 2E'$, whereas that of a XY_3 pyramidal (C_{3v}) moleculer as $\Gamma = 2A_1 + 2E$. Accordingly, in a planar molecule only three frequencies (A_2' and $2E'$) are infrared active, while in a pyramidal system all the four frequencies ($2A_1$ and $2E'$) should be active in the infrared. In both the systems, the ν_1 and ν_3 stretching modes are expected to occur at frequencies higher than the ν_2 and ν_4 bending deformations. The appearance of two high frequency infrared bands at 1000 and 850 cm^{-1} suggests the C_{3v} molecular symmetry for this molecule, which is in consistence with those concluded by Hewett et al.[4], The assignment of the high frequency fundamentals (stretching modes) can be made on the basis of their relative intensity. For slightly non-planar molecules, on expects the $\nu_3(E)$ mode to be much more intense than $\nu_1(A_1)$. On this basis we assign the band at 850 cm^{-1} to be$\nu_1(A_1)$ and that at 1000 cm^{-1} to be $\nu_3(E)$.

However the low frequency $\nu_2(A_1)$ and $\nu_4(E)$ bands are more difficult to assign, as no definite guidelines exist for intensity and relative magnitude of the frequncies.

TABLE I

Assignments of fundamental infrared frequencies (cm^{-1}) of Molybdenum trioxide

Region	Frequency (Intensity*)		Assignment
Infrared	850	(S)	ν_1 (Mo — O symmetric stretch)
	1000	(VS)	ν_3 (Mo — O asymmetric stretch)
	1150	(W)	$2\nu_3 - \nu_1$
	1305	(VW)	$2\nu_3 - 2\nu_1$
	1340	(W)	$2\nu_1 - \nu_3$
	1625	(W)	$2\nu_3 - \nu_4$
Fourier	106	(VW)	$\nu_1 - 2\nu_4$
far	147	(VW)	$\nu_1 - 2\nu_2$
infrared	280	(S)	$\nu_3 - 2\nu_2$
	350	(M)	ν_2 (O — Mo — O symmetric bending)
	373	(S)	ν_4 (O — Mo — O asymmetric bending)

*VS : Very Strong; M : Medium; VW : Very Weak; S : Strong; W : Weak;

It has been observed that in the case of pyramidal systems $\nu_2(A_1) < \nu_4(E)$. Hence, following the assignment of bending modes due to Wesley and Dekock[5-7], we have assigned $\nu_2(A_1)$ mode at 350 cm^{-1} and $\nu_4(E)$ to 373 cm^{-1} band. This is in agreement with the assignment $\nu_2(A_1)$ 300 cm^{-1} and $\nu_4(A_1)$ 350 cm^{-1} in case of WO_3[8].

NORMAL COORDINATE ANALYSIS

A normal coordinate analysis of Molybdenum trioxide has been carried out following Wilson's F-G matrix method on the basis of C_{3v} point group, using a general quadratic potential function and molecular kinetic constants and a set of force constants have been reported.

The symmetry coordinate and the other details of the procedure are the same as those given in the earlier papers[9,10].

The kinetic constants, the force constants, the compliance constants and the mean square amplitudes of vibration at 298.16 K are given in Table I. As expected, the interaction force constants $f_{dd}, f_{\alpha\alpha}$ and $f_{d\alpha}$ assume negative sign for this type of molecule. Further, the same sign is noted for the kinetic constants and potential constants in the case of bond angle interaction. For the molecule under study, the bond-bond interaction force constant assumes a negative sign. This result is in line with the previous observation made with respect to the molecules having oxygen as the Y atom[11]. The present set of force constants have been utilized in evaluating compliance constants, valence mean square amplitudes, coriolis coupling constants and centrifugal distortion constants.

The compliance constants are evaluated for this molecule by Decius method[12]. These constants naturally show the trend opposite to that relating to the force constants. Using the force constants in Cyvin's secular equation[13] the symmetrized mean square amplitude elements and hence the vibrational mean amplitudes have been obtained. From Table II, it may be seen that the mean amplitudes for the bonded

TABLE II

Values of kinetic constants (10^{-23} g); Force constants (10^5 dynes/cm), Compliance constants (m dyne/A) and Mean square amplitudes (Both bonded and nonbonded (10^{-3} A^2) at 298.16K)

Constants	d (Mo — O)	dd	α	$\alpha\alpha$	$d\alpha$	$d\alpha'$
Kinetic constants	2.3341	0.0647	0.2855	0.0123	— 0.0215	0.0825
Force constants	7.3454	— 0.5858	0.1349	— 0.0001	— 0.0135	0.0379
Compliance constants	0.1385	0.0121	1.8598	0.0015	0.0035	— 0.0206
Bonded mean square amplitudes	1.3237	0.0481	9.5691	— 0.0638	0.0525	— 0.1904
Non bonded mean square amplitudes	σ_q (0...0)	σ_{qq}	σ_{dq}	σ'_{dq}		
	5.2022	0.6960	0.9264	0.1074		

as well as the non-bonded distances obtained in the present investigation are in the characteristic range for $Mo - O$ vibration. As expected, $l_{o \cdots o}$ is greater than l_{Mo-o}, which is contrary to the corresponding force constants. Thus, it is clear that in the metal oxides, mean vibrational amplitudes are characteristic to some extent. The present set of values will be useful in the interpretation of electron-diffraction data relating to this molecule. The present set of values for the vibrational mean amplitudes once again confirms the correctness of our assignment.

The first order Coriolis coupling constants of the $E \times E$ type as well as the second order constants of the type $A_1 \times E$ type have been evaluated by following the matrix relation, $\zeta^\alpha = L^{-1} C^\alpha (L^{-1})$, making use of kinetic constants. The $C^\alpha (\alpha = x, y, z)$ matrix elements have been obtained by the vector method of Meal and Polo[14,15]. The Zeta values listed in Table IV obey the sum rules given by Oka[16]. These values further satisfy the relations :

$$(\zeta^y_{1a3_1})^2 + (\zeta^y_{1a4a})^2 + (\zeta^y_{2a3a})^2 + (\zeta^y_{2a4a})^2 + (\zeta^y_{3a4a})^2 = 1$$

$$2[(\zeta^y_{1a3a})^2 + (\zeta^y_{1a4a})^2 + (\zeta^y_{2a3a})^2 + (\zeta^y_{2a1a})^2 - \tfrac{1}{2}]$$

$$- (\zeta^z_{3a4b})^2 + (\zeta^z_{3a3b})(\zeta^z_{4a4b}) = 0$$

$$(\zeta^y_{1a3a})(\zeta^y_{2a4a}) - (\zeta^y_{1a4a})(\zeta^y_{2a3a}) = 0$$

As expected, the values of ζ^y_{13}, ζ^y_{15} and ζ^z_{44} are negative. Further, the magnitude of ζ^y_{23} and ζ^z_{34} are of the same order. The high values of the constants ζ^y_{23} and ζ^z_{34} show that the coupling concerned is much stronger.

TABLE III

Mean amplitudes ($10^{-2} A$) at 298.16 K; Coriolis coupling constants and centrifugal distortion constants (KHz)

Mean amplitudes	Coriolis coupling constants					Centrifugal distortion constants		
	ζ^z_{3a3b} ζ^y_{3a4a} ζ^y_{1a4a} ζ^y_{2a4a}					D_J		
1 ($M_0 - o$)						D_{JK}		
	ζ^z_{4a4b} ζ^y_{1a3a} ζ^y_{2a3a}							
1 ($o \cdots o$)	ζ^z_{3a4b}					D_K		
	0.1604	0.3708	-0.0872	0.5242	4.5385			
3.6383								
	-0.4353	-0.1250	0.7514			-6.3962		
7.2126	0.8095					3.4436		

The determination of the exact rotation energy levels of a non-rigid molecule requires the knowledge of centrifugal distortion constants. The centrifugal distortion constants of Molybdenum trioxide have been calculated by Kivelson and Wilson method[17,18] using the force constants obtained in the present investigation. They are reported in Table III. As expected, the value of D_{JK} is negative for this molecule.

The thermodynamic functions for MoO_3 have been evaluated for the ideal gas state at 1 atm assuming a rigid rotor harmonic oscillator model. The influence of spin contribution, anharmonicity and non rigidity are neglected. The contribution to the vibrational part of these thermodynamic functions have been calculated from the tables given by Johnson *et al*[19]. The values are presented in Table IV. The constants are useful to interpret the experimental results on thermodynamic properties.

TABLE IV

Heat content, free energy, entropy and heat capacity (in cal deg^{-1} mol^{-1}) of MoO_3 for the ideal gaseous state at 1 atmospheric pressure

T (K)	$(H_0 - E_0)/T$	$-(F_0 - E_0)/T$	C_p^0	S^0
298.16	10.4183	51.2280	13.9064	61.6463
400	11.4705	54.5093	15.5703	65.9798
500	12.4530	57.1167	16.6980	69.5697
600	13.2675	59.5352	17.4727	72.6740
700	13.8717	61.5407	18.0086	75.4124
800	14.4231	63.4477	18.3967	77.8708
900	14.8738	65.1521	18.6741	80.0259
1000	15.2706	66.7557	18.8854	82.0263

CONCLUSION

A complete vibrational analysis of MoO_3 using the vibrational frequencies obtained from infrared and Fourier far infrared spectra is available on the basis of C_{3v} symmetry in the present study.

ACKNOWLEDGEMENT

REFERENCES

1. G Herzberg, *Infrared and Raman Spectra of Polyatomic molecules*, van Nostrand (1945).
2. K H Shmidt and A Muller, *Coord. Chem. Rev.* **14** (1974) 115.
3. G Nagarajan, *Indian J. Pure & Appl. Phys.* **4** (1966) 158.

4. W D Hewett, J H Newton Jr and W Weltner Jr., *J. Phys. Chem.* **79** (1975) 2640.
5. R D Wesley and C W Dekock, *J. Phys. Chem.* **17** (1973) 466.
6. M Leisieki, J W Nibler and C W Dekock, *J. Chem. Phys.* **57** (1972) 1352.
7. J W Hastie, R H Hauge and J L Margrave, *High Temp. Sci.* **3** (1971) 56.
8. L Dixit, S K Kapoor, L D Singh and P L Gupta. *Indian J. Phys.* **51** (1977) 116.
9. S Mohan, *Acta Phys. Pol.* A52 (1977) 747.
10. S Mohan and S Rajaram, *J. Pure & Appl. Phys.* **20** (1982) 228.
11. P Thiruganasambandam and S Mohan, *Indian J. Phys.* **52**B (1977) 173.
12. J C Decius, *J. Chem. Phys.* **38** (1963) 241.
13. S J Cyvin *Molecular vibrations and mean square amplitudes*, Elsevier Pub. Co., New York (1968).
14. J H Meal and S R Polo, *J. Chem. Phys.* **24** (1956) 1911.
15. ———, *J. Chem. Phys.* **24** (1956) 1126.
16. T Oka, *J. Mol. Spectrosc.* **29** (1969) 84.
17. D Kivelson and E B (Jr.) Wilson, *J. Chem. Phys.* **20** (1952) 1575.
18. ———, *J. Chem. Phys.* **21** (1953) 1229.
19. H L Johnson, L Saradoff and J Belzer, (Office of Naval Research. Washington) (1949).

A COMPARATIVE STUDY OF THE 'LOCAL POTENTIAL METHOD' AND THE 'EXACT NUMERIAL PROCEDURE' (APPLICATION TO THE STABILITY ANALYSIS OF A HOT LAYER OF FLUID)

S P Bhatacharyya *and* S Nadoor

Department of Mathematics, Indian Institute of Technology, Powai, Bombay 400 076

In this paper both the local potential method as introduced by Prigogine and Glansdorff[1-3] and applied to hydrodynamic stability problems by Schechter and Himmelblau[1] and a numerical method known as 'the exact numerical procedure used by Harris and Reid[5] and others have been applied to determine the stability criteria of a hot layer of fluid having uniform distribution of heat sinks (or sources). After comparing the results obtained by the two methods with those obtained by Watson (1968) by variational technique, it is concluded that a suitable combination of the two methods leads to a more useful procedure giving accurate results.

INTRODUCTION

THE exact analytical solution of many boundary value problems, particularly many problems of hydrodynamic stability cannot be found and hence one has to look for approximate and numerical solutions. The local potential method due to its simplicity may be utilized to find an approximate solution of many of these problems. The concept of local potential had been introduced by Prigogine and Glansdroff[1,2] and was applied to hydrodynamic stability problems by Schechter and Himmelblau[4,6,7].

It is also possible to obtain exact numerical solutions of the hydrodynamic stability problems by a method called 'the exact numerical procedure' used by Harris and Reid[5], Chock and Schechter[8] and Sastry and Rao[9]. Venderborck and Platten[10] had investigated the usefulness of the two methods and in this paper we have studied further and considered the hydrodynamic stability problem of a horizontal layer of fluid having a uniform distribution of heat sinks (or sources) which had already been studied by Watson using the variational method. The results obtained by the two methods mentioned in this paper have been compared with those given by Watson.

BASIC EQUATIONS AND BOUNDARY CONDITIONS

A coordinate system $Ox_1x_2x_3$ is chosen having ox_3 vertically upwards and ox_1, ox_2 in the horizontal plane. The fluid is assumed to be infinite in horizontal extent and confined between two rigid, perfectly conducting boundaries $x_3 = 0$ and $x_3 = d$. The lower and upper plates are maintained at constant temperatures T_0 and T_1 respectively, such that $\Delta T = T_0 - T_1 > 0$. It is assumed that the heat is lost at a constant rate throughout the volume of the fluid. The basic equations, with Boussinesq approximations[11].

$$\frac{\partial u_i}{\partial t} + u_j \frac{\partial u_i}{\partial x_j} = -\frac{\partial}{\partial x_i}\left(\frac{P}{\rho_0}\right) - g\frac{\rho}{\rho_0}\mathbf{k} + \nu\Delta^2 u_i \qquad \text{... (1)}$$

$$\frac{\partial T}{\partial t} + u_j \frac{\partial T}{\partial x_j} = k_t \nabla^2 T - q \qquad \text{... (2)}$$

$$\frac{\partial u_i}{\partial x_i} = 0 \qquad \text{... (3)}$$

$$\rho = \rho_0 [1 - \alpha(T - T_0)] \qquad \text{... (4)}$$

where $u_i(i = 1, 2, 3)$, ν, ρ, p, g, k_t and α are the components of the velocity field, kinematic viscosity, the density, the pressure, the accleration due to gravity, thermal diffusivity and the cofficient of volume expansion respectively. q is taken to represent the heat loss within the fluid layer per unit volume per unit time and $\mathbf{k}$ is the unit vector in the direction of ox_3 axis.

The boundary conditions : Since the boundaries are rigid and perfectly conducting we have

$$u_i = 0 \text{ for } x_3 = 0, d \qquad \text{... (5)}$$

and

$$T = T_0 \text{ for } x_3 = 0 \text{ and } T = T_1 \text{ for } x_3 = d. \qquad \text{... (6)}$$

LINEARIZED EQUATIONS AND NORMAL MODES

In the stationary state, when $u_i = 0(i = 1, 2, 3)$, $T(x_3)$, the temperature, is obtained from (2) and (6) as

$$T(x_3) = \frac{q}{2k_t}(x_3^2 - dx_3) - \frac{\Delta T}{d}x_3 + T_0 \qquad \text{... (7)}$$

where $\Delta T = T_0 - T_1$. We take p and ρ to be the values in the undisturbed state, and in the disturbed state, assume $u_i(i = 1, 2, 3)$, $p + \delta p$, $\rho + \delta \rho$ and $T + \theta$ to be the components of the velocity, pressure, density and temperature respectively, where $u_i(i = 1, 2, 3)$, δp, $\delta \rho$ and θ are small in magnetudes. Substituting the above quantities in (1)-(6), linearizing the equations and introducing the following non-dimensional variables denoted by dashes

$$x_i = dx_i' \; (i = 1,2,3), \quad u_i = \frac{k_t}{d} u_i' \; (i = 1,2,3),$$

$$t = \frac{d^2}{\nu} t', \quad \theta = (\Delta T)\theta' \; \delta p = \frac{\rho_0 k_t \nu}{d^2} \delta p' \,,$$

we have the following equations :

$$\frac{\partial u_i}{\partial t} = - \frac{\partial}{\partial x_i} \delta p + R\theta \mathbf{k} + \nabla^2 u_i \qquad \text{... (8)}$$

$$Pr \frac{\partial \theta}{\partial t} = \nabla^2 \theta + u_3 + \frac{Q_h}{R} (1 - 2x_3) u_3 \qquad \text{... (9)}$$

$$\frac{\partial u_i}{\partial x_i} = 0 \qquad \text{... (10)}$$

(the dashes have been dropped for convenience). Here R and Q_h are the Rayleigh number $g^\alpha \Delta T d^3 / \nu k_t$ and heat source parameter $g^\alpha q d^5 / 2k_t^2 \nu$ respectively, $Pr - \nu/k_t$ being the Prandtl number.

A normal mode analysis is performed, supposing

$$(u_3, u_1, u_2, \delta p, \theta) = \left[W(x_3), \frac{ik}{a^2} DW(x_3), \frac{im}{a^2} DW(x_3), P(x_3), \textcircled{\tiny H} (x_3) \right]$$

$$\cdot \exp (ikx_1 + imx_2 + \sigma t) \qquad \text{... (11)}$$

which after substitution in (8)-(9) and elimination of $P(x_3)$ give

$$(D^2 - a^2)(D^2 - a^2 - \sigma) W = Ra^2 \textcircled{\tiny H} \qquad \text{... (12)}$$

$$(D^2 - a^2 - \sigma Pr) \textcircled{\tiny H} = -W - \frac{Q_h}{R} (1 - 2x_3) W \qquad \text{... (13)}$$

and taking into account (5) and (6) gives

$$W = DW = \textcircled{\tiny H} = 0 \text{ at } x_3 = 0, 1 \qquad \text{... (14)}$$

where

$$D \equiv \frac{d}{dx_3}.$$

SOLUTION : LOCAL POTENTIAL METHOD

Since the local potential method has been described in details[1,6,7], we present here only at outline before presenting the local potential ϕ_L, for our problem. If $X^{(0)}$ denotes any of the quantities $W^{(0)} (x_3)$, or $\textcircled{\tiny H}^{(0)} (x_3)$, the true solutions of equations (12) and (13) satisfying the boundary conditions (14), and if δx is an arbitrary variation, then, as

$$\frac{\partial x}{\partial t}\, \delta x = \left(\frac{\partial x^{(0)}}{\partial t} + \frac{\partial}{\partial t}\, dx\right) \delta x = \frac{\partial x^{(0)}}{\partial t}\, \delta x - \frac{1}{2}\frac{\partial}{\partial t}\,(\delta x)^2,$$

we have

$$-\frac{1}{2}\frac{\partial}{\partial t}\int_0^1 (\delta x)^2\, dx_3 = + \int_0^1 \frac{\partial x}{\partial t}\, \delta x\, dx_3 - \int_0^1 \frac{\partial x^{(0)}}{\partial t}\, \partial X\, dx_3 \qquad \text{...(15)}$$

after integrating with respect to x_3 from $x_3 = 0$ to $x_3 = 1$. Using the equations (12)–(14) and taking $X^{(0)}$ to represent $W^{(0)}$ and $\text{ⓗ}^{(0)}$ in turn in (15) and adding, we finally obtain from the right hand side of (15) the quantity $\int \phi_L\, dx_3$, where ϕ_L, the local potential, is given by

$$\phi_L = \; < \sigma a^2\, W^{(0)}W + \sigma DW^{(0)}DW + \sigma a^2\, Pr\,\text{ⓗ}^{(0)}\text{ⓗ}$$
$$- Ra^2\text{ⓗ}^{(0)}W - a^2 W^{(0)}\text{ⓗ} + a^4 W^{(0)}W - \tfrac{1}{2}(D^2W)^2$$
$$+ 2D^2W^{(0)}\, D^2W + a^2\, exp\,(2)\,(DW)^2 + a^2 DW^{(0)}DW$$
$$+ \frac{a^2}{2}(D\text{ⓗ})^2 + a^4\text{ⓗ}^{(0)}\text{ⓗ} - a^2\frac{Q_h}{R}(1 - 2x_3)\, W^{(0)}\text{ⓗ} > \qquad \text{...(16)}$$

Here $< \, >$ represents integration with respect to x_3 from 0 to 1.

The Euler-Lagrange equations

$$\frac{\delta\phi_L}{\delta W} = \frac{\delta\phi_L}{\delta\text{ⓗ}} = 0 \qquad \text{...(17)}$$

and the subsidiary conditions

$$W = W^{(0)}, \quad \text{ⓗ} = \text{ⓗ}^{(0)}. \qquad \text{...(18)}$$

restore the original equations (12) and (13). We take

$$W = \sum_{i=1}^{N} a_i f_i : \quad \text{ⓗ} = \sum_{i=1}^{N} b_i t_i \qquad \text{...(19)}$$

$$W^{(0)} = \sum_i a_i^{(0)} f_i ; \quad \text{ⓗ}^{(0)} = \sum_{i=1}^{N} b_i^{(0)} t_i \qquad \text{...(20)}$$

where f_i's and t_i's are the sets of trial functions satisfying the boundary conditions (14). Substituting (19) and (20) into (16), minimizing with respect to the variational parameters a_i's and b_i's, finally putting $a_i = a_i^{(0)}$ and $b_i = b_i^{(0)}$ $(i = 1, 2,......, N)$ and eliminating $a_i^{(0)}$'s and $b_i^{(0)}$'s we obtain the following $(2N \times 2N)$ determinant to vanish :

$$Det \begin{vmatrix} A_{ij} & B_{ij} \\ C_{ij} & D_{ij} \end{vmatrix} + \sigma \begin{vmatrix} E_{ij} & F_{ij} \\ G_{ij} & H_{ij} \end{vmatrix} = 0 \qquad \text{...(21)}$$

where

$$A_{ij} = a^4 <f_i f_j> + 2a^2 <f_i' f_j'> + <f_i'' f_j''>$$

$$B_{ij} = - a^2 R <f_i\, t_j>$$

$$C_{ij} = - <f_j t_i> - \frac{Q_h}{R} <(1 - 2x_3) f_j t_i>$$

$$D_{ij} = <t_i'\, t_j'> + a^2 <t_i t_j>$$

$$E_{ij} = a^2 <f_i f_j> + <f_i' f_j'>$$

$$H_{ij} = Pr <t_i t_j>$$

$$F_{ij} = 0 = G_{ij}. \qquad\qquad ...(22)$$

Here the ′ and ″ indicate the first and second derivatives with respect to x_3.

The nature of the problem see equations (12)–(14) imples that the eigenfunctions cannot fall into two separate groups of even and odd functions. Thus we select the trial functions without symmetry properties satisfying the boundary conditions (14). We take

$$\left.\begin{array}{l} f_i = x_3^2 (1 - x_3)^2 (1 - 2x_3)^{i-1} \\[2mm] t_i = x_3 (1 - x_3)(1 - 2x_3)^{i-1} \end{array}\right\} \qquad ...(23)$$

Substituting (23) into (22), using (21) and varying i and j from 1 to N, we obtain the critical Rayleigh number for different values of Q_h.

For our present study, we pay our attention to the case when the principle of exchange of stabilities is valid and hence set $\sigma = 0$ in (21). The approximate values of R for various values of a and a particular value of Q_h are determined for $N = 2$ and $N = 10$. The minimum value R_c and the corresponding value a_c are calculated for $N = 2$ and $N = 10$. The results are presented in the table.

SOLUTION : EXACT NUMERICAL PROCEDURE

Following Harris and Reid[5] and Chock and Schechter[8] we convert the boundary value problem (12)–(14) into an initial value problem. Taking $\sigma = 0$, when the principle of exchange of stabilities is vaild, we rewrite (12)–(14) as follows :

$$DY_1 = Y_2 : \quad DY_2 = Y_3 : \quad DY_3 = Y_4$$

$$DY_4 = (- a^2 Y_1 + 2Y_3 + RY_5)a^2 : \quad DY_5 = Y_6$$

$$DY_6 = a^2 Y_5 - Y_1 - \frac{Q_h}{R}(1 - 2x_3) Y_1 \qquad\qquad ...(24)$$

with

$$Y_1(0) = Y_2(0) = Y_5(0) = 0 \qquad\qquad ...(25a)$$

$$Y_1(1) = Y_2(1) = Y_5(1) = 0 \qquad \text{...(25b)}$$

where

$$W = Y_1 ; \quad DW = Y_2, \quad D^2W = Y_3, \quad D^3W = Y_4$$

$$\textcircled{H} = Y_5 ; \quad D\textcircled{H} = Y_6 \qquad \text{...(26)}$$

For any particular i, Y_i has six linearly independent solutions which we call as $Y_i^{(j)}$ $(j = 1, 2, ..., 6)$ and thus the general solution for Y_i is written as

$$Y_i = \sum_{j=1}^{6} C_j Y_i^{(j)} \ (i = 1, 2 ......, 6). \qquad \text{...(27)}$$

We make a particular choice for the initial condition $Y_i^{(j)}(0)$, namely

$$Y_i^{(j)}(0) = \delta_{ij}. \qquad \text{...(28)}$$

Due to the above choice, the conditions (25a) put the restriction

$$C_1 = C_2 = C_5 = 0, \qquad \text{...(29)}$$

so that

$$Y_i = C_3 Y_i^{(3)} + C_4 Y_i^{(4)} + C_6 Y_i^{(6)} \qquad \text{...(30)}$$

and the conditions (25b) lead to

$$\text{Det} \begin{vmatrix} Y_1^{(3)}(1) & Y_1^{(4)}(1) & Y_1^{(6)}(1) \\ Y_2^{(3)}(1) & Y_2^{(4)}(1) & Y_2^{(6)}(1) \\ Y_5^{(3)}(1) & Y_5^{(4)}(1) & Y_5^{(6)}(1) \end{vmatrix} = 0 \qquad \text{...(31)}$$

Using the initial conditions (28) integrate the system of equations (24) numerically and obtain the values of the elements of the determinant in (31). For a particular value of Q_h, R_e, the minimum value of R, gives the critical value of the Rayleigh number. Starting with an initial guess for R, we use Newton-Raphson method to get a better approximate value and the process is continued until the value of R is correct upto three decimal places. From the values of R obtained for different values of a by the above method, R_c and a_c, the corresponding value of a, for which the minimum is attained, and determined. We have presented the results in the table.

DISCUSSION

It may be remembered that Watson (1968) had shown that if the strengths of heat source or sink are the same, then they have the same destabilizing effect. In the

Table I, we have presented the values of R_c along with a_c for various values of Q_h obtained by the above two methods, as well as those obtained by Watson. We find that both the methods are successful in showing that Q_h has destabilizing effect whereas a_c increases or in other words, the horizontal dimensions of the cells decrease as Q_h increases.

To have a comparative study between the usefulness of the two methods, we observe from the table that if $N = 2$, the local potential method gives a poor approximation whereas if N is taken large, in particular $N = 10$, the results obtained are sufficiently close to the accurate results. But with $N = 10$, the evaluation of the determinant in (21) becomes lengthy. The exact numerical procedure on the other hand gives accurate results, though the process may be very long unless the initial guess is sufficiently close. From this study, it may be concluded that if the results obtained by the local potential method for $N = 2$ are taken as the initial values for the exact numerical procedure, one should be able to obtain sufficiently accurate results by the exact numerical procedure after only a few iterative processes.

TABLE I. *Critical Rayleigh numbers and related constants*
(A comparative study of the results)

Watson			The present study					
			Local potential method				Exact numerical procedure	
			$N = 2$		$N = 10$			
Q_n	a_c	R_c	a_c	R_c	a_c	R_c	a_c	R_c
0	3.116	1707.8	3.10	1749.97	3.116	1707.7618	3.117	1707.7677
1000	3.120	1703.3	3.10	1735.82	3.120	1703.3069	3.120	1703.3129
2000	3.130	1689.9	3.13	1733.36	3.131	1689.9124	3.120	1689.9190
4000	3.173	1636.0	3.16	1683.03	3.173	1635.8928	3.173	1635.9022
6000	3.243	1544.5	3.23	1597.90	3.244	1544.3632	3.243	1544.3766
8000	3.338	1413.6	3.32	1476.30	3.339	1413.3719	3.338	1413.3914
10000	3.454	1241.4	3.43	1316.49	3.454	1240.8433	3.454	1240.8706
12000	3.581	1026.2	3.54	1117.16	3.583	1025.2346	3.581	1025.2719
14000	3.712	767.6	3.66	877.96	3.713	766.1096	3.712	766.1500
16000	3.840	466.7	3.78	599.79	3.841	464.3470	3.840	464.4078
18000	3.959	125.5	3.90	284.66	3.961	121.9450	3.960	121.9511

$R_c = 0$ for	$R_c = 0$ for	$R_c = 0$ for
$a_c = 4.0$, $Q_h = 18674$	$a_d = 4.0$, $Q_h = 18665$	$a_c = 4.0$, $Q_h = 18673.54$

REFERENCES

1. P Glansdroff and I Prigogine, *Physica* **30** (1964) 351.
2. I Prigogine and P Glansdroff, *Physica* **31** (1965) 1242.
3. I Prigogine, *Non equilibrinm thermodynamics, variational tecniques and stability.* Ed. by R. J. Donnely, R. Herman and I. Prigogine, Chicago University Press, Chicago (1966).
4. R S Schechter and Himmelblau, *Phys. Fluids* **8** (1965) 1431.
5. D L Harris and W H Reid, *J. Fluid Mech.* **20** (1964) 95.

6. J K Platten,   *Int. J. Engng. Sci.* **9** (1971) 37.

7. J K Platten,   *Int. J. Engng. Sci.* **9** (1972) 855.

8. D P Chock and R S Schechter,   *Phys. Fluids,* **16** (1973) 329.

9. V U K Sastry and K V R Rao,   *Int. J. Engng. Sci.* **15** (1977) 405.

10. G Vanderborck and J K Platten,   *Int. J. Engng. Sci.* **12** (1974) 897.

11. S Chandrasekhar,   *Hydrodynamic   and   hydromagnetic   stability,*   Oxford   University   Press, London (1961)

THERMAL STRESSES DUE TO PRESCRIBED FLUX OF HEAT WITHIN A FLAT ANNULAR REGION IN AN ELASTIC PLATE

M LAL

*Department of Mathematics and Computer Sciences, R D University,
Jabalpur-482001*

In the present paper we discuss the distribution of thermal stresses in an elastic plate when the flux is prescribed within a flat annular region. The problem reduces to that of the solution of an infinite system of simultaneous equations. Finally, the distributions of temperature and flux are illustrated graphically for different values of *a*, *b* and plate thickness *h*.

1. INTRODUCTION

THE problem of determining the distribution of thermal stresses in an elastic body is of interest because there arise many practical problems where meachanical structures are subjected to high temperature and pressure. The steady—state thermoelastic problem for the half—space and thick plate was considered by Sneddon and Locket[1], Martin and Payton[2], Mahalanabis[3], Dhaliwal[4] and Lal and Sharma[5]. Sneddon Locket[1] and Martin and Payton[2] restricted their analysis to the cases where the temperature was prescribed within a circular region on both the faces of the plate. Two cases, one face stress-free and the other resting on a rigid foundation or both the faces are stress—free, where studies. Mahalanabis[3] studied the thermoelastic problem for an elastic layer when the temperature is arbitrarily prescribed within a circular region on the upper free surface of the layer, the remainder of the surface radiating in accordance with Newton's law. Dhaliwal[4] studied the steady-state thermal stresses in an elastic layer with one face stress free and the other resting on an insulated foundation. Subsequenlly Mori *et al.*[6] studied the linear thermoelastic problem of a slab containing an annular crack. They reduced the problem into two singular integral equations of the first kind by using integral transform techniques and solved these equations numerically. They also illustrated the stress intensity factors graphically for different values of *r*, *a* and *h*. Recently Lal and Sharma[5] studied the steady-state thermal stresses in an elastic layer when the flux is prescribed in a flat annular region. They reduced the problem to solution of triple integral equations which are further reduced to that of Fredholm integral equation. They solved this equation by an iterative procedure. The iterative solution was found to be very complex.

The present paper is concerned with the determination of thermal stresses in an elastic plate with one face stress free and the other resting on a rigid frictionless foundation. The free surface of the layer is subjected to a known flux on an annular region with the temperature zero inside and outside the annular region. The surface in contact with the foundation is assumed to be insulated. The triple integral equations occurring in this problem are reduced to the solution of an infinite system of simultaneous linear algebraic equations which are numerically computed. Finally, the temperature and flux distributions in the plate are illustrated graphically.

2. SOLUTION OF GOVERNING EQUATIONS

The steady-state thermoelastic equations for an axisymmetric case may be written as

$$(\lambda + \mu) \frac{\partial E}{\partial r} + \mu \Delta^2 v - (3\lambda + 2\mu) \alpha \frac{\partial T}{\partial r} = 0, \qquad \ldots(2.1)$$

$$(\lambda + \mu) \frac{\partial E}{\partial z} + \mu \Delta^2 w - (3\lambda + 2\mu) \alpha \frac{\partial T}{\partial z} = 0, \qquad \ldots(2.2)$$

$$\Delta^2 T = 0, \qquad \ldots(2.3)$$

where,

$$E = \frac{1}{r} \frac{\partial(ru)}{\partial r} + \frac{\partial w}{\partial z} ; \quad \Delta^2 = \frac{\partial^2}{\partial r^2} + \frac{1}{r} \frac{\partial}{\partial r} + \frac{\partial^2}{\partial z^2},$$

(r, θ, z) is a cylindrical coordinate system; u, w and T are, respectively radial and vertical displacements and temperature distribution; λ, μ are the Lame's constants and α is the coefficient of linear thermal expansion.

The components σ_{rr}, $\sigma_{\theta\theta}$, σ_{zz}, σ_{rz} of the stress tensor associated with the displacement field are given by :

$$\sigma_{rr} = (\lambda + 2\mu) \frac{\partial u}{\partial r} + \lambda \left(\frac{u}{r} + \frac{\partial w}{\partial z} \right) - (3\lambda + 2\mu) \alpha T, \qquad \ldots(2.4)$$

$$\sigma_{\theta\theta} = (\lambda + 2\mu) \frac{u}{r} + \lambda \left(\frac{\partial u}{\partial r} + \frac{\partial w}{\partial r} \right) - (3\lambda + 2\mu) \alpha T, \qquad \ldots(2.5)$$

$$\sigma_{zz} = (\lambda + 2\mu) \frac{\partial w}{\partial z} + \lambda \left(\frac{u}{r} + \frac{\partial u}{\partial r} \right) - (3\lambda + 2\mu) \alpha T, \qquad \ldots(2.6)$$

$$\sigma_{rz} = \mu \left(\frac{\partial u}{\partial z} + \frac{\partial w}{\partial r} \right).$$

To solve the above equations, we introduce $\bar{F}(\xi, z)$, the nth order Hankel transform of $F(r, z)$, as

$$\bar{F}(\xi, z) = \int_0^\infty r J_n(\xi r) F(r, z) \, dr. \qquad \ldots(2.8)$$

The inverse transform of $\bar{F}$ is given by

$$F(r, z) = \int_0^\infty \xi J_n(\xi r)\, \bar{F}(\xi, z)\, d\xi, \qquad\qquad \text{...(2.9)}$$

where, $J_n(\xi r)$ is a Bessel function of the first kind and nth order. Now, *if $\{u^*, \sigma^*_{rz}\}$* and $\{\bar{w}, \bar{T}, \bar{\sigma}_{zz}\}$ denote respectively the first and zeroth order Hankel transforms of $\{u, \sigma_{rz}\}$ and $\{w, T, \sigma_{zz}\}$, it can be shown that the equations (2.1) — (2.3), (2.6) and (2.7) may be written as

$$(D^2 - k^2\,\xi^2)\, u^* - (k^2 - 1)\, \xi\ \bar{D}w = -\,\beta\xi\bar{T}, \qquad\qquad \text{...(2.10)}$$

$$(k^2 D^2 - \xi^2)\, \bar{w} + (k^2 - 1)\, \xi\ Du^* = \beta D\bar{T}, \qquad\qquad \text{...(2.11)}$$

$$(D^2 - \xi^2)\, \bar{T} = 0, \qquad\qquad \text{...(2.12)}$$

$$\bar{\sigma}_{zz} = \mu\,[(k^2 - 2)\, \xi\, u^* + k^2\, D\bar{w} - \beta\bar{T}], \qquad\qquad \text{...(2.13)}$$

$$\overset{*}{\sigma}_{rz} = \mu\,(Du^* - \xi\bar{w}), \qquad\qquad \text{...(2.14)}$$

where,

$$D = \frac{d}{dz};\ \beta = \frac{2\,(1 + \eta)\,\alpha}{(1 - 2\eta)};\ k^2 = \frac{2\,(1 - \eta)}{(1 - 2\eta)},$$

and η it poisson's ratio.

The solution of the set of simultanoeus ordinary differential equations (2.10)-(2.12) may be written as

$$\left.\begin{aligned}
\bar{T} &= A \cosh(\xi z) + B \sinh(\xi z), \\
u^* &= (A_1 + \xi z A_2) \cosh(\xi z) + (B_1 + \xi z B_2) \sinh(\xi z), \\
\bar{w} &= (A_3 + \xi z A_4) \cosh(\xi z) + (B_3 + \xi z B_4) \sinh(\xi z)
\end{aligned}\right\} \qquad \text{...(2.15)}$$

where $A, B, A_i, B_i, i = 1, 2, 3, 4$ are arbitrary functions of ξ only. Substitution for $\bar{T}, u^*, \bar{w}$ from (2.15) into (2.10) and equating the coefficients of $\cosh(\xi z)$, $\sinh(\xi z)$, $\xi z \cosh(\xi z)$, $\xi z \sinh(\xi z)$ on both the sides, we obtain :

$$\left.\begin{aligned}
A_2 &= -\,B_4 = \frac{1}{(k^2 + 1)}\,[(k^2 - 1)\,(B_1 + A_3)\,\xi - \beta\,B], \\
A_4 &= -\,B_2 = \frac{-1}{(k^2 + 1)}\,[(k^2 - 1)\,(A_1 + B_3)\,\xi - \beta\,A].
\end{aligned}\right\} \qquad \text{...(2.16)}$$

Subtituting from (2.15) into (2.13) and (2.14) we obtain the expressions for the components of stress :

$$\bar{\sigma}_{zz} = \mu\,[\{\xi(k^2 - 2)\,(A_1 + \xi z A_2) + \xi k^2(A_4 + B_3 + \xi z B_4)$$
$$-\ \beta A\}\cosh(\xi z) + \{\xi\,(k^2 - 2)\,(B_1 + \xi z B_2) + \xi k^2(B_4$$
$$+\ A_3 + \xi z A_4) - \beta B\}\sinh(\xi z)], \qquad\qquad \text{...(2.17)}$$

$$\sigma_{rz}^{*} = \mu\xi[(B_2 - B_3 + A_1 + 2\xi z A_2)\sinh(\xi z)$$
$$+ (A_2 - A_3 + B_1 + 2\xi z B_2)\cosh(\xi z)]. \qquad ...(2.18)$$

3. Boundary Conditions and Solution of the Triple Integral Equations

We consider an infinite, homogeneous elastic plate occupying the region $0 \leqslant z \leqslant h$ such that the surface $z = 0$ is stress free and the surface $z = h$ is resting on a rigid frictionless foundation. The above mechanical conditions are written as :

$$\sigma_{zz} = \sigma_{rz} = 0, \text{ on } z = 0,$$
$$w = \sigma_{rz} = 0, \text{ on } z = h. \qquad \qquad ...(3.1)$$

Using (2.15) — (2.17) to satisfy the boundary conditons (3.1), we are able to express u^*, $\bar{w}$ and $\bar{T}$ in terms of only two arbitrary functions A, B in the following form :

$$u^* = \frac{\beta}{2\xi(k^2 - 1)}[A(\xi)\cosh(\xi z) + B(\xi)\sinh(\xi z)],$$
$$\bar{w} = \frac{\beta}{2\xi(k^2 - 1)}[A(\xi)\sinh(\xi z) + B(\xi)\cosh(\xi z)], \qquad ...(3.2)$$

$$\bar{T} = A(\xi)\cosh(\xi z) + B(\xi)\sinh(\xi z). \qquad ...(3.3)$$

Now, let us consider the following mixed thermal boundary conditions .

$$T = 0, \quad 0 \leqslant r \leqslant a, \qquad \text{on } z = 0, \qquad ...(3.4)$$

$$\frac{\partial T}{\partial z} = -T_0, \quad a \leqslant r \leqslant b, \quad \text{on } z = 0, \qquad ...(3.5)$$

$$\frac{\partial T}{\partial z} = 0, \quad 0 \leqslant r < \infty, \qquad \text{on } z = h, \qquad ...(3.6)$$

where, T_0 is the constant flux of heat. The boundary condition (3.6) will be satisfied if we take

$$B(\xi) = -A(\xi)(1 - e^{-2\xi h})/(1 + e^{-2\xi h}). \qquad ...(3.7)$$

Now, substituting for $B(\xi)$ in (3.2) and (3.3) and taking the appropriate inverse transforms we find that

$$u = (1 + \eta)\alpha \int_0^\infty e^{-\xi z} \frac{1 + e^{-2\xi(h-z)}}{1 + e^{-2\xi h}} A(\xi) J_1(\xi z)\, d\xi, \qquad ...(3.8)$$

$$w = -(1 + \eta)\alpha \int_0^\infty e^{-\xi z} \frac{1 - e^{-2\xi(h-z)}}{1 + e^{-2\xi h}} A(\xi) J_0(\xi r)\, d\xi, \qquad ...(3.9)$$

$$T = \int_0^\infty \xi \, e^{-2\xi z} \frac{1 + e^{-2\xi(h-z)}}{1 + e^{-2\xi h}} A(\xi) J_0(\xi r) \, dz. \qquad \qquad \text{...(3.10)}$$

Substituting for T from (3.10) into (3.4) and (3.5), we find that the mixed boundary condition leads to the triple integral equations

$$\int_0^\infty \xi A(\xi) J_0(\xi r) \, d\xi = 0, \, 0 \leqslant r \leqslant a; \, r \geqslant b, \qquad \qquad \text{...(3.11)}$$

$$\int_0^\infty \xi^2 A(\xi)[1 - H(2 \, \xi h)] J_0(\xi r) \, d\xi = T_0, \, a \leqslant r \leqslant b, \qquad \qquad \text{...(3.12)}$$

where

$$H(x) = 2 \, e^{-x} (1 + e^{-x})^{-1} \qquad \qquad \text{...(3.13)}$$

It is very difficult to solve the integral equations directly. We use a similar method to that in the paper [7]. By putting

$$a = c - d, \, b = c + d,$$

$$r^2 = c^2 + d^2 - 2 \, cd \cos \varphi,$$

$$[(r^2 - a^2)(b^2 - r^2)]^{1/2} = 2cd \sin \varphi, \qquad \qquad \text{...(3.14)}$$

where, c denotes the means radius and $2d$ is the width of the annular region. The variable r in $a \leqslant r \leqslant b$ will be replaced by a new one φ in $0 \leqslant \varphi \leqslant \pi$. Moreover, the temperature at $z = 0$ has singularities in the forms of $(r^2 - a^2)^{-1/2}$ at $r = a$ and $(b^2 - r^2)^{-1/2}$ at $r = b$, taking continuous and finite values in $a < r < b$. Then we can represent temperature T at $z = 0$ without loss of generality as

$$[T]_{z=0} = \frac{r}{\sqrt{[(r^2 - a^2)(b^2 - r^2)]}} \sum_{n=0}^\infty a'_n \cos(n\varphi), \, a < r < b, \quad \text{...(3.15)}$$

where a'_n are unknown coefficients. Here, putting

$$I_n(\xi) = J_n(\xi c) J_n(\xi d), \, n = 0, 1, 2 \,,..., \qquad \qquad \text{...(3.16)}$$

and using the integral formula of [8]

$$\int_0^\infty \xi J_0(\xi z) J_n(\xi c) J_n(\xi d) \, d\xi = \begin{cases} 0, \, 0 < r < a, \, r > b \\ \dfrac{1}{\pi cd} \dfrac{\cos(n\varphi)}{\sin(\varphi)}, \, a < r < b \end{cases}$$

and subtracting I_{n+1} from I_{n-1}, we get

$$\int_0^\infty J_0(\xi r) G_n(\xi) \, d\xi = \begin{cases} 0, \, 0 \leqslant r \leqslant a, \, r \geqslant b, \\ \dfrac{2}{\pi cd} \sin(n\varphi), \, a \leqslant r \leqslant b, \end{cases} \qquad \text{...(3.17)}$$

where,

$$G_n(\xi) = \xi[I_{n-1}(\xi) - I_{n+1}(\xi)]$$

Putting,

$$\xi A(\xi) = T_0 \sum_{n=1}^{\infty} a_n G_n(\xi)$$

in equation (3.11) and (3.12) and making use of the result (3.17), the equation (3.11) is automatically satisfied and (3.12) is rewritten as follows :

$$\sum_{n=1}^{\infty} a_n \int_0^{\infty} \xi[1 - H(2\xi h)]\, G_n(\xi)\, J_0(\xi r)\, d\xi = 1, a \leqslant r \leqslant b, \qquad \dots(3.18)$$

Equation (3.18) must be satisfied independently for all values of r. We represent $J_0(\xi r)$ by the fourier series in the interval $a \leqslant r \leqslant b$ by using the relation (3.14).

$$J_0(\xi r) = J_0(\xi \sqrt{\overline{\{c^2 + d^2 - 2cd \cos \varphi\}}})$$

$$= J_0(\xi c)\, J_0(\xi d) + 2 \sum_{m=1}^{\infty} J_m(\xi c)\, J_m(\xi d) \cos (m\varphi). \qquad \dots(3.19)$$

Substituting equation (3.19) into (3.18), we can obtain

$$\sum_{n=1}^{\infty} a_n \int_0^{\infty} \xi[1 - H(2\xi h)]\, G_n(\xi)\, [J_0(\xi c)\, J_0(\xi d)$$

$$+ 2 \sum_{m=1}^{\infty} J_m(\xi c)\, J_m(\xi d) \cos (m\varphi)]\, d\xi = 1. \qquad \dots(3.20)$$

Here, if we equate the coefficients of cos $(m\varphi)$ on both sides of equation (3.20), we can introduce a set of an infinite number of simultaneous equations with respect to unknown coefficients a_n,

$$\sum_{n=1}^{\infty} a_n \int_0^{\infty} \xi[1 - H(2\xi h)]\, G_n(\xi)\, J_m(\xi c)\, J_m(\xi d)\, d\xi = \delta_{0m}, m = 0, 1, 2, \dots,$$

$$\dots(3.21)$$

where, δ_{0m} denotes the Kronecker delta.

We can readily recognize the asymmetry of the matrix of the simultaneous equation (3.21). Then it is not always possible to compute a_n from these equations. For the simplicity of numerical treatment, taking the difference between the m-th and $(m + 2)$ th equations, we get the following result that has the symmetric matrix,

$$\sum_{n=1}^{\infty} a_n \int_0^{\infty} [1 - H(2\xi h)]\, G_n(\xi)\, G_m(\xi)\, d\xi = \delta_{1m}, m = 1, 2, \dots, \qquad \dots(3.22)$$

Consequently, the present mixed boundary value problem is reduced to the solution of equations (3.22). In particular, the temperature on the surface $z = 0$ is

$$(T/T_0)_{s=0} = \sum_{n=1}^{\infty} a_n \begin{cases} 0, & 0 \leqslant r \leqslant a, r \geqslant b \\ \dfrac{2}{\pi cd} \sin(n\varphi), & a \leqslant r \leqslant b. \end{cases} \qquad ...(3.23)$$

4. NUMERICAL CALCULATIONS

To determine the unknown coefficients a_n, we must solve the infinite set of simultaneous equations (3.22). For this purpose, first, we must evaluate the infinite integrals in equation (3.22). Let us put A_{mn} as the coefficient at the m-th line and n-th coloumn in the coefficient matrix of (3.22). Thus

$$A_{mn} = A_{nm} = \int_0^{\infty} [1 - H(2\xi h)] \, G_n(\xi) \, G_m(\xi) \, d\xi. \qquad ...(4.1)$$

Since the magnitude of $[1 - H(2\xi h)]$ converges to unity rapidly with increasing ξ, A_{mn} may be expressed approximately by the equation

$$A_{mn} = \int_0^{\delta} [1 - H(2\xi h)] \, G_n(\xi) \, G_m(\xi) \, d\xi + A'_{mn} \qquad ...(4.2)$$

where δ is a very large value, and A'_{mn} is represented by the equation

$$A'_{mn} = A'_{nm} = \int_0^{\infty} G_n(\xi) \, G_m(\xi) \, d\xi \qquad ...(4.3)$$

The first term on the right hand side of equation (4.2) is integrated numerically by means of Simpson's rule. Here we choose $\delta = 300$ and the interval in the numerical integrals is taken to be 0.2. The second term is integrated by using the approximate form of Bessel functions

$$J_m(\xi r) \approx \sqrt{\frac{2}{\xi \pi r}} \cos\left(\xi r - \frac{2m - 1}{4} \pi\right),$$

in the limit of large ξ. Thus,

$$A'_{mn} = \frac{4mn}{\pi^2 c^3 d^3} \int_{\delta}^{\infty} \xi^{-2} [a^2 \sin^2(\xi a) - \{(-1)^m$$

$$+ (-1)^n\} ab \sin(\xi a) \cos(\xi b) + (-1)^{m+n} b^2 \cos^2(\xi b)] \, d\xi. \qquad ...(4.4)$$

Integrating equation (4.4) by parts and introducing sine and cosine functions $si(x)$, $ci(x)$, the following approximate formula for A'_{mn} is obtained.
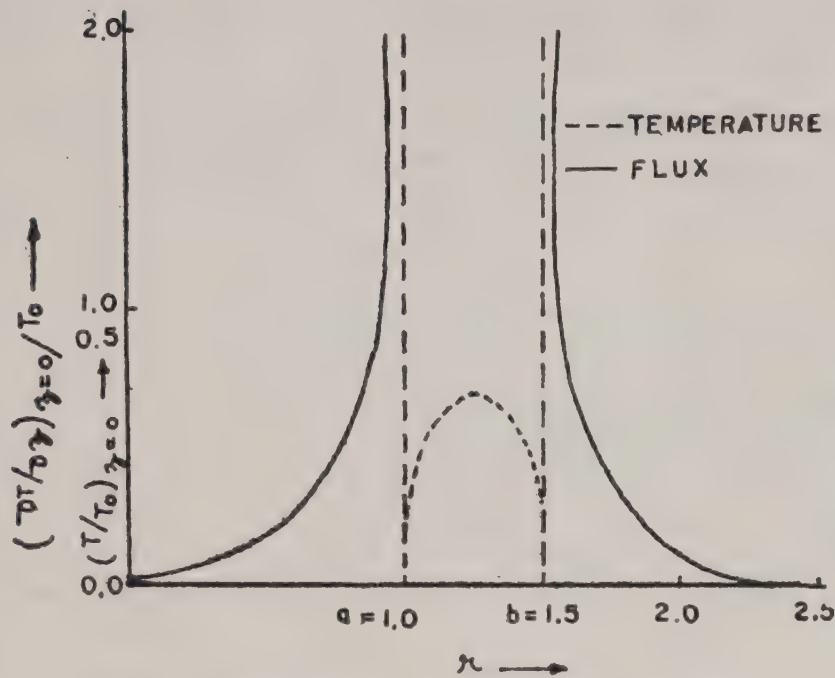
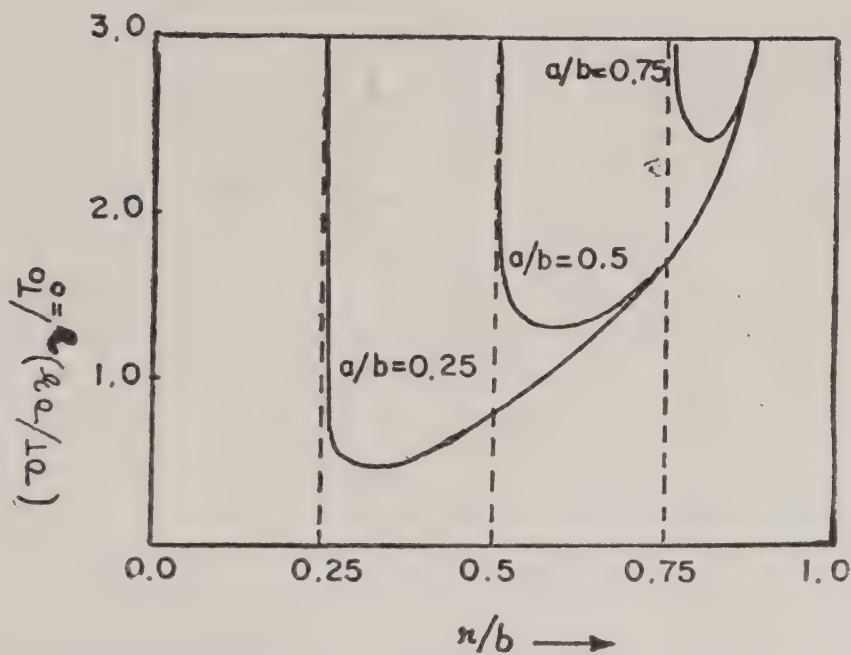FIG. 1. THE RADIAL DISTRIBUTIONS OF TEMP. AND FLUX FOR a=1.0, b=1.5, h=1.0

FIG. 2. The distribution of flux for various values of a/b (h/b = 1.0)

$$A'_{mn} \approx \frac{4mn}{\pi^2 c^3 d^3} \left[a^2 \left\{\delta^{-1} \sin^2 (\delta a) - a\, si(2\delta a)\right\}\right.$$

$$+ (- 1)^{m+n} b^2 \left\{\delta^{-1} \cos^2 (\delta b) + b si(2\delta b)\right\} - \left\{(- 1)^m\right.$$

$$\left.+ (- 1)^n\right\} ab \left\{\delta^{-1} \sin (\delta a) \cos (\delta b) - cci(2\delta c) + dci(2\delta d)\right\}].$$

$$...(4.5)$$

After A'_{mn} are obtained as above we take only the first n roots of a set of simultaneous equations. It was checked that we could get numerically good results taking $n = 15$ in case of $a/b \leqslant 0.2$ and $n = 10$ for $a/b > 0.2$.

In Figure 1 the radial distributions of the temperature and flux are shown for the case of $a = 1.0$, $b = 1.5$ and $h = 1.0$.

Figure 2 shown the radial distributions of flux for various values of a/b under $h/b = 1.0$. It is seen that the flux becomes large with increasing a/b.

REFERENCES

1. I N Sneddon and F J Locket, *Quart. Appl. Math.* **18** (1960) 145.
2. C J Martin and R G Payton, *J. Math. Mech.* **13** (1964) 1.
3. R K Mahalanabis, *Indian J. Mathematics* **11** (1969) 115.
4. R S Dhaliwal, *SIAM J. Appl. Math.* **20** (1971) 131.
5. M Lal and J P Sharma, *J. Jiwaji Univ.* **8** (1980) 1.
6. Y Mori, Y Shindo and A Atsumi, *Lett. Appl. Engng. Sci.* **18** (1980) 1161.
7. M Lal, *Bull. Inst. Poli. Insi.* **31** (1981) 37.
8. A Erdelyi, *Tables of Integral Transforms*, Vol. 2, McGraw Hill Book Comp., New York (1954).

MHD FLOW IN A CHANNEL WITH WAVY POROUS BOUNDARY

D R V Prasada Rao *and* R Sivaprasad

Department of Mathematics, S K University, Anantapur 515 003

An attempt has been made to study the flow and heat transfer aspect of an incompressible, viscous, electrically conducting fluid in a horizontal porous channel bounded by a wavy wall and a flat wall in the presence of a constant heat source. Using long wave approximation the governing equations of flow and heat transfer have been solved. The influence of heat source, suction and wavyness of the boundaries on the flow has been brought out through the numerical analysis of the velocity, tempreature distributions, skin friction and Nusselt number.

Keywords : Heat Transfer ; Wavy porous boundaries

1. Introduction

Heat transfer studies with internal heat sources have been proposed for Earth mantle[1-3] and for the outer region of star interiors[4]. The volumetric rate of heat generation has been assumed to be either constant[5-9] or a function of space variables[10-14]. Some authors have considered directly the viscous dissipation and the expansion effect[15,16].

In all these investigations the boundaries are assumed to be flat. But there are many physical situations in which the surface of the solid boundaries are wavy in nature. For examples, the surface formed by cleavage of mica contains irregulasities of the order of 20A in size, and the irregularities of the surface of an ideally smooth quartz crystal can be up to 100A in height[17]. Flow over a wavy wall has attracted the attention of several authors because of its applications in different areas such as transpiration cooling of re-entry vehicles and rocket boosters, cross-hatching on ablative surfaces and film vapourisation in combusion chambers. Keeping this in view, Lekeoudis *et al.*[18] have discussed the viscous flow part wavy walls using linear analysis without restricting the mean flow in the disturbance layer. The effect of wavyness on a viscous flow past an infinite wall has been investigated by Sankar and Sinha[19]. Using a perturbation technique similar to Lighthill's method, Vajravelu and sastry[20] have extended the above analysis to free convention flow in a vertical wavy channel in the presence of a constant heat source. The hydromagnetic case of this problem has been studied by Rao *et al.*[21]

In this paper an attempt has been made to study the flow and heat transfer aspect of an incompressible, viscous, electrically conducting fluid in a horizontal porous channel bounded by a wavy wall and a flat wall in the presence of a constant

heat source. Using long wave approximation the governing equations of flow and heat transfer have been solved. The influence of heat source, suction and wavyness of the boundaries on the flow has been brought out through the numerical analysis of the velocity, temperature distributions, Skin friction and Nusselt number.

2. FORMULATION AND SOLUTION

Consider the flow of an incompressible, electrically conducting horizontal porous channel bounded below by a flat wall and above by a wavy wall. Choosing the cartesian frame of references $o(x', y')$ such that y' —axis is vertical. Let $y' = 0$ be the lower flat wall and let the wavy wall be represented by $y' = d + \epsilon^* \cos(\lambda' x')$ where ϵ^* the amplitude of the wave, is assumed to be small. A uniform magnetic field of strength H_0 is applied parallel to the y'—axis. The equations governing the steady two-dimensional flow and heat transfer in a viscous incompressible fluid occupying the channel are the momentum equations

$$u' \frac{\partial u'}{\partial x'} + v' \frac{\partial u'}{\partial y'} = -\frac{\partial p'}{\partial x'} + \nu \nabla^2 u' - \frac{(\sigma \mu_e^2 H_0^2)}{\rho} u' \qquad \text{...(2.1)}$$

$$u' \frac{\partial v'}{\partial x'} + v' \frac{\partial v'}{\partial y'} = -\frac{\partial p'}{\partial y'} + \nu \nabla^2 v' \qquad \text{...(2.2)}$$

The continuity equation

$$\frac{\partial u'}{\partial x'} + \frac{\partial v'}{\partial y'} = 0 \qquad \text{...(2.3)}$$

and the energy equation

$$\rho c_p \left(u' \frac{\partial T}{\partial x'} + v' \frac{\partial T}{\partial y'} \right) = k \nabla^2 T + Q \qquad \text{...(2.4)}$$

$$\left(\Delta^2 = \frac{\partial^2}{\partial x'^2} + \frac{\partial^2}{\partial y'^2} \right)$$

where u' and v' are the velocity components, p' is the pressure, σ is the electrical conductivity, μ_e, is the magnetic permeability, c_p is the specific heat at constant pressure, k is the thermal conductivity of the fluid and Q is the constant heat addition/absorption.

The boundary conditions are

$$u' = 0, v' = -v_0 (v_0 > 0), T = T_0 \text{ at } y' = 0$$

$$v' \cos \phi - u' \sin \phi = -v_0 \cos \phi$$

$$v' \sin \phi + u' \cos \phi = v_0 \sin \phi \qquad \left. \right\} \text{ on } y' = \eta(x') \qquad \text{...(2.5)}$$

$$T = T_1$$

where $\tan \phi = \frac{d\eta}{dx}$ is small.

Defining the non-dimensional variables (x, y, u, v, p, θ) as

$$(x, y) = (x', y')/d, \qquad : \qquad (u, v) = \frac{(u', v') \, d}{v}$$

$$\qquad\qquad : \qquad \qquad\qquad\qquad\qquad \theta = \frac{T - T_0}{T_1 - T_0} \qquad ...(2.6)$$

$$p = p'/\rho(v/d)^2$$

The governing equations and the boundary conditions in the non-dimensional form reduce to

$$\left. u \frac{\partial u}{\partial x} + v \frac{\partial u}{\partial y} = - \frac{\partial p}{\partial x} + \nabla^2 u - M^2 u \right\} \qquad\qquad ...(2.7)$$

$$\left. u \frac{\partial v}{\partial x} + v \frac{\partial v}{\partial y} = - \frac{\partial p}{\partial y} + \nabla^2 v \right. \qquad\qquad ...(2.8)$$

$$\frac{\partial u}{\partial x} + \frac{\partial v}{\partial y} = 0 \qquad\qquad ...(2.9)$$

$$P\left(u \frac{\partial \theta}{\partial x} + v \frac{\partial \theta}{\partial y} \right) = \nabla^2 \theta + \alpha \qquad\qquad ...(2.10)$$

$$u = 0 \; ; \; v = - S \; ; \; \theta = 0 \qquad \text{on } y = 0$$

$$\left. \begin{array}{l} v \cos \phi - u \sin \phi = - S \cos \phi \\[2mm] v \sin \theta + u \cos \theta = S \sin \phi \\[2mm] \qquad\qquad \theta = 1 \end{array} \right\} \text{ on } y = \eta(x) \qquad ...(2.11)$$

where

$$M^2 = \frac{\sigma \mu_e^2 H_0^2 d^2}{\rho v}, \qquad \text{the Hartmann number}$$

$$P = \mu(c_v)/k, \qquad \text{the Prandtl number}$$

$$\alpha = Qd^2/k(T_1 - T_0), \quad \text{the heat source parameter}$$

$$\epsilon = \frac{\epsilon^*}{d}, \qquad \text{the amplitude parameter}$$

$$\lambda = \lambda' d, \qquad \text{the frequency parameter}$$

Using the perturbation method we write the total velocity and total temperature distributions as

$$\left. \begin{array}{l} u(x, y) = u_0(y) + \epsilon u_1(x, y) + \cdots\cdots \\[2mm] v(x, y) = - S + \epsilon v_1(x, y) + \cdots\cdots \\[2mm] p(x, y) = p_0(x) + \epsilon p_1(x, y) + \cdots\cdots \\[2mm] \epsilon(x, y) = \theta_0(y) + \epsilon \theta_1(x, y) + \cdots\cdots \end{array} \right\} \qquad ...(2.12)$$

$(u_0 \, (y), \, - \, S)$, $\theta_0(y)$ and $p_0(x)$ are the velocity distributions, temperature distribution and applied pressure of mean flow. $(u_1, \, v_1)$, θ_1, $p_1 \, (x, \, y)$ are the perturbations over the velocity, temperature and pressure distributions respectively due to wavyness of the boundary substituting (2.12) in equations (2.7)–(2.10) and equating the like powers of ϵ we get

$$\frac{d^2 u_0}{dy^2} + S \frac{du_0}{dy} - M^2 u_0 = c \qquad \qquad ...(2.13)$$

$$\frac{d^2 \theta_0}{dy^2} + (PS) \frac{d\theta_0}{dy} = - \alpha \qquad \qquad ...(2.14)$$

to the zeroth order and

$$u_0 \frac{\partial u_1}{\partial x} + v_1 \frac{du_0}{dy} - S \frac{du_1}{dy} = - \frac{\partial p_1}{\partial x} + \nabla^2 u_1 - M^2 u_1 \qquad \qquad ...(2.15)$$

$$v_0 \frac{\partial v_1}{\partial x} - S \frac{\partial v_1}{\partial y} = - \frac{\partial p_1}{\partial y} + \nabla^2 v_1 \qquad \qquad ...(2.16)$$

$$\frac{\partial u_1}{\partial x} + \frac{\partial v_1}{\partial y} = 0 \qquad \qquad ...(2.17)$$

$$P \left(u_0 \frac{\partial \theta_1}{\partial x} - S \frac{\partial \theta_1}{\partial y} + v_1 \frac{\partial \theta_0}{\partial y} \right) = \nabla^2 \theta_1 \qquad \qquad ...(2.18)$$

to the first order, where $c = \dfrac{\partial p_0}{\partial x}$.

Assuming the slope of the wavy wall $\left(\dfrac{d\eta}{dx} \right)$ to be small with the help of (2.12) the boundary conditions (2.11) can be simplified to

$$\left. \begin{array}{l} u_0 = 0 \, : \quad \theta_0 = 0 \quad \text{on } y = 0 \\[2mm] u_0 = 0 \, ; \quad \theta_0 = 1 \quad \text{on } y = 1 \end{array} \right\} \qquad \qquad ...(2.19)$$

$$\left. \begin{array}{l} u_1 = 0 \, ; \quad v_1 = 0 \, ; \quad \theta_1 = 0 \quad \text{on } y = 0 \\[2mm] u_1 = - \exp{(i\lambda x)} \, u_0' \, ; \, v_1 = 0 \, ; \, \theta_1 = - \theta_0' \exp{(i\lambda x)} \text{ on } y = 1 \end{array} \right\} ...(2.20)$$

where a prime denotes differentiation w.r.t. y. Introducing the stream function $\bar{\psi}_1$ as

$$u_1 = - \frac{\partial \bar{\psi}_1}{\partial y} \, ; \quad v_1 = \frac{\partial \bar{\psi}_1}{\partial x}$$

into (2.15) and (2.16) and eliminating the non-dimensional pressure p_1, we get

$$u_0' \bar{\psi}_{1,x} \quad u_0(\bar{\psi}_{1,xyy} + \bar{\psi}_{1,xxx}) + S(\bar{\psi}_{1,yyy} + \bar{\psi}_{1,xxy}) +$$

$$2\bar{\psi}_{1,xxyy} + \bar{\psi}_{1,xxxx} + \bar{\psi}_{1,yyyy} - M^2 \bar{\psi}_{1,yy} = 0 \qquad \qquad ...(2.21)$$

$$P(u_0\theta_{1,x} - S\theta_{1,y} + \theta_0' \bar{\psi}_{1,x}) = \theta_{1,xx} + \theta_{1,yy} \qquad \text{...(2.22)}$$

keeping in view the conditions (2.20), we write the general solutoin for $\bar{\psi}$ under the long-wave approximation ($\lambda \ll 1$) as

$$\bar{\psi}(x, y) = \sum_i (\lambda^i \psi_i) \exp(i\lambda x) \qquad \text{...(2.23)}$$

$$(i = 0, 1, 2, \ldots\ldots\ldots)$$

Substituting (2.23) in (2.21) and (2.22) and separating the terms of various orders in λ, we obtain the following differential equations to the order of ϵ^2,

$$\psi_0'^{\bullet} + S \psi_0''' - M^2 \psi_0' = 0 \, ; \, t_0'' + S P t_0' = 0 \qquad \text{...(2.24)}$$

$$\left.\begin{array}{l} \psi_1'^{\bullet} + S \psi_1''' - M^2 \psi_1' = i(u_0\psi_0' - u_0' \psi_0) \\[2mm] t_1'' + S P t_1' = i P (u_0 t_0 + \theta_0' \psi_0) \end{array}\right\} \qquad \text{...(2.25)}$$

$$\left.\begin{array}{l} \psi_2'^{\bullet} + S \psi_2''' - M^2\psi_2' = 2\psi_2'' + S \psi_0' + i(u_0\psi_1' - u_1' \psi_1) \\[2mm] t_2'' + P S t_2' = t_0 + i P(u_0 t_1 + \theta_0' \psi_1) \end{array}\right\} \qquad \text{...(2.26)}$$

The boundary conditions (2.20) in terms of ψ_i are

$$\left.\begin{array}{l} \psi_0 = 0 \, ; \, \psi_0' = 0 \, ; \, t_0 = 0 \quad \text{on } y = 0 \\[3mm] \psi_0 = 0 \, ; \, \psi_i' = u_0' \, ; \, t_1 = -\theta_0' \quad \text{on } y = 1 \end{array}\right\} \qquad \text{...(2.27)}$$

$$\left.\begin{array}{l} \psi_i = 0 \, ; \, \psi_i' = 0 \, ; \, t_i = 0 \text{ on } y = 0 \\[3mm] \psi_i = 0 \, ; \, \psi_i' = 0 \, ; \, t_i = 0 \text{ on } y = 1 \end{array}\right\} \text{ for } i \geq 1 \qquad \text{...(2.28)}$$

Solving the equations (2.13) and (2.14) using the conditions (2.19), we obtain the mean flow solution as

$$u_0(y) = \frac{c}{M^2}\left[1 + \frac{(\sinh m(y-1) - \exp(S/2)\sinh(my))\exp(-Sy/2)}{\sinh m}\right]$$

$$\theta_0(y) = c_2(\exp(-PSy) - 1) - a_{40}y$$

where

$$m = \frac{(S^2 + 4M^2)^{1/2}}{2} \, ; \quad a_{40} = \alpha/PS \, ; \quad c_2 = \frac{(1 + a_{40})}{(\exp(-PS) - 1)}$$

The perturbed flow solutions in terms of ψ and θ_1 are abtained by solving (2.15)–(2.18) using the conditions (2.20) which are given by

$$\psi_0 = A_1 + A_2 y + [A_3 \cosh(my) + A_4 \sinh(my)] \exp(-Sy/2)$$

$$\psi_1 = i \, (B_1 + B_2(y) + [B_3 \cosh(my) + B_4 \sinh(my)] \exp(-Sy/2)$$
$$+ \phi_1(y))$$

$$t_0 = c_4 \, (\exp(-SPy) - 1)$$

$$t_1 = i \, (D_1 + D_2 \exp(-SPy) + \phi_2(y))$$

The perturbed velocity components u_1, v_1 and temperature θ_1 are given by

$$u_1 = - \, [\psi'_r \cos(\lambda x) - \psi'_i \sin(\lambda x)]$$

$$v_1 = - \, \psi_r \, [\sin(\lambda x) + \psi_i \cos(\lambda x)]$$

and

$$\theta_1 = t_r \cos(\lambda x) - t_i \sin(\lambda x)$$

where

$$\psi_r + i \, \psi_i = \psi; \quad \psi'_r + i \, \psi'_i = \psi'$$

$$t_r + i \, t_i = t; \quad t'_r + i \, t'_i = t'$$

3.   SKIN FRICTION AND HEAT TRANSFER CO-EFFICIENT (NUSSELT NUMBER) AT THE WALLS

The shear stress τ_{xy} at any point in the fluid is given by $\tau'_{xy} = \mu \left(\dfrac{\partial u'}{\partial y'} + \dfrac{\partial v'}{\partial x'} \right)$ which in the dimensionless form reduces to $\tau_{xy} = h^2 \tau'_{xy}/\rho v^2 = \dfrac{\partial u}{\partial y} + \dfrac{\partial v}{\partial x}$. At the wavy wall and at the flat wall, τ_{xy} becomes

$$\left.\begin{aligned}
\tau_w &= u'_0(1) + \epsilon \, [(u'_0(1) - \psi''_0(1) \cos(\lambda x) + \lambda \psi'_1 \sin(\lambda x)] \\
\tau_0 &= u'_0(0) + \epsilon \, [(\psi''_0(0) \sin(x) - \psi''_0(0) \cos(\lambda x)]
\end{aligned}\right\} \quad ...(3.1)$$

The heat transfer co-efficient N' is defind as

$$N' = - \, k \frac{\partial T}{\partial y}$$

which in non-dimensional form reduces to

$$N = - \, \frac{\partial N'}{k(T_1 - T_0)} = \frac{\partial \theta}{\partial y}$$

At the wavy wall and flat wall, (3.1) takes the form

$$N_w = \theta'_0(1) + \epsilon \, [(\theta''_0(1) + t'_0(1) \cos(\lambda x) - \lambda t'_0(1) \sin(\lambda x)]$$

$$N_0 = \theta'_0(0) + \epsilon \, [t'_0(0) \cos(\lambda x) - t'_1(0) \sin(\lambda x)]$$

4. DISCUSSION

We follow the convention that the fluid region in one half of the channel bounded by the plane wall denotes region I and the remaining half bounded by the wavy wall denotes region II. The profiles for zeroth order axial velocity (u_0) (Fig. 1) are asymmetric bell shaped curves with the maximum attained in the mid plane. The magnitude of the velocity u_0 is general at any point in the region I is large in compared to its magnitudes in region II. For an increase in the Hartmann number M, the velocity u_0 decays rapidly and the decay in the region II is less rapid compared to its decay in the region I. Also it can be observed that when the suction parameter reverse its sign from positive to negative, the velocity in the region I decreases while the velocity near the wavy wall increases. Keeping M fixed, for an increase in suction parameter $S(> 0)$, the axial velocity u_0 increase uniformly in the region I and decreases in the region II. This shows that an increase in the suction parameter $S(> 0)$, causes an increase in the flux in the region I along the channel while an increase in S through negative values causes an increase in flux in the region II.

The zeroth order temperature profiles are drawn in (Figs. 2, 3) for different values of S, α and P. In either case, the temperature grows rapidly in the region I till it attains its maximum in the other half of the channel near the mid plane and then rapidly falls towards the wavy boundary to attain its prescribed value. In case of water ($P = 0.71$) for positive values of suction parameter the growth of the
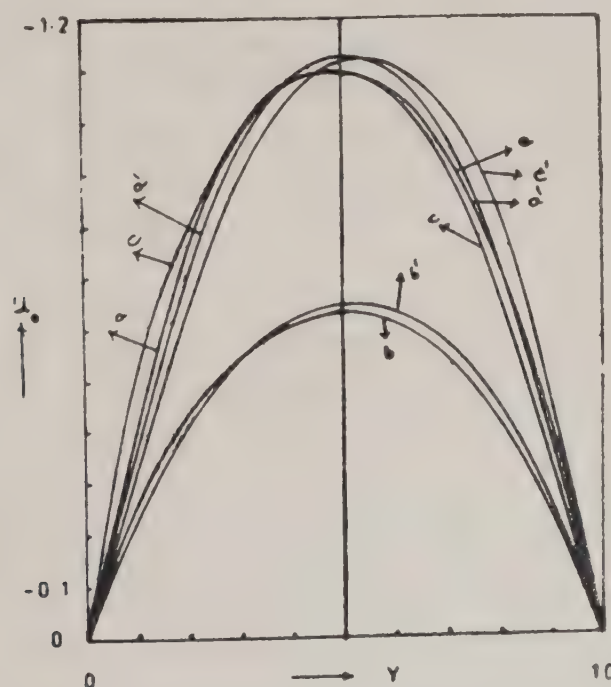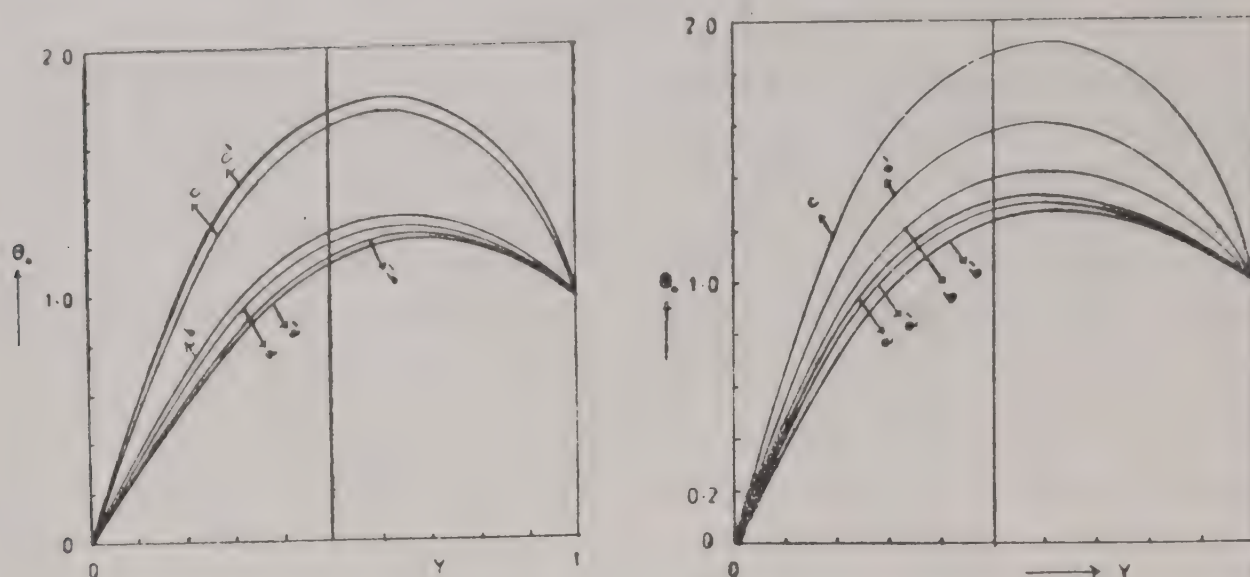

FIG. 1 : Profiles for the zeroth order velocity (u_0)

	a	a′	b	b′	c	c′
M	1	1	3	3	1	1
S	0.2	−0.2	0.2	−0.2	0.4	−0.4

FIG. 2   : Profiles for the zeroth order temperature (θ_0) with $P = 0.71$.

	a	a'	b	b'	c	c'
M	1	1	1	1	1	1
S	0.2	-0.2	0.4	-0.4	0.2	-0.2
α	5	5	5	5	10	10

FIG. 3   : Profiles for θ_0 with $P = 7$ Curves as in Fig. 2.

temperature near the plane wall is rapid in compared to its growth when S is nega-
tive.   This difference in the growth rates in much pronounced in case of air ($P = 7$).
For an increase in $S(> 0)$ the temperature increase uniformly although the region
while for an increase in $S(< 0)$ the temperature decrease throughout the channel.
Where as for fixed S (positive or negative) an increase in the heat parameter α in-
creases the temperature w. r. t. an increase in α is much large in compared to its
growth w.r.t. an increase in $S (> 0)$.

The perturbation in the axial velocity (u_1) (Figs. 4, 5) contributes to the growth
of the total axial velocity in region I and retards the same in the region II.   This
perturbation has a steep rise near the plane wall and a similar fall near the wavy
boundary.   The maximum in either region is attained very near the boundary.   In
the region I it rapidly falls from its maximum value to the lowest value near the
mid plane and once again rises in a narrow strip adjacent the mid plane before
getting reversed in the region II.   This u_1 contributes to the fluid acceleration along
the channel in the region I and retards the motion in the region II.   For all the
values of the governing parameters, the extreme of the total axial velocity occur
very near the boundaries the minimum value being near the wavy wall.   For an
increase in the wave length (λ) the growth in the magnitude of u_1 is almost pro-
portional to variation in λ.   When the suction (or injection) rate is maintained, an
increase in the Hartmann number decreases the positive perturbations in region I
and increases the reversed flow magnitudes in region II.   Thus the axial motion is
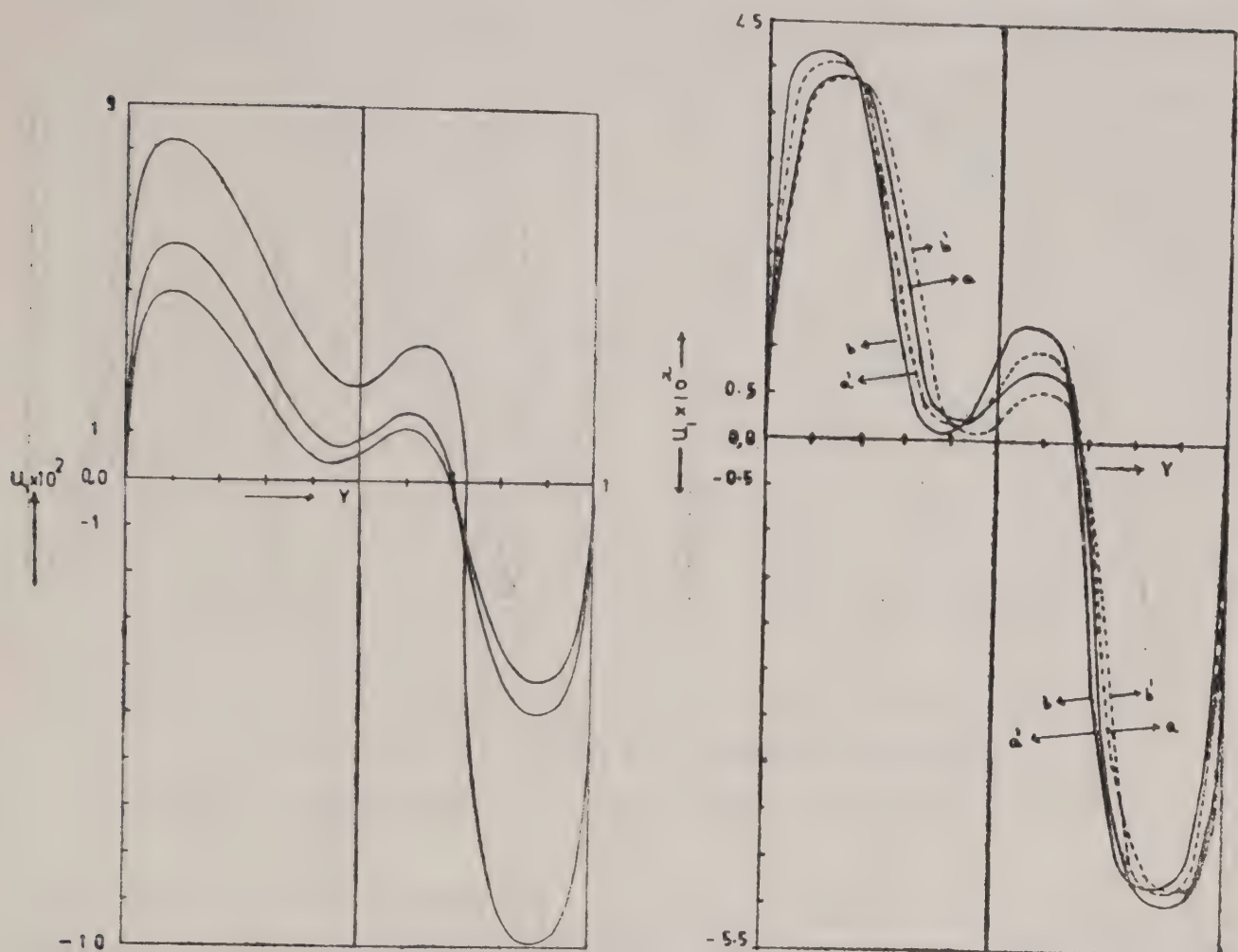
FIG. 4 : First order axial velocity (u_1) with $S = 0.2$, $\alpha = 5$

	a	b	c
M	1	1	1
λ	0.01	0.02	0.01

FIG. 5 : Variation of u_1 for different S with $M = 1$, $\lambda = 0.01$

	a	a'	b	b'
S	0.2	−0.2	0.4	−0.4

retarded in general due to an increase in M. For a fixed M, an increase in $S(> 0)$, decreases the magnitude of the perturbations in region I and increases their magnitude in region II away from the boundaries. Thus the total axial velocity retards in general, except in a narrow layer abetting the boundary, due to an increase in the suction parameter. When S increases through negative values the reversal is true and hence the axial velocity grows everywhere except near the boundary layers.

The profiles for the induced transverse velocity v_1 (Figs. 6, 7) are asymmetric bell shaped curves with peaks attaining in the region II and v_1 is negative, for all values of the governing parameters. For fixed S and λ, an increase in M reduces the transverse velocity everywhere in the fluid region except in a narrow layer near
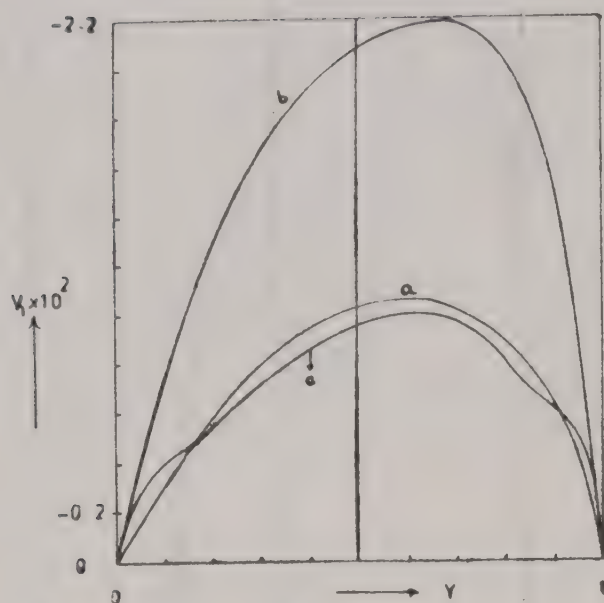
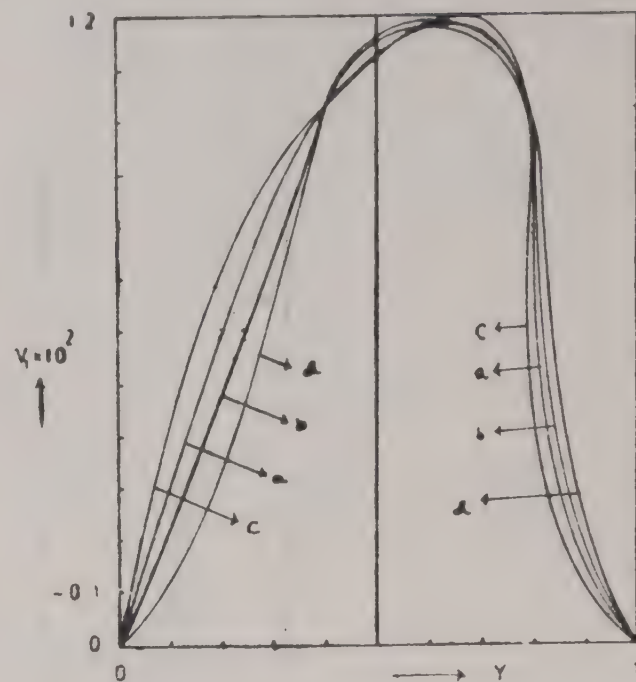FIG. 6   : Variation of V_1 with $S = 0.2$ and $\alpha = 5$ Curves in Fig. 4.

FIG. 7   : Variation of (V_1) with S for $M = 1$, $\lambda = 0.01$. Curves as in Fig. 5.

the boundaries. Thus the effect of wavyness is to induce reversed transverse velocity whose peak values are attained near in the mid plane in the region II. v_1 rises in proportion to rise in the wave length λ. Also w.r.t. an increase in $S(> 0)$ and for a fixed M, v_1 is found to experience a depression near the mid plane with rise and fall towards the boundaries. In fact it rises near the plane wall to a certain extent and decreases towards the mid plane and later rises in region II before decaying towards the wavy wall. When S is negative, the reversal is true with an elevation in the mid plane.

The perturbed temperature θ_1 depends on M, λ, P, S and α the profiles are drawn for variations in these governing parameters (Figs. 8, 9, 10, 11). It is to be noted that θ_1 is negative for all variations in the parameters. The profiles for the perturbed temperature θ_1 are also asymmetric bell shaped curves with their peaks on the mid plane except in the case of large values of heat source parameter α. Keeping λ, P, S, (> 0) and α fixed an increase in M, θ_1 increses although the region almost uniformly. For fixed M, S and λ, in case of water ($P = 0.71$) (Figs. 8, 9) θ_1 decreases in the region I and increases in the region II, for an increase in the heat source parameter α. In case of air ($P = 7$) (Figs. 10, 11) θ_1 decreases in a narrow layer near the plane wall and later increases although the region. This perturbed temperature θ_1 is found to decrease althrough the region for an increase in S either through positive or negative values for $P = 7$. However, in case of water it increase in region I to a certain extent and later decreases with an increase in $S(> 0)$. This behaviour gets reversed for an increase in $S(< 0)$. In general the effect of wavyness is to reduce the total temperature in the entire flow field. This
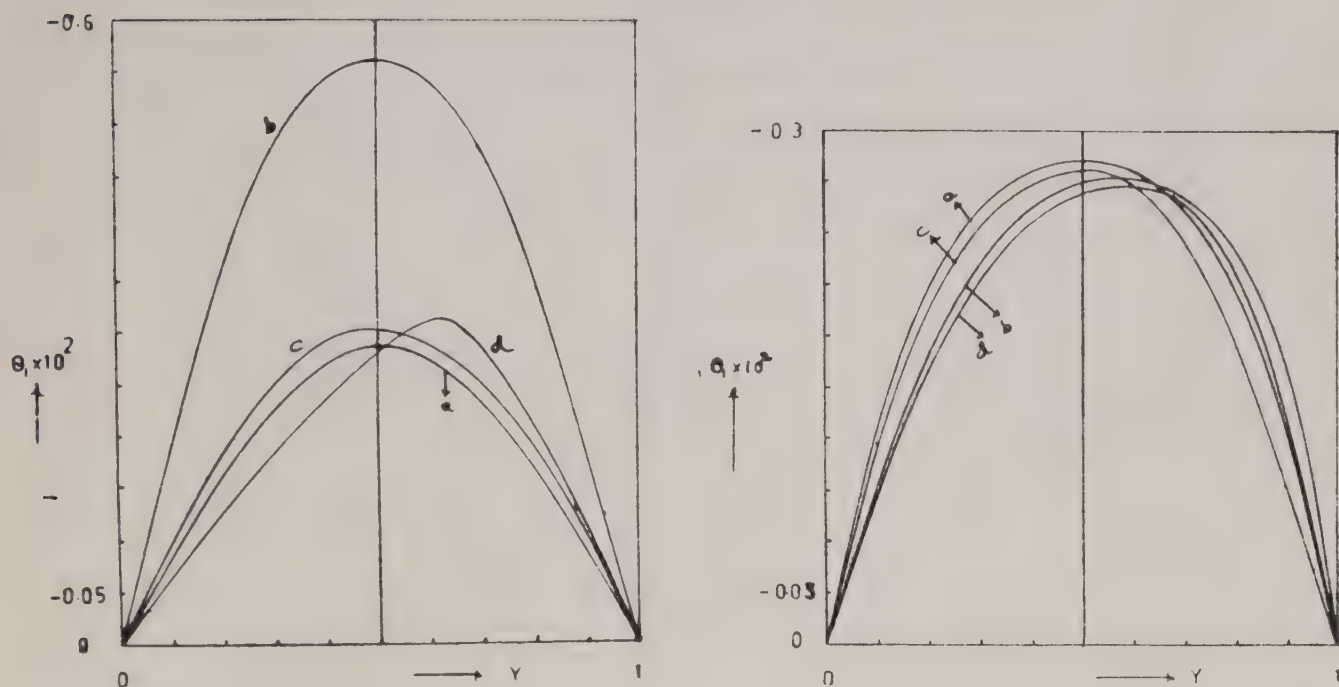
FIG. 8 : Profiles for the first order temperature distribution (θ_1) with $P = 0.71$.

	a	b	c	d
M	1	1	3	1
λ	0.01	0.02	0.01	0.01
α	5	5	5	10

FIG. 9 : Variation of θ_1 for different S for $M = 1$, $\lambda = 0.01$, $\alpha = 5$.

	a	b	c	d
S	0.2	—0.2	0.4	—0.4
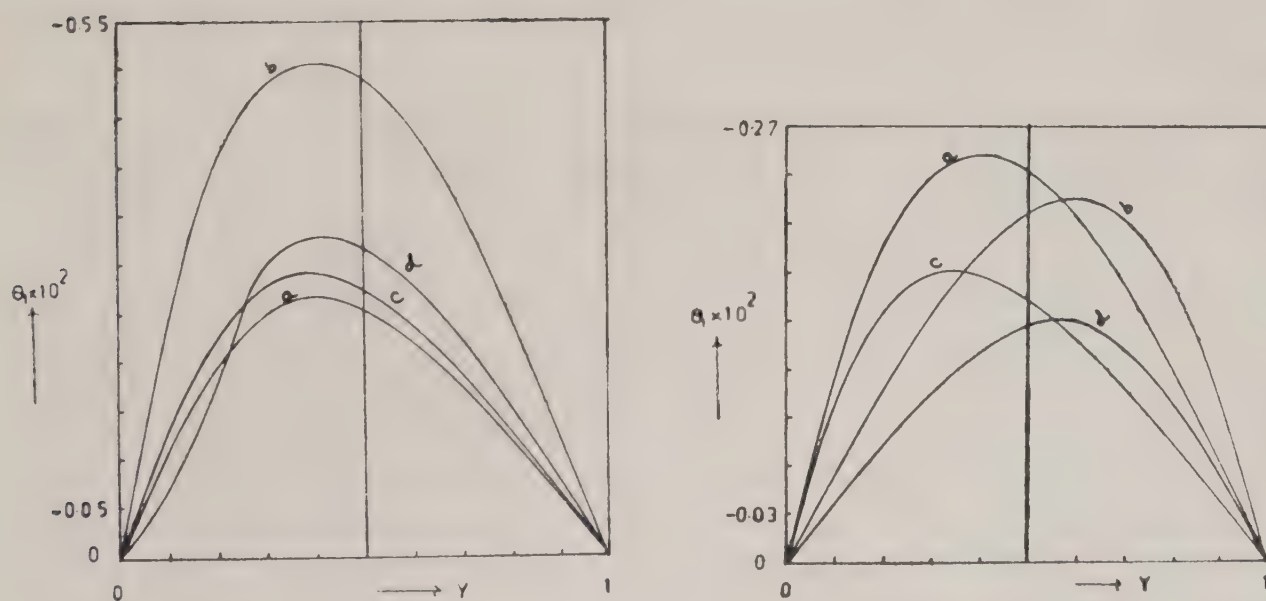
FIG. 10 : Variation of θ_1 when $S = 0.2$ and $P = 7$.
Curves as in Fig. 8.

FIG. 11 : Variation of θ_1 with S for $M = 1$, $\lambda = 0.01$, $\alpha = 5$.
Curves as in Fig. 9.

TABLE I

Skin friction at the plane gall (τ_1)

S \ τ_0	M = 1	M = 3
0.2	−0.8475	−0.6879
−0.2	−0.8114	−0.6659
0.4	−0.8655	−0.6990
−0.4	−0.7936	−0.6552

TABLE II

Skin friction at the wavy wall (τ_1)

S \ τ_1	M = 1	M = 3
0.2	0.09979	−0.07461
−0.2	0.1281	−0.05062
0.4	0.08578	−0.06884
−0.4	0.1423	−0.05676

reduction is more pronounced in the middle region of the channel compared to the boundary regions. A marginal increase in the magnetic parameter increases the decay of the total temperature to a little extent. Also this decay in the total temperature is found to vary for different variations in S, in both the cases of water and air.

The skin friction and the Nusselt number at plane and wavy walls are tabulated for variations in the governing parameters in Tables I–IV. On either of the boundaries the skin friction is found to decrease for an increase in M, keeping S fixed. But when M is fixed, an increase in $S(> 0)$ increases the skin friction at the plane wall while it is found to decrease for an increase in $S(< 0)$. At the wavy wall, the skin friction is found to decrease for an increase in $S(> 0)$ and increase for an increase in $S(< 0)$. Also it can be observed that the magnitude of the skin friction at the plane wall is very much large compared to its magnitude of the wavy wall. This shows that the effect of the wavyness is to reduce the skin friction on the boundaries to a very large extent. The Nusselt numbers at the boundaries almost do not vary for small variations in the magnetic parameter. The Nusselt numbers is found to decrease for an increase in $S(> 0)$ for all M, α and P. However, its behaviour w.r.t. an increase in $S(< 0)$ depends on α. A similar behaviour is found w.r.t. variations in λ. At the plane wall the Nusselt number (in case of water and air) increases with an increase in M or $S(> 0)$. But it decreases with an increase in $S(< 0)$ for all M and P.

Table III

Nusselt Number (N_0) at the plane wall

α / N_0	a		a'		b		b'		c		c'		d		d'	
	P=0.71	P=7	P=0.71	P=7	P=0.71	P=7	P=0.71	P=7	P=0.71	P=7	P=0.71	P=7	P=0.71	P=7	P=0.71	P=7
0	1.018	1.863	0.936	0.462	1.078	1.863	0.93	0.462	1.154	2.984	0.87	0.187	1.154	2.97	0.854	0.17
5	3.623	4.908	3.364	2.39	3.623	4.908	3.364	2.39	3.757	6.499	3.24	1.643	4.131	2.96	3.543	1.93
10	6.168	7.954	5.792	4.317	6.168	7.954	5.792	4.319	6.361	10.01	5.609	3.101	6.917	11.24	6.25	4.05

	a	a'	b	b'	c	c'	d	d'
M	1	1	3	3	1	1	1	1
S	0.2	-0.2	0.2	-0.2	0.4	-0.4	0.4	-0.4
λ	0.01	0.01	0.01	0.01	0.01	0.01	0.02	0.02

Table IV

Nusselt Number (N_1) at the wavy wall

α / N_1	a		a'		b		b'		c		c'		d		d'	
	P=0.71	P=7	P=0.71	P=7	P=0.71	P=7	P=0.71	P=7	P=0.71	P=7	P=0.71	P=7	P=0.71	P=7	P=0.71	P=7
0	0.93	0.454	1.074	1.872	0.93	0.4548	1.074	1.872	0.863	0.178	1.151	3.036	0.883	5.76	1.127	2.83
5	-1.563	-1.52	-1.542	-1.27	-1.563	-1.15	-1.497	-1.12	-1.569	-1.32	-1.526	-0.62	-1.389	-1.93	-1.056	-2.5
10	-4.056	-3.49	-4.157	-4.41	-4.056	-3.49	-4.157	-4.41	-4.001	-2.81	-4.202	-4.27	-3.651	-4.03	-3.243	-11.1

REFERENCES

1. T F Gaskell, The Earth's Mantle, New York, Academic Press (1967).
2. S K Runcorn, *Nature* **195** (1962) 1248.
3. D C Tozer, *Proc. R. Soc. A.* **58** (1966) p. 251.
4. H A Bethe, *Science* **161** (1968) 541.
5. R B Bird, *J. Soc. Plastic Engns.* **11** (7) (1955).
6. R M Inman, *Int. J. Heat Mass Transfer* **5** (1962) 1053.
7. S Ostrach, *NACA, TN.* (1952) 2863.
8. H F Poppendick, *Chem. Eng. Symp. Ser.* **50** (11) (1954) 93.
9. K S Sastri, Doctoral thesis, I.I.T. Kharagpur (1964).
10. P L Chambre, *Appl. Sci. Res., Sec.* A, **6** (1957) 393.
11. W N Gill, *J. Amer. Inst. Chem. Engns.* **8** (1962) 137.
12. R J Grosh and R D Cess, *Trans. Amer. Soc. Mech. Engns.* **80** (1958) 667.
13. S K Helmann, G Habeller, and H Babrov, *Trans. Amer. Soc., Mech., Engns.* **78** (1956) 1155.
14. G M Low, *J. Aero Sci.* **22** (1955) 329.
15. R E Gee and J B Lyon, *Industry Engg. Chem.* **49** (1957) 596.
16. J Modejskii, *Int. J. Heat mass Transfer* **6** (1963) 49.
17. I V Kragelskii, *Friction and Wear*, Butterworths, London (1965).
18. S G Lekeoudis, A M Nayfeh, and W S Saric, *Phys. fluids* **19** (1976) 514.
19. P N Sankar and U N Sinha, *J. Fluid Mech.* **77** (1976) 243.
20. K Vajravelu and K S Sastri, *J. Fluid Mech.* **86** (2) (1978) 365.
21. D R V Prasada Rao, D V Krishna and L Debnath, *Int. J. Engg. Sci. V.* (1983) 21.

APPENDIX

$$a_1 = (m \sinh m - S/2 \cosh m) \exp(-S/2)$$

$$a_2 = (m \cosh m - S/2 \sinh m) \exp(-S/2)$$

$$a_3 = \exp(-S/2 \cosh(m)) \qquad a_4 = \exp(-S/2 \sinh(m))$$

$$a_{47} = (a_3 - 1 + S/2)(a_2 - m)(a_1 + S/2)(a_4 - m)$$

$$A_1 = u'_0(1)(a_4 - m)/a_{47}$$

$$A_3 = -A_1$$

$$A_4 = u'_0(1)(a_3 - 1 + S/2)/a_{47}$$

$$A_2 = S/2\, A_3 - mA_4$$

$$a_5 = (m^2 + S^2/4) \qquad a_6 = mS$$

$$a_{42} = m^2 + S/2 \qquad a_7 = a_4, \exp(S/2)$$

$$a_8 = -m(1 + S/2)\exp(S/2)$$

$$a_9 = a_{42}A_3 - a_6A_4$$

$$a_{10} = a_{42}A_4 - a_6A_3$$

$$a_{11} = \frac{c}{M^2}\left(\frac{a_9}{\sinh m} - a_5A_3\right)$$

$$a_{12} = \frac{c}{M^2}\left(\frac{a_{10}}{\sinh m} - a_5A_4\right)$$

$$a_{43} = ca_5/M^2 \qquad\qquad a_{44} = ca_6/M^2$$

$$a_{45} = ca_7/M^2 \qquad\qquad a_{46} = ca_8/M^2$$

$$a_{13} = a_{43}A_1 \qquad\qquad a_{14} = a_{43}A_2$$

$$a_{15} = a_{44}A_1 \qquad\qquad a_{16} = a_{44}A_2$$

$$a_{17} = a_{44}A_3 \qquad\qquad a_{18} = a_{44}A_4$$

$$a_{19} = \frac{c}{M^2}\left(a_8A_4 - a_7A_3 - \frac{a_9\,(\exp S/2)}{\sinh m}\right)$$

$$a_{20} = a_{45}A_4 \qquad\qquad a_{21} = a_{45}A_1$$

$$a_{22} = a_{45}A_2 \qquad\qquad a_{23} = a_{46}A_3$$

$$a_{24} = a_{46}A_1 \qquad\qquad a_{25} = a_{46}A_2$$

$$b_8 = m - S/2 \qquad\qquad b_9 = m + S/2$$

$$a_{26} = (m+1)S/2$$

$$a_{27} = (m^2\cosh m - mS\sinh m + S^2/4\cosh m)\exp(-S/2)$$

$$a_{28} = (m^2\sinh m - mS\cosh m + S^2/4\sinh m)\exp(-S/2)$$

$$c_2 = (1 + a_{40})(\exp(-PS) - 1)$$

$$c_4 = \theta_0'(1)/(1 - \exp(-SP))$$

$$a_{41} = PS\,c_2 \qquad\qquad a_{31} = cc_4/M^2$$

$$a_{29} = a_{31}/\sinh m \qquad\qquad a_{30} = a_{29}\exp(S/2)$$

$$a_{32} = a_{41}A_1 \qquad\qquad a_{33} = a_{40}A_1$$

$$a_{34} = a_{41}A_2 \qquad\qquad a_{35} = a_{40}A_2$$

$$a_{36} = a_{41}A_3 \qquad\qquad a_{37} = a_{40}A_3$$

$$a_{38} = a_{41}A_4 \qquad\qquad a_{39} = a_{40}A_4$$

$$b_1 = 2b_8^2(b_8^2 + Sb_8 - M^2)$$

$$b_2 = 2b_9^2(b_9^2 - Sb_9 - M^2)$$

$$b_3 = 16b_8^2(4b_8^2 + 2Sb_8 - M^2)$$

$$b_4 = 16b_9^2(4b_9^2 - 2Sb_9 - M^2)$$

$$b_5 = \frac{4b_8^2 + 3Sb_8 - 2M^2}{b_8(b_8^2 + Sb_8 - M^2)}$$

$$b_6 = \frac{4b_9^2 - 3Sb_9 - 2M^2}{b_9(b_9^2 - Sb_9 - M^2)}$$

$$b_7 = 8S^2M^2$$

$$d_1 = [\exp(-m)((a_{14} - a_{16}) b_5 + (a_{15} - a_{13})) - c(a_9 - a_{10})/M^2$$
$$+ (a_{21} + a_{24}) - (a_{22} + a_{25})b_5]b_1$$

$$d_2 = [\exp(-m)(a_{14} - a_{16}) - a_{25} - a_{22})]/b_1$$

$$d_3 = [\exp(m)(a_{13} + a_{15} + (a_{14} + a_{16}) b_6) - c(a_9 + a_{10})/M^2$$
$$- a_{31} + a_{24} + (a_{25} - a_{22})b_5]/b_2$$

$$d_4 = [\exp(m)(a_{14} + a_{16}) + (a_{25} - a_{23})]/b_2$$

$$d_8 = (c\, a_{10} \exp(S/2)/M^2 \sinh m + a_{20} + a_{23})$$

$$d_5 = [\exp(-m)(a_{11} + a_{12} + a_{17} + a_{18}) - a_{19} - d_8)]/b_3$$

$$d_6 = [\exp(m)(a_{11} - a_{12} - a_{17} + a_{18}) - a_{19} - d_8]/b_4$$

$$d_7 = [\cosh(m)(a_{12} - a_{17}) + \sinh m\, (a_{11} + a_{18}) - d_8]/b_7$$

$$\phi_1(y) = (d_1 - d_2 y) \exp(b_8 y) + (d_3 + d_4 y) \exp(-b_9 y)$$
$$+ d_5 \exp(2b_8 y) - d_6 \exp(-2b_9 y) + d_7 \exp(-Sy)$$

$$B_3 = c_5/a_{47}$$

$$B_4 = (\phi_1'(0) - \phi_1'(1) - B_3(a_1 + S/2))/(a_2 - m)$$

$$B_1 = -\phi(0) - B_3$$

$$B_2 = -a_1 B_3 - a_2 B_4 - \phi_1'(1)$$

$$c_5 = (\phi_1'(1) - \phi_1'(0))(a_4 - m) - (a_2 - m)(\phi_1(1) - \phi(0) - \phi'(0))$$

$$d_{11} = (a_{29} \exp(-m) - (a_{20} + a_{38} + a_{36}))/b_{13}$$

$$d_{12} = (a_{29} \exp(m) - (a_{30} + a_{38} - a_{36}))/b_{14}$$

$$d_{13} = (a_{29} \exp(-m) - (a_{30} - a_{39} - a_{37}))/b_{15}$$

$$d_{14} = (a_{29} \exp(m) - (a_{30} - a_{39} + a_{37}))/b_{16}$$

$$d_{15} = a_{31} + a_{33}$$

$$d_{16} = (a_{31} - a_{32}) PS - a_{34}/P^3 S^3$$

$$d_{17} = a_{34}/2PS$$

$$d_{18} = a_{34}/(PS)^2$$

$$d_{19} = a_{35}$$

$$\phi_2(y) = P[d_{11} \exp(b_8 - PS) y - d_{12} \exp(-(b_9 PS) y)$$
$$- a_{13} \exp(b_8 y) + (d_{17} y^2 + d_{18} y - d_{16}) \exp(-PS)y$$
$$+ d_{13} \exp(-b_9 y) - d_{15} - a_{25} y]$$

$$D_2 = (\phi_2(0) - \phi_2(1))/(\exp(-PS) - 1)$$

$$D_1 = -D_2 - \phi_2(0)$$

DEFLECTION OF A CLAMPED ECCENTRIC CIRCULAR RING PLATE AND AN INFINITE PLATE WITH TWO CLAMPED CIRCULAR HOLES

Ibrahim H El-Sirafy *and* Nawal A El-Boray

Department of Mathematics, Faculty of Science, Alexandria University, Egypt

We consider the theorem of Levi-Civita for biharmonic functions to obtain exact expression for the deflection of an eccentric circular ring plate and for an infinite plate with two circular holes subject to a concentrated couple or concentrated force at any point and clamped on the edges. The form of the deflection of the plate bent by a concentrated couple is obtained by two different methods. The problems of a concentric circular ring plate and a half-plane plate with a circular hole follow as special cases.

1. Introduction

Problems dealing with the solution of the biharmonic equation for doubly-connected regions of isotropic homogenous plates have been investigated by many authors[1-4]. Bassali and Gorgui[5] discussed the problem of the bending of a circular annular plate under a concentrated load or a concentrated couple acting at any point of the plate under various edge conditions. The problem of determining the complex potentials and deflection of a circular ring plate with free edges and loaded normally by any system of concentrated forces or concentrated couples in equilibrium was considered by Bassali[6].

In this work we consider the theorem of Levi-Civita for biharmonic functions to obtain expressions for the deflections of the following doubly-connected regions of plates with clamped edges :

(a) An eccentric circular ring plate bent by a concentrated couple at a given point.

(b) An eccentric circular ring plate bent by a concentrated force at a given point.

(c) An infinite plate with two circular holes subject to a concentrated couple at a given point.

(d) An infinite plate with two circular holes subject to a concentrated force at a given point.

The form of the diflection of the plate bent by a concentrated couple is obtained by two different methods. The problems of a concentric circular ring plate and a half-plane plate with a circular hole follow as special cases.

2. Mapping Function

The bilinear tranformation[5]

$$z = \frac{\zeta - a}{a\zeta - 1},$$
         ... (2.1)

where

$$a = [1 + \xi_1 \xi_2 + \sqrt{(1 - \xi_1^2)(1 - \xi_2^2)}]/(\xi_1 + \xi_2)$$
    ...(2.2)

conformally maps the eccentric circular ring plate bounded by the outer unit circle $|\zeta| = 1$ and the inner eccentric circle

$$|\zeta - \tfrac{1}{2}(\xi_1 + \xi_2)| = \tfrac{1}{2}(\xi_1 - \xi_2)$$
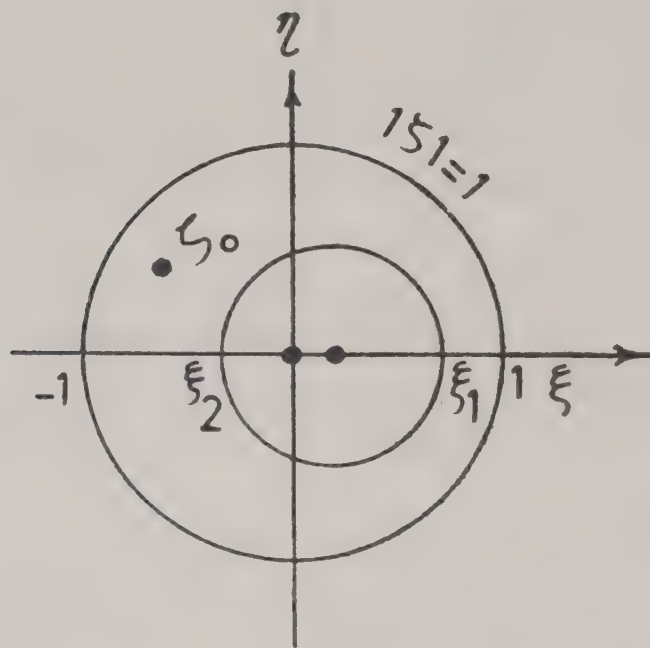
on the region of a concentric circular ring $1 < |z| < c$. Also the infinite plate with the two holes $|\zeta| = 1$ and $|\zeta - \tfrac{1}{2}(\xi_1 + \xi_2)| = \tfrac{1}{2}(\xi_1 - \xi_2)$ is conformally mapped on the region of a concentric circular ring $1 > |z| > c$, by the same tranformation (see Figs. 1–3).

For the eccentric circular ring plate c is given by

$$c = [1 - \xi_1 \xi_2 + \sqrt{(1 - \xi_1^2)(1 - \xi_2^2)}]/(\xi_1 - \xi_2),$$

$$|\xi_2| < \xi_1 < 1 < c, \, a > 1,$$
    ...(2.3)

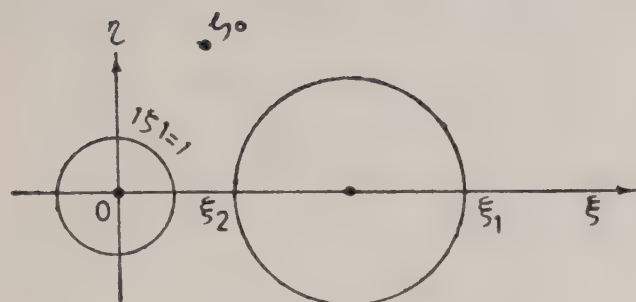and for the infinite plate with the two circular holes c is given by

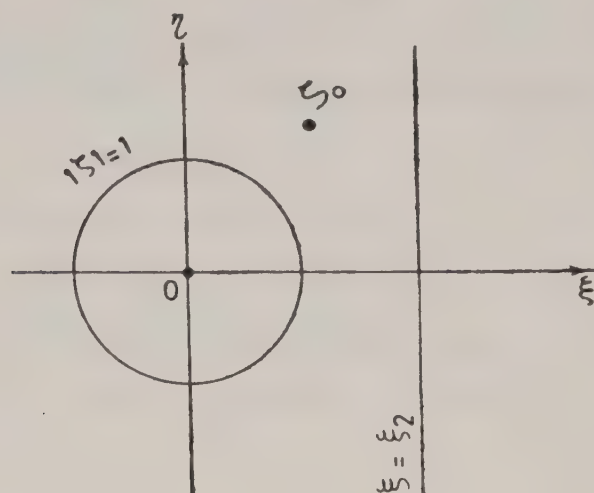$$\xi_1 = 0.7, \quad \xi_2 = -0.3,$$

$$a = 3.678, \quad c = 1.891$$

ζ-plane

Fig. 1

ζ-plane

$\xi_1 = 6$, $\xi_2 = 2$, $a = 2.906$, $c = 0.188$

FIG. 2

ζ-plane

$\xi_1 \longrightarrow \infty$, $\xi_2 = 2$, $a = 3.732$, $c = .268$.

FIG. 3

$$c = [\xi_1 \xi_2 - 1 - \sqrt{(\xi_1^2 - 1)(\xi_2^2 - 1)}]/(\xi_1 - \xi_2),$$

$$c < a \, c < 1 < \xi_2 < a < \xi_1. \qquad \qquad \qquad ...(2.4)$$

In the limitting case $a \to \infty$ ($| \xi_2 | = \xi_1$), (2.3) gives $c = \xi_1^{-1}$ and (2.1) becomes $z = -\zeta^{-1}$ which maps the region of the concentric ring of the inner edge $| \zeta | = \xi_1$ and the outer edge $| \zeta | = 1$ on to the region of the concentric ring $| z | = 1$ and $| z | = \xi_1^{-1}$. Also when $\xi_1 \to \infty$, $a \to \xi_2 + (\xi_2^2 - 1)^{1/2} = c^{-1}$ and the half-plane plate Re $\zeta \leqslant \xi_2$ with a hole $| \zeta | = 1$ is mapped on the region of the concentric ring $1 > | z | > c$ by means of (2.1).

3. METHOD OF SOLUTION

Let $\zeta = \xi + i \eta = \rho \, e^{i\psi}$ be the complex variable of any point in the middle plane of the eccentric circular ring plate or the infinite plate with the two circular holes. The deflection $W(\xi, \eta)$, measured positively upwards, satisfies the biharmonic equation

$$\left(\frac{\partial^2}{\partial \xi^2} + \frac{\partial^2}{\partial \eta^2} \right)^2 W(\xi, \eta) = 16 \, \frac{\partial^4 W}{\partial \zeta^2 \partial \bar{\zeta}^2} = 0 \qquad \qquad ...(3.1)$$

at all points except at the load point ζ_0.

The function $W(\xi, \eta)$ can be put in the form

$$W(\xi, \eta) = w_0(\xi, \eta) + w_*(\xi, \eta), \qquad \qquad ...(3.2)$$

where w_* is a regular function over the plate and the singular part $w_0(\xi, \eta)$ at the point ζ_0 may be written as [6]

$$w_0(\xi, \eta) = 4k \, G \, \text{Re} \; \{\bar{\lambda} \, (\zeta - \zeta_0)\} \, \ln | \zeta - \zeta_0 | \qquad \qquad ...(3.3)$$

or

$$w_0(\xi, \eta) = -2k \, F \, | \zeta - \zeta_0 |^2 \ln | \zeta - \zeta_0 | \qquad \qquad ...(3.4)$$

according as the plate is subject to a concentrated couple G or a concentrated normal force F respectively. Here the plane of the couple G is taken to be normal to the plate and making an angle ϕ with the x-axis, where

$$\lambda = e^{i\phi}, \qquad \qquad \qquad \qquad \qquad \qquad ...(3.5)$$

$$k = \frac{1}{16 \pi D} \qquad \qquad \qquad \qquad \qquad ...(3.6)$$

and D is the flexural rigidity of the plate.

Using the following theorem or Levi-Civita[1] :

Let

$$w_*(\xi, \eta) = w(x, y)/ \mid az - 1 \mid^2. \qquad \qquad ...(3.7)$$

If w is biharmonic in the ζ-plane, then $w(x, y)$ is biharmonic in the z-plane, where the relation between ζ and z is given by (2.1).

The general solution of the biharmonic equation

$$\nabla^2\nabla^2 w(x, y) = 0$$

may be represented by[4]

$$\frac{w}{2k} = \text{Re} \left\{ \sum_{n=1}^{\infty} \left[\left(r^2 P_n + \frac{1}{n} Q_n \right) z^n + \left(r^2 P_{-n} - \frac{1}{n} Q_{-n} \right) z^{-n} \right] \right.$$

$$\left. + r^2 P_0 + H_0 + (r^2 P + Q_0) \ln r + H(2 \ln r - 1) z \right\}, \qquad ...(3.8)$$

where H, H_0, P_n and $Q_n(n = 0, \pm 1, \pm 2, ...)$ are, in general, complex constants to be determined, P_0, Q_0 may be taken as real and Q_1 may be taken as zero.

From (3.2) and (3.7) the deflection W is furnished by

$$W(\xi, \eta) = w_0(\xi, \eta) + \frac{w(x, y)}{|az - 1|^2}. \qquad \qquad ...(3.9)$$

Thus the boundary conditions

$$W = 0, \frac{\partial W}{\partial \zeta} = 0$$

along any point of the circular edges of the plate lead to

$$w(x, y) = - \mid az - 1 \mid^2 w_0, \qquad \qquad ...(3.10)$$

$$\frac{\partial w}{\partial \bar{z}} = - a (az - 1) w_0 - (a^2 - 1) \frac{az - 1}{a\bar{z} - 1} \frac{\partial w_0}{\partial \zeta}. \qquad ...(3.11)$$

Using (3.3) and (3.4), the expressions on the right side of (3.10) and (3.11) in the cases (a) and (c) can be written in the following forms

$$- 4k(a^2 - 1) G \text{ Re} \left\{ \tau(1 - az) (\bar{z} - \bar{z}_0) \right\} \ln \left| \frac{(a^2 - 1)(z - z_0)}{(1 - az_0)(1 - az)} \right| \quad ...(3.12)$$

$$- k(a^2 - 1) \, G \left\{ \lambda \, \frac{az - 1}{a\bar{z} - 1} + \lambda \, \frac{\tau(z - z_0)}{\tau(\bar{z} - \bar{z}_0)} \right.$$

$$\left. + 2 \left[(\tau + \bar{\tau})(1 - az) - \bar{\lambda} \right] \ln \left| \frac{(a^2 - 1)(z - z_0)}{(1 - az_0)(1 - az)} \right| \right\}, \qquad \qquad ...(3.13)$$

while for the problems (b) and (d) the corresponding expressions become

$$2k(a^2 - 1)^2 \, F \, | \, \mu \, |^2 \, | \, z - z_0 \, |^2 \ln \left| \frac{(a^2 - 1)(z - z_0)}{(1 - az_0)(1 - az)} \right|, \qquad ...(3.14)$$

$$- k(a^2 - 1)^2 \, F \left[\mu \, \frac{z - z_0}{a\bar{z} - 1} - 2 \, | \, \mu \, |^2 \, (z - z_0) \ln \right.$$

$$\left. \left| \frac{(a^2 - 1)(z - z_0)}{(1 - az_0)(1 - az)} \right| \right], \qquad \qquad ...(3.15)$$

where

$$\mu = (1 - az_0)^{-1}, \ \tau = \bar{\lambda} \, \mu \ \text{and} \ z_0 = \frac{\zeta_0 - a}{a\zeta_0 - 1}. \qquad ...(3.16)$$

Substituting from (3.8) in the boundary conditions and (3.11) and expanding the expressions of (3.12)−(3.15) we get

$$2 \, \text{Re} \left\{ \sum_{n=2}^{\infty} (c_j^2 \, P_n + n^{-1} \, Q_n) z^n + (c_j^2 \, P_{-n} - n^{-1} \, Q_{-n}) z^{-n} \right.$$

$$+ (c_j^2 \, P_1 - H + 2H \ln c_j) \, z + c_j^2 \, P_0 + H_0 + (c_j^2 \, P + Q_0) \ln c_j$$

$$\left. + (c_j^2 \, P_{-1} - Q_{-1}) z^{-1} \right\} = - \left[\alpha_0^{(j)} + \sum_{n=1}^{\infty} (\alpha_n^{(j)} \, z^n + \bar{\alpha}_n^{(j)} \, c_j^{2n} \, z^{-n}) \right]$$

$$...(3.17)$$

and

$$z \left\{ \sum_{n=-\infty}^{\infty} \left[P_n z^n + (n+1) \, \bar{P}_n \, c_j^{2n} \, z^{-n} + \bar{Q}_n \, c_j^{2n-2} z^{-n} \right] + H \, \bar{c}_j^2 \, z \right.$$

$$\left. + (1 + 2 \ln c_j) \, P + 2\bar{H} \ln c_j \, z^{-1} \right\} = v_1^{(j)} + \sum_{n=1}^{\infty} \left[v_{n+1}^{(j)} \, z^{-n} + u_{n-1}^{(j)} \, z^n \right].$$

$$...(3.18)$$

Here

$$c_j = \begin{cases} 1, \ j = 1 \ \text{on} \ | \, z \, | = 1 \\ c, \ j = 2 \ \text{on} \ | \, z \, | = c \end{cases},$$

$$n\alpha_n^{(j)} = c_j^2 \, u_n^{(j)} - c_j^{2-2n} \, \bar{v}_n^{(j)}, \ n = 1, 2, 3, \, ...$$

and the values of $\alpha_0^{(j)}$, $v_n^{(j)}$ and $u_n^{(j)}$ are given by:

case (a)

$$\alpha_0^{(j)} = -2(a^2 - 1) \, G \operatorname{Re} \left\{ (ac_j^2 + z_0) \, \tau \gamma^{(j)} + v \sigma_1^{(j)} \right\},$$

$$v_1^{(j)} = -(a^2 - 1) \, G \left[\bar{v} \gamma^{(j)} + (\tau + \bar{\tau}) \, a \sigma_1^{(j)} + \frac{\lambda \tau}{\bar{z}_0^2 \, \bar{\tau}} \, (r_0^2 - 1) \, \delta_j \right],$$

$$v_{n+1}^{(j)} = -(a^2 - 1) \, G \, (\tau + \bar{\tau}) \, a \, \sigma_{n+1}^{(j)} - \bar{v} \sigma_n^{(j)} + \frac{\lambda \tau}{\bar{z}_0^{n+2} \bar{\tau}} (r_0^2 - 1) \, \delta_j,$$

$$n = 1, 2, 3, \ldots$$

$$u_0^{(j)} = -2 \, (a^2 - 1) \, G \operatorname{Re} \left\{ \bar{\tau} \, \left(-a \gamma^{(j)} + \frac{r_0^2 - 1}{z_0} \, \delta_j \right) \right\}$$

and

$$c_j^{2n} \, u_{n-1}^{(j)} = -(a^2 - 1) \, G \left[(\tau + \bar{\tau}) \, a \, c_j^2 \, \bar{\sigma}_{n-1}^{(j)} - \bar{v} \, \bar{\sigma}_n^{(j)} + \lambda \, (a^2 c_j^2 - 1) \, a^{-n} \right.$$

$$\left. + \lambda \, \frac{\tau}{\bar{\tau}} \, \bar{z}_0^{n-2} \, (c^2 - r_0^2) \, \delta_j^* \right], \quad n = 2, 3, \ldots$$

where

$$v = \tau + \bar{\tau} - \lambda, \quad r_0 = | z_0 |,$$

$$\gamma^{(1)} = 2 \ln \left| \frac{(a^2 - 1) z_0}{(1 - az_0) \, a} \right| = \gamma^{(2)} + 2 \ln r_0,$$

$$\sigma_n^{(1)} = n^{-1} \, (\bar{z}_0^{-n} - a^{-n}), \quad \sigma_n^{(2)} = n^{-1} \, (z_0^n - a^{-n}),$$

$$\delta_j = \left\{ \begin{array}{ll} 1 & j = 1 \\ 0 & j = 2 \end{array} \right. \text{and } \delta_j^* = \left\{ \begin{array}{ll} 0 & j = 1 \\ 1 & j = 2 \end{array} \right.$$

case (b)

$$\alpha_0^{(j)} = -(a^2 - 1)^2 \, F \, | \mu |^2 \operatorname{Re} \{ (c_j^2 + r_0^2) \, \gamma^{(j)} + 2 \sigma_1^{(j)} \, \bar{z}_0 \},$$

$$v_1^{(j)} = (-a^2 - 1)^2 \, F \, | \mu |^2 \, [\sigma_1^{(j)} + \gamma^{(j)} \, z_0],$$

$$v_{n+1}^{(j)} = -(a^2 - 1)^2 \, F \, | \mu |^2 \, [\sigma_{n+1}^{(j)} - \sigma_n^{(j)} \, z_0], \quad n = 1, 2, \ldots$$

$$u_0^{(j)} = (a^2 - 1)^2 \, F \, | \mu |^2 \, [\gamma^{(j)} + (1 - r_0^2) \, \delta_j]$$

and

$$c_j^{2n} \, u_{n-1}^{(j)} = -(a^2 - 1)^2 \, F \, \mu \, [(ac_j^2 - z_0) a^{-n} + \bar{\mu} \{ c_j^2 \, \bar{\sigma}_{n-1}^{(j)} - z_0 \, \bar{\sigma}_n^{(j)} \}],$$

$$n = 2, 3, \ldots$$

case (c)

$$\alpha_0^{(j)} = -2 \, (a^2 - 1) \, G \operatorname{Re} \{ (ac_j^2 + \bar{z}_0) \, \bar{\tau} \gamma_*^{(j)} + \bar{v} c_j^2 \, \omega_1^{(j)} \},$$

$$v_1^{(j)} = - (a^2 - 1) G [\bar{v}\gamma_*^{(j)} + ac_j^2 (\tau + \bar{\tau}) \varpi_1^{(j)}$$

$$+ \lambda \left\{ (1 - a^2 c^2) + \frac{\tau}{\bar{\tau} z_0^2} (r_0^2 - c^2) \right\} \delta_j^*],$$

$$c_j^{-2n} v_{n+1}^{(j)} = - (a^2 - 1) G [- \bar{v} \varpi_n^{(j)} + ac_j^2 (\tau + \bar{\tau}) \varpi_{n+1}^{(j)}$$

$$+ \lambda \left\{ (1 - a^2 c^2) a^n + \frac{\tau}{\bar{\tau} z_0^{n+2}} (r_0^2 - c^2) \right\} \delta_j^*],$$

$$u_0^{(j)} = (a^2 - 1) G [a (\tau + \bar{\tau}) \gamma_*^{(j)} + (r_0^{-2} - a^2) (\tau z_0 + \bar{\tau} \bar{z}_0) \delta_j^*],$$

$$u_{n-1}^{(j)} = - (a^2 - 1) G [- \bar{v} \omega_n^{(j)} + a (\tau + \bar{\tau}) \omega_{n-1}^{(j)}$$

$$+ \lambda \left\{ (a^2 - 1) a^{-n} + \frac{\tau}{\bar{\tau}} (1 - r_0^2) \bar{z}_0^{n-2} \right\} \delta_j],$$

where

$$\gamma_*^{(1)} = 2 \ln \left| \frac{a^2 - 1}{(1 - a z_0) a} \right|, \gamma_*^{(2)} = 2 \ln \left| \frac{(a^2 - 1) r_0}{1 - a z_0} \right|,$$

$$\omega_n^{(1)} = n^{-1} (\bar{z}_0^n - a^{-n}) \text{ and } \omega_n^{(2)} = n^{-1} (z_0^{-n} - a^n).$$

case (d)

$$\alpha_0^{(j)} = - (a^2 - 1)^2 F | \mu |^2 \text{ Re } \{ (c_j^2 + r_0^2) \gamma_*^{(j)} + 2\omega_1^{(j)} z_0 c_j^2 \},$$

$$v_1^{(j)} = - (a^2 - 1)^2 F [| \mu |^2 c_j^2 \varpi_1^{(j)} + | \mu |^2 \gamma_*^{(j)} z_0 + \mu (z_0 - ac^2) \delta_j^*]$$

$$c_j^{-2n} v_{n+1}^{(j)} = - (a^2 - 1)^2 F [| \mu |^2 \{ c_j^2 \varpi_{n+1}^{(j)} - \varpi_n^{(j)} z_0 \} + \mu (z_0 - ac^2) a^n \delta_j^*],$$

$$n = 1, 2, \ldots$$

$$u_0^{(j)} = (a^2 - 1)^2 F [| \mu |^2 \gamma_*^{(j)} + (\mu + \mu) \delta_j^*],$$

$$u_{n-1}^{(j)} = - (a^2 - 1)^2 F [| \mu |^2 (\omega_{n-1}^{(j)} - \omega_n^{(j)} z_0) + \mu (a - z_0) a^{-n} \delta_j],$$

$$n = 2, 3, \ldots .$$

Equating the coefficients of powers of z in each of the formulae (3.17) and (3.18) we obtain the following simultaneous equations

$$c_j^2 P_n + c_j^{2-2n} \bar{P}_{-n} + \frac{1}{n} (Q_n - \bar{c}_j^{2n} \bar{Q}_{-n}) = - \alpha_n^{(j)}, \quad n = 2, 3, 4, \ldots$$

$$c_j^2 P_1 + H (2 \ln c_j - 1) + \bar{P}_{-1} - c_j^{-2} \bar{Q}_{-1} = - \alpha_1^{(j)},$$

$$2 c_j^2 P_0 + 2H_0 + 2 (c^2 P + Q_0) \ln c_j = - \alpha_0^{(j)},$$

$$P_{-n} + (1 + n) c_j^{2n} \bar{P}_n + c_j^{2n-2} \bar{Q}_n = v_n^{(j)}, \quad n = 2, 3, 4, \ldots$$

$$P_n + (1 - n) c_j^{-2n} \bar{P}_{-n} + c_j^{-2n-2} \bar{Q}_{-n} = u_n^{(j)}, \quad n = 2, 3, 4, \ldots$$

$$P_{-1} + 2 c_j^2 \bar{P}_1 + 2\bar{H} \ln c_j = v_1^{(j)},$$

$$P_1 + c_j^{-4} \bar{Q}_{-1} + c_j^{-2} H = u_1^{(j)},$$

$$2P_0 + c_j^{-2} Q_0 + (1 + 2 \ln c_j) P = u_0^{(j)}.$$

Solving this consistent system of equations leads to

$$P_n = J_n \left[t_{1-n} \left\{ u_n^{(2)} c^{3+2n} - u_n^{(1)} \right\} + (n - 1) t_1 \left\{ \bar{v}_n^{(2)} c^{2-2n} - \bar{v}_n^{(1)} \right\} \right],$$

$$\bar{P}_{-n} = J_n \left[t_{1+n} \left\{ \bar{v}_n^{(2)} c^{2-2n} - \bar{v}_n^{(1)} \right\} - (n + 1) t_1 \left\{ u_n^{(2)} c^{3+2n} - u_n^{(1)} \right\} \right],$$

$$Q_n = c^2 J_n \left[c^2 t_{-n-1} \left\{ \bar{v}_n^{(2)} - v_n^{(1)} \right\} + (n^2 - 1) t_1 \left\{ \bar{v}_n^{(1)} - c^{-2n} \bar{v}_n^{(2)} \right\} \right.$$
$$\left. - (n + 1) t_{-n} \left\{ u_n^{(2)} c^{3+2n} - u_n^{(1)} \right\} \right],$$

$$\bar{Q}_{-n} = c^2 J_n \left[c^2 t_{n-1} \left\{ u_n^{(2)} - u_n^{(1)} \right\} + (n^2 - 1) t_1 \left\{ u_n^{(1)} - c^{2n} u_n^{(2)} \right\} \right.$$
$$\left. - (n - 1) t_n \left\{ c^{2-2n} \bar{v}_n^{(2)} - v_n^{(1)} \right\} \right], n = 2, 3, 4, \ldots;$$

$$2P_1 = (c^2 - 1)^{-1} \Delta_1 \left[(c^2 - 1) \left\{ \bar{v}_1^{(2)} - \bar{v}_1^{(1)} \right\} - 2 \ln c \left\{ c^4 u_1^{(2)} - u_1^{(1)} \right\} \right],$$

$$P_{-1} = v_1^{(1)} - 2\bar{P}_1,$$

$$Q_{-1} = \frac{c^4}{c^4 - 1} \left\{ \bar{u}_1^{(1)} - \bar{u}_1^{(2)} \right\} - \frac{c^2}{c^2 + 1} \bar{H},$$

$$2H = \Delta_1 \left[2 \left\{ c^4 u_1^{(2)} - u_1^{(1)} \right\} - (c^2 + 1) \left\{ \bar{v}_1^{(2)} - \bar{v}_1^{(1)} \right\} \right],$$

$$- 2H_0 = \alpha_0^{(1)} + 2 P_0,$$

$$2P_0 = \Delta_0 \left[2 \left\{ \alpha_0^{(2)} + \alpha_0^{(1)} - u_0^{(1)} + c^2 u_0^{(2)} \right\} c^2 \ln c \right.$$
$$+ 2 \left\{ u^{(1)} - u_0^{(2)} \right\} c^2 \ln c + (c^2 - 1) \left\{ \alpha_0^{(2)} - \alpha_0^{(1)} \right\} + 4c^2 u_0^{(1)} \ln^2 c \right],$$

$$P = \Delta_0 \left[(c^2 - 1) \left\{ \alpha_0^{(1)} - \alpha_0^{(2)} + u_0^{(1)} - c^2 u_0^{(2)} \right\} \right.$$
$$\left. - 2c^2 \left\{ u_0^{(1)} - u_0^{(2)} \right\} \ln c \right],$$

$$Q_0 = \Delta_0 \left[2c^2 \left\{ \alpha_0^{(1)} - \alpha_0^{(2)} + u_0^{(1)} - c^2 u_0^{(2)} \right\} + c^2 (c^2 - 1) \left\{ u_0^{(2)} - u_0^{(1)} \right\} \right],$$

where

$$J_n^{-1} = t_{1-n} t_{1+n} + (n^2 - 1) t_1^2, \quad t_n = c^{2n} - 1;$$

$$\Delta_1^{-1} = c^2 - 1 - (c^2 + 1) \ln c,$$

and

$$\Delta_0^{-1} = 4c^2 \ln^2 c - (c^2 - 1)^2.$$

The deflection of the clamped concentric circular ring plate $\xi_1 < |\zeta| < 1$ subject to the concentrated couple G or the concentrated force F at the arbitrary point ζ_0 can be obtained as the limiting case of the formula (3.9) when a tends to infinity,

$$W(\xi, \eta) = w_0(\xi, \eta) + 2k \, \mathrm{Re} \left\{ \sum_{n=1}^{\infty} \left[\left(P_n^* + \frac{\rho^2}{n} Q_n^* \right) \zeta^{-n} \right. \right.$$

$$+ \left(P_{-n}^* - \frac{\rho^2}{n} Q_{-n}^* \right) \zeta^n \right] + P_0^* + H_0^* \rho^2 - (P^* + Q_0^* \rho^2) \ln \rho$$

$$\left. + (2 \ln \rho + 1) \bar{H}^* \zeta \right\}, \qquad \qquad ...(3.19)$$

where

$$P_n^* = J_n \left[\tilde{t}_{n-1} (u_n' - u_n'' \xi_1^{-2n-2}) + (n-1) \tilde{t}_{-1} (\bar{v}_n' - \bar{v}_n'' \xi_1^{2n-2}) \right],$$

$$\bar{P}_{-n}^* = J_n \left[\tilde{t}_{-n-1} (\bar{v}_n' - \bar{v}_n'' \xi_1^{2n-2}) + (n+1) \tilde{t}_{-1} (u_n'' \xi_1^{-2n-2} - u_n') \right],$$

$$Q_n^* = \xi_1^{-2} J_n \left[\xi_1^{-2} \tilde{t}_{n+1} (\bar{v}_n' - \bar{v}_n'') + (n^2 - 1) \tilde{t}_{-1} (\bar{v}_n'' \xi_1^{2n} - \bar{v}_n') \right.$$

$$\left. + (n+1) \tilde{t}_n (u_n'' \xi_1^{-2n-2} - u_n') \right],$$

$$\bar{Q}_{-n}^* = \xi_1^{-2} J_n \left[\xi_1^{-2} \tilde{t}_{1-n} (u_n' - u_n'') + (1 - n^2) \tilde{t}_{-1} (u_n' - u_n'' \xi_1^{-2n}) \right.$$

$$\left. + (n-1) \tilde{t}_{-n} (\bar{v}_n' - \bar{v}_n'' \xi_1^{2n-n}) \right], \quad n = 2, 3, 4,....$$

$$2P_1^* = (\xi_1^{-2} - 1)^{-1} \Delta_1 \left[(\xi_1^{-2} - 1) (\bar{v}_1'' - \bar{v}_1) + 2 (u_1'' \xi_1^{-4} - u_1') \ln \xi_1 \right],$$

$$P_{-1}^* = \bar{v}_1' - 2\bar{P}_1^*,$$

$$Q_{-1}^* = (1 - \xi_1^4)^{-1} (\bar{u}_1' - \bar{u}_1'') + (1 + \xi_1^2)^{-1} \bar{H}^*,$$

$$2H^* = \Delta_1 \left[2 (u_1' - u_1'' \, \xi_1^{-4}) - (1 + \xi_1^{-2}) (\bar{v}_1' - \bar{v}_1'') \right],$$

$$H_0^* = - \tfrac{1}{2} \alpha_0' - P_0^*,$$

$$2P_0^* = \Delta_0 \left[- 2(\alpha_0'' - \alpha_0' - u_0' + \xi_1^{-2} u_0'') \, \xi_1^{-3} \ln \xi_1 + 2(u_0'' - u_0') \xi_1^{-2} \ln \xi_1 \right.$$

$$\left. + (\xi_1^{-2} - 1) (\alpha_0'' - \alpha_0') + 4 \, \xi_1^{-2} \, u_0' \, \ln^2 \xi_1 \right],$$

$$P^* = \Delta_0 \left[(\xi_1^{-2} - 1)(\alpha_0' - \alpha_0'' + u_0' - \xi_1^{-2} u_0'') + 2 \, \xi_1^{-2} (u_0' - u_0'') \ln \xi_1 \right],$$

$$Q_0^* = \Delta_0 \left[2 \, \xi_1^{-2} (\alpha_0' - \alpha_0'' + u_0' - \xi_1^{-2} u_0'') + \xi_1^{-2}(\xi_1^{-2} - 1) (u_0' - u_0'') \right],$$

$$\Delta_0^{-1} = 4 \, \xi_1^{-2} \ln^2 \xi_1 - (\xi_1^{-2} - 1)^2, \quad \Delta_1^{-1} = \xi_1^{-2} - 1 + (\xi_1^{-2} + 1) \ln \xi_1,$$

$$J_n^{-1} = \tilde{t}_{n-1} \, \tilde{t}_{-n-1} + (n^2 - 1) \, \tilde{t}_1^2,$$

$$\tilde{t}_n = 1 - \xi_1^{2n} \text{ and } n = 2, 3, 4,\dots.$$

For the case of the concentrated couple the values of

$$\alpha_0' \, , \ \alpha_0'' \, , \ v_n' \, , \ v_n'' \, , \ u_n' \text{ and } u_n'' \text{ become}$$

$$\alpha_0' = - 2G \, \mathrm{Re} \, (\lambda \, \bar{\zeta}_0) \, , \ \alpha_0'' = - 2G \, \mathrm{Re} \left\{ 2 \, \xi_1^{-2} \, \zeta_0 \bar{\lambda} \ln \rho_0 + \lambda \bar{\zeta}_0^{-1} \right\},$$

$$v_1' = - G \left[\bar{\lambda} (2 \, \rho_0^2 - 1) + \lambda \bar{\zeta}_0^2 \right], \ v_1'' = - G \, (\bar{\lambda} + \lambda \bar{\zeta}_0 \, \zeta_0^{-1} + 2 \, \bar{\lambda} \ln \rho_0),$$

$$\bar{v}_n' = - G \left[\lambda \left(\frac{n+1}{n} \, \rho_0^2 - \frac{n}{n-1} \right) \zeta_0^{n-1} + \frac{\lambda}{n} \, \zeta_0^{n+1} \right],$$

$$\bar{v}_n'' = - \frac{1}{n} G \left[\frac{\lambda}{n-1} \, \bar{\zeta}_0^{1-n} - \bar{\lambda} \zeta_0 \, \bar{\zeta}_0^{-n} \right],$$

$$u_0' = 0 \, , \ u_0'' = 4G \ln \rho_0 \, \mathrm{Re} \, (\lambda \, \bar{\zeta}_0),$$

$$u_1' = - G \left[\lambda(\rho_0^2 - 1) + \tfrac{1}{2} \bar{\lambda} \bar{\zeta}_0^2 \right], \ u_1'' = - \tfrac{1}{2} G \, \bar{\lambda} \, \xi_1^4 \, \bar{\zeta}_0^{-2},$$

$$u_n' = - \frac{1}{n} G \left(\lambda \bar{\zeta}_0 \, \zeta_0^n + \frac{\bar{\lambda}}{n+1} \, \zeta_0^{n+1} \right),$$

$$u_n'' = - \xi_1^{2n+2} G \left[\frac{1}{n} \left(\lambda \bar{\zeta}_0 + \bar{\lambda} \zeta_0 \right) \xi_1^{-2} \bar{\zeta}_0^{-n} - \frac{\lambda}{n+1} \, \bar{\zeta}_0^{-n-1} \right.$$

$$\left. - \bar{\lambda}(\xi_1^{-2} - \rho_0^{-2}) \zeta_0 \, \bar{\zeta}_0^n \right] n \quad 2, 3, 4\dots.$$

while for the case of the concentrated force we have

$$\alpha'_0 = -2F\rho_0^2 , \; \alpha''_0 = -2F[\, 1 + (1 + \xi_1^{-2} \, \rho_0^2) \ln \rho_0],$$

$$v'_1 = -F\rho_0^2 \, \bar{\zeta}_0 , \; v''_1 = -F\rho_0^2 \, (1 + 2 \ln \rho_0) \, \zeta_0^{-1},$$

$$v'_n = -F\left(\frac{\rho_0^2}{n} - \frac{1}{n-1} \right) \bar{\zeta}_0^n, \; v''_n = \frac{F\rho_0^2 \, \zeta_0^{-n}}{n(n-1)},$$

$$u'_0 = -(1 - \rho_0^2) \, F, \; u''_0 = 2F\rho_0^2 \ln \rho_0,$$

$$u'_1 = -F(\tfrac{1}{2} \rho_0^2 \zeta_0 - \bar{\zeta}_0), \; u''_1 = \tfrac{1}{2}F\xi_1^{-4} \bar{\zeta}_0^{-1},$$

$$u'_n = -\frac{F\rho_0^2 \, \zeta_0^n}{n(n+1)}, \; u''_n = -F\xi_1^{2n+2} \left(\frac{1}{n} \, \xi_1^{-2} \, \rho_0^2 - \frac{1}{n+1} \right) \bar{\zeta}_0^{-n},$$

$$n = 2, 3, 4, \ldots.$$

It is easily seen that the expression (3.19) for the deflection due to a concentrated force F at arbitrary point ξ_0 is in agreement with formula (54) for the case of a concentric circular ring plate $\xi_1 < \rho < 1$ with clamped edges[5].

Letting ξ_1 tend to infinity and $a = c^{-1} = \xi_2 + \sqrt{\xi_2^2 - 1}$ in the values of $\alpha_0^{(j)}$, $v_n^{(j)}$ and $u_n^{(j)}$ appearing in the cases (c) and (d), we obtain the deflection of the plate $\mathrm{Re}\,\zeta \leqslant \xi_2$ with the circular hole $|\,\zeta\,| = 1$ when the plate is subject to a concentrated couple or a concentrated force at an arbitrary point ζ_0 and clamped on the edges

$$\mathrm{Re}\,\zeta = \xi_2, \; |\,\zeta\,| = 1.$$

It was shown in [2], for the case $G_2 = 0$, that the deflection W_G in the case of a concentrated couple G can be obtained in terms of the deflection W_F in the case of a concentrated force F by the relation

$$G^{-1} W_G = F^{-1} \Lambda W_F, \qquad\qquad \ldots(3.20)$$

where

$$\Lambda = \lambda \frac{\partial}{\partial \zeta_0} + \bar{\lambda} \frac{\partial}{\partial \zeta_0}.$$

This relation can be easily checked to hold true in our case using the relations

$$G^{-1} \left[\alpha_0^{(j)} \right]_{(a)} = F^{-1} \Lambda \left[\alpha_0^{(j)} \right]_{(b)} + 2(a^2 - 1) \, \mathrm{Re} \left\{ (z_0 + ac_j^2) \, \tau \right\},$$

$$G^{-1} \left[v_1^{(j)} \right]_{(a)} = F^{-1} \Lambda \left[v_1^{(j)} \right]_{(b)} + (a^2 - 1) \, \bar{v},$$

$$G^{-1} \left[v_n^{(j)} \right]_{(a)} = F^{-1} \Lambda \left[v_n^{(j)} \right]_{(b)} , \; n = 2, 3, 4, \ldots,$$

$$G^{-1} \left[u_0^{(j)} \right]_{(a)} = F^{-1} \Lambda \left[u_0^{(j)} \right]_{(b)} - 2(a^2 - 1) \, a \, \mathrm{Re}\,\tau,$$

$$G^{-1} \left[u_n^{(j)} \right]_{(a)} = F^{-1} \Lambda \left[u_n^{(j)} \right]_{(b)} \; n = 1, 2, 3, \ldots,$$

Similar expressions can be written connecting cases (c) and (d).   In these relations f_a denotes the value of f for the case (a).   This provide an alternate method to find the deflections in the cases (a) and (c) once those for cases (b) and (d).

REFERENCES

1. S M Belonosov, *Akad. Nauk. SSSR, Novosibirsk,*, (1962).
2. S G Mikhlin, *Integral Equations*, Oxford, U K (1964).
3. N I Muskhelishvili, *Some Basic Problems of the Mathematical Theory of Elasticity*, Moscow, (1949).
4. S Timoshenko, *Theory of plantes and Shells*, New York, (1940).
5. W A Bassali and M A Gorgui, *Proc. Camb. Phyl. Soc.* (1960) 75.
6. W A Bassali, J. *Mech. Phys. Solids* **8** (1960) 123.

GRAVITY WAVES DUE TO A PERIODIC SURFACE PRESSURE ON A SLOPING BEACH

KRIPASINDHU CHAUDHURI

Department of Mathematics, Jadavpur University, Calcutta-700 032

The linearised two-dimensional problem of water waves due to a surface pressure of the form $f(x) \exp(i\omega t) H(t)$, $H(t) =$ Heaviside unit function, has been explicity solved for a beach with a slope angle of $\pi/2q$, q being any integer. A general method of finding the complete asymptotic expansion of the surface displacement over different possible ranges of large times and distances is illustrated with $q = 2$. For a certain class of pressure distributions, the gradual attainment of a steady state is shown to take place throughout the fluid. The average rate of transmission of energy by the pressure system to the fluid is calculated in the steady state. Some characteristics of the wave motion are described.

Keywords : Water Waves; Gravity Waves; Steady State; Surface Pressure

INTRODUCTION

THE linearised initial—value problem of gravity waves due to an oscillating surface pressure in water of infinite depth, and also of constant finite dipth has been discussed by Stoker[1], Wehausen and Latione[2], Miles[3] and Chaudhuri[4].

The corresponding problem for water with a sloping bottom has been discussed by Shen[5] with less details regarding the asymptotic behaviour of freesurface elevation.

The theory of formation of standing wave-systems on sloping beaches is also given by Stoker[1].

In this paper, the linearized two-dimensional problem of water waves due to a surface pressure of the form $f(x) \exp(i\omega t) H(t)$, $H(t) =$ Heaviside Unit function, has been explicitly solved for a beach of slope angle $\pi/2q$, q being any positive integer. This involves the solution of a Fredholm integral equation of the first kind by means of a generalised Fourier trasformation. The author[3] outlined a solution of this type of integral equation for positve integral values of q. Subsequently, Sen[6] presented a general proof involving seperate treatment of the cases q odd, $q = 0$ (mod 4) and $q = 2$ mod (4). Later Morris[7,8] gave a brief and unified proof of the result which holds for all integral values of q. Griffel and Morris[9] further extended the method of the author[3] to beaches of arbitrary angle $v(0 < v \leqslant \pi)$ and to a more general initial-value problem that considered by the author. All these subsequent works were mainly concerned with the solution of the integral equation and none of them deal with the asymptotic behaviour of the wave pattern. In the present work, a method of finding the complete asymptotic expansion of the surface displacement over different possible ranges of large time and distances is illustrated for $q = 2$. For a certain class of

pressure distribuions, the gradual attainment of steady state is shown to take place throughout the fluid. The average rate of energy by the pressure system is calculated in the steady state and it is shown that no energy is transmitted through the fluid in the steady at certain frequencies. This phenomenon of zero energy radiation has also been noted by Sretenskii[10], Morris[7,8] and Stoker[1]. In fact, the limit of the present results as the surface-pressure tends to a delta-function coincides with the results of Sretenskii[10] in the case where the source lies on the free surface.

The paper ends with a brief description of the characteristics of the wave motion.

PROBLEM

A heavy homogeneous inviscid liquid lies between two half planes namely the free surface $y = 0$ $(x \geqslant 0)$ and a rigid sloping beach $y = x \tan \beta$, $(y \leqslant 0)$, in its state of rest at time $t = 0$. Surface waves are generated in the liquid by the continued application of a surface pressure $p_0(x, t)$ of the form

$$p_0(x, t) = f(x) \exp (i\omega t), (y = 0, t > 0). \qquad \qquad ...(1)$$

Here the function $f(x)$ is assumed to possess Fourier and Laplace transforms or a generalised Fourier transform in x as defined by (9) and (14) below.

The equations of motion together with boundary and initial conditions are

$$\varphi_{xx} + \varphi_{yy} = 0, \qquad \qquad ...(2)$$

$$g\rho\eta = -f(x) \exp (i\omega t) + (\rho\varphi_t)_{y=0}, \qquad \qquad ...(3)$$

$$(\varphi_{tt} + g\varphi_y)_{y=0} = \frac{i\omega}{\rho} f(x) \exp (i\omega t), \qquad \qquad ...(4)$$

$$\frac{\partial\varphi}{\partial\eta} = 0 \text{ on the beach}, \qquad \qquad ...(5)$$

$$\varphi(x, 0; 0+) = 0, \eta(x; 0+) = 0. \qquad \qquad ...(6)$$

Here $\varphi(x, y; t)$ is the velocity potential, $\eta(x, t)$ the surface elevation above the undisturbed surfrce, ρ the density of the liquid, and g the acceleration due to gravity.

The boundedness conditions require that φ and its space-derivatives should tend to zero at infinity for fixed time t and that φ has at most a logarithmic infinity at the origin.

The problem is to find a solution $\varphi(x, y; t)$ of (2) which satisfies the equations (4), (5), (6) and the boundedness conditions mentioned above. The surface elevation η is then found out by (3).

SOLUTION

We assume a solution for φ of the form

$$\varphi = \int_0^\infty A(m, t) \, \Phi(x, y, m) \, dm$$

such that

$$\Phi_y = m\Phi \text{ on } y = 0 \qquad \qquad \text{...(7)}$$

and $\Phi(x, y, m)$ is harmonic within the region of flow, and it also satisfies the equations (5) together with boundedness conditions consistent with those mentioned above. Equation (4) now gives

$$A_{tt} + gmA = i\omega\rho^{-1}\bar{f}(m) \exp(i\omega t). \qquad \qquad \text{...(8)}$$

Here $\bar{f}(m)$ is determined from the following Fredholm integral equation of the first kind with the kernal $B\Phi(x, 0, m)$, B being a non-zero constant :

$$Bf(x) = \int_0^\infty \bar{f}(m). \ B\Phi(x, 0, m) \ dm. \qquad \qquad \text{...(9)}$$

The solution of (8) subjected to (6) is

$$A = (\rho\sigma)^{-1} \bar{f}(m) \{\sin \sigma t + i\omega \int_0^t \exp(i\omega s) \sin \sigma(t - s) \ ds\} \qquad \text{...(10)}$$

where $\sigma^2 = gm.$ \qquad \qquad \text{...(11)}

For a beach of slope angle $v = \dfrac{\pi}{2q}$, $q = 1, 2, 3, \ldots$ it is know that[2]

$$\Phi(x, y, m) = \text{Re} \sum_{k=0}^{q-1} C_k \exp\left[i\left\{\frac{k\pi}{2} - \frac{\pi(q-1)}{4}\right.\right.$$

$$\left.\left. - m(x + iy) \exp\left(\frac{-i\pi k}{q}\right)\right\}\right] \qquad \qquad \text{...(12)}$$

where $C_0 = 1, C_k = \cot v \cot 2v \ \ldots\ldots \cot kv.$ \qquad \qquad \text{...(13)}

For integral values of q, it has been proved that the kernel of (9) is a Fourier kernel because it satisfies the functional equation 15

$$k(s) k(1 - s) = 1 \ \ldots\ldots\ldots(f)$$

for $B = (2/\pi)^{1/2}$, $k(s)$ being the Mellin transform of the function $k(x) = B\Phi(x, 0, 1)$. Consequently, (9) represents a generalised Fourier transformation and its inversion leads to

$$\bar{f}(m) \int_0^\infty B^2\Phi(\alpha, 0, m) f(\alpha) \ d\alpha. \qquad \qquad \text{...(14)}$$

Therefore

$$\varphi = 2(\pi\rho)^{-1} \int_0^\infty \phi(\alpha, 0, m) f(\alpha) \ d\alpha \int_0^\infty \phi(x, y, m) \sigma^{-1}\{\sin \sigma^{-t}$$

$$+ i\omega \int_0^t e^{i\omega s} \sin \sigma(t - s) \ ds\} \ dm \qquad \qquad \text{...(15)}$$

and

$$g\rho\eta = -f(x)\, e^{i\omega t} + \left(\frac{2}{\pi}\right) \lim_{y\to 0} - \frac{\partial}{\partial t} \int_0^\infty \phi(\alpha, 0, m)\, f(\alpha)\, d\alpha$$

$$\times \int_0^\infty \phi(x, y, m)\, \sigma^{-1} \{\sin \sigma t + i\omega \int_0^t e^{i\omega s} \sin \sigma(t - s)\, ds\}\, dm. \quad \ldots(16)$$

ASYMPTOTIC EVALUATION OF THE WAVE INTEGRAL

For simplicity, we restrict the discussion to the case $q = 2$ and assume $p_0(x, t)$ non-zero over only a finite strip

$$0 \leqslant a \leqslant x \leqslant b.$$

Then

$$g\rho\eta = -f(x)\, e^{i\omega t} + \left(\frac{1}{\pi}\right) \lim_{y\to 0} - \frac{\partial}{\partial t} \int_{m=0}^\infty \int_{\alpha=a}^b \sigma^{-1}\{\sin \sigma t$$

$$+ i\omega \int_0^t e^{i\omega s} \sin \sigma(t - s)\, ds\} \{e^{my}(\cos mx - \sin mx)$$

$$+ e^{-mx}(\cos my + \sin my)\} (e^{-m\alpha} + \cos m\alpha - \sin m\alpha)\, f(\alpha)\, d\alpha\, dn.$$
$$\ldots(16A)$$

We transform (16A) to the form (19) below for $x > b$. This form shows clearly the possible large dimensionless parameters and their ranges in question, yields at once the complete asymptotic expressions in which the presence of algebraic and exponential parts are exhibited, and the whole process simultaneously justifies itself. For $x > b$, we have

$$\pi\rho g\eta = \frac{\partial}{\partial t} \int_a^b f(\alpha)\, d\alpha \int_0^\infty \sigma^{-1}\{\sin \sigma t + i\omega \int_0^t e^{i\omega s} \sin \sigma(t - s)\, ds\}$$

$$\times [\cos mx_1 - \sin mx_2 + 1/\sqrt{2}\, e^{i(mx_3 0 + \pi/4)}$$

$$+ 1/\sqrt{2}\, e^{-i(mx_4 + \pi/4)} + \sum_2^4 e^{-mxn}]\, dm. \quad \ldots(17)$$

The notations used are

$$x_1 = x - \alpha,\ x_2 = x + \alpha,\ x_3 = x + i\alpha,\ x_4 = x - i\alpha,$$

$$A_2 = 1,\ A_3 = 2^{-1/2} \exp(-i\pi/4),\ A_4 = 2^{-1/2} \exp(i\pi/4). \quad \ldots(18A)$$

We also define

$$r = \frac{x}{b},\ \tau = g\frac{t^2}{4x},\ \tau' = \omega t,\ \Theta = \frac{\tau'}{2\tau} = \frac{2\omega x}{gt},$$

$$(r_n, \tau_n, \Theta_n) = (t, \tau, \Theta)_{x-x_n}\ \ C(x) \pm iS(x) = CiS(x),\ CiS(x). \quad \ldots(18B)$$

In what follows, these functions $C(x)$ and $S(x)$ will denote Fresnel's integrals of, in general, complex arguments having a positive real part, and may be supposed as given by their expressions[4] in terms of Kummer's confluent hypergeometric series $_1F_1(\frac{1}{2}; \frac{3}{2}; -x \exp(\pm i\pi/2))$. Further square roots of complex numbers are defined in such a way that their values are real and positive when z is real and positive.

In (17), we first carry out the integration with respect to m, —part of it under the s-integral sign, by the help of the following results :

(ia) $\int\limits_0^\infty \sigma^{-1} e^{-mx} \sin \sigma t \, dm = (2\omega/g\Theta) \, _1F_1(1; \frac{3}{2}; -\tau)$, Re $x > 0$;

(ib) $\int\limits_0^\infty \sigma^{-1} e^{+imx} \sin \sigma t \, dm = i(2\pi/gbn)^{1/2} e^{-i\tau} CiS(\tau)$, $x > 0$

In the resulting s-integrals, we replace the special functions above by their following representations :

(iia) $_1F_1(1; \frac{3}{2}; -z) = \frac{1}{2}iz^{-1/2} [\int\limits_0^\infty \lambda^{-1/2} \exp(-\lambda - 2i\sqrt{\lambda z}) \, d\lambda - \pi e^{-z}]$

(iib) $e^{-iz} CiS(z) = 2^{-1/2} \exp i(\pi/4 - z) - i(2/\pi)^{1/2} \int\limits_0^\infty$

$$\exp(-i\lambda^2 - 2\lambda\sqrt{z}) \, d\lambda,$$

where Re $z \geqslant 0$. On completion of the s-integrations some of which are taken under the s-integral sign, the expression for η finally transforms to

$$\pi g^2 \rho \eta = \frac{\partial}{\partial t} \int\limits_a^b f(\alpha) \, d\alpha \left[2\omega \sum\limits_2^4 A_n(R_n + I_n) \right.$$

$$\left. - (U + V + W + I) \right] \qquad \text{...(19)}$$

where

$$R_n = (\theta_n)^{-1} \, _1F_1(1; \frac{3}{2}; -\tau_n) + (\pi\tau_n)^{1/2} \{(1 + i\Theta_n) \exp(-\tau_n)$$

$$\times \, _1F_1(1; \frac{3}{2}; \tau_n(1 + i\theta_n)^2 - i\theta_n \exp(i\tau') \, _1F_1(1; \frac{3}{2}; -\tau_n\theta_n^2)\},$$

$$I_n = \frac{1}{2} i \exp(i\tau') \int\limits_0^\infty [\lambda + (\lambda\tau_n)^{1/2} \theta_n]^{-1} \exp(-\lambda) \, d\lambda - i \int\limits_0^\infty (\lambda + \tau_n^{1/2}\theta_n)^{-1}$$

$$\times \exp(-\lambda^2 - 2i\lambda\tau_n^{1/2}) \, d\lambda,$$

$$U = (\pi g)^{1/2} \left\{ \left(\frac{x_1}{2}\right)^{-1/2} (\cos \tau_1 S(\tau_1) - \sin \tau_1 c(\tau_1)) + \left(\frac{x_2}{2}\right)^{-1/2} \right.$$

$$\times (\cos \tau_2 C(\tau_2) + \sin \tau_2 S(\tau_2)) + x_3^{-1/2} \exp(-i(\tau_3 + \pi/4) (iS(\tau_3))$$

$$\left. + x_4^{-1/2} \exp i(\tau_4 + \pi/4) CiS(\tau_4)\right\},$$

$$V = i\pi\omega \exp{(i\tau')} [i(\cos\tau_1\theta_1^2 - \sin\tau_2\theta_2^2) + 2^{-1/2} i\{\exp - (i)(\tau_1\theta_1^2 + \pi/4))$$

$$\times sgn\,(1 - \theta_2)\,CiS\tau_2(1 - \theta_2)^2 + \exp{(i)}(\tau_2\theta_2^2 + \pi/4))\,CiS\tau_2$$

$$\times (1 + \theta_2)^2\} + \exp{(i\tau_3\theta_3^2)}\,\{CiS\tau_3(1 + \theta_3)^2 - 2^{-1/2}\exp{(-i\pi/4\}}$$

$$+ \exp{(-i\tau_4\theta_4^2)}\,\{sgn(1 - Re\,\theta_4)\,CiS\tau_4(1 - \theta_4)^2 + 2^{-1/2}$$

$$\times \exp{(i\pi/4)\}],$$

$$W = i\omega\,e^{i\tau'}[\cos\beta\,Ci\beta + \sin\beta\,si\,\beta) + (\cos\nu\,\sin\nu - \sin\nu\,ci\,\nu)$$

$$+ 2^{-1/2} \exp{(i(\tau_3\theta_3^2 + \pi/4))}\,Ei(-i\tau_3\theta_3^2)^{\beta=\tau_1\theta_1^2} + 2^{-1/2}$$

$$\times \exp{(-i(\tau_4\theta_4^2 + \pi/4))}\,Ei(i\tau_4\theta_4^2)],$$

$$I = 2^{1/2}i\omega[2^{1/2} \int_0^\infty (\lambda + i\tau_1^{1/2}\theta_1)^{-1} \cos\lambda^2 \exp{(-2\lambda\tau_1^{1/2})}\,d\lambda$$

$$+ 2^{1/2} \int_0^\infty (\lambda + i\tau_2^{1/2}\theta_2)^{-1} \sin\lambda^2 \exp{(-2\lambda\tau_2^{1/2})}\,d\lambda$$

$$+ \exp{(+i\pi/4)} \int_0^\infty (\lambda + i\tau_3^{1/2}\theta_3)^{-1} \exp{(-2\lambda\tau_3^{1/2})} - i\lambda^2 {}_d\lambda$$

$$+ \exp{(-i\pi/4)} \int_0^\infty (\lambda + i\tau_4^{1/2}\theta_4)^{-1} \exp{(-2\lambda\tau_4^{1/2} + i\lambda^2)}\,d\lambda] \quad ...(20)$$

In the above the functional symbols $si = (-\pi/2) + Si$, Ci, Ei are those of the integral sine and cosine and the exponential integrals[11-13].

The confluent hypergeometric functions ${}_1F_1$ and the related incomplete gamma functions of (20) are at once replaceable by their well known asymptotic expansions for large arguments. Furthermore, the second λ-integral of I_n may be taken as a Fourier integral while the other λ-integrals of I_n and I are Laplace integrals so that their asymptotic values for large values of τ_n may be completely found by repeated integrations by parts[5]. Considering smallness of α/x and τ/r^3, and performing the α-integration and the subsequent operation by $\partial/\partial t$, one can then obtain the complete asymptotic representation of η for different ranges of large values of the dimensionless parameters τ, τ', r or $\tau\theta^2$. In what follows, we shall generally give only the first or the first two terms of this expansion in the various possible cases.

It appears that the dominant contributions to the asymptotics are those of U and V. These are of the forms $A\exp{(i(\tau' - \tau_n\theta_n^2))}$ and $B\exp{(i\tau_n)} + C\exp{(-i\tau_n)}$ which represent respectively travelling waves and dispersive waves of the Cauchy-Poisson type. In addition, the asymptotics, contain (a) an algebraic part and (b) an exponential part. The part (a) consists of I, the second term of I_n, a part of U and of the first term of R_n. The part (b) has terms of the following types :

(c) $De^{i\tau'}$ due to W, the third ${}_1F_1$ of R_n, the first term of I_n;

(d) $E\exp{(-\tau_n)}$ due to the first two ${}_1F_1$'s of R_n;

(e) $F\exp{(i\tau' - \tau_n\theta_n^2)}$ due to last two ${}_1F_1$'s of R_n.

Here A, B, C, D, E, F generally represent some series of negative powers of the large parameters present in the special functions and the integrals of (20). The groups of terms (a) to (e) of which (c) and (e) represent standing wave-systems dying out at large distances, are unimportant for our present purpose.

4.1 When $r^2 \gg \tau \gg \max. [1, (1 - \theta)^{-2}]$, $\tau'^2 \gg 4\tau$,   ...(21)

we have

$$\rho\eta \sim 2^{-1/2} \left(\frac{\pi\omega}{g}\right)^2 \bar{f}(\omega^2/g) \exp i(\omega t - \omega^2 x/g + \pi/4) H(1 - \theta)$$

$$+ \omega \left(\frac{2g^3 x}{\pi^3}\right)^{-1/2} [1 - (2\omega x/gt)^2]^{-1} \bar{f}(gt^2/4x^2)$$

$$\times \left[(gt/2\omega x) \sin \frac{gt^2}{4x} - i \cos \frac{gt^2}{4x} \right]$$ ...(22)

where $\bar{f}(m)$ is the generalised Fourier transform (14) of $f(x)$, $q = 2$.

The condition $r^2 \gg \tau$ in (21), may be removed when the α-integration can be exactly performed

When $\tau' \gg \tau \gg 1$, we have

$$\rho\eta \sim (ig^{1/2} t^2/\sqrt{2\pi} \omega x^{5/2}) [\cos \tau + (igt/2\omega x) \sin \tau$$

$$+ (2x/gt^2) \sin \tau]. \int_a^b f(\alpha) \, d\alpha.$$ ...(23)

When $r^2 \gg \tau \gg \tau' \gg (4\tau/\tau')$, (22) gives

$$\rho\eta \sim 2^{-1/2} (\pi\omega/g)^2 \bar{f}(\omega^2/g) \exp i(\omega t - \omega^2 x/g + \pi/4)$$

$$+ t(8gx^3/\pi^3)^{-1/2} \bar{f}(gt^2/4x^2) \sin \tau.$$ ...(24)

To show that the condition $r^2 \gg \tau$ is unnessary when $\tau \gg \tau'$, we consider the case

$$f(x) = \frac{P}{a} \quad \text{when } 0 < x < a$$
$$= 0 \quad \text{when} \quad x > a$$ ...(25)

We do away with the approximation for smallness of α/x and perform the α-integration of the pertinent terms in terms of Böhmer's integrals $C(v, n)$ and $S(v, n)$ (see 4, § 9.10) and get the result :

$$\pi g \rho\eta \sim 2^{-3/2} \pi^{1/2}(P/a) \frac{\partial}{\partial t} \{t[C(\tau_1, -\tfrac{1}{2}) - C(\tau_2, -\tfrac{1}{2})$$

$$- \sum_1^2 S(\tau_n, -\tfrac{1}{2}) + iCiS(\tau_3, -\tfrac{1}{2}) - iCiS(\tau_4, -\tfrac{1}{2})]^b_{\alpha=a}\}$$

Since $\mid \tau_n \mid \gg 1$, these C- and S-functions may be replaced by their asymptotic representations, (§ 9.10). Finally, we approximate for $(a/x) \ll 1$ and obtain, after a little simplification,

$$\rho\eta \sim (4P/a) \, (\pi g^3 t^3/x)^{-1/2} \sin \{gt^3 x(x^2 - a^2)^{-1}/4\} \cos \{agt^2$$

$$\times \frac{(x^2 - a^2)^{-1}}{4} - \frac{\pi}{4}\} + 2^{1/2} (P/ga) [1 + 2^{3/2} \sin (a\omega^2/2g)$$

$$\times \cos \left(a\omega^2/2g + \frac{\pi}{4} \right) - \exp(-a\omega^2/g) \right] \exp i(\omega t - \omega^2 x/g + \frac{\pi}{4}).$$

$$...(26)$$

when $\tau \gg \tau' \gg (4\tau/\tau')$ and $a > 0$.

Transition zone between (4.11) & (4.12).

When

$$\theta \simeq 1, r \mid 1 - \theta \mid > 2, r^2 \gg \tau \gg 1 \qquad\qquad ...(27)$$

$$\rho\eta \sim (\pi\omega/g\sqrt2)^2 \, \bar{f}(\omega^2/g) \, \{2^{-1/2} \exp (i\pi/4 + sgn (1 - \theta)$$

$$\times \, CiS\tau(1 - \theta)^2\} \exp (i(\omega t - \omega^2 x/g)) \qquad\qquad ...(28)$$

ATTAINMENT OF A STEADY STATE

When the s-integration is completed in (16A), we have

$$g\rho\eta = -f(x) \, e^{+i\omega t} - \left(\frac{1}{\pi}\right)\left(\frac{\partial^2}{\partial t^2} + i\omega \frac{\partial}{\partial t}\right) \int_0^\infty (\sigma^2 - \omega^2)^{-1}$$

$$\times (\cos \sigma t - \cos \omega t) \, (e^{-mx} + \cos mx - \sin mx) \, dm$$

$$\int_a^b (e^{-m\alpha} + \cos m\alpha - \sin m\alpha) \, f(\alpha) \, d\alpha \qquad\qquad ...(29)$$

For the initial pressure (25), we evaluate the α-integral and write (29) in the form

$$g\rho\eta = -f(x) \, e^{i\omega t} - \left(\frac{P}{\pi a}\right)\left(\frac{\partial^2}{\partial t^2} + i\omega \frac{\partial}{\partial t}\right)\left[\int_0^{p/2} F(m) \, dm\right.$$

$$\left. + \int_{p/2}^\infty F(m) \, dn\right],$$

where

$$F(m) = \{m(\sigma^2 - \omega^2)\}^{-1} (\cos \sigma t - \cos \omega t) \, (e^{-mx} + \cos mx - \sin mx)$$

$$\times (\cos ma + \sin ma - e^{-ma}) \qquad\qquad ...(30)$$

where

$$p = \frac{\omega^2}{g}.$$

Known results on Fourier integrals show that $\int_0^{p/2} F(m) \, dn$ equals

$$O(t^{-1}) - \cos \omega t \int_0^{p/2} \{m(\sigma^2 - \omega^2)\}^{-1} (e^{-m x} + \cos mx - \sin mx)$$

$$\times (\cos ma + \sin ma - e^{-m x}) \, dm.$$

Writings $\int_{p/2}^{\infty}$ of (30) in the form

$$- 2 \cos \omega t \int_{2^{-1/2}\omega}^{\infty} G(\sigma) (\sigma - \omega)^{-1} \{1 - \cos (\sigma - \omega) t\} \, d\sigma - 2 \sin \omega t$$

$$\times \int_{2^{-1/2}\omega}^{\infty} G(\sigma)(\sigma - \omega)^{-1} \sin (\sigma - \omega) \, t d\sigma$$

We get for the sum of the m-integrals of (30) the result

$$O(t^{-1}) - 2 \cos \omega t [\int_0^{\infty} (\sigma - \omega)^{-1} G(\sigma) \, d\sigma - \int_{2^{-1/2}\omega}^{\infty} G(\sigma)(\sigma - \omega)^{-1}$$

$$\times \cos (\sigma - \omega) \, t d\sigma] - 2 \sin \omega t \int_{2^{-1/2}\omega}^{\infty} G(\sigma)(\sigma - \omega)^{-1} \sin (\sigma - \omega) \, t d\sigma.$$

$$...(31)$$

Here

$$G(\sigma) = \{\sigma(\sigma + \omega)\}^{-1} (e^{-h} + \cos h - \sin h)_{h=(\sigma^2 x/g)}$$

$$\times (\sin l + \cos l - e^{-l})_{l=(\sigma^2 a/g)}, \quad \sigma > 0 \ G(0) = 0,$$

and $\int_0^{\infty} = \lim_{\epsilon \to 0+} (\int_0^{\omega - \epsilon} + \int_{\omega + \epsilon}^{\infty})$ is the Cauchy Principal value of $\int_0^{\infty}$. By the aid of Bochner's results, the second and the third σ-integrals of (31) are respectively replaced by $O(t^{-1})$ and $\pi G(\omega) + O(t^{-1})$ while the first σ-integral is evaluated directly to obtain

$$g \rho \eta = (P/a) \, e^{i \omega t} [2^{1/2} \exp i(\pi/4 - px) (\cos pa + \sin pa - e^{-pa}) - T]$$

when $\quad x > a$ $\qquad \qquad \qquad ...(32)$

$$= (P/a) \, e^{i \omega t} [(1 - i) \, e^{-ipa} (\sin px - \cos px) - (1 + i) \, e^{-p(a + ix)} - T]$$

when $\quad x < a$ $\qquad \qquad \qquad ...(33)$

where

$$T = O(t^{-2}) + ie^{-\nu x} (e^{-pa} - \sin pa - \cos pa)$$

$$+ (1/\pi) [e^{-p(x+a)} \, \bar{E}_i(p(x + a)) - (\cos \chi \ Ci \, \chi + \sin \chi \ si \, \chi)_{\chi = p(x+a)}$$

$$- sgn(x - a) (\cos \mu \ si \ \mu - \sin \mu \ Ci\mu)_{\mu=p \ | \ x-a \ |}$$

$$+ \tfrac{1}{2}(1 - i) \{e^{-ip\bar{z}} E_i(ip\bar{z}) - e^{-p\bar{z}} \bar{E}_i(p\bar{z})\}$$

$$+ \tfrac{1}{2}(1 + i) \{e^{ipz} E_i(-ipz) - e^{-pz} \bar{E}_i(pz)\}] \qquad \text{...(34)}$$

$p = \omega^2/g$, $z = x + ia$, $\bar{z} = x - ia$, $\bar{E}_i(x) = $ a related exponential integral. In the general case we may show similarly that when (1) $\sigma \bar{f}(\sigma^2/g)$ is differentiable with respect to σ in $(0, \infty)$,

(2) $\dfrac{d^2}{d\sigma^2}\left[\bar{f}(\sigma^2/g)\right]_{\sigma=\omega}$ exists,

(3) $\bar{f}(\sigma^2/g), \bar{f}'(\sigma^2/g)$ are each absolutely integrable with respect to σ in $(2^{-1/2}\omega, \infty)$ then, as $t \to \infty$,

$$g\rho\eta = -f(x) \ e^{i\omega t} + (p\pi/2) \ e^{i\omega t}[i\pi \bar{f}(p)(e^{-px} + \cos px$$

$$- \sin px) - \int_0^\infty (m - p)^{-1}\bar{f}(m) \ (e^{-mx} + \cos mx - \sin mx) \ dm]$$

$$+ O(t^{-2}) \qquad \text{...(35)}$$

The average rate W_{av} at which the pressure distribution does work upon the fluid is

$$W_{av} = (\omega^3/2\rho) \ [(\pi^2/2g) \ \bar{f}(\omega^2/g)]^2. \qquad \text{...(36)}$$

If $f(x) = P\delta(x)$, where $\delta(x)$ is Dirac's function and P the amplitude of the total force per unit width on the free surface, we pass to the limit $a \to 0$ in (32):

$$\pi g^2 \rho \eta = 2 \ P\omega^2 \ e^{i\omega t}[2^{1/2}\pi \ e^{i(\pi/4 - px)} + e^{-px}\{i\pi + \bar{E}_i(px)\}$$

$$+ \cos px \ (si \ px + ci \ px) + \sin px(\sin (si \ px - di \ px)] + O(t^{-2})$$

$$\text{...(37)}$$

The average rate of transmission of energy by the pressure to the fluid is now

$$W_{av} = \frac{2\omega^3}{\rho g^2}. \qquad \text{...(38)}$$

Discussion of the motion for $q = 2$.

In the steady state $(t \to \infty)$, the dominant part of η is a non-decaying (with x) travelling wave at every distant place [cp. eqn. (37)], provided the part $\bar{f}(\omega^2/g)$ of the amplitude of this wave is non-zero. If $\bar{f}(\omega^2/g) = 0$, we have a standing wave everywhere [cp. (35) for (37)].

At any fixed distance, the transient part of η decays with time like a term of the order $O(t^{-2})$.

When time gradually grows to infinity at large distances from the shore line, we have the following results from (22) and (23):

When $f(\omega^2/g) \neq 0$, $f(x) \neq P\delta(x)$ and $1 - (2\,\omega x/gt)$ is not too small, we have

$$\rho\eta \sim 2^{-1/2}(\pi\omega/g)^2\ \bar{f}(\omega^2/g)\ e^{i(\omega t - \omega^2 x/g + \pi/4)}$$

when $2\,\omega x < gt$ ...(39.1)

and

$$\rho\eta \sim (2\,\pi g^3 x)^{-1/2}\,\pi^2\omega[1 - (2\,\omega x/gt)^2]^{-1}\,\bar{f}(gt^2/4x^2)$$

$$\times \left\{ \frac{gt}{2\,\omega x} \sin\frac{gt^2}{4x} - i\cos\frac{gt^2}{4x} \right\} \text{ when } 2\,\omega x > gt \qquad\qquad ...(39.2)$$

subject to the conditions $r^2 \gg \tau \gg 1$, $\tau'^2 \gg 4\tau$.

Equation (39.1) gives the steady-state monochromatic travelling wave already referred to; it has the frequency ω, the phase velocity g/ω and wavelength $2\,\pi g/\omega^2$. Its dispersive precursor represented by (39.2) is a wave of the Cauchy-Poisson type. The change of character of the asymptotic form of η from a fixed-amplitude progressive wave to decaying dispersive waves as $(2\,\omega x/gt)$ increases through the value 1, signifies the occurrence of a Stokes' phenomenon in the neighbourhood of the line $x = gt/2\omega$.

Asymptotic Envelope

If $\bar{f}(\omega^2/g) \neq 0$, we have near the line $x = gt/2\omega$ a travelling wave (23) that has the frequency ω, and the phase velocity g/ω. For $f(x) = P\delta(x)$, this has the envelope $|P|\,\omega^2 R(u)/\rho g^2$ where $R(u) = (A^2 + B^2)^{1/2}$, $A + i\beta = 1 + i + 2sgn\,(1 - \theta)\,Cis \times (\tfrac{1}{2}\,\pi u^2)$,,

$$u = \frac{gt - 2\omega x}{(2\alpha g x)^{1/2}}.$$

and the phase angle is $\tan^{-1} B/A$. The centre of the normalised envelope $R(u)$, defined by $u = 0$, advances with the group velocity $g/2\omega$; its distribution is plotted in Figure 1.

Considered as a time-wise envelope at a fixed point x, $R(u)$ rises monotonically to a maximum of 3.3 at $u = 1.25$ and then enters an oscillatory epoch in which the asymptotic behaviour may be easily obtained from those of the Fresnel integrals involved in $R(u)$. The rise-time T may be defined as the time for R to rise from 0.1 to its first maximum

$$T \doteq 18\,(x/g)^{1/2}.$$

T is independent of ω and also by hypothesis $\omega T \gg |$.

We also may regard $R(-u)$ as the spacewise envelope at a fixed time, since

$$-u = 2\omega^{3/2}g^{-1}(\pi t)^{-1/2}\left[x = \frac{gt}{2\omega}\right]\left[1 + O\left((\omega^2 x/g)^{-1/2}\right)\right].$$
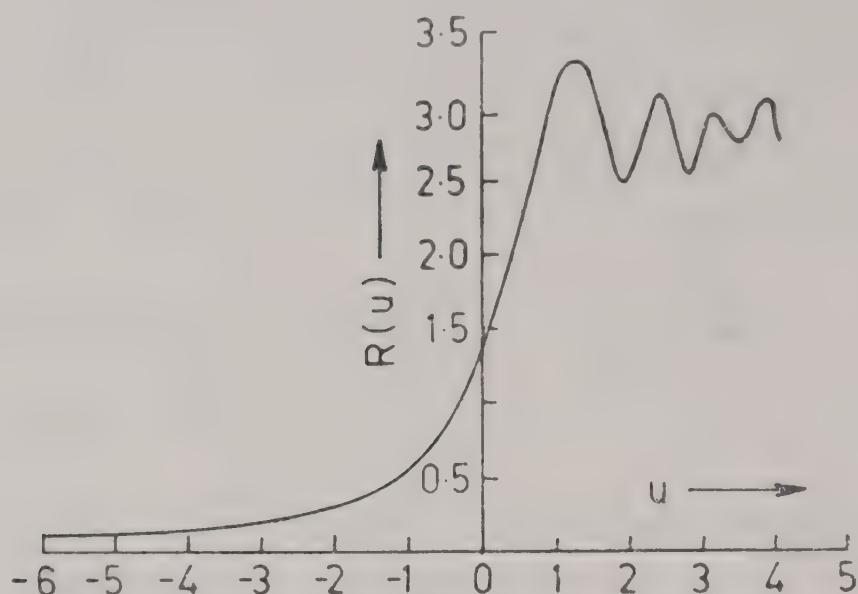
FIG. 1

Regarded in this way, the wave front envelope rises monotonically to its maximum value as x decreases from $+\infty$ and then tends in an oscillatory manner to its steady-state value. The width X of the transition zone may be defined as the distance between the point at which the precursor reaches 0.1 of the steady-state amplitude and its maximum amplitude

$$X \doteq 6g\omega^{-3/2}t^{1/2}.$$

The phase terms in the different expressions for η are generally unaffected by the parameters and b; the finiteness of the pressure strip serves to damp the surface oscillations at large distances and times.

The distinction between an osillatory pressure point and a finite pressnre strip disappears when $\tau' \gg \tau \gg 1$ [cp. (23)] provided the amplitude (P) of the total force per unit width on the surface remains the same in the two cases.

When $\bar{f}(\omega^2/g) = 0$, the steady-state form of η consists of a standing wave at every place (§5). For these exceptional values of ω, the dispersive character of η then prevails everywhere until $t \to \infty$. The vanishing of W_{av} of (36) in this signifies that no energy is transmitted through the fluid in the steady state for these frequencies. A wave generating machine may thus fail to function for some frequencies given by equation $\bar{f}(\omega^2/g) = 0$ in the steady state. This phenomenon of zero energy radiation has also been noted by Morris[8], and Sretenskii[10] and by Stoker[1] for fluid of infinite depth.

For the pressure model (25), these exceptional frequencies are given by

$$\frac{a\omega^2}{g} = x_n$$

where x is the nth positive root of the equation.

$$e^{-x} = \sin x + \cos x$$

Out results being closely connected with those of Morris and Sretenskii, this pheno-menon of zero energy radiation at certain frequencies is a distinctive feature of the wave motion due to an oscillatory pressure segment of finite or zero length.

ACKNOWLEDGEMENT

REFERENCES

1. J J Stoker, *Water Waves*, Interscience, New York (1966).
2. J V Wehausen and E V Laitone, *Handbuch der Physik*, Band IX. Springer-Verlag, Berlin (1960) p. 539.
3. J W Miles, *J. Fluid Mech.*, **13** (1962) 145.
4. K. Chaudhri, *J. Appl. Mech. Trans. ASME* 93 *Ser. E*, **38** (1971) 700.
5. M C Shen, *Rep. IMM 342, Courant Indt. of Math. Sci.*, New York University (1965).
6. A R Sen, A R *ZAMM*, **53** (1973) 642.
7. C A N Morris, *Proc. Camb. Phil. Soc.*, **76** (1974) 545.
8. C A N Morris, *ZAMM*, **56** (1976) 167.
9. D H Griffel and C A N Morris, *SIAM J. Appl. Math.*, **33** (1977) 535.
10. L N Sretenskii, *Prikl. Math. Mekh.*, **27** (1963) 1012.
11. A Erdelyi, *Higher Transcendental Functions*, Vol. II. McGraw Hill, New York (1953).
12. A Erdelyi, *Asymptotic Expansions*, Dover, New York (1955).
13. A Erdelyi, *Tables of Integral Transforms*, Vols. I-II. McGraw Hill, New York (1954).

MINERALOGY AND GENESIS OF CLAY DEPOSITS FROM SANVORDE, GOA, INDIA

A G Dessai

Department of Geology, University of Poona, Pune 411 007

The mineralogy of the clays from Sanvorde, Goa has been investigated with the help of DTA, X-ray Diffraction, Infrared Spectroscopy, Scanning Electron Microscopy and Chemical Analysis. The clays are white in colour and are stained at places by iron oxides. They exhibit relict hypidiomorphic texture and progressively grade into granite gneisses and migmatites.

The mineralogical studies indicate that the clay minerals are predominantly kaolinite and halloysite and are associated with mica, quartz and the accessory minerals which are present in varying proportions in the different horizons. The clays are moderately stacked and therefore fall within the clay group broadly designated as "fire clays".

It is concluded that the clays have been derived from the granitic rocks by leaching and oxidation under subtropical climatic conditions.

INTRODUCTION

THE clay deposits from Sanvorde (Fig. 1) are situated around Marutigarh and Kakoda in the Sanguem district of Goa. Although they have been known for a long time their mineralogy and genesis have not been studied. In recent years the clays are being increasingly used in various industries and hence it was considered desirable to investigate their mineralogy. The preliminary results are presented in this communication.

GEOLOGY OF THE AREA

The area around Sanvorde is predominantly occupied by the Precambrian Dharwar metasediments represented by quartz-chlorite biotite schists, quartz-mica schists with thin bands of quartzite. These are intruded by granite gneisses and migmatites of the Peninsular Gneissic Complex. The metasediments along their contact with the gneisses exhibit a zone of migmatisation. The gneisses have been intruded by gabbroic rocks and by dolerite dykes[1,2,3].

The clay deposits are found to occur as capping on the granite gneisses and migmatites and are found to grade into them. The clays found at lower elevations have been preserved *in situ* while those formed at higher elevations have been eroded and in part redeposited as transported clays. The best section of clay is seen about one km. south of Sanvorde at Marutigarh where a small hillock about 40
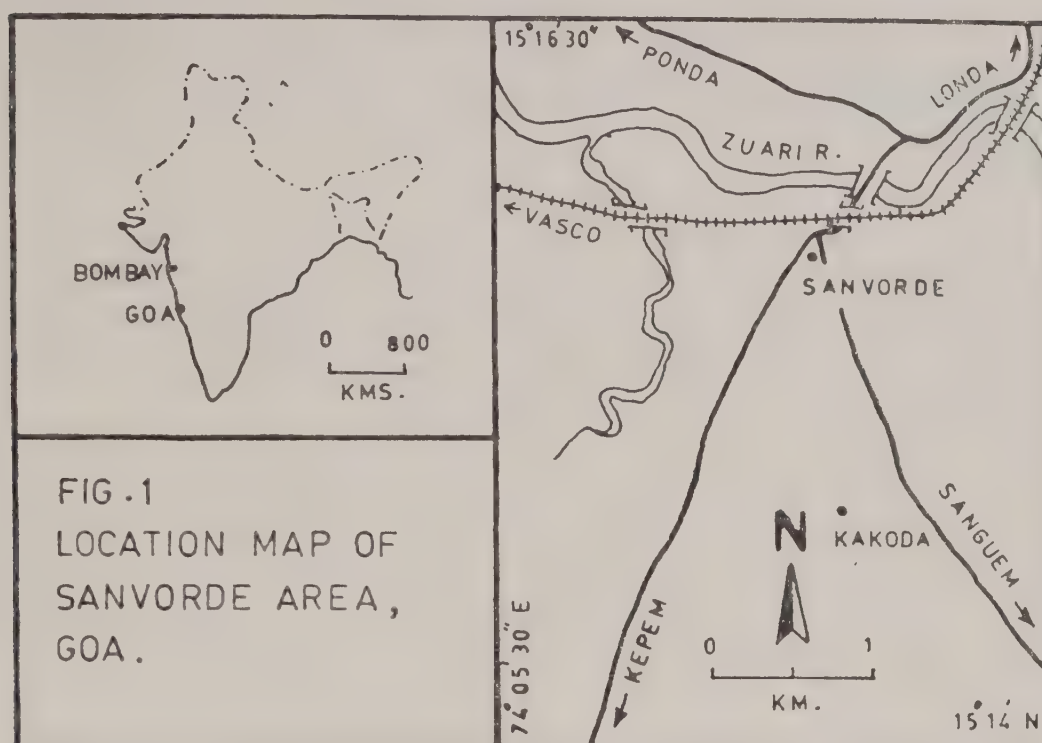
Fig. 1.   Map showing location of the area around Sanvorde, Goa.

metres high is present in an otherwise flat terrain. The hillock offers an ideal section of clay for observation and sampling. The clays exhibit relict foliation of the gneisses which trends roughly in NW-SE direction. The hillock has a hard cover of laterite duricrust about a metre thick. This grades downwards into an aluminous laterite of about the same thickness which eventually grades into clay. Two other sections were examined in dug wells each about 12 metres deep one occurring west of Marutigarh and the other at Kakoda.

The sections exhibit progressive zoning marked by an increase in the proportion of unweathered minerals of the parent rock. Both quartz and sericite are common in the most thoroughly weathered zones and felspar and biotite are present in varying amounts in the intermediate and unweathered zones. The deposits differ greatly in thickness and lateral extent. They may extend laterally over a distance of 50 m to a maximum of 400 m. They may pinch out along the length or may thin out for some distance and again resume their normal thickness. The thickness of the individual pockets varies along the length and ranges from about 5 m to over 10 m. At the top, the clays are pinkish and at places are buff in colour. The buff horizon becomes progressively white with depth. Rusty iron staining due to the presence of limonite is common along joints and fracture planes.

MINERALOGY OF THE CLAYS

The mineralogy of the clays has been interpreted primarily from X-ray diffraction characteristics of oriented aggregates of $< 2\,\mu$ size. The same samples have been subjected to DTA. The precise identification of all the phases present by thermal

and X-ray analysis alone, is not possible especially when a mineral phase is present in a very small amount. Therefore, the samples were also studied with the help of IR spectroscopy. Selected samples were investigated by SEM and chemical analysis.

Clay minerals

The X-ray diffractograms of oriented specimen were obtained on a Philips X-ray diffractometer using *CuK$_\alpha$* radiation and Nickel filter. The diffraction characteristics were recorded using a linear scale of 4000 cycles/second with slit width of 0.2 mm and chart speed of 1° per minute.

In most of the samples kaolinite is by far the most dominant mineral and is identified by its strong characteristic diffraction maxima at 7.2 Å and 3.58 Å. These maxima are unaffected by glycolation and heat treatment at 300°. The representative diffraction pattern of an untreated mixture of kaolinite and halloysite is presented in Fig. 2. It is seen that the 001 reflections at 7.1 Å and also the pyramidal and prismatic reflections are not very sharp reflecting poor degree of crystalinity. Poorly crystallised "fire clay" kaolinites and 7 Å halloysites give a broad 001 reflection at slightly greater than 7.1 Å and the reflections from the pyramidal and prismatic planes are diffuse. The degree of crystallinity of kaolinite varies with the proportion of other clay minerals present[4].

The differential thermal analysis was carried out with a MOM derivetograph upto a temperature of 1000 °C with a heating rate of 10 °C per minute. A representative curve is presented in Fig. 3. The curve shows a first endothermic peak at 85 °C followed by the second one at 535 °C and an exothermic hump at 945 °C. The low temperature endothermic peak is related to dehydration. It may be water sorbed on the surface of the particles, inter layer water or water associated with alumina gels. The second endothermic peak at 535 °C can be ascribed to both kaolinite and halloysite. The endothermic peak for kaolinite normally lies between 500° and 700 °C[5] and the exothermic peak between 950° and 980 °C. Halloysite shows endothermic peaks between 110° and 130 °C and between 530° and 700 °C with an exothermic peak between 940 °C and 1000 °C. Thus the endothermic peak at 530 °C and the exothermic peak at 945 °C may be ascribed to the presence of both kaolinite and halloysite. However, the absence of an additional peak between 110° and 130 °C indicates absence of 10 Å halloysite. The endothermic peak at 535 °C is due to dehydration and decomposition of the crystal structure while the exothermic peak at 945 °C is due to the recrystallisation of a spinel phase[6]. The magnitudes of these peaks vary with particle size and the degree of disorder in the
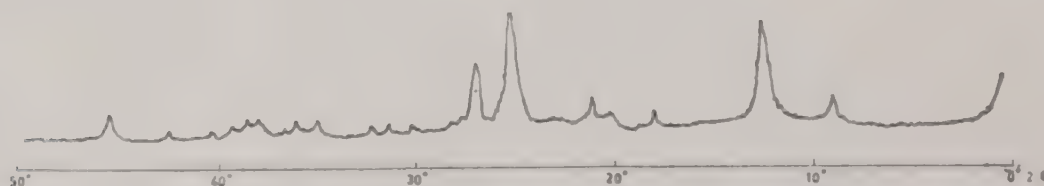

Fig. 2.   X-ray diffractogram (CuK$_\alpha$ radiation) of clay from Sanvorde, Goa.

D.T.A.

80

945

535

I·R·

L⁻

K

K

K
K
H

H

H

L

K H K
H

H

H

L

K Q K

L
K

K

H

K

K

40   35   30 12   11   10   9   8   7   6   5   4×100
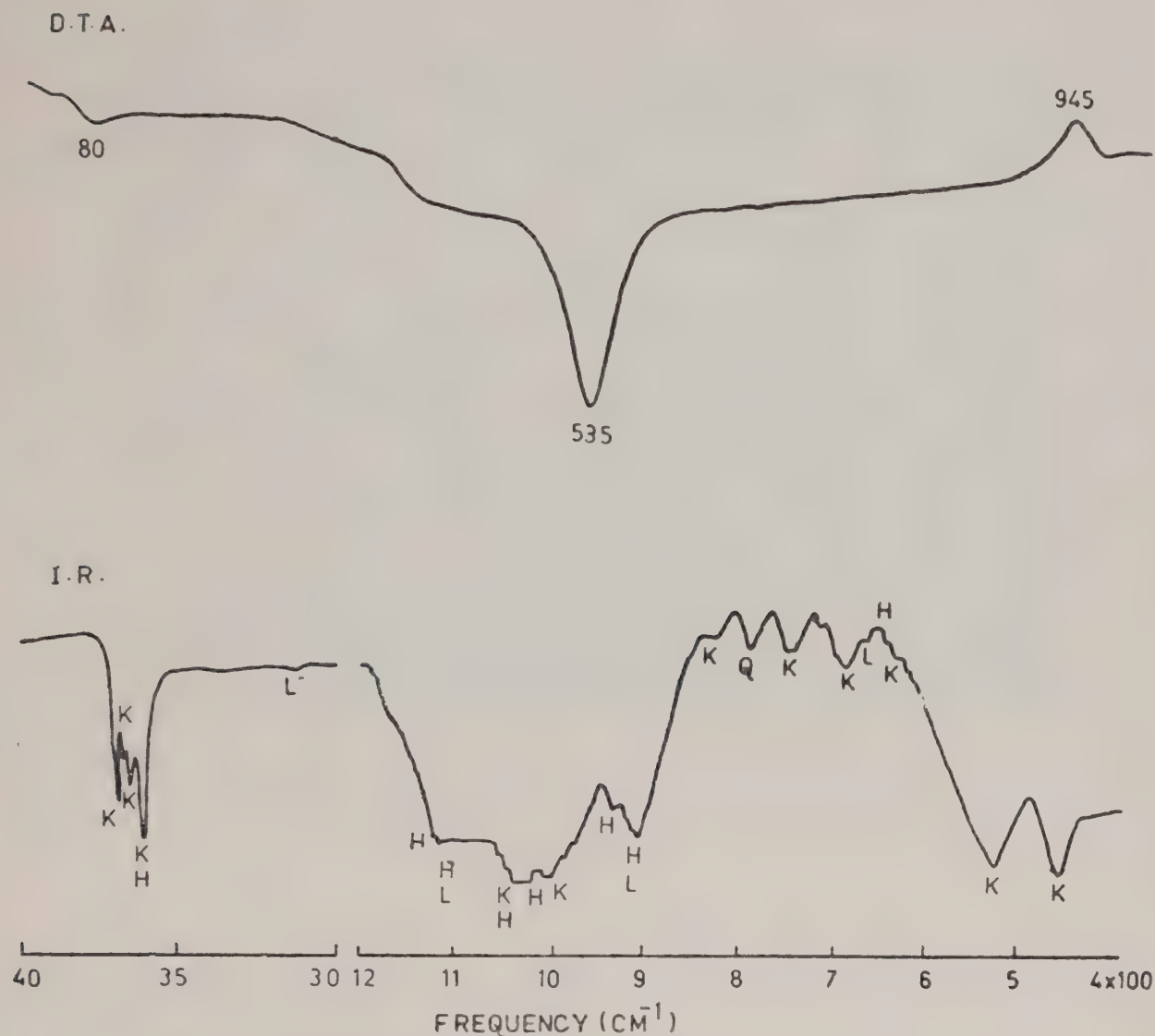
FREQUENCY (CM⁻¹)

Fig. 3.   DTA curve and IR spectrum of clay from Sanvorde, Goa.

stacking of structural layers.   Small peaks are associated with finer particle size and more disordered structure.

These observations are supported by infrared spectroscopic analysis carried out with a Perkin-Elmer Infrared Grating Spectrometer 221.   A representative IR spectrum of a bulk sample is presented in Fig. 3.   The IR spectra were determined in the frequency range 400–4000 CM⁻¹ using nujol as a medium to prepare the absorption cell.

Kaolinite has been identified by bands of large intensity at 3685, 3660, 3635, 3620 and 475 CM⁻¹ supported by less intense bands at 1032, 935, 828, 750, 690, 605, 530 and 470 CM⁻¹ by comparing with the bands given by Van der Marel and Beutelspacher⁷.   The absorption bands of kaolinite and halloysite almost overlap; however, presence of absorption bands at band widths 1094, 1012, 941, 692, 650 and 562 CM⁻¹ indicate the presence of halloysite.

The surface morphology of the clay minerals was studied under a Philips Scanning Electron Microscope.   Generally 25 KV accelerating voltage and 10 picoampere current intensity were used, however, in some cases to achieve better resolution the current intensity had to be lowered.

The samples were scanned without pretreatment in order to eliminate the possible introduction of artifacts which could lead to erroneous interpretation[9]. The broken surfaces of specimens and fine loose particles were studied. The surface of the sample was coated by a 20 μm silver layer using a vacuum evaporator. Micrographs were made on selected points of the samples with magnification increasing upto 5,000 times in some cases.

The mineralogy of the clays differs slightly from place to place around Sanvorde. In general the residual clays can be divided into three graditional horizons. The clays in the upper horizon are composed predominantly of kaolinite with little amount of halloysite. In this well drained upper horizon, alteration of felspars mainly gives rise to kaolinite[8] with some halloysite. Kaolinite occurs as platy particles with pseudohexagonal outlines. Halloysite is in the form of laths, tubes and elongated blobs with a large length to width ratio. The poorly crystallised kaolinite and halloysite are seen in Fig. 4.

The upper horizon grades downwards into a second horizon which differs from the former in that it contains more halloysite and less kaolinite with some grains of fresh felspar, muscovite and quartz. In this horizon mainly halloysite develops from the alteration of the felspars (Fig. 5). A well developed halloysite crystal is shown in Fig. 6. This horizon further progressively grades downwards into a third horizon that is rich in micas, felspars, quartz with little halloysite.

Non-clay minerals

The material other than clay minerals includes allogenic minerals that have escaped alteration or are partly altered. These include zircon, tourmaline, ilmenite, sphene, pyrite and chalcopyrite and they occur in trace amounts. Quartz occurs in proportions ranging from traces to about 50 per cent. Subangular to subrounded quartz grains range in size from very fine silt to medium sand. Quartz invariably occurs as frosted grains that show evidence of leaching, the margins being serrated and etched, and it shows replacement by clay minerals. The absence of grains of felspars in higher horizons also suggests leaching. Iron oxide minerals including limonite and rarely hematite are present as finely disseminated particles that result in red, brown and yellow colouration of the clays.

CHEMICAL ANALYSIS

The clays have been chemically analysed for the major elements. The chemical analysis of clays are presented in Table I. The silica content is fairly high varying between 60 and 61.25 per cent. The high silica content is partly due to the presence of free quartz in the clay. It is a relatively inert constituent and acts as diluent in the clay. The Fe_2O_3 content ranges from 4.5 to 5.2 per cent. This may have been partly contributed by iron minerals such as hematite and limonite and partly by weathered ilmenite and sphene. The presence of iron oxide is undesirable as it greatly decreases the refractory properties of the clay. Fluxes such as titanium and alkalies are quite low.
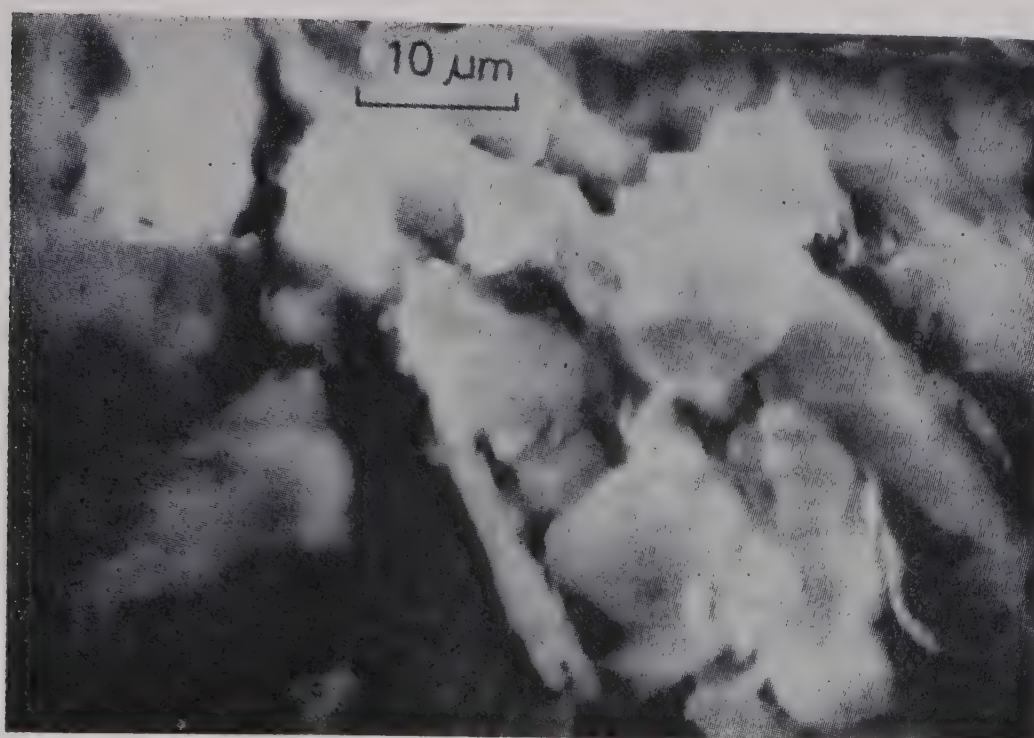
Fig. 4.   Electron micrograph of poorly crystallised kaolinite and halloysite.

TABLE I

Average chemical analyses of clays from Sanvorde, Goa.

SiO_3	61.25	60.85
Al_2O_3	22.45	22.70
Fe_2O_3	4.56	5.20
FeO	0.50	0.62
MgO	0.16	0.18
CaO	0.18	0.20
Na_2O	0.25	0.21
K_2O	0.30	0.25
TiO_2	0.10	0.15
P_2O_5	—	—
MnO	0.01	0.02
LOI	10.15	9.68
Total	99.91	100.96

The loss on ignition is regarded as an important characteristic of clay. It can be used as a rough means of estimating the total content of kaolin minerals in a clay mixture, though it may not be possible to ascertain individual proportions of the different mineral phases in the mixture. The loss on ignition at 900 °C amounts to about 10 per cent. Therefore, as a first approximation, it may be concluded that the amount of kaolin minerals in the clay is not less than 70 per cent, considering the weight loss of pure kaolinitic clay to be 13.9 per cent.
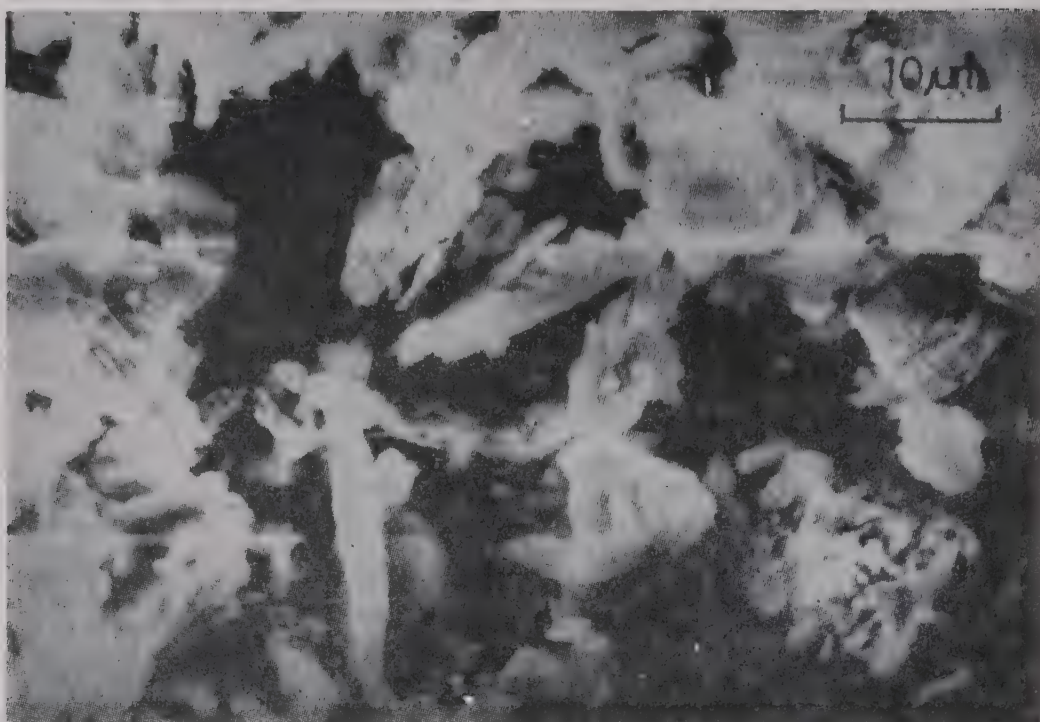
Fig. 5.   Electron micrograph of elongated halloysite crystals.

Fig. 6.   Electron micrograph of well developed halloysite at higher magnification.

DISCUSSION

From the mineralogical studies it is possible to visualise the environmental condi-
tions leading to the formation of clay minerals and the mechanism of alteration
taking place in the parent rock.   From the mode of occurrence it is clear that the

clays have been produced due to weathering and alteration of the granitic gneisses and related rocks under subtropical climatic conditions with alternating wet and dry spells. Under these conditions the parent rock undergoes transformation by decomposition of its mineral constituents. Hydration and oxidation are the two important processes involved in chemical weathering. Depending upon the Eh-pH conditions of the environment, and the internal drainage conditions, either hydroxides of Al or clay minerals are produced. In general good drainage conditions can be visualised in near surface environments rather than at depth and the pH of the solutions at the surface is in the range of acidic to alkaline as the rocks undergoing decomposition are of granitic composition. The abrasion pH value[10] ranges from 5 in completely weathered rock to 9 in fresh rock.

Rainfall is one of the important components which affects the trend of weathering, while temperature has a modifying effect on the rate of transformation[11]. Alkaline conditions can be visualised by the abrasion pH of the fresh rock. Under these conditions the waters break down the primary silicates with the alkalies and alkaline earths being first to be removed. At this pH, silica becomes mobile[12] compared to alumina. However, as the waters percolate deeper, they are not at the same pH as the original water. Depending upon the length of time the water is retained in the voids in the lithorelicts, an equilibrium pH will be reached. Further weathering will proceed at this pH and this is different from the abrasion pH of the rocks. Depending upon the rate of renewal of water, the equilibrium pH will vary. If removal is fast, it will tend to be on the acid side of equilibrium pH. This indicates that the minerals will show different alteration products depending upon the microenvironments. Thus felspar will show alteration to kaolinite in well drained environments whose abrasion pH ranges from 5.2 to 7.3[13] and to halloysite in poorly drained deeper environments. Similarly as discussed earlier kaolinite will form from micas in shallower environments while the latter remains unaltered in the lower zones.

SUMMARY

From the study it may be concluded that the clays from Sanvorde area are essentially made up of a mixture of kaolinite and halloysite, the former being in larger proportions in the higher horizons while the latter predominates in the deeper sections. The clays are residual in nature having been formed from the decomposition of granite gneisses and migmatites.

From the study of XRD, DTA, IR and SEM, it may be deduced that they are moderately stacked and therefore fall within the clay group broadly designated as "fire clays". Being moderately stacked they could be used in paper industry as poorer the crystallinity better the gloss that is imparted to the paper. This is because poorly crystallised kaolins are thinner flakes and hence readily orient parallel to the sheet and form a smooth surface.

The clays are low in Fe and Ti oxides and alkalies which may render them suitable for use as refractory material, foundry molds etc. Further detailed work on their suitability for these industries is required.

REFERENCES

1. A R Gokulam, *Bull. Geol. Surv. Ind.* **37** (1972) 1.
2. A G Dessai and G G Deshpande, *N. Jb. Miner. Abh.* **135** (1979a) 209.
3. A G Dessai and G G Deshpande, *Bull. Earth Sci.* **7** (1979b) 5.
4. S H Patterson and J Hosterman, *Clays and Clay Minerals* **5** (1960) 178.
5. R C Mckenzie, *Mineralogical Society*, London (1957) p. 456.
6. W Smykatz-Kloss, *Differential Thermal Analysis Application and Resutls in Mineralogy.* Springer-Verlag, Berlin-Heidelberg, (1974) p. 185.
7. H W Van der Marel and H Beutelspacher, *Atlas of Infrared spectroscopy of clay minerals and their admixtures.* Elsevier Publishing Company (1976) p. 396.
8. W D Keller, *Geology* **7** (1978) 184.
9. W D Keller, *Econ. Feol.* **74** (1979) 116.
10. R E Stevens and M K Carron, *Amer. Mineral.* **33** (1948) 31.
11. R J Pickering, *Econ. Geol.* **57** (1962) 1185.
12. K B Krauskopf, *Geochim. Cosmochim. Acta.* **10** (1956) 1.
13. W H Grant, *Clays and Clay Minerals* **13** (1963) 65.

INHIBITION CHARACTERISTICS OF SOME ORGANIC HETEROCYCLES DURING ACID CORROSION OF NICKEL AS STUDIED IN THE LIGHT OF THEIR STRUCTURAL PARAMETERS AND INTERFACIAL REACTIONS*

Amarnath Maitra*, Gurmeet Singh, Ramash Kumar Kaushik *and*
Kalyan Bhattacharyya

Department of Chemistry, University of Delhi, Delhi-110 007

The corrosion inhibition characteristics of organic heterocycles like pyridine, pyrrole, furan and thiophene during acid corrosion of nickel have been investigated and it has been found that the results cannot be explained only on the basis of their structural parameters like aromaticities, charge densities on the heteroatoms, ionisation potentials of the molecules, basicities etc. and the simple chemisorption mechanism through p_π—d_π interaction cannot explain all of their electrochemical behaviours at the nickel-acid interface. Rather protonation of the heterocycle ring and subsequent chemical transformation into some other species determine the route of inhibition mechanism in some cases. Pyridine, pyrrole and furan were found to inhibit the nickel corrosion in acid solution whereas thiophene catalysed the dissolution process. The catalytic activity of thiophene in acid corrosion of nickel has been explained from the fact that the compound in acid solution is adsorbed on the metal surface and is subsequently decomposed into metal sulphide which leads to higher dissolution of the metal. On the contrary the relatively higher inhibition characteristics of pyrrole were explained to be due to formation of dimeric and trimeric species in acid solutions which effectively blanket the metal surface from the corrosive media.

Keywords : Pyridine, Pyrrole, Furan; and Thiophene

INTRODUCTION

THE correlation between the inhibition characteristics and the structural parameters of the various organic inhibitors have been the field of interest for many years[1,9]. Most of the studies are based on the assumption that metal-inhibitor interactions are mainly chemisorption in nature and the reactive centre of inhibitor molecules establish the adsorption bond with the metal surface by Lewis acid-Lewis base interaction generally with the inhibitor as electron donor and metal surface as electron acceptor. Although these attempts led to successful correlation between structural parameters and inhibition characteristics of many organic compounds, deviations are not unusual in some corrosive media particularly in which the

---

organic additives undergo chemical changes by the influence of the medium as well as by the surface active metal atoms.

As a logical extension of the above observation we have taken a group of organic heterocycles with extensively delocalised π-electron systems and which may undergo chemical transformations in acid solutions particularly catalyzed by the metal substrates. This paper describes the corrosion inhibition characteristics of some structurally related organic heterocycles like pyridine, pyrrole, furan and thiophene during acid corrosion of nickel and an attempt to correlate this property with their structural parameters as well as chemical transformations in solutions at the metal/solution interface. Nickel has been chosen as corroding metal because of its well-known catalytic influence on many organic reactions.

EXPERIMENTAL

Nickel beads (99.99 per cent purity, Johnson Mathey) were used without further analysis. The detailed procedures for surface preparation of the electrode and the electro-chemical cell assembly have been described elsewhere[10]. Pyridine, pyrrole, furan and thiophene were procured from BDH (AR grade) and they were purified by distillation.

Corrosion currents, anodic and cathodic tafel slopes were calculated from polarisation resistence data. A small increment of 2mV potential was applied from the potentiostat through the counter electrode and the corresponding current was found out from the potential difference accross a standard resistance in series in the circuit. Experiments were carried out in deaerated solutions and the temperature of the system was maintained thermostatically constant at $25 \pm 1°C$. The metal electrodes were kept in solution for 2–3 hours to allow to come in equilibrium and the experiments were started when the open-circuit potential came practically to constant values. Cathodic and anodic polarisation data were taken maximum up to 20mV overpotential.

Corrosion currents were calculated from the measured polarisation data closed to open circuit potential by the method as described by Mansfeld[11]. The calculation is based on the Stern-Geary equation[12]

$$I_{corr} = \frac{b_a.b_c}{2.3\,(b_a + b_c)} \cdot \frac{1}{R_p}$$

where $\quad R_p = \dfrac{b_a.b_c}{2.3\,I(b_a + b_c)}\, \exp\left(\dfrac{2.3\,\Delta E}{b_a}\right) - \exp\left(\dfrac{2.3\,\Delta E}{b_c}\right)$

in which I and ΔE are the polarization current and corresponding overvoltage in the neighbourhood of corrosion potential ($\Delta E \rightarrow 0$).

Corrosion currents were calculated as follows :

(*i*) Current density-potential relationship for the anodic and cathodic polarisation studies were plotted between $\pm \Delta E = 20$mV. A tangent was then drawn along $\Delta E = 0$ and the slope of the tangent was then determined from $(dE/dI)_{i_{corr}} = R_p$.

(*ii*) At a certain value of ΔE, the corresponding current density was multiplied by 2.3 R_p and a plot of 2.3 R_p against ΔE was made.

(*iii*) From the above curves, tafel slopes b_a and b_c were determined by curve fitting method using theoretical curves calculated for various values of b_a and $b'_o s$.

(*iv*) I_{corr} was then finally calculated ushing the above Stern-Geary equation substituting the calculated values of R_p, b_a and b_c.

Results

Corrosion currents and other dissolution parameters of nickel in sulphuric acid in absence and in presence of organic additives are shown in Table I. Solutions containing pyridine, pyrrole and furan exhibit higher polarisation resistance than that in pure sulphuric acid and the calculated corrosion current values are all lower in presence of these additives than that in pure sulphuric acid. Very little changes in the cathodic tafel slope values depict that these organic compounds have little influence on the mechanism of cathodic hydrogen evolution reaction. Furan, however, at high concentration changed the cathodic tafel slope considerably. Anodic tafel slopes are increased in solutions containing pyridine whereas those in solutions containing pyrrole are decreased slightly. Pyridine and furan did not inhibit at low concentrations but significant lowering of corrosion currents occurred in presence of these additives at higher concentrations. Pyrrole, of course, exhibited as an effective inhibitor for nickel in sulphuric acid at all concentrations.

TABLE I

Polarisation data of acid corrosion of nickel in presence of various amounts of organic heterocycles

Solution	R_p (Ohm)	2.3 $R_p I$ at	b_c mv/dec. (calculated)	b_a mv/dec.	I_{corr} µA/cm³ (calculated)	I_{corr} µA/cm³ (Galvet)	Inhibition efficiency (I%) calculated
¹N H₂SO₄	1.84	23.06	115	120	13.23	13.0	—
+10⁻⁵M pyridine	1.94	22.94	119	130	13.92	10.8	—
+10⁻³M ,,	4.0	22.84	113.5	130	6.59	7.4	48.67
+10⁻¹M ,,	6.0	22.63	105	132	4.32	4.5	67.34
+10⁻⁵M pyrrole	2.5	23.96	120	90	8.944	8.0	33.93
+10⁻³M ,,	3.16	23.31	115	108	7.66	7.8	42.10
+10⁻¹M ,,	5.4	23.16	110	110	4.42	4.4	66.51
+10⁻⁵M Furan	1.84	23.06	115	120	13.23	9.0	—
+10⁻³M ,,	2.68	23.11	116	118	9.5	8.7	28.19
+10⁻¹M ,,	4.0	22.08	79	120	5.18	6.0	60.84
+10⁻⁵M Thiophene	1.31	20.93	120	130	13.9	13.5	—
10⁻³M ,,	1.15	20.53	54	135	14.53	15.0	—
10⁻²M ,,	1.32	22.05	85	135	17.18	22.5	—

Thiophene does not behave in the same way as the other three heterocycles. On the contrary this compound catalysed the dissolution of nickel in sulphuric acid.

DISCUSSION

In order to understand the various inhibition characteristics of these organic heterocycles during acid corrosion of nickel it is necessary to discuss their chemical behaviour in sulphuric acid solution particularly at the nickel/acid interface. All the four compounds-pyridine, pyrrole, furan and thiophene are conjugated molecules with various ring heteroatoms and the aromaticity of the molecules and the charge density at the various ring atoms depend on the electronegativity of the heteroatom and the tendency of the π-electrons of the heteroatom to participate in the extensively delocalized π-electron system. If the inhibition by these compounds is supposed to be due to adsorption of these mulecules on the metal surface through their d_π-p_π interaction, then the π electron charge densities on the heteroatoms, their electronegativities and electron affinities should play important roles during acid corrosion of nickel in presence of these organic additives. The values, as shown in the following Table II show that a strong adsorber is rather a weak inhibitor in this case.

From Table II it is apparent that simple d_π-p_π interaction is not the only phenomenon which is responsible for corrosion inhibition action by these organic heterocycles.

The π-electron charge densities at the various positions of the pyridine ring have been calculated by self consistent field method[13] which shows that there is a considerable drift of electrons from the ring towards the nitrogen atom. Pyridine is thus a weak monoacid base and forms stuble pyridinium cation in acid solution. On the other hand the two of the six π-electrons required for aromaticity for other five membered heterocycles-pyrrole, furan and thiophene must come from the heteroatoms. Hoffman and Cronowitz[14] have found from NMR measurements that chemical shifts of α- and β-hydrogen atoms in pyrrole, furan and thiophene

TABLE II

Some quantum chemical parameters of the organic heterocycles and corrosion current data of nickel in sulphuric acid and presence of these heterocycles

	Pyridine	Pyrrole	Furan	Thiophene
π-electron charge density on heteroatom	1.194[a]	1.692[a]	1.705[a]	1.810[a]
Ionization Potential (eV.)		8.40[b]	8.99[b]	9.12[b]
Corrosion Current of Ni in presence of 10^{-1}M organic additive (μA/cm^2)	4.50[c]	4.40[c]	6.00[c]	22.50[c]

(a) Same as ref. 17.
(b) P Linda, G Marino and S Pignataro, Ris. Sci. **39**, 666 (1969).
(c) Data taken from Table I.

are 0.6ppm, 1.05ppm and 0.125ppm respectively with respect to that of benzene as zero. This shows that the aromatic character of the thiophene ring is much closer to benzone. The increasing aromatic character of the series furan, pyrrole and thiophene can, therefore, be related to both the polarizability and electonegativity of the heteroatoms as the electronegativity decreases and the polarizability increases in this order O-N-S.

Pyridine has produced a shift in open-circuit potentials slightly towards negative direction. The direction of the shift of potential is an indication that the compound has either little influence on the cathodic partial process or influence on both cathodic and anodic processes simultaneously. It is quite obvious that, owing to the acidity of the medium, pyridine interacts with the metal surface through ion-pair formation between positively charged pyridinium ions and negatively charged metal surface. Pyridine does not reduce the corrosion current appreciably at low concentrations although at high concentrations considerable inhibition of the dissolution of nickel takes place. Felloni and Cozi[15] have studied the effect of pyridine on the acid corrosion of iron and have observed that the compound is adsorbed on the metal surface as free base which is formed by the electrochemical reduction of proton at the electrode surface. Pyridine was found to have no influence on the dissolution parameters during anodic dissolution of nickel in sulphuric acid[16]. This shows that the compound acts mainly as a cathodic inhibitor and is adsorbed on the nickel surface through electrostatic interaction between pyridinium cation and negatively charged metal surface. The charge on nickel surface in sulphuric acid at open-circuit potential is very near to zero (relative to pzc of nickel)[17]. So the electrostatic interaction between pyridine and metal surface, at open circuit potential, cannot be strong. Relatively low inhibition characteristics of pyridine on nickel corrosion, particularly at low pyridine concentration, show that the inhibition is mainly cathodic in nature and unlike in iron-acid system, the adsorption through π-electron system is not so predominant.

Pyrrole behaves mainly as a very reactive aromatic compound towards electrophilic reagents and hence this compound is expected to be adsorbed on the cathodically charged metal surface and thereby behaves as a cathodic inhibitor. The high inhibition characteristics of the compound cannot be explained simply on the basis of its adsorption on the metal surface because pyrrole ring possesses neither very high aromatic character nor strong basicity like pyridine. Nuclear magnetic resonance studies show that in aqueous acid solutions pyrrole accepts protons at the α-position to give stable cations[18]. These cations have no aromatic stability due to lack of π-electron sextet but they are very reactive and can readily polymerize by radical and/or ionic mechanism as follows[19].
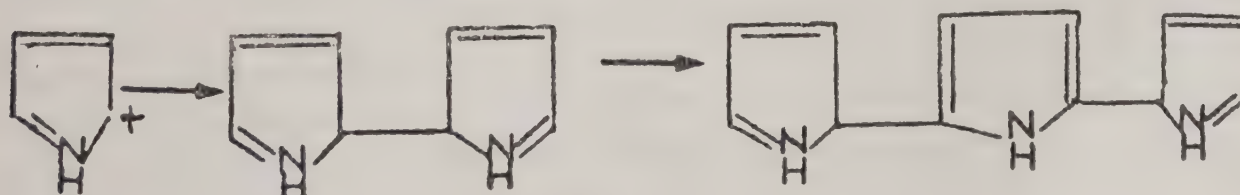
In presence of pyrrole sudden increase of passive current density during potentiostatic anodic polarivation of nickel in sulphuric acid between the potential range + 550mV and + 800mV was observed[16] and was explained to be due to rupture of the polymeric coatings and subsequent formation of the stable passive layer. Pyrrol solution in sulphuric acid turns turbid during the experiment because of polymerization. The above physico-chemical characteristics of pyrrole show that the corrosion inhibition property of the compound is, perhaps, due to interaction between the positively charged organic species and the metal surface as well as π-electron system of the polymeric molecule and the vacant d-orbitals of the metal atoms. The lowering of the anodic tafel slopes as calculated from the polarisation resistance data is supposed to be due to formation of (Metal-inhibitor)$_{ads}$ or (Metal oxide-inhibitor)$_{ads}$ species on the anodic metal surface. The slight shift of the open circuit potentials to the negative direction indicate that although pyrrole acts as a mixed inhibitor, the cathodic inhibition is more predominant than anodic inhibition. The preferential adsorption of the compound on the cathodically charged metal surface has been observed from the fact that inhibition by pyrrole is considerably reduced in presence of chloride ions. Hudson *et al.*[20] have studied the effects of pyrrole-halide mixture on the acid corrosion of iron and concluded that in presence of chloride ions, the pzc of the metal is shifted more towards anodic direction and thereby reduces the adsorbability of the protonated pyrrole species. At very high concentrations, of course, the polymeric species blanket the metal surface and influence both on the cathodic and anodic reactions.

Furan, like pyrrole, is an aromatic heterocyclic five membered ring. The physico-chemical data suggest that furan behaves chemically as diene ether which possesses unusually great resonance stabilization. Although enol ethers are, in general, very easily hydrolysed by dilute acids to the corresponding carbonyl compounds furan is not so easily hydrolysed because of the initial attack of the proton involves the electrons of the oxygen atom which contribute to the six π-electron system required for aromaticity. Their withdrawal reduces the resonance energy of the ring and converts aromatic furan into very much less stabilized cation. Hockerman
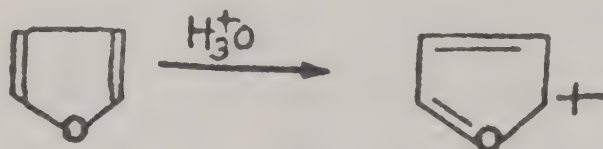

and after[21,22] have shown that the extent of adsorption of furan derivatives on the metal surface depends on the charge density of the oxygen atom of furan. Because of the electrophilic nature of the heterocyclic oxygen atom, the compound is less effective as inhibitor than pyridine in pyrrole. Shifting of the open circuit potentials towards negative direction may be an indication of the intraction of the positively charged oxygen atom of the ring and metal surface. Calculations of anodic tafel slopes from the polarisation data show that the compound has no influence on the anodic metal dissolution reactions. Furan, as shown in the table, is not an effective

inhibitor for acid corrosion nickel particularly at lower concentrations. At high concentration, it may be concluded that furan inhibits the acid corrosion of nickel by suppressing mainly the hydrogen evolution reaction and therefore, the inhibition action is perhaps, due to adsorption, primarily through coulombic interaction between nickel surface and positively charged furan species. Anodic dissolution of nickel in presence of furan in sulphuric acid showed that the compound has no influence on the dissolution parameter of nickel and so the anodic interaction between the π-electron system of the compound and the positively charged metal surface is thought to be very weak[16].

Thiophene resembles benzene rather than furan and pyrrole in many of its physico-chemical characteristics. Since sulphur atom is less electronegative than oxygen or nitrogen atom, it releases more readily the π-electrons to the ring system to form sextet required for aromaticity. Similarity between benzene and thiophene, thus, allows us to assume that thiophene may be adsorbed on the metal surface through its π-electron system also.

The influence of thiophene on the acid corrosion of nickel in sulphuric acid shows that the compound behaves in a completely different way from that of other three compounds. Thiophene accelerates the rate of metal dissolution at all concentrations. The electrochemical behaviour of the iron group of metals in acid solutions containing organic sulphur compounds have been investigated by many investigators[9]. In most of the cases it was observed that organic sulphur compounds inhibit the acid dissolution of iron through adsorption of the compounds on the metal surface by their extensively delocalised π-electron system whereas they activate the dissolution of nickel in acid solutions by being decomposed into S^{2-} or HS^- ions at the metal/solution interface. Rosey and Shreir and others[23] have interpreted the results of inhibition or activation of nickel in acid solutions in presence of organic sulphur compounds in terms of the actual relative concentration of sulphur compound and its decomposition products (S^{-2} or HS^-). Desulphurization of thiophene and its derivatives by hpdrogenolysis in presence of nickel catalyst is a well known reaction[24].

$$\text{thiophene} \xrightarrow[\text{Ni}]{H^+ + e^-} CH_3-CH_2-CH_2-CH_3 + H_2S$$
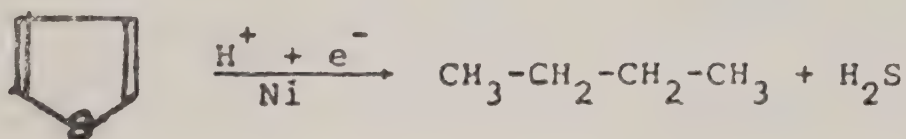
Nickel catalysts are shown to be rapidly poisoned by thiophene indicating formation of nickel sulphide on the metal surface. The strong catalytic activity of thiophene on the acid corrosion of nickel should, thus, be explained on the basis of its adsorption and subsequent decomposition equilibrium at the metal/solution interface. The compound shifts the open circuit potentials in the negative direction indicating thus that the interaction of the compound with the metal surface takes place through ion-pair formation between the positively charged protonated thiophene species and negatively charged surface metal atoms.

Low cathodic Tafel slope values indicate that thiophene influences on the mechanism of the hydrogen evolution reaction. Moreover, from the galvanostatic studies[25] in the higher overpotential ranges, thiophene is shown to increase the rate of hydrogen evolution reaction during cathodic polarisation, thus indicating that the compound, after adsorption on the metal surface, is decomposed into some degraded product which are rapidly desorbed from the metal surface. In the cathodic potential range, because of the presence of hydrogen ions in the vicinity of the interface, the decomposed sulphide ions come into the bulk phase leaving the metal surface exposed into the corrosive media. In the anodic potential region, due to lack of aqueous hydrogen ions near the interface, the decomposed sulphide ions unite with nickel ions forming insoluble nickel sulphide coatings and thereby exhibiting irregular corrosion current densities as are usually shown from the potentiostatic polarisation curves of nickel in presence of organic sulphur compounds.

Conclusion

From the overall investigations of the acid corrosion of nickel presence of pyridine, pyrrole, furan and thiophene, it may be concluded that all the compounds are adsorbed on the metal surface primarily through the interaction between the positively charged protonated organic species and surface metal atoms. This interaction is very weak because of very small negative charge on the nickel surface in sulphuric acid at the open circuit potential. Pyridine and furan exhibit relatively poor inhibition action particularly at low concentration because of this weak electrostatic interaction. Pyridine, however, acts as a better inhibitor than furan due to stronger basicity of nitrogen atom and thereby forms stable protonated species. Pyrrole, in acid solution, is protonated and polymerizes at the metal/solution interface which blankets the metal surface and thereby protects it effectively from further dissolution. The compound behaves as a mixed inhibitor and shows that in addition to electrostatic metal-cation interaction, the compound, in the form of polymeric species, is adsorbed on the metal surface through $d_\pi - p_\pi$ interaction which might lead to the formation of (Metal-inhibitor)$_{ads}$ or (Metal-OH-inhibitor)$_{ads}$ complexes and thereby charges the mechanism of anodic reactions. Thiophene catalyzes the dissolution of nickel in sulphuric acid. In the acid solution the compound reacts with proton and the adsorbed species is desulphurized at the metal/solution interface in contact with nickel as catalyst. The rapid desorption of sulphide ions thus increases the rate of hydrogen evolution reaction at the cathodic surface and consequently increases metal dissolution.

Acknowledgement

References

1. H Fischer, *Ist Europ. Symp. of Corrosion inhibitors, Ferrara*, Suppl. No. 3 (1961).
2. R R Ayer and N Hackerman, *J. Electrochem. Soc.* **112** (1965) 507.

3. F M Donahue and Ken Nobe, *J. Electrochem. Soc.* **112** (1965) 886.

4. F M Donahue, A Akyama and Ken Nobe, *J Electrochem. Soc.* **114** (1967) 1006.

5. F M Donahue and Ken Nobe, *J. Electrochem. Soc.* **114** (1967) 1012.

6. V P Grigoryev and O A Osipov, Extended Abstract 3rd Int. Cong. Metallic Corros. Moscow (1966) p. 116.

7. N Hackerman and R M Hurd, *Ist Int. Cong. Metallic Corros.* London (1962) p. 166.

8. O L Riggs and R L Every, *Corrosion* **18** (1962) 262.

9. G Trabanelli and V Carasetti, *Mechanism and phenomenology of Organic Inhibitors.* Corrosion Science and Technology, (Eds. Fontana and Staehle) Vol. 1, pp 147, Plenum Press.

10. A N Maitra and Kalyan Bhattacharya, *Trans. SEAST* **14** (1979) 221.

11. F Mansfeld, *J. Electrochem. Soc.* **120** (1973) 515.

12. M Stern and A I Geary, *J. Electrochem. Soc.* **104** (1957) 56.

13. A Muller, M Lykos and P Schmelsing, *J. Amer. Chem. Soc.* **84** (1962) 4623.

14. A R Hoffman and S Cronowitz, *kriv. Kemi.* **16** (1960) 539.

15. L Felloni and A Cozzi, Proceedings of the Second International Congress on Metallic Corrosion, Inhibititors, Ferrara (1965) p. 279.

16. A N Maitra, G Singh, K Bhattacharyya and R K Kaushik, *Effects of some organic heterocycles on the anodic dissolution of nickel in acid solutions* (1983).

17. L I Antropov, *Theoretical Electrochemistry.* Mir Publishers (1964).

18. R M Acheson, *Introduction to the Chemistry of Heterocycles compounds.* Interscience Publications, 3rd Edition p. 174.

19. G F Smith, *Adv. Heterocycl. Chem.* **2** (1963) 287.

20. R M Hudson, T J Butler and C J Warning, *Corros. Sci.* **17** (1977) 571.

21. N Hackerman and H Vidyanathan, *Corros. Sci.* **11** (1971) 737.

22. A N Maitra, *Indian J. Chem.* **15** (1977) 451.

23. (i) C G W Rosey and L L Shreir, *Trans. Inst. Met. Fin.* **45** (1967) 206.
    (ii) A N Maitra, A Hecht, B Droste and H G Feller, *Metalloberflache* **3** (1979) 112.

24. H Hauptmann and W F Walter, *Chem. Revs.* **62** (1962) 347.

25. R K Kaushik, *Ph.D. thesis*, Delhi University (1980).

SOIL CHARACTERISTICS AND FLORISTIC COMPOSITION OF SOME SUB-ALPINE FORESTS OF DARJEELING (WEST BANGAL)

S K Banerjee, D K Pal *and* S P Banerjee*

Forest Soil-Vegetation Survey, Eastern Region, Kotebazar, Midnapore 721 101

Soil characteristics and floristic composition between the altitudes 3,500 and 3,962 m in Sandakphu Block of Darjeeling (special) Forest Division were studied. The soils are highly acidic, poor in base status and are very rich in organic matter which is maximum at the surface. They do not manifest any translocation of either Al or Fe. The forest of the region, classified as the East Himalayan Sub-alpine forest comparises mainly of evergreen conifers (Silver fir) with admixture of some broad-leaved species (*Rhododendron*). Silver fir (*Abies densa*) is the dominant species characterised by its low branching habit with very poor regeneration status, in general.

INTRODUCTION

The soil characteristics and vegetational composition between the altitudes 3500 and 3962 m were studied in Sandakphu Block of Darjeeling Himalayan Region with a view to find out the extent of variation from and semblance with our previous works in this line[1-4]. Informations on similar lines for the other parts of Himalayas are available in some earlier studies[5-8].

DESCRIPTION OF THE STUDY AREA

The study area in Sandakphu Block, Singalila Range stretches between 87°59′ and 88°53′ east longitudes and 26°31′ to 27°13′ north latitudes. The mean annual precipitation varies from 3200 to 3700 mm. Summer temperature rises to as high as 8 to 9°C. During winter temperature drops down below 0°C and the whole area remains covered with snow for a good part of the season. Sandakphu is at the highest place in the Singalila Range.

Vegetation cover mainly comprises pure consociation of *Abies densa* (Silver fir) admixed with various species of *Rhododendron* and some other broadleaved species. In this region forests are generally evergreen.

EXPERIMENTAL

Three representative pedons were selected and the morphology of the pedons as well as the general features of the profile sites were recorded (Appendix). Particle

---

*Forest Soil-Vegetation Survey, F. R. I. & Colleges, Dehradun.

size analysis, pH (1 : 2.5 water and 1 (N) — KCl), organic carbon, total N, C.E.C. (NH_4OAc method), exchangeable bases and extractable H^+ and Al^{3+} and elemental chemical composition were determined by standard procedures[9,10]. Extraction and fractionation of humus was done as per Banerjee and Mukherjee[11] and carbon of humic and fulvic acids determined according to Kononova[12].

For vegetational study quadrat analysis as suggested by Dombois and Ellenberg[13] was followed and quadrats of 100 sq m (10m × 10m) were laid out to study trees (tree quadrat), 25 sq. m. (5m × 5m) for shrubs (shrubs qudrat) and 1 sq. m. (1m × 1m) for regeneration (regeneration quadrat). In each stand, 12 tree quadrats were laid out continuously (belt transect) and girth at breast height and height of each tree measured storeywise. Important value index (I–VI) of each species was than calculated from the relative values of frequency, density and basal area. The community was named after the dominant species of top storey securing the highest I–VI[14,15].

RESULTS AND DISCUSSION

A. *Soils* — Data pertaining to the physico-chemical and chemical characteristics of the profile samplesare shown in Tables I, II and III and vegetational parameters have been presented in Table IV.

All the pedon samples are strongly acidic and can be grouped under acid soils according to Soil Taxonomy. The ΔpH (difference between pH water and

TABLE I

Physico-chemical characteristics of the soils

Depth (cm)	Mechanical separates			pH (1 : 2.5)		Organic carbon	Total N	Mobile form		Exchangeable acidity	
	Sand	Silt (%)	Clay	Water	KCl			Fe_2O_3	Al_2O_3	H+	Al³+ me/100g
Upland											
0–32	52.3	30.1	17.6	4.0	3.1	6.32	0.435	0.400	0.308	0.87	7.58
32–53	43.6	23.6	32.8	4.0	2.9	4.05	0.252	2.100	6.400	0.89	7.07
53–110	61.6	16.8	21.6	4.5	3.1	2.55	0.161	0.686	1.646	0.33	4.48
Midland											
0–23	57.5	28.9	13.6	4.1	2.8	4.86	0.444	0.871	0.961	0.46	5.34
23–40	72.4	18.4	9.2	4.7	3.0	0.98	0.056	0.471	0.235	0.10	1.89
40–57	74.4	16.4	9.2	5.3	3.3	0.56	0.028	0.257	0.135	0.11	1.38
57–100	81.2	6.8	12.0	5.4	3.2	0.52	0.023	0.100	0.260	—	1.20
Lowland											
0–20	42.6	35.8	21.6	3.9	3.1	8.33	0.325	0.886	1.286	1.68	8.27
20–38	44.0	25.8	30.2	3.8	2.9	5.39	0.318	0.629	1.553	0.62	9.99
38–56	48.9	21.5	29.6	4.2	3.0	3.07	0.217	0.571	1.373	0.41	6.72
56–74	56.4	12.8	30.8	4.7	3.0	1.16	0.098	0.557	1.077	0.52	3.96
74–120+	78.7	8.5	12.8	5.3	3.2	0.48	0.037	0.186	1.422	0.25	2.07

TABLE II

Chemical characteristics of the soils

Depth (cm)	C.E.C.	Exchangeable cations me/100g				Base satura-tion(%)	Total chemical analysis % ignited basis						
		Ca++	Mg++	K+	Na+		SiO₂	Fe₂O₃	Al₂O₃	CaO	MgO	K₂O	P₂O₅
Upland													
0–32	26.7	0.76	0.27	0.86	0.02	7.2	78.1	2.23	3.82	0.36	0.13	0.66	0.131
32–53	24.9	0.50	0.23	0.72	0.02	6.0	69.8	4.99	8.38	0.39	0.23	0.57	0.213
53–110	16.1	0.43	0.04	0.51	0.01	6.0	76.4	5.62	7.23	0.64	0.31	0.72	0.025
Midland													
0–23	24.4	0.85	0.12	0.54	0.01	6.2	71.7	4.82	8.68	0.57	0.13	0.72	0.202
23–40	6.1	0.37	0.08	0.43	0.01	14.6	75.2	4.46	11.04	0.99	0.48	1.22	1.120
40–57	4.7	0.39	0.06	0.46	0.02	19.8	78.4	3.85	12.25	0.78	0.51	1.19	0.120
57–100	3.8	0.43	0.12	0.32	0.01	25.8	71.7	4.55	23.95	1.17	0.56	1.43	0.593
Lowland													
0–20	38.4	0.93	0.45	1.02	0.02	6.3	57.2	5.63	24.39	0.50	0.28	1.07	0.332
20–38	27.8	0.45	0.33	1.06	0.02	6.7	62.6	6.96	20.29	0.67	0.43	1.10	0.272
38–56	10.7	0.37	0.25	1.01	0.01	15.3	62.1	6.96	17.54	0.18	0.64	1.13	0.176
56–74	18.7	0.33	0.17	0.98	0.02	8.0	72.2	6.34	17.76	0.43	1.02	1.21	0.426
74–120+	7.9	0.37	0.10	0.82	0.03	16.7	71.6	5.35	20.52	0.09	1.14	1.39	0.094

TABLE III

Quantity and Composition of humus in soils

Depth (cm)	Humus carbon	Humic acid % carbon	Per cent over total humus	Fulvic acid carbon (%)	Per cent over total humus	$C_{ha}*/C_{fa}$
Upland						
0–32	3.79	2.09	55.14	1.70	44.85	1.23
32–53	2.92	1.52	52.05	1.41	48.28	1.08
53–110	2.05	1.03	50.24	1.02	49.76	1.01
Midland						
0–25	3.20	1.58	49.37	1.62	50.62	0.97
23–40	0.77	0.36	46.75	0.41	53.24	0.88
40–57	0.40	0.19	47.50	0.21	52.50	0.90
57–100	0.40	0.15	37.50	0.25	62.50	0.60
Lowland						
0–20	4.44	1.88	42.34	2.56	57.65	0.73
20–38	3.05	1.44	47.21	1.61	52.78	0.89
38–56	1.94	0.85	43.81	1.09	56.18	0.78
56–74	0.85	0.30	35.49	0.55	64.70	0.55
74–120 +	0.28	0.09	32.10	0.19	67.85	0.47

*ha—Humic acid
fa—Fulvic acid

KCl) is fairly wide and suggests that pH values are not near their zeropoint charge. Orgnic matter content is generally very high with maximum at the surface. It decreases uniformly down the profile. The soils are highly melanished and the spheriodal structure in several cases can be ascribed to the intimate mixing up of the humus with the soil separates unlike in previous studies[1-3]. The humic to fulvic acid ratio in Pedon I is greater than unity, uncommon to the high-altitude forest soils. In other Pedons, however, fulvic acid predominates over humic acid and tend to increase with increasing depth. Transportation of humus to develop a zone of humus enrichment in the profile is not very pronounced.

It was interesting to see that inspite of high accumulation of organic matter in the 01 layer under the prevailing high rainfall, cool climate and acidic conditions (the acids are unsaturated with bases as the base saturation is very low) there was no release of Al and Fe due to acid hydrolytic breakdown of soil minerals and their interaction with humic constituents and as evidenced from the more or less gradual decreases of the mobile form of Fe_2O_3 down the profile, did not manifest any move· ment of either Al or Fe constituents (Table I). These humus substances also found to contain a very negligible amount of Fe and Al but the soil nitrogen content, as expected, was fairly high (0.023 to 0.444 percent).

Amongst the exchangeable cations Al^{3+} is the most preponderant on the exchange complex followed by H^+, Ca^{++} and Mg^{++}. The C.E.C. shows a very

TABLE IV

Ecological values of Sub-apline Silver fir forests

	Relative			I VI
	Frequency	Density	Basal area	
Top storey				
Abies densa	100	100	100	300
Second Storey				
Abies densa	45.5	47.4	49.0	141.9
Rhododendron sp.	27.3	36.8	41.2	105.3
Pyrus foliolosa	9.1	5.3	3.9	18.3
Betula alnoides	18.2	10.5	5.9	34.6
Lyonia ovalifolia	9.1	5.3	3.9	18.3
Shrubs/Herbs				
Anaphalis cunecifolia	13.9	14.2		
Polygonum molle	11.0	12.8		
Saxifrag diversifolia	11.0	12.3		
Berberis conceinna	10.0	11.5		
Perimula deuticulates	12.0	10.6		
Senecio chrysanthemoides	9.0	10.2		
Anaphalis araneosa	8.0	9.3		
Dubyaeo hispida	7.0	5.8		
Rosa sericea	7.0	6.6		
Rhododendron sp.	8.0	4.4		
Gaultheria nummuleriodies	2.0	0.8		
Arundinaria aristata	2.0	0.8		

poor base status (Table II) and indicates predominance of illitic clay minerals over others. Higher amount of K_2O in soils also substantiates this contention. The depleting trend of the base ions may be attributed to the standing calcifugous plants which can not efficiently recycle these ions which, in turn, are leached with the percolating water out of the root zone.

B. *Vegetation*—The forests of the study area may be classified as East Himalayan subalpine Forests comprising mainly of evergreen conifers (Viz. Silver fir) admixed with some broad leaved species Viz. *Rhododendron.* Silver fir (*Abies densa*) is the dominant species characterised by its low branching habit. Broad-leaved species of Birch also grow in the vicinity of Silver fir at places. Though few trees of *Rhododendron* occur sporadically, it is mainly a consociation of Silver fir in Sandakphu Block.

(i) *Distribution* : Pure consociation of Silver fir are distributed between 3000m to 4000m altitudes. Above 4000m altitude the forests lose their quality and join the alpine scrub type scrub type of vegetation.

(ii) *Floristics* : This community is a consociation of *Abies densa* with scattered *Rhododendron companulatum* and *Betula alnoids* in the second storey. The third

storey comprises of *Arundinaria aristata, Rosa sericea* etc. under a moderately open canopy, and few scattered grass like *Agropyron bromus* etc. under a closed one. There is also an appreciable amount of epiphytic moss and lichens on the stems.

(iii) *Structure and composition* : Vertical stratification is quite difficult due to variation in height of trees. At open places pure patches of *Rhododendron companulatum* are seen. At other places dense growth of *Arundinaria aristata, Rosa sericea, Berbaris concinna, Rubus* sp., *Gaultheria* sp. etc. are found. The undergrowth is variable from practically nil (under heavier thickets) to few (under thin cover). The average height of dominant trees varies between 10 and 15m. *Abies densa* naturally regenerates in the area. Places prone to frequent fires and high biotic pressure support *Gaultheria nummularioides* in patches, *Berberis conceinna, Rosa sericea* etc. admixed with scattered shrubs like *Polygonum molle, Saxifraga diversifolia, Primula deuticulata, Senecio chrysanthemodes, Anaphelis cunecifolia, Dubyasa hispidea* etc.

(iv) *Vegetation community values* : As can be seen from the various ecological values of the community (Table IV) the top storey comprises of pure Silver fir, where as the second storey though dominated by Silver fir has scattered occurence of *Rhododendron, Betula alnoids, Pyrus foliolosa* etc. also and excepting *Rhododendron* sp. others are of low values of relative frequency, density and basal area with resultant low values of I–VI.

The results of quadrat study carried out to determine the distribution of other shrubs/herbs within the study area (Table IV) show that *Anaphalis cunceifolia* has got the highest value of relative frequency and density followed by *Pollygonum molle* and *Saxifrage diversifolia*. Regeneration in this community is rather poor and excepting recruitment of seedlings of *Rhadodendron* sp. regeneration of the deminant trees is inadequate. The soils of the three landscapes although differ appreciably from one another in their physicochemical attributes but commensurate to that differences in the floristic compositions do not exist.

REFERENCES

1. D K Pal, S Nath, and S K Banerjee, *J. Indian Soc. Soil Sci.* (1982) (In Press)
2. D K Pal, S Nath, and S K Banerjee, *J. Indian Soc. Soil Sci.* (1983 *a*) (Communicated)
3. D K Pal, S Nath, and S K Banerjee, *Indian Agric.* (1983 *b*) (In press)
4. S Nath, D K pal, and S K Banerjee, *Indian Agric.* 27 (1983) 125
5. R P Dhir, *J. Indian Soc. Soil Sci.* 15 (1967) 61
6. R P Dhir, *Indian Forester* 96 (1970) 573
7. R P Dhir, *J. Indian Soc. Soil Sci.* 19 (1971) 179
8. S K Ghabru, and S K Ghosh, *Indian Agric.* 23 (1979) 73
9. M L Jackson, *Soil Chemical Analysis*, Prentice Hall of India Pvt. Ltd., New Delhi (1973)
10. C A Black, *Methods of Soil Analysis*, Am. Soc. Agron. Inc., Madison, Wisconsin, U.S.A. (1965)
11. S K Banerjee, and S K Mukherjee, *J. Indian Soc. Soil Sci.* 23 (1975) 310
12. M M Kononova, *Soil Organic Matter*, 2ndEnglish Edn,. Pergamon Press, New York (1966)
13. D M Dombois, and H Ellenberg, *Amms and methods of Vegetation Ecology*. John Willey & sons., New York, (1974)
14. J T Curtis, and G Cottom, *Plant Ecology work Book*, Laboratory Field Reference Manual. Bugess Publishing Co. Minisota. (1956)
15. R Mishra, *Ecology Work Book*, Oxford & I B H Publishing Co., New Delhi. (1968)

Appendix

The morphological feautures of the three profiles are given below :

Pedon 1

Harizon	*Depth (cm)*		*Description*

A$_1$ 0–32   :   Black (10 YR 2/1 M) loam; granular; very friable and slightly sticky; many fine iron concretions with many quartz particles; many roots; clear wavy boundary.

B$_{21}$ 32–53   :   Very dark brown (10 YR 2/2M) clay loam; granular; very friable and sticky; many fine to medium quartz with many iron concretions; many roots; clear wavy boundary.

B$_{22c_n}$ 53–110   ;   Dark yellowish brown (10 YR 3/4M) gravelly loam; weak fine subangular blocky; quartz particles many; many fine to medium iron concretions with some rusty specks; fine to medium gray (10 YR 6/1) mottles common; roots common.

C   110 +   :   Decomposed rocks.

Location	:	Singalila Range, Sandakphu Block, Darjeeling Division.
Vegetation	:	Silver fir (*Abies densa*) Rhododendron etc, natural forests.
Altitude	:	3962 m.
Physiography	:	Upland
Aspect	:	Easterly
Slope	:	40%
Remarks	:	Poorly drained, moderate errosion.

Pedon 2

Horison	*Depth (cm)*		*Destribution*

A$_1$ 0–23   :   Very dark brown (10 YR 2/2M) loam; granular; very friable and slighlty sticky; many fine iron concretions with many quartz particles; many roots; clear wavy boundary.

B$_{21}$ 23–40   :   Dark yellowish brown (10 YR 4/6M) sandy loam; single grained; loose and nonsticky; many fine iron concretions with many fine quartz particles; many roots; clear wavy boundary.

B$_{22c_n}$ 40–57   :   Brown (10 YR 4/3M) gravelly sandy loam; week fine sub-angular blocky; friable and slightly sticky; many medium to coarse iron concretions with many quarts particles; few roots; clear wavy boundary.

B$_3$ 57–100+   ·   Light yellowish brown (10 YR 6/4M) gravelly sandy loam; medium moderate subangular blocky; slightly firm and sticky; many iron concretions and quartz particles.

Location	:	Singalila Range, Sandakphu Block, Darjeeling Division.
Vegetation	:	Silver fir (*Abies densa*), Rhododendron etc.,
Altitude	:	3655m.
Physiography	;	Midland
Aspect	:	Westerly
Slope	:	10%
Remarks	:	Moderately drained, slight errosion.

Pedon 3

A₁	0–20	:	Very dark brown (10 YR 2/2M) silt loam; granular; very friable and slightly sticky; many fine iron concretions with many fine quartz particles; many roots; clear wavy boundary.

A₁   0–20   : Very dark brown (10 YR 2/2M) silt loam; granular; very friable and slightly sticky; many fine iron concretions with many fine quartz particles; many roots; clear wavy boundary.

B₂₂t   20–38   : Dark yellowish brown (10 YR 3/6M) clay loam; granular; very friable and sticky; discontinuous clay skins on ped surface; many fine iron concretions with many fiine quartz particles; many roots; clear wavy boundary.

B₂₂t   38–56   : Dark yellowish brown (10 YR 4/6M) clay loam; granular to fine subangular blocky; slightly firm and sticky; many distinct clay skins on ped surfaces; many medium to coarse quartz particles with few fine iron concretions; many roots; clear wavy boundary.

B₂₃t   56–74   : Dark yellowish brown (10 YR 4/6M) clay loam; medium moderate subangular blocky; firm and very sticky; many distinct clay skins on ped surfaces; many fine to medium quartz particles with many very concretions; few roots; clear wavy boundary.

BC   74–120+   : Brown (10 YR 5/3M) gravelly sandy loam; single grained; very friable and nonsticky; many medium to coarse quartz particles with many iron concretions; very few roots.

Location	:	Singalila Range, Sandakphu Block, Darjeeling Division.
Vegetation	:	Silver fir (*Abies densa*), Rhododendron etc.
Altitude	:	3530m,
Physiography	:	Lowland
Aspect	:	Westerly
Slope	:	10%
Remarks	:	Wall drained, slight errosion.

EXTRACTIVE SPECTROPHOTOMETRIC DETERMINATION OF ZINC IN COPPER BASE ALLOYS USING 1.10 PHENANTHROLINE AND ROSE BENGAL[+]

Y Anjaneyulu*, P Chandramouli *and* L Narasimha Murthy

Department of Chemistry, Nagarjuna University, Nagarjuna Nagar 522 510 (A. P.)

A method is described for the spectrophotometric determination of zinc (0.05 to 0.4 µg/ml) based on the extraction of zinc into nitrobenzene with 1–10 phenanthroline and rose bengal (Extra) as an ion pair. The interference of various other cations commonly encountered in some commercial alloys can be completely eliminated by carrying out prior extraction with diethyl dithio carbamate in presence of sodium thiosulphate and selectively back extracting zinc (II) with hydrochloric acid and this procedure has been very successfully applied for the determination of zinc (II) in copper base alloys. The extracting species of the ternary system is found to be [$Zn(Phen)_3^{2+} : RB^{2-}$] in nitrobenzene ($\epsilon = 1 \times 10^5$) and [$Zn(Phen)_2^{2+} : RB^{2-}$] ($\epsilon = 6. 5 \times 10^4$) in chloroform. The difference in the composition of the extracting species and higher molar absorptivity in nitrobenzene from that in chloroform is explained on the basis of donocity and dielectric constant of the solvent. With various fluorescein dyes as counter ions the conditional extraction of ternary systems in nitrobenzene is found to be in the order rose bengal > erythrosin > eosin > dichlorofluorescein > fluorescein.

Introduction

Zinc (II) reacts with 1.10 phenanthroline and 2.2' bipyridyl to give stable 1 : 2 and 1 : 3 complex cations[1] Spectrophotometric determination of zinc (II) with 1.10 phenanthroline (phen) was reported by Tananaiko and Bilenko[2] who extracted it as bispheanthroline zinc (II) cation paired by two rose bengal E(RB = tetrachlorotetraiodofluorescein) anions as an ion pair [$Zn(phen)_2^{2+} : 2(RB)^-$] into chloroform. The molar absorptivity of this coloured species was repooted to be 5.1×10^4 1 mole^{-1}cm^{-1} at 575 nm. We have observed that when nitrobenzene is used for the extraction instead of chloroform the molar absorpivity of the system is greatly enhanced, with a change in the composition of the coloured extracting species. The corresponding bipyridyl system also behaves similarly.

The availability of a number of strongly coloured nonchelating anionic dye stuffs such as the carboxylic acid members of the fluorescein series with substituted

---

halogens which can act as counter ions has led us to take up a systematic study on these ternary systems both in chloroform and nitrobenzene.

EXPERIMENTAL

Apparatus :

A Beckman DU-2- spectrophotometer was used for all absorbance measurements pH measurements were made on a ELICO expanded scale pH meter model No. pH 821B.

Reagents :

Zinc sulphate, 1,10 phenanthroline and 2,2'–bipyridyl solutions (3 × 10⁻²M were prepared from analytical grade (B.D.H.) reagents in doubly distilled water, which is acidified by adding 1 ml of concentrated sulphuric acid. 1 × 10⁻³M solutions of fluorecein C.I.No. 54350, dichlorofluorescein C.I.No. 45365, eosin C.I. No. 45380 (tetrabromofluorescein) erythrosin B.C.I. No. 45430 (tetraiodofluorescein and rose bengal extra C.I.No. 45440 (tetrachlorotetraiodofluoescein) were prepared by dissolving the required amount (all BDH/ENGLAND—samples) in doubly distilled water rendered alkaline by adding 2 ml of 1M sodium hydroxide. All the solvents were distilled before use.

PROCEDURE

Extraction :

To an aliquot of 1–10 ml of zinc (II) solution (containing 1–10 μg of zinc) in a 125 ml separatory funnel add 3.0 ml of the dye solutions (1.0 × 10⁻³M) and 2.0 ml of 1, 10 phenanthroline (3 × 10⁻²M) and 2.0 ml of 1 M sodium acetate. Adjust the pH to 7.0 by adding required decinormal sodium hydroxide and dilute to 20 ml with distilled water. Shake the solution with 20 ml of nitrobenzene for 2 min. After separation, centrifuge the organic phase and measure its absorbance at 575 nm against a similarly prepared reagent blank. Determine the zinc content by computing the absorbance from a standard Beer's law curve.

Determination of zinc in copper base alloys :

Transfer a known weight (75–150 mg of BCS 183/2 or 750–1200 mg of BCS 304) of Copper base alloy in a 250 ml beaker and add 10 ml of water. Cover this with a watch glass and add 10 ml of HNO₃. After the initial vigorous reaction subsides, digest on a hot plate until the sample dissolves complemetely and boil gently for 5 min. till brown fumes are expelled. Dilute to 50 ml with hot water and maintain the temperature of the solution just below the boiling point for 1 h. Separate the residue if any from the hot solution through a whatman filter paper and wash the precipitate with hot 1 per cent nitric acid and 5 times with hot water. To the filtrate add 4 ml of concentrated sulphuric acid and evaporate the solution carefully until white fumes are evolved. Allow the solution to cool and wash down the beaker with 50 ml of water and heat nearly to boiling. Stir for 5 min. and filter the solution through a porcelain filtering crucible. Wash the precipitate thoroughly with cold 1:50 sulphuric acid, collect the filtrate quantitatively, and make up to 250 ml so that the zinc concentration falls in the Beer's law range.

Transfer 5 ml of this solution to a 125 ml separatory funnel. Add to this solution 2.5 ml of 1×10^{-1} M thiosulphate and 5 ml of 10^{-3} M diethyl dithiocarbamate (DDTC). Adjust the pH to 4 by adding sufficient decinormal sodium hydroxide, and equilibrate with 10 ml of chloroform for 2 min. Separate the organic phase and back extract zinc selectively from this solution by shaking with 10 ml of 0.4 M hydrochloric acid for 5 min. in another separatory funnel. Remove the organic phase and neutralise the aqeous phase in the funnel by using 1 ml of 4 M sodium hydroxide, add 1 ml of 1×10^{-1} M sodium thiosulphate solution and determine zinc as described in the extraction procedure.

RESULTS AND DISCUSSION

It is observed that zinc (II) is not extracted into benzene dichlorobenzene, nitrobenzene chloroform, n-hexane, carbontetrachloride, 1,2 dichloroethane, n-butanol, methyliso butylketone and diethyl ether in the presence of either 1,10 phenanthroline or any of above mentioned anions alone. Chloroform or nitrobenezene extract the zinc (II) in the presence of 1,10 phenanthroline and any one of the anionic dyes giving rise to intensely coloured ternary complexes. With fluorescein the colour of the ternary extracting system is found to be less intense. Benzene, or carbontetrachloride, extract neither the dye nor the ternary complex. Alcohols, ketones the esters are not useful for spectrophotometric determination as they extract free dye also along with the complex. The formation of a third phase (solid) at the interface is observed in the case of diethylether and dichlorobenzene but no extraction.

Optimum conditions: A two-minute equilibration period is found to be sufficient for obtaining maximum absorbance in all these ternary systems. The colour is stable at least for 24 h. The optimum pH range is found to be 6.5 to 7.5. In order to obtain maximum colour response of the ternary comlex in nitrobenzene, 5-fold excess of 1,10 phenanthroline and 10-fold excess of the dye are found to be sufficient in all the ternary systems. The volume of the aqueous phase is. found to have no effect on the absorption characteristics of the extracted species, and the absorbance of the nitrobenezene extract remains constant even when extraction of zinc was carried out from aqueous phase twice to the volume of nitrobenzene. The absorption and extraction characteristics of zinc-phenanthroline dye anion ternary systems in choloform and nitrobenzene are given in Table I. Rose bengal is found to be most sensitive counter ion out of ali dyes, since it produces an intensely coloured ternary complex, the absorption spectra of which in chloroform and in nitrobenzene are shown in Fig. 1.

Although bipyridyl also forms similar ternary comlexes, it is found that they are of little analytical use since many foreign ion interfere seriously in the formation of these complexes.

Analytical applications : In view of the high moral absorptivity of the zinc (II) penanthraline-rose bengal E system extracted into nitrobezene analytical applications are explored with this system. This system obeys Beer's law up to 10 μg of zinc per 20 ml at 575 nm. However from Ringbom's (1938) plot the optimum range for the photometric determination zinc (II) is found to be 1 to 7 μg per 20 ml. The

TABLE I

Absorption and extraction characteristics of zinc (II)–phenanthroline dye anion ternary system

System	max^{a}m		Molar extinction coefficient		Beer's law range	Composition of the extracting species		Extraction constants
	A	B	A	B	B	A Zinc-phen-dye	B Zinc-phen-dye	B
Fluorescein	—	535	Not extractable	5,500	0.40 µg	1 : 2 : 1	1 : 3 : 1	1.2×10^3
Dichloro fluorescein	530	540	11,500	58,000	0.16 µg	1 : 2 : 1	1 : 3 : 1	2.6×10^6
Eosin	545	545–550	75,000	90,000	0.13 µg	1 : 2 : 1	1 : 3 : 1	2.7×10^8
Erythrosin	550	550–555	60,000	90,000	0.12 µg	1 : 2 : 1	1 : 3 : 1	5.68×10^8
Rose bengal (Extr)	575	575–580	65,000	1,00,000	0.10 µg	1 : 2 : 1	1 : 3 : 1	4.1×10^2

A. Results with chloroform as solvent
B. Results with nitrobenzene as solvent

interference of various foreign substances in the photometric determination of 10 µg of zinc (II) in 20 ml by the above method has been studied. Acetate, sulphate, citrate, chloride, nitrate, phosphate and tartarate do not interfere even when present in 100-fold concentration of zinc (II). Perchlorate even when in very low concentrations interfere seriously; this may be due to the formation of a colourless ion association complexes of the type [Zn (Phen)$_3^{2+}$ (ClO$_4$)$_2^{2-}$] in preference to the dye anion. Al^{3+}, Ba^{2+}, Mg^{2+}, Cr^{3+} do not interfere even when present in 100-fold excess to Zn(II). Ni^{2+}, Cd^{2+}, Pb^{2+}, Co^{2+}, Cu^{2+}, Mn^{2+} and Fe^{2+} interfere seriously. However, the interference of these ions can be eliminated completely by prior extraction along with zinc (II) into 10 ml of chloroform with 5 ml of 10^{-3} M sodium salt of diethyl
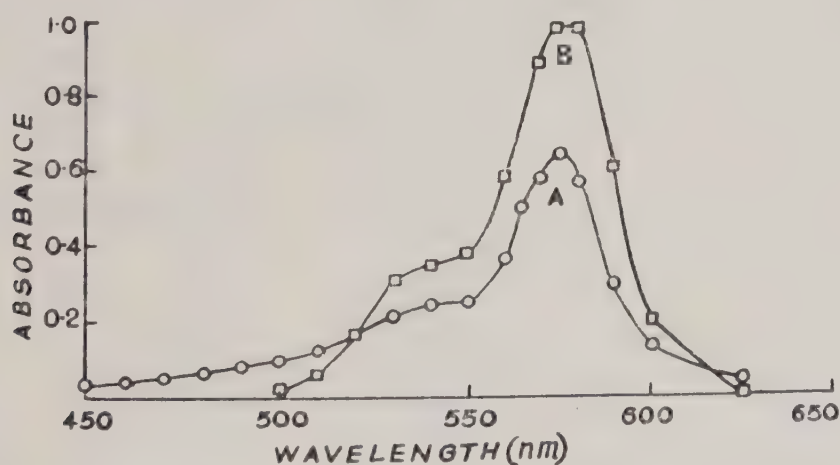

FIG. 1. Absorption spectra of zinc-phenanthroline-rose bengal ternary complexes in chloroform and in nitrobenzene. Zinc 1 × 10^{-5}M, phenanthroline 2.5 × 10^{-4}M, rose bengal 2.5 × 10^{-4}M.

A. CHLOROFORM   B. NITRO BENZENE

dithiocarbamate (DDTC) at pH 4, followed by back extraction of zinc (II) from the organic phase with 10 ml of 0.4 M hydrochloric acid. Then after adding 1 ml of 10^{-1} M sodium thiosulphate to this solution, zinc (II) can be determined quantitatively by adopting the extraction procedure.

The above procedure has been applied for the determination of zinc in BCS copper base alloys No. 183/2 and 304 and the results are presented in Table II. The present method is more sensitive ($\epsilon = 1 \times 10^5$), rapid and selective than the widely use dithizone method ($\epsilon = 8.69 \times 10^4$) for the spectrophotometric determination of the zinc[3]. In the dithizone method for the determination of zinc mixed colour procedures are not applicable in the presence of appreciable quantities of copper, manganese, tin, lead and iron etc., while the monocolour procedures involve tedious washing process for the removal of excess of dithizone. While a number of other ternary systems[4-8] of zinc with thiocyanate and some dye stuffs have been repoted for the extraction and spectrophotometric determination of zinc, they are also less sensitive than the present method and not suitable for the analysis of practical samples.

Nature of the extracting species : In order to examine the composition of the extracting species in these ternary systems in chloroform and in nitrobenzene, job's continuous variation plots were made, keeping either the dye or the phenanthroline concentration in constant excess, and varying the mole ratio of zinc to phenanthroline or zinc to dye respectively. The curves confirm that ratio of zinc : phenanthroline : dye anion in the extracting species is 1 : 2 : 1 in chloroform and 1 : 3 : 1 nitrobenzene. Fluorescein and its halogen substituted dyes are known to exist as divalent anions in the pH range 5.4 to 10[9,10] Fig. 2 shows the job's curve for zinc (II) to phenanthroline ratio of the zinc-phenanthroline-rose bengal ternary system in chloroform and in

TABLE II

Analysis of B. C. S. copper base alloys for zinc .

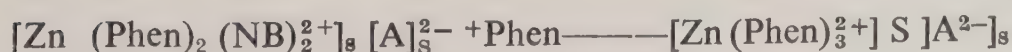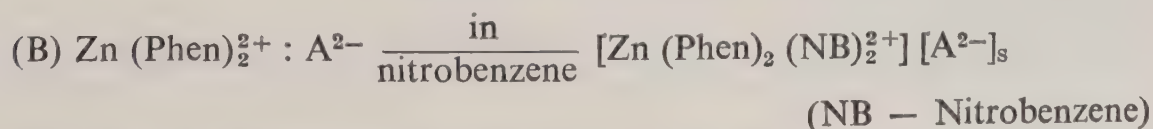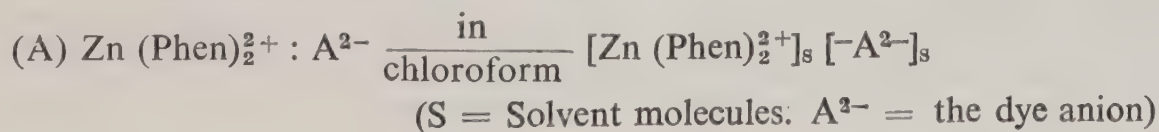| Alloy Composition %	Sample taken mg	Zinc found %	Relative error %	Relative mean deviation	Standard deviation
BCS No. 183/2 Bronze	80.2	5.14,5.09,5.25 5.22	0.39,1.36,1.74 1.16	1.16	7.33×10^{-2}
Cu 85.0 Sn 5.03	100.2	5.08,5.11,5.12 5.19	1.55,0.97,0.78 0.58	0.63	4.65×10^{-2}
Zn 5.16 Pb 3.3 P 0.51 Ni 0.51 Sb 0.24 As 0.14	118.0	5.10,5.12,5.16 5.21	1.16,0.78,0.00 0.97	0.73	4.86×10^{-2}
BCS No. 304 Alluminium Bronze Cu 80.4 Al 8.92	760.0	0.58,0.60,0.61 0.62	3.33,0.00,1.67 3.33	2.08	1.71×10^{-2}
Ni 4.75 Fe 4.71 Mn 0.51 Zn 0.60	900.0	0.58,0.59,0.61 0.61	3.33,1.67,1.67 1.67	2.08	1.50×10^{-2}
Si 0.19	998.8	0.59,0.60,0.59 0.60	1.67,0.00,0.00 0.00	0.84	5.77×10^{-3}
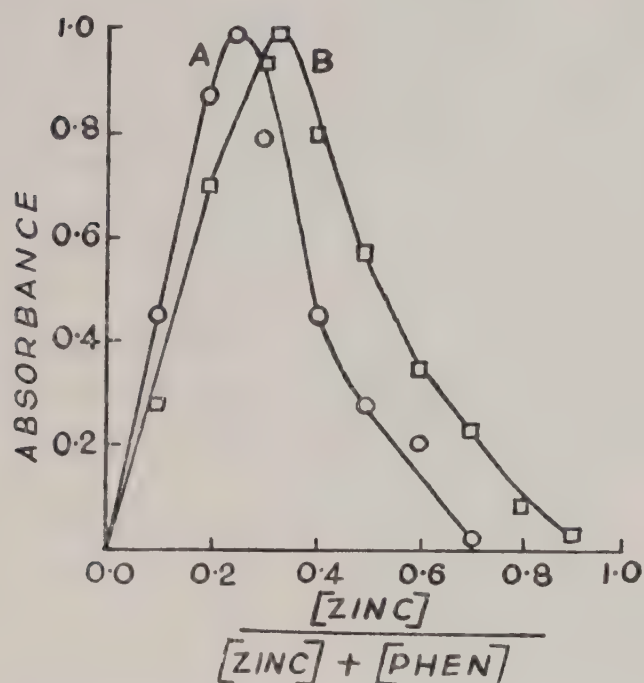
FIG. 2. Determination of phenanthroline number of zinc-phenanthroline-rose bengal ternary systems Job's method of continuous variations. Zinc(II) + 1, 10 phenanthroline 5×10^{-5}M rose bengal 5×10^{-4}M.

A. NITROBENZENE   B. CHLOROFORM

nitrobenzene. The results were further confirmed by log (distribution ratio) vs log (reagent) plot. Similar observation were made with 2,2' bipyridyl as chelating agent in place of 1.10 phenanthroline.

The difference in the composition of the extracting species in chloroform and in nitrobenzene is very interesting; this can be explained on the basis of the donocity and dielectric costant of the solvent. According to Gutmann[11] chloroform has donocity number zero and acceptor number 23.1 while those for nitrobenzene are 4.4 and 14.8 respectively. Because of the large dielectric constant of nitrobenzene (34.4) the distance between the cationic and anionic components of ion association complexes in nitrobenzene medium is large compared to that of in chloroform, which has a small dielectric constant. In view of the donor properties of nitrobenzene, it is assumed that solvent coordinates with the metal in 2:1 and is subsequently displaced by phenanthroline as shown below:

(A) $Zn (Phen)_2^{2+} : A^{2-} \xrightarrow[\text{chloroform}]{\text{in}} [Zn (Phen)_2^{2+}]_s [^-A^{2-}]_s$

(S = Solvent molecules. A^{2-} = the dye anion)

(B) $Zn (Phen)_2^{2+} : A^{2-} \xrightarrow[\text{nitrobenzene}]{\text{in}} [Zn (Phen)_2 (NB)_2^{2+}] [A^{2-}]_s$

(NB — Nitrobenzene)

$[Zn (Phen)_2 (NB)_2^{2+}]_s [A]_s^{2-} + Phen \text{———} [Zn (Phen)_3^{2+}] S]A^{2-}]_s$

Harris and Mckenzie[12] showed evidence for such type of solvent displacement in their work on copper complexes. Masoud[13] observed that octahedral nickel complexes

are preferentially stabilized in nitrobenzene. The conditional extraction of these ternary systems with various dye anions were determined by method of Likussar and Boltz[14]. The extracion efficiency of various fluorescein dye anions as counter ions in extracting the zinc-phenanthroline cationic complexes into nitrobenzene as indicated from their conditional extractions constants determined as above (See Table I) is found to be in the order rose bengal E (tetrachlorotetraiodofluorecein) > erythrosin (tetraiodofluorescein) > eosin (tetrabromofluorescein) > dichlorofluorescein > fluorescein. This order is further confirmed by comparing the extraction of zinc (II) achieved in the presence of a large excess phenanthroline and insufficient fixed concentration of the various dye anions. From these findings and the absorption charcteristics, it can be generalised that degree of extraction of these ternary complexes increase accompanied by bathochromic shift in the absorption maxima with increase in halogenation and increase in the atomic number of the halogen substituents in the fluorescein dyes which serve as counter ions. These may be due to the decrease in the degree of hydration of these counter ions in that order. In the case of 2,2' bipyridyl, only rose bengal, erythrosin and eosin could extract the ion association complex, where as with fluorescein and dichlorofluorscein the extraction of ion pairs is negligible, both in chloroform and in nitrobenzene.

ACKNOWLEDGEMENT

REFERENCES

1. I M Kolthoff, D L Leussing and T S Lee, *J. Am. Chem. Soc.* **73** (1951) 390.
2. M M Tonanaiko and N S Bilenko, *Anal. Khim.* **30** (1975) 689.
3. S S Cooper and M L Sullivan, *Analyt. Chemistry* **23** (1951) 613.
4. P P Kish, I I Zimomorya and Yu A Zoltov, *Zh. Anal. Khim.* **28** (1973) 252.
5. A K Babko and Z I Chalaya, *Zh. Anal. Khim.* **17** (1962) 286.
6. A T Philipenko, P P Kish and I I Zimomorya, *Ukr. Khim. Zh.* **37** (1971) 186.
7. Z Slovak and M Pribyl, *Collect Chech. Chem. Commun.* **31** (1966) 1742.
8. A K Babko and Z I Chalaya, *Zh. Anal. Khim,* **16** (1961) 268.
9. R A Bhobe and L Pardeshi, *J. Indian Chem. Soc.* **8** (1969) 755.
10. B W Bailey, A M Dagnall and T S West, *Talanta* **13** (1966) 753.
11. V Gutmann, *Chimia* **31** (1977).
12. C M Harris and E D Mckanzie, *J. Inorg. nucl. Chem.* **29** (1967) 1047
13. M S Masoud, *J. Inorg. nucl. Chem.* **39** (1977) 413.
14. W Likussar and D F Boltz, *Analyt. Chem.* **43** (1971) 1265.

FORM IV

(See Rule 8)

Place of Publication   .. New Delhi

Periodicity of its Publication   .. Monthly (Published as a part in alternate
                 months of January-November)

Printer's Name   .. A. K. Bose
Nationality   .. Indian
Address   .. Indian National Science Academy
                 Bahadur Shah Zafar Marg
                 New Delhi 110002

Publisher's Name   .. A. K. Bose
Nationality   .. Indian
Address   .. Indian National Science Academy
                 Bahadur Shah Zafar Marg
                 New Delhi 110002

Editor's Name   .. A. N. Mitra
Nationality   .. Indian
Address   .. Indian National Science Academy
                 Bahadur Shah Zafar Marg
                 New Delhi 110002

Names and addresses of individuals
who own the Newspaper and partners
or shareholders holding more than
one per cent of the total capital

   I, A. K. Bose hereby declare that the particulars given above are true to the
best of my knowledge and belief.

                        Sd/- A. K. Bose
                      Signature of Publisher

Dated : 31 March, 1985

Procedure for submitting manuscript

General : Manuscripts should be sent, *in triplicate* (with 3 sets af illustrations, *one* original and *two* photocopies) to the *Editor of Publications, Proceedings A, Indian National Science Academy, Bahadur Shah Zafar Marg, New Delhi*-110 002.

Submission of the manuscript will be held to imply that it has not been previously published in any form and is not under consideration for publication elsewhere.

Presentation : Articles should be as brief as full documentation allows. They should not usually exceed 12 printed pages (approx. 12,000 words). Review articles may be upto 20 pages. Papers must be written clearly and concisely with consistency in style and spelling (spellings should be according to Oxford Dictionary), and typed double spaced with ample margins on durable bond paper. The usual format is: 'Abstract', 'Key words', 'Introduction', 'Materials and Methods', 'Results', 'Discussion', and 'Acknowledgement' (if any) and 'References'.

Classification : The exact classification of the paper (e.g., Astrophysics, Inorganic, Organic and Physical Chemistry, Seismology etc.) should be provided at the top of the manuscript.

Title : Title should be brief, specific and informative of the subject discussed. It should not begin with such general words as 'The', 'A', 'Study', 'Effect'. If a paper forms part of a series, this may be indicated through a symbol in the title and a footnote "This is paper X in series. Paper on IX is ref ....". The preceding paper must then be included in the list of references.

Running Title : Should not exceed 50 characters (including spaces).

Keywords : Up to five important key words should be provided for indexing and for information retrieval.

Abbreviations : Non-standard abbreviations used five or more times in the text should be listed in the footnote. Define where first mentioned followed by abbreviation in parentheses. Subsequently, the abbreviations should be used. However, these should be kept to a minimum and should not be used in the titles, key words or abstract.

Abstract : The abstract (typed on a separate page) should summarize the principal findings within 250 words.

Text : The paper must be divided into sections preferably starting with 'Introduction' and ending with 'Discussion' (or 'Acknowledgement', if any). All measurements must be given in SI units. Avoid numbers at the beginning of a sentence or spell them out. The scientific names of plants minerals, and animals should be underlined. Authors of name of taxa should be cited at the first mention of a taxon, but not elsewhere. Accepted common names of plants and animals should neither be capitalized nor placed within quotation marks. Words and phrases of foreign origin in common use need not be underlined (e.g., *et al.*, viz. e.g.,

i.e., etc.) whereas the rest should be underlined (e.g., *in vitro, in situ*).

Tables : All tables must be numbered serially in roman numerals and placed at the end. The table should have brief titles (*underlined*) and contents should be self-explanatory. Non-standard abbreviations should be used sparingly and defined at the bottom of the table. Also details of the experiment (not mentioned in the text) may be indicated below the table.

Illustrations : Original drawings (in India ink in clean uniform lines on tracing paper or Bristol paper) and sharp photographs (with high contrast and glossy prints) numbered in arabic numerals should be provided. Illustrations on reduction must fit into a minimum of 6.5 cm and a maximum of 12.5 cm width. Labelling of figures should therefore be done keeping in view the reduction (blow-up) into (6.5 cm or 12.5 cm). Magnification should be indicated in the legend be scale or figures (x ....). For composite figures. mounting should be done carefully with even spacing in between. Illustrations should be supported wjth cardboard to avoid damage in transit.

References : References in the text should be cited by number. References at the end of the paper should be listed by number, author's name, title of paper, name of journal (underlined and abbreviated according to the *World List of Scientific Periodicals* Butterworths, London), Vol. no, year of publication and page no. References to book should include : name of author, title of the book (underlined), name of editor if any, preceded by 'Ed(s)', place of publication, publisher, year of publication chapter or pages referred to. References to thesis, the degree, the year for which submitted, the university and the place. Sample citation are given below :

For periodicals
[1]R. H. Fox, *Fund Math.* **34** (1947) 278

For books
[1]H. Rund, *The Differential Geometry of Finsler Spaces*, Springer-Verlage, Berlin (1953) p. 283

Proofs : Proofs will be sent to the author(s) and should be returned to the Editor within 48 hours. Major corrections or alterations will be accepted only at author's expense*. If proofs are not returned within the specified time, they will be read in the Editorial Office and print-ordered.

Reprints : Fifty reprints will be supplied free of charge to the authors. Additional copies should be ordered on the order-from accompanying the proofs. Payment for extra reprints must accompany the order-form.

---

*The recomposition cost will be charged to the author. In case the author desires to withdraw the paper, he shall pay towards the composition charges, if the paper has already been type-set.

Proceedings of the
Indian National Science Academy

CONTENTS   *Page*